

2021

A New Generation of Smart Multifunctional Additive for High-Temperature Lubrication in Metal Forming Processes

Sang T. Pham

Follow this and additional works at: <https://ro.uow.edu.au/theses1>

University of Wollongong

Copyright Warning

You may print or download ONE copy of this document for the purpose of your own research or study. The University does not authorise you to copy, communicate or otherwise make available electronically to any other person any copyright material contained on this site.

You are reminded of the following: This work is copyright. Apart from any use permitted under the Copyright Act 1968, no part of this work may be reproduced by any process, nor may any other exclusive right be exercised, without the permission of the author. Copyright owners are entitled to take legal action against persons who infringe their copyright. A reproduction of material that is protected by copyright may be a copyright infringement. A court may impose penalties and award damages in relation to offences and infringements relating to copyright material.

Higher penalties may apply, and higher damages may be awarded, for offences and infringements involving the conversion of material into digital or electronic form.

Unless otherwise indicated, the views expressed in this thesis are those of the author and do not necessarily represent the views of the University of Wollongong.

Research Online is the open access institutional repository for the University of Wollongong. For further information contact the UOW Library: research-pubs@uow.edu.au



UNIVERSITY
OF WOLLONGONG
AUSTRALIA

A New Generation of Smart Multifunctional Additive for High-Temperature Lubrication in Metal Forming Processes

Sang T. Pham

Supervisors:

Senior Professor Anh Kiet Tieu

Dr Vitor Sencadas

Professor Shanhong Wan

This thesis is presented as part of the requirement for the conferral of the degree:
Doctor of Philosophy

University of Wollongong

School of Mechanical, Materials, Mechatronics and Biomedical Engineering

August - 2021

DECLARATION

I, Sang T. Pham, declare that this thesis submitted in fulfillment of the requirements for the conferral of the degree Doctor of Philosophy, from the University of Wollongong, is wholly my own work unless otherwise referenced or acknowledged. This document has not been submitted for qualifications at any other academic institution.

Sang T. Pham

Wollongong, August 2021

ACKNOWLEDGMENTS

First and foremost, I would like to express my heartfelt gratitude to my principal supervisor, Professor Kiet Anh Tieu. Thank you for accepting me into your research group to embark on postgraduate study. Thank you for your dedicated guidance, your support; and most importantly, your inspiration. I really appreciate our fruitful discussions during my postgraduate study which not only sharpened my thought process but also showed me how to create new ideas for the research. I also truly appreciate your generosity in supporting me to pursue my research ambition on the application of advanced electron microscopies and *in-situ* facilities during my research. Your wisdom was very much my pillar of support which indeed inspire me to pursue my career as an independent researcher in the future. I consider myself blessed to have you as my principal supervisor.

I am also indebted to my co-supervisor, Dr. Vitor Sencadas: Thank you for all the instructive advice and valuable knowledge that you have provided me during my research. Thank you very much for allowing me to work in your lab. Without your support, I would not finish my research works with satisfaction. I also enjoy our informal chat about your life, your research, and your teaching experiences when working with you. Thank you for also being my mentor in both academic research and life as well as providing me with the necessary materials for my research studies.

I am also grateful to my other co-supervisor, Professor Shanhong Wan, for your constant encouragement and guidance in the first two years of my doctoral study. Thank you so much for your thoughtfulness in both my research and my living. Although we had only worked with each other for two years in Australia, I truly acknowledge your physical and mental supports.

I would like to express my gratitude to Dr. Mitchell Nancarrow, Dr. David Mitchell, and Dr. Gilberto Casillas at the Electron Microscopy Centre for their professional assistance and training in advanced electron microscopies. To Dr. Mitchell Nancarrow: Thank you for your patience in teaching and training SEM-EDS, FIB, and TOF-SIMS for me which has a huge contribution to my research works. Congratulations on the new little addition to your family! To Dr. David Mitchell: I truly appreciate your assistance and advice when working with you in aberration-corrected STEM and EELS. I am always indebted for your sharing and guidance in writing a good scientific paper as well as your teaching in electron microscopies. To Dr. Gilberto Casillas: Thank you so much for your dedicated assistance, training, and teaching in TEM, electron diffraction patterns, and *in-situ* TEM experiments. Your creativity in utilizing *in-situ* facilities as well as your extensive knowledge about TEM has impressed and inspired me a lot. Best wishes for your new role in Belgium!

I also owe a thank to Professor Paul Else, Dr. Buyung Kosasih, Dr. Hongtao Zhu, Dr. Shaogang Cui, and Dr. Bach Tran for their help and support in the early days of my study.

I also specifically appreciate the prioritizing supports from all the staff within the Faculty of Engineering and Information Sciences, especially Mr. Steward Rodd, Mr. Leighton Hill, and Mr.

Alex Gonzalez for their kind assistance in the sample preparation and equipment repair.

Thank you so much Mr. Matthew Franklin for your kind assistance in organizing my extensive experiments in Material Lab and in providing the essential materials and chemicals during my research works. Without your dedicated and keen supports, my research studies would not be completed.

Thank you my best coffee buddy – Mr. Huynh H. Nguyen. You are indeed my precious friend during a Ph.D. journey. I truly appreciate every moment that we shared during doctoral research. The time that we studied and grew together in Ph.D. research will be one of my vivid and joyful memory.

I would like to extend my appreciation to my fellow lab mates: Dr. Ta Dinh Thi, Dr. Ta Thi Thuy Huong, Mr. Tran Van Nam, Ms. Dao Ly Kiet Tuong, Mr. Huynh Kim Khai, Dr. Tran Manh Ha, Mr. Nguyen Do Xuan Vinh, Mr. Nguyen Ba Hieu, Mr. Long Wang, and Dr. Guanyu Deng who have been working with me and sharing their knowledge and experience to me. I am delighted to be part of such a dynamic and thoughtful team. Thank you for all the joy and friendships that help me overcome depression and make my research smoother.

I also would like to express my great gratitude and love to my beloved family in Vietnam for their unconditional love and support both physically and mentally that encourage me to concentrate on my pursuits. To my dear grandfathers, may you rest in eternal peace. Although you cannot be here to see me obtaining a Ph.D. degree as promised, I believe that you are watching over my step in heaven as you always did from the beginning of my Ph.D. study. You are ever in our hearts and I believe that we will see you again one day.

Finally and most importantly, I would love to express my deepest gratitude to my dearest fiancé, Ms. Do Thi Phuong, for your true love and your dedication during my doctoral research. Although we are always over 10,000 km apart, you always encouraged and did pick me up several times when I was at the peak of desperation with my study and paper submission. Without you, this work would be nowhere near done. You mean the world to me and I miss you a lot.

LIST OF PUBLICATIONS

1. **Sang T. Pham**, Kiet A. Tieu, Shanhong Wan, Jingcheng Hao, Hongtao Zhu, Huynh H. Nguyen, David R. G. Mitchell, *Oxidative and Frictional Behavior of a Binary Sodium Borate–Silicate Composite in High-Temperature Lubricant Applications*, **Ind. Eng. Chem. Res.** 2020 59 (7), 2921-2933.
2. **Sang T. Pham**, Kiet A. Tieu, Shanhong Wan, Jingcheng Hao, Hongtao Zhu, Nam V. Tran, Phuong T. Do, *Intrinsic Effect of Alkali Concentration on Oxidation Reactivity and High-Temperature Lubricity of Silicate Melts between Rubbed Steel/Steel Contacts*, **Langmuir** 2020 36 (27), 7850-7860.
3. **Sang T. Pham**, Kiet A. Tieu, Shanhong Wan, Jingcheng Hao, Huynh H. Nguyen, David R. G. Mitchell, Vitor Sencadas, *Intrinsic Effect of Nanoparticles on the Mechanical Rupture of Doubled-Shell Colloidal Capsule via In Situ TEM Mechanical Testing and STEM Interfacial Analysis*, **Small** 2020, 16, 2001978.
4. **Sang T. Pham**, Kiet A. Tieu, Vitor Sencadas, Weiwei Lei, Dan Liu, Shanhong Wan, Jingcheng Hao, *Smart-Responsive Colloidal Capsules as an Emerging Tool to Design a Multifunctional Lubricant Additive*, **ACS Appl. Mater. Interfaces**, 2021 13 (6), 7714-7724.
5. **Sang T. Pham**, Kiet A. Tieu, Vitor Sencadas, Mitchell J. B. Nancarrow, Germanas Peleckis, Huynh H. Nguyen, *Insight into the mechanical behavior of hybrid colloidal capsule at elevated temperatures by direct visualization of the interfacial solid-state reactions*, **J. Phys. Chem. C.**, 2021 125 (31), 17462-17473.
6. **Sang T. Pham**, Kiet A. Tieu, Shanhong Wan, Weiwei Lei, Dan Liu, Nam V. Tran, *Anti-Oxidation Mechanism and Interfacial Chemistry of BN@CaCO₃-SiO₂ Microcapsule-Added Sodium Borate Melt on the Sliding Steel Surfaces at Elevated Temperatures*, **Appl. Surf. Sci.**, 2021, 150556.
7. **Sang T. Pham**, Kiet A. Tieu, Vitor Sencadas, Paul Joseph, Malavika Arun, Khai K. Huynh, Long Wang, *Thermo-Responsive Water-Containing Hybrid Colloidal Capsules as an Inorganic Additive for Fire-Resisted Silicone-Based Polymeric Coatings*, submitted to **Ind. Eng. Chem. Res.** (in peer review).
8. **Sang T. Pham**, Khai. H. Huynh, Kiet A. Tieu, *Tribological performances of ceramic oxide nanoparticle additives in sodium borate melt under steel/steel sliding contacts at high temperatures*, **Tribol. Int.** 2022, 165, 107296.
9. **Sang T. Pham**, Shanhong Wan, Kiet A. Tieu, Ming Ma, Hongtao Zhu, Huynh H. Nguyen, David R. G. Mitchell, Mitchell J. Nancarrow, *Unusual Competitive and Synergistic Effects of Graphite Nanoplates in Engine Oil on the Tribofilm Formation*, **Adv. Mater. Interfaces.** 2019, 6, 1901081.

10. Huynh H. Nguyen, Shanhong Wan, Kiet A. Tieu, Hongtao Zhu, **Sang T. Pham**, *Rendering Hydrophilic Glass-Ceramic Enamel Surfaces Hydrophobic by Acid Etching and Surface Silanization for Heat Transfer Applications*, **Surf. Coat. Technol.** 2019, 370, 82-96.
11. Huynh H. Nguyen, Shanhong Wan, Kiet A. Tieu, **Sang T. Pham**, Hongtao Zhu, *Tribological Behaviour of Enamel Coatings*, **Wear** 2019, 426, 319-329.
12. Shanhong Wan, Yana Xia, **Sang T. Pham**, Kiet A. Tieu, Hongtao Zhu, Qinglin Li, *Unveiling Oil-Additive/Surface Hierarchy at Real Ring-Liner Contact*, **Surf. Interfaces.** 2019, 15, 1-10.
13. Shanhong Wan, Huynh H. Nguyen, **Sang T. Pham**, Kiet A. Tieu, Hongtao Zhu, Thi Dinh Ta, Qiang Zhu, *Temperature/Shear-Induced Interface Reconstruction of Hot Rolled Carbon Steel Lubricated by Polyphosphate Composite Lubricants*, **Tribol. Int.** 2019, 140, 105863.
14. Nam V. Tran, Kiet A. Tieu, Hongtao Zhu, Huong T. T. Ta, **Sang T. Pham**, Ha M. Le, Thi D. Ta, *Insights into the Tribochemistry of Sliding Iron Oxide Surfaces Lubricated by Sodium Silicate Glasses: An Ab Initio Molecular Dynamics Study*, **Appl. Surf. Sci.** 2020, 528, 147008.
15. Liuyang Bai, Shanhong Wan, Gewen Yi, Yu Shan, **Sang T. Pham**, Kiet A. Tieu, Yan Li, Rendong Wang, *Temperature-Mediated Tribological Characteristics of 40CrNiMoA Steel and Inconel 718 Alloy during Sliding Against Si₃N₄ Counterparts*, **Friction** 2020, 1-23.
16. Huynh H. Nguyen, Kiet A. Tieu, Shanhong Wan, Hongtao Zhu, **Sang T. Pham**, Benjamin Johnston, *Surface Characteristics and Wettability of Superhydrophobic Silanized Inorganic Glass Coating Surfaces Textured with a Picosecond Laser*, **Appl. Surf. Sci.** 2021, 537, 147808.
17. Long Wang, Kiet A. Tieu, Jun Wang, **Sang T. Pham**, Chunyang Xia, Hongtao Zhu, Guanyu Deng, *High Load Capability, Sticking Scale Inhabitation and Promising Lubrication of Sodium Carbonate Coating for Steel/Steel Contact at High Temperature*, **Tribol. Int.** 2021, 153, 106594.
18. Huwei Sun, Gewen Yi, Shanhong Wan, Peiyong Shi, Jun Yang, **Sang T. Pham**, Kiet A. Tieu, Thi Dinh Ta, *Effect of Adding Soft Bi₂O₃ on Structural Modification and Tribological Regulation of Ni-5 wt% Al Composite Coating in Wide Temperatures Range*, **Surf. Coat. Technol.** 2021, 405, 126517.
19. Peiyong Shi, Gewen Yi, Shanhong Wan, Huwei Sun, Xiaochun Feng, **Sang T. Pham**, Kiet A. Tieu, Erqing Xie, Qihua Wang, *High Temperature Tribological Performance of Nickel-Based Composite Coatings by Incorporating Multiple Oxides (TiO₂-ZnO-MoO₃)*, **Tribol. Int.** 2021, 155, 106759.
20. Khai K. Huynh, Kiet A. Tieu, **Sang T. Pham**, *Synergistic and Competitive Effects between Zinc Dialkyldithiophosphates and Modern Generation of Additives in Engine Oil*, **Lubricants** 2021, 9 (4), 35.

21. Fei Ma, **Sang T. Pham**, Shanhong Wan, Lingyan Guo, Gewen Yi, Yana Xia, Shaobao Qi, Hongtao Zhu, Thi Dinh Ta, *Evaluation of Tribological Performance of Oxide Nanoparticles in Fully Formulated Engine Oil and Possible Interacting Mechanism at Sliding Contacts*, **Surf. Interfaces**. 2021, 101127.
22. Huynh H. Nguyen, Kiet A. Tieu, Bach H. Tran, Shanhong Wan, Hongtao Zhu, **Sang T. Pham**, *Porosity-Induced Mechanically Robust Superhydrophobicity by the Sintering and Silanization of Hydrophilic Porous Diatomaceous Earth*, **J. Colloid Interface Sci.** 2021, 589, 242-251.
23. Long Wang, Kiet A. Tieu, Guojuan Hai, Jiaqing Li, Hongtao Zhu, **Sang T. Pham**, Jun Yang, *Na₂CO₃ and Graphene Nanocomposites Toward Efficient Lubrication*, **Carbon** 2021, 177, 138-150.

ABSTRACT

High-temperature lubrication plays a critical role in various engineering processes of hot metal forming (e.g. hot forging, hot rolling, hot extrusion...). It has been acknowledged that high energy efficiency, low material losses, and optimum product quality can be achieved by the application of effective lubricants. Although sodium-containing glass melts have proven themselves as the outstanding candidate lubricant for hot metalworking processes, they have reached their performance limit. In addition, the concern about the corrosion of sodium toward oxide scale is also highlighted. The current study not only puts an effort into improving the lubricity of the existing melt lubricants but also concentrates on the formulation of the lubricant package for high-temperature manufacturing processes. Particularly, the development of the novel multifunctional lubricant additives from the existing solid lubricants is at the heart of the research activities.

In the very first part of the research work, the effect of different nanoparticles in the tribological performance of the sodium borate melt at 930°C is investigated. Characterizations of wear surfaces in terms of morphology and interfacial chemistry have also been conducted to address the lubrication and anti-oxidation mechanisms. SiO₂ nanoparticles show the best improvement (by over 50%) in anti-oxidation and lubrication performance of sodium borate outperforming other nanoparticles and nanoplates which is due to the reaction between SiO₂ and sodium borate to form sodium borosilicate. In contrast, CaCO₃ nanoparticles show no improvement in anti-oxidation and lubrication of the sodium borate melt, however, it can reduce the corrosion attack of sodium and the boriding effect on the oxide scale. Meanwhile, Al₂O₃ nanoparticles show good improvement in the anti-oxidation performance of sodium borate, however, they promote sodium corrosion on the oxide scale and deteriorate the lubrication performance. TiO₂ and ZrO₂ nanoparticles moderately improve the friction and wear reductions of sodium borate melt although their contribution in anti-oxidation and inhibition of boriding effect on the oxide scale is negligible. h-BN nanosheets and graphite nanoplates show no improvement in the anti-oxidation and lubrication performance of sodium borate which is due to their decomposition at 930°C.

In a second part, an attempt to combine SiO₂ and CaCO₃, as the outstanding lubricant and anti-oxidant additives in synergy with sodium borate melt at high temperatures, is first carried out by the utilization of Pickering emulsion templated assembly microencapsulation. Different synthesis conditions are conducted to examine the formation of an intact CaCO₃-decorated SiO₂ double-shell colloidal capsule containing a water core. The intact spherical colloidal capsules with a size distribution of $7.5 \pm 1.8 \mu\text{m}$ are obtained at 1g CaCO₃ nanoparticles in 10 ml toluene (continuous phase), 1 ml water as a dispersed phase, 50 mg/ml n-hexylamine concentration, 1 ml (0.5, 0.3, 0.2 ml) TEOS addition within 24 hrs of reaction. Morphological and structural characterizations show the bi-layered hierarchical structure of the colloidal capsule with the densely packed CaCO₃ nanoparticles as an outer shell ($460 \pm 20 \text{ nm}$) and an inner homogeneous SiO₂ shell ($166 \pm 14 \text{ nm}$).

The next study in this dissertation dedicates to investigate the mechanical and thermal properties of the CaCO₃-decorated SiO₂ double-shell colloidal capsules which are imperative for high-

temperature applications. The thermal robustness of the colloidal capsule can reach over 1000°C as examined by *in-situ* SEM heating. The mechanical strength of the CaCO₃-decorated SiO₂ double shell is superior to the single SiO₂ shell as demonstrated by an *in-situ* TEM mechanical compression testing. The presence of a densely packed outer shell, which chemically bonds to the inner shell, results in such enhancement as discovered by aberration-corrected STEM coupled with EELS analysis. Intriguingly, the transformation from brittle to ductile with significant improvement in the compressive strength and strain at failure of the colloidal capsule is observed after annealing at 1000°C. This change is unusual and has not been observed before for the inorganic shell materials. For the first time, direct visualization of the chemical diffusion through the shell interface during annealing has been introduced by the application of a newly developed multi-modal correlative *in-situ* TOF-SIMS heating technique. Combining with *in-situ* TEM heating, the chemical diffusion in correlation with the structural transformation at the nanoscale can be correlated that elucidates the mechanics of the double-shell at high temperatures.

The CaCO₃-decorated SiO₂ double-shell shows excellent thermo-mechanical stability with a tunable mechanical strength which has a huge potential in the protection of the heat-sensitive core. In the next part of this dissertation, the double-shell is applied to encapsulate the h-BN nanosheets. The innovative CaCO₃-decorated SiO₂ double-shell colloidal capsule containing h-BN nanosheets has been used as a lubricant additive in conjunction with sodium borate melt. It has been found that the anti-oxidation of sodium borate melt improves by 93.3% while friction and wear reduce by over 70% when this novel additive is added. Advanced characterization and analysis are performed to address the working mechanics of this additive under the sodium borate melt in terms of friction, wear, oxidation, and sodium corrosion at elevated temperatures. The superior anti-oxidation mechanism with a less corrosive attack and boriding effect on the steel is due to the presence of calcium and silica phase in the melt network that reduces the mobility and the reactivity of sodium toward the oxide scale. Meanwhile, the formation of plate-like non-layered M-type hexaferrite particles at the sliding interfaces in combination with the presence of h-BN nanosheets and the grain-refinement of the sliding surfaces is responsible for the superior friction reduction (by 71.2%) compared to sodium borate melt. The obtained results are believed to introduce the new strategy for the formulation and customization of the high-temperature lubricant packages.

TABLE OF CONTENTS

CHAPTER 1	1
Introduction	1
CHAPTER 2	3
Literature Review	3
2.1. Problems encountering at high-temperature steel/steel contacts	3
2.2. Oxidation, friction, and wear behavior under steel/steel contacts at elevated temperatures	3
2.3. Lubrication of steel/steel contacts at high temperatures	7
2.4. Solid lubricants for high-temperature lubrication processes	9
2.5. Recent progress in high-temperature inorganic melt lubricants	18
2.6. Microencapsulation in the development of lubricant additives	30
2.7. Designing a strategy for novel high-temperature lubricant additives based on microencapsulation	41
2.8. Proposed research scopes	43
CHAPTER 3	46
Experimental methodology and characterization techniques	46
3.1. High-temperature friction and wear experiments	46
3.2. Analytical methodology	48
CHAPTER 4	52
A study on the tribological performances of nanoparticles under sodium borate melt lubrication	52
4.1. Experimental details	53
4.2. Results and Discussion	57

4.3. Conclusions	77
CHAPTER 5	78
Synthesis of the hybrid shell structure for the smart microcapsule from potential additives	78
5.1. Experimental details	79
5.2. Results and discussion	81
5.3. Conclusions	94
CHAPTER 6	95
Thermo-mechanical properties of the hybrid shell structure elucidated by novel <i>in-situ</i> analytical techniques	95
6.1. Experimental details	96
6.2. Results and Discussion	99
6.3. Conclusions	118
CHAPTER 7	120
Lubrication and anti-oxidation of colloidal capsule encapsulating h-BN nanosheets under sodium borate melt at elevated temperatures	120
7.1. Experimental details	121
7.2. Results and Discussion	124
7.3. Conclusions	143
CHAPTER 8	144
Anti-oxidation and lubrication mechanisms of the sodium borate formulated with the smart-responsive colloidal capsules under simulated hot rolling conditions at elevated temperatures	144
8.1. Experimental details	144

8.2. Results and Discussion	145
8.3. Conclusions	164
CHAPTER 9	166
Conclusions and recommendations for future work	166
9.1. Conclusions	166
9.2. Recommendations for future work	168
Appendix A.	170
LIST OF REFERENCES	173

List of Figures

Figure 2-1. Schematic showing the complex phenomena that occurred in high-temperature tribological processes ²⁵	3
Figure 2-2. Elementary steps during metal oxidation ³³	4
Figure 2-3. Coefficient of friction and wear scar volume as a function of time during like-on-like reciprocating sliding in the air (load-15 N; speed-8.3 Hz; amplitude-2.5 mm) ⁴⁵	6
Figure 2-4. Schematic of a Stribeck curve where η is the dynamic viscosity of the lubricant, N is the rotational speed, and P is the applied pressure ^{57, 58}	8
Figure 2-5. Schematic presenting the lubrication regimes of the hot rolling of steel processes ⁴	9
Figure 2-6. Possible lubrication mechanisms of nanoparticles with engine oils between the frictional surfaces ^{66, 73}	11
Figure 2-7. Schematic presenting the lubrication mechanism of TiO ₂ nanoparticles at the rubbing interfaces. ⁸⁸⁻⁹⁰	12
Figure 2-8. (a) Rolling force reduction from the hot rolling of stainless steel lubricated by CaCO ₃ -added oil lubricant and the lubrication mechanism at different sizes; (b) Mechanism of SiO ₂ nanoparticles in enhancing the surface qualities of the hot strip rolling. ^{91, 92}	13
Figure 2-9. Various types of layered materials and friction reduction mechanisms. Picture courtesy of Spear and colleagues ¹⁰²	14
Figure 2-10. AB and AA' interaction between layers in graphene and h-BN, respectively ¹⁰⁸	15
Figure 2-11. Common lubrication mechanism of 2D layered nanosheets as lubricant additive in the base lubricant ¹¹¹	15
Figure 2-12. Schematic of phosphate-tribofilm induced at elevated temperature under tribological test. ¹¹⁹	16
Figure 2-13. Schematic of phosphate-tribofilm induced at elevated temperature under tribological test. ¹³	17
Figure 2-14. Schematic of the tribofilm formation on the counterparts after sodium metasilicate lubrication at elevated temperatures. ¹⁴	18
Figure 2-15. a) Dynamic coefficient of friction for sliding couples in unlubricated and lubricated (various silicate lubricants) conditions for 600 seconds at 950°C. The inset shows the average coefficient of friction at steady state; b) Corresponding disc and ball wear loss volumes after frictional tests using various lubricants at 950°C. The inset picture is the 2D wear depth image of the disc and ball after the friction test.	19
Figure 2-16. Cross-sectional SEM images and EDS maps of the oxide layer formed on the lubricant-coated	

steel disc following isothermal oxidation at 920°C for 600 seconds: a) Sodium trisilicate; b) Sodium disilicate; c) Sodium metasilicate; and d) No-lubricant.	20
Figure 2-17. STEM-BF image of the cross-section taken from a disc wear track after sliding under trisilicate lubrication at 950°C. b) EDS maps of a) showing an elemental distribution; c) STEM-BF image of a cross-section taken from thick tribofilm region on the disc wear scar after being lubricated by disilicate at 950°C; d) EDS maps of (c) showing elemental distribution; e) STEM-BF image of a cross-section of a disc wear track following sliding under metasilicate lubrication at 950°C, and; f) EDS maps of e) showing elemental distribution in the tribofilm.	22
Figure 2-18. a) Magnified STEM-BF image of the tribofilm on the ball surface after being lubricated by sodium metasilicate; b) EDS line profile marked in a); c) HR-STEM image of silica-like layer, and; d) HR-STEM image of the reaction product layer.	23
Figure 2-19 Tribological results for a) Compositional dependence of the coefficient of friction at 800°C; b) Compositional dependence of the coefficient of friction at 950°C; and c) Temperature-dependence of the coefficient of friction for sample Si-B-1; d) Mean steady-state friction coefficient as a function of temperature and composition; e) Disc wear loss volume and f) Ball wear loss volume after friction testing as a function of temperature and composition.	24
Figure 2-20. Elemental distribution between the coated lubricants and the oxide layers after oxidation test at 800°C and 950°C by ESD mapping: (a)-(b) B; (c)-(d) Si-B-2; (e)-(f) Si-B-1; and (g)-(h) Si.	25
Figure 2-21. STEM-BF and STEM-HAADF images of the various layers produced in the disc wear scar after sliding under Si-B-1 lubrication at 800°C: a)-c) Details of the outermost carbon species layer and the adjacent reaction products layer; d)-f) Details of the mid-regions of the tribolayer showing the reaction products layer at the top; the amorphous glassy layer in the center and the iron oxide adjacent to the steel substrate at the bottom.	26
Figure 2-22. a) EELS B-K edge taken at the topmost layer (EELS 1); the adjacent reaction products layer (EELS 2); the mid amorphous glassy layer (EELS 3); and the oxide adjacent to the steel substrate (EELS 4). b) EELS C-K edge showing the distinct peaks of carbonate and amorphous carbon taken at the topmost layer.	27
Figure 2-23 Schematic displaying the microstructure evolution on a disc surface after friction test under sodium borax-silicate (Si-B-1) lubricant at 800°C, with the double bond switching phenomena of trigonal boron oxide unit in the intermediate borosilicate melt layer.	27
Figure 2-24 a) STEM-HAADF image of the outermost mixed reaction products layer on the ball under Si-B-1 lubrication at 800°C; b) STEM-HAADF image of the densely packed nano-crystalline layer between the outermost layer in a) and the steel substrate; c) SADP 1 captured from the region marked in a); d) SADP 2 captured from the region marked in b).	28
Figure 2-25. Lubrication performance and mechanism of the mixture between sodium metasilicate and expanded graphite. ¹⁶¹	29

Figure 2-26. Schematic presenting the idea behind the chemical-triggered release of the core ingredients. ¹⁶⁷	31
Figure 2-27. Schematic presenting the idea behind the thermal-triggered release of the core ingredients. ¹⁶⁷	32
Figure 2-28. Microcapsules coated on the inner end of the tape-referenced steel. ¹⁸⁰	34
Figure 2-29. (a) Partially embedded and (b) Fully embedded microcapsules inside the epoxy matrix. ^{164, 186}	35
Figure 2-30. Proposed lubrication mechanism of the lubricant containing friction modifier loaded in the PMMA microcapsules. ¹⁸⁷	36
Figure 2-31. Concept of the controlled release of friction modifiers or chemical additives from the microcapsules. ¹⁶⁴	36
Figure 2-32. Overview of the colloidal capsules and the approaches to fabricate them. ²⁰²	43
Figure 2-33. The schematic presenting the structure of the proposed colloidal capsule for this research.	44
Figure 2-34. Schematic presenting the flowchart of the intended works for the proposed study.	45
Figure 3-1. Digital image and simplified schematic of the high-temperature tribometer UMT3.	46
Figure 3-2. Digital image and simplified schematic of dual-beam FIB-SEM instrument ^{223, 224} .	50
Figure 3-3. Digital images of the in-situ facilities used in this study.	51
Figure 4-1. X-ray diffraction (XRD) analysis of the lubricant and as-received nanoparticles: (a) sodium tetraborate; (b) ceramic crystallite oxide nanoparticles; (c) ceramic amorphous oxide nanoparticles; and (d) layered nanoparticles.	54
Figure 4-2. TEM images of different nanoparticles used in this study: (a) Al ₂ O ₃ ; (b) CaCO ₃ ; (c) SiO ₂ ; (d) TiO ₂ ; (e) ZrO ₂ ; (f) h-BN nanosheets; (g) graphite nanoplates.	55
Figure 4-3. Z-average measurement by dynamic light scattering (DLS) showing the size distribution of the nanoparticles within the formulated water-based lubricants after ultrasonication and 24h-after ultrasonication.	56
Figure 4-4. (a) Dynamic friction behavior of dry friction, sodium borate lubrication, and sodium borate + nanoparticles lubrication tests; (b) Mean friction coefficient; (c) Disc wear loss volume; and, (d) Ball wear loss volume from different friction tests.	58
Figure 4-5. Disc wear track analysis by SEM and EDS from (a)-(c) Dry friction test and (d)-(f) NBO friction test.	60
Figure 4-6. Ball wear track analysis by SEM and EDS from (a)-(c) Dry friction test and (d)-(f) NBO friction test.	60

Figure 4-7. Disc wear track analysis by SEM and EDS from (a)-(c) NBO-Cal; (d)-(f) NBO-Si; (g)-(i) NBO-Al; (j)-(l) NBO-Ti; and (m)-(o) NBO-Zr friction tests.....	62
Figure 4-8. Ball wear track analysis by SEM and EDS from (a)-(c) NBO-Cal; (d)-(f) NBO-Si; (g)-(i) NBO-Al; (j)-(l) NBO-Ti; and (m)-(o) NBO-Zr friction tests.....	64
Figure 4-9. Disc wear track analysis by SEM and EDS from (a)-(c) NBO-BN; and (d)-(f) NBO-Gr friction tests.....	65
Figure 4-10. Ball wear track analysis by SEM and EDS from (a)-(c) NBO-BN; and (d)-(f) NBO-Gr friction tests.....	66
Figure 4-11. Cross-sectional analysis of the (a) non-coated steel and (b) NBO-coated steel after isothermal oxidation at 930°C.....	67
Figure 4-12. Cross-sectional analysis of the (a) NBO-Cal-coated steel; (b) NBO-Si-coated steel; (c) NBO-Al-coated steel; (d) NBO-Ti-coated steel; and (e) NBO-Zr-coated steel after isothermal oxidation at 930°C.....	68
Figure 4-13. Cross-sectional analysis of the (a) NBO-BN-coated steel and (b) NBO-Gr-coated steel after isothermal oxidation at 930°C.....	68
Figure 4-14. XRD analysis of the phases in the non-coated steel and lubricant-coated steel after isothermal oxidation test at 930°C.....	70
Figure 4-15. Cross-sectional analysis of the disc wear track after being lubricated by: (a) NBO-Cal; (b) NBO-Si; (c) NBO-Al ₂ O ₃ ; (d) NBO-Ti; and (e) NBO-Zr. As marked in the images, region (I) is the steel base; region (II) is the tribofilm, and; region (III) is the mounting resin.....	71
Figure 5-1. The synthesis process of colloidal capsules by Pickering emulsion-templated assembly using stearic acid-modified calcium carbonate nanoparticles.....	80
Figure 5-2. Capsule coating prepared on the mild carbon steel disc for thermal diffusivity measurement: a) Before thermal diffusivity test; and, b) After the thermal diffusivity test at 550°C.....	80
Figure 5-3. (a) Bright-field TEM image showing the CaCO ₃ nanoparticles morphology; (b) High-resolution TEM image at high magnifications; (c) XRD analysis; and (d) FTIR analysis of the CaCO ₃ nanoparticles.....	81
Figure 5-4. Optical observation of Pickering emulsion and droplet size distribution via the adjustment of the synthesized conditions. Variation of nanoparticles concentration with a W/O ratio of 1/10: (a) 1 g, (b) 0.5 g, and (c) 0.25 g CaCO ₃ nanoparticles. Variation of W/O ratio with 1 g CaCO ₃ nanoparticles: (d) 0.5/10, and (e) 0.25/10. (f) Summary of mean size of Pickering emulsion droplets via the adjustment of the amount of CaCO ₃ nanoparticles and water-oil-ratio (W/O ratio).....	82
Figure 5-5. SEM images showing the effect of CaCO ₃ nanoparticle concentration on the formation of the colloidal capsules: (a)-(b) 0.25 g, (c)-(d) 0.5 g, and (e)-(f) 1 g with a constant water-in-oil (w/o) ratio of	

1/10 and TEOS addition of 1 ml; (g) Summary of the SiO₂ and densely external CaCO₃ nanoparticles shell thickness..... 84

Figure 5-6. SEM images showing the effect of CaCO₃ nanoparticle concentration on the formation of the colloidal capsules: (a)-(b) 0.25 g, (c)-(d) 0.5 g, and (e)-(f) 1 g with a constant water-in-oil (w/o) ratio of 1/10 and TEOS addition of 1 ml; (g) Summary of the SiO₂ and densely external CaCO₃ nanoparticles shell thickness..... 85

Figure 5-7. SEM images showing the effect of TEOS concentration on the formation of the colloidal capsule: (a)-(b) 0.5 ml; (c)-(d) 1 ml; (e)-(f) 1.5 ml with 1 g of CaCO₃ and a w/o ratio of 1/10; (g) The variation of silica shell thickness under different TEOS additions. 86

Figure 5-8. SEM images showing the effect of the reaction duration on the formation of the colloidal capsule: (a)-(b) 12 h; (c)-(d) 24 h; (e)-(f) 48 h with 1 g of CaCO₃, 1/10 w/o ratio, and 1 ml TEOS addition; (g) The silica shell thickness under different reaction durations. 87

Figure 5-9. Size distribution of the hybrid CaCO₃-SiO₂ colloidal capsules obtained at the optimum synthesizing conditions. 88

Figure 5-10. Schematic representation of the stearic acid-modified CaCO₃ nanoparticles at the water-oil interface..... 89

Figure 5-11. (a) FT-IR spectra and (b) XRD analysis of stearic acid-modified CaCO₃ nanoparticles, SiO₂, and as-obtained colloidal capsule..... 90

Figure 5-12. (a) Secondary electron (SE) image of the external morphology of the colloidal capsule; (b) TEM-BF image showing the hollow interior structure and the packing assembly of the nanoparticles on the inner shell; (c) SE image of a sectioned colloidal capsule; and (d) EDS mapping analysis of the elemental distribution within the hybrid shell structure..... 91

Figure 5-13. XPS survey spectrum of SiO₂, CaCO₃ nanoparticles, and the hybrid CaCO₃-SiO₂ colloidal capsules; (d) XPS detail analysis and the deconvolution of these spectra of Si 2p, C 1s, Ca 2p, and O 1s from the hybrid colloidal capsule. 92

Figure 5-14. (a) Thermogravimetric Analysis (TGA) of the colloidal capsule, CaCO₃ nanoparticles, and SiO₂; (b) Derivative Thermogravimetry (DTG) of the colloidal capsule and CaCO₃ nanoparticles; (c) Differential Scanning Calorimetry (DSC) of the colloidal capsule and CaCO₃ nanoparticles; and (d) Thermal diffusivity measurement of the mild carbon steel and capsule-coated mild carbon steel. 93

Figure 6-1. Cross-sectional specimen preparation in dual FIB-SEM before the in-situ heating TOF-SIMS experiment..... 98

Figure 6-2. (a) SEM images of silica hollow spheres. Inset is the particle size distribution (mean diameter = 3.5 ± 0.7 μm); (b) SEM images of the colloidal capsule. Inset is the particle size distribution (mean diameter = 6.3 ± 1.8 μm); (c) SEM images showing smooth shell surface of silica hollow sphere; (d) TEM image showing the hollow structure and shell wall; (e) SEM image of a fractured sphere showing rough

internal surface from silica hollow sphere; (f) SEM image showing a rough colloidal capsule surface; (g) TEM image showing the hollow structure, shell thickness and particle assembly in the shell; and (h) SEM image of a sectioned colloidal capsule.	100
Figure 6-3. FE-SEM images and the mechanical properties of the prepared silica hollow sphere and the colloidal capsule picked for in-situ TEM compression. (a) FE-SEM image of the silica hollow sphere; (b) FE-SEM images of the colloidal capsule.	101
Figure 6-4. Representative load-displacement curves of: (a) a single silica hollow sphere; (b) non-heat treated colloidal capsule; (c) different crystalline polymorphs of calcium carbonate ³¹¹ and silica amorphous ³¹² particles. The inset pictures are the TEM image showing the dynamic change of the tested particle during the compression. The scale bar is 1 μm	102
Figure 6-5. The calculated normalized strength and compressive strain via a slight variation in the tested particle's diameter (3-4 μm) of: (a)-(b) the doubled-shell colloidal capsule; (c)-(d) silica hollow sphere. Distribution of the normalized strength (e) and compressive strain (f) of the doubled-shell colloidal capsule and silica hollow sphere. The averages of the rupture properties for each tested individual are displayed in the red dot.	103
Figure 6-6. Preparation of the thin ring from the picked colloidal capsule for STEM observation.	104
Figure 6-7 (a) STEM-HAADF image of the thinned ring; (b) EDS mapping images of elemental distribution; (c) SADP of the nanoparticles; (d) SADP of the silica shell; (e) the inner shell BF imaging of the interfacial structure at very high magnification marked in (a); (f) Corresponding HAADF imaging of the interfacial structure from (e); (g) EELS analysis of Si-L, C-K, Ca-L, and O-K edges from the silica inner shell to the nanoparticles marked in (f).	106
Figure 6-8. (a) Load-displacement curve of the mechanical compression of the representative 7.5 μm individual colloidal capsule; (b) Normalized strength and compressive strain of the colloidal capsule via diameter.	107
Figure 6-9 Mechanical deformations of the thin-rings prepared from the large (a) and small (b) colloidal capsules; (c) Schematic representing the possible mechanisms of different mechanical behavior from the large and small colloidal capsules.	108
Figure 6-10 In-situ observation of the capsule's shell morphology transformation at elevated temperatures.	109
Figure 6-11 (a) Dynamic observation of the in-situ TEM mechanical compression of 1000°C-annealed hybrid microcapsules; (b) Corresponding load-displacement curve of the 1000°C-annealed colloidal microcapsule; and (c) Changes in compressive strength and strain of the colloidal microcapsules after heat treatment at different temperatures.	110
Figure 6-12. Statistical distribution of the normalized compressive strength (a) and compressive strain (b) of the individual colloidal capsules after annealed at different temperatures. The red dot with the error bar is the average from at least three in-situ compression tests of each individual.	111

Figure 6-13 (a) SEM image of the sample on the heating chip and high-resolution TOF-SIMS elemental mapping of $^{28}\text{Si}^+$ and $^{40}\text{Ca}^{2+}$ from the ring sample; (b) TOF-SIMS positive ion spectra (m/z 0-60) of the cross-sectioned ring sample.	112
Figure 6-14 (a) Schematic showing the conditions for the TOF-SIMS analysis at elevated temperatures; (b) Intensity variation thermogram of $^{28}\text{Si}^+$ and $^{40}\text{Ca}^{2+}$ ions as a function of temperature. Elemental mapping of $^{28}\text{Si}^+$, $^{40}\text{Ca}^{2+}$, and the merging of these two ions corresponds to different temperatures, including: (c) 200°C; (d) 555°C; (e) 720°C; (f) 900°C; and (g) 1000°C.	114
Figure 6-15. The structural transformation of the doubled-shell at different temperatures conducted by in-situ TEM heating observation, including: (a1-a2) room temperature; (b1-b2) 555°C; (c1-c2) 650°C; (d1-d2) 720°C; (e1-e2) 900°C; and (f1-f2) 1000°C.	116
Figure 6-16. Normalized strength and compressive strain of silica hollow sphere, non-heat treated, and heat-treated colloidal capsule, compared with other reported capsule systems.	118
Figure 7-1. Schematic representing the advantages of encapsulating h-BN nanosheets inside the designed $\text{CaCO}_3\text{-SiO}_2$ doubled-shell for high-temperature lubrication application.	121
Figure 7-2. (a) Low-magnification TEM image of the h-BN nanosheets; (b) High-magnification TEM image of the h-BN nanosheets showing the layered structure; (c) Inverse Fast Fourier Transform (IFFT) from the white marked area in (b). The inset picture in (c) indicating the d-spacing between each layer; (d) a photograph of the water droplet on pristine h-BN and amine-functionalized h-BN nanosheets from Lei et al. ³⁵⁰ . Digital images show the stable h-BN colloidal dispersion in water after 6 months.	124
Figure 7-3. The synthesis process of the smart functional BN-containing colloidal capsules: a) h-BN nanosheets solution preparation; and b) Fabrication of BN-containing colloidal capsules.	125
Figure 7-4. SEM image and size distribution of the formed colloidal capsule at different h-BN nanosheets concentration in water: (a)-(b) no h-BN nanosheets in water; (c)-(d) 2.8 ml/mg h-BN nanosheets in water; and (e)-(f) 5.6 mg/ml h-BN nanosheets in water.	126
Figure 7-5. (a) X-ray diffraction analysis of the materials; (b) Raman analysis of the hybrid microcapsules and h-BN nanosheets; (c) SEM image of the external shell morphology of a single colloidal capsule; (d) Internal structure inspection by TEM.	127
Figure 7-6. a) SEM image showing the cross-sectioned shells by FIB which were prepared for the STEM characterization; b) Bright-field (BF) STEM image of the biggest ring.	128
Figure 7-7. (a) STEM-BF image of the cross-sectioned shell; (b) High-angle annular dark-field (HAADF) image of the cross-sectioned shell; (c) EDS mapping showing the elemental distribution within the cross-sectioned shell; (d) AC-STEM image of the red square marked in (a); (e) EELS B-K edge and EELS N-K edge spectrums extracted from the yellow square marked in (d). An inset image in (d) is the d-spacing measurement between the fringes from the IFFT of the fringe area.	129
Figure 7-8. High dispersibility of the BN-containing colloidal capsules in the borate-based aqueous	

lubricant.	130
Figure 7-9. Oxide scale development after isothermal oxidation test at 880°C with different lubricant coatings: (a) no lubricant coating (D-L); (b) colloidal capsule-coating (C-L); (c) sodium borate melt coating (B-L); (d) colloidal capsule (without h-BN nanosheets) + sodium borate melt coating (C-B (1:1)); and (e) colloidal capsule (with h-BN nanosheets) + sodium borate melt coating (BN@C-B (1:1)). (f) Measured oxide thickness on steel under different coatings.....	131
Figure 7-10. EDS mapping of the oxide and coating on the stainless steel after isothermally heat-treatment at 880°C from: a) Dry oxidation (D-L); b) Capsule-coating (C-L); c) Sodium borate-coating (B-L); d) capsule without h-BN + Sodium Borate (C-B (1:1)); and e) BN-containing capsule + Sodium Borate (BN@C-B (1:1)) test.....	132
Figure 7-11. (a) Dynamic friction coefficient of the lubricants at 880oC, 10 N (1.04 GPa), and 1 Hz; (b) Average coefficient of friction at the steady-state; (c) Disc wear rate; and (d) Ball wear rate after hot friction tests with different lubricants.	134
Figure 7-12. Friction and wear rate results of the hot friction tests at different conditions, including: a)-d) different capsule/borate ratios; e)-h) different temperatures; i)-l) different loadings; m)-p) different sliding velocity.....	136
Figure 7-13. SEM/EDS inspection of the worn surfaces on the plate wear track after hot friction tests at 880°C from: (a) D-L; (b) C-L; (c) B-L; (d) C-B (1:1); and (e) BN@C-B (1:1).	138
Figure 7-14. SEM/EDS inspection of the worn surfaces on the ball wear scar after hot friction tests at 880°C from: (a) D-L; (b) C-L; (c) B-L; (d) C-B (1:1); and (e) BN@C-B (1:1).	138
Figure 7-15. High magnification SEM images of the worn plate (a) and ball (b) surfaces. Wide-scan (c) and narrow-scan (d) Raman analysis conducted at (1) non-sliding area on the plate; (2) the disc wear track; and (3) the ball wear track.....	139
Figure 7-16. (a) XPS survey spectrum; (b) B 1s deconvolution; (c) N 1s deconvolution; and (d) O 1s deconvolution from the inspected regions of (1) non-sliding area on the plate; (2) the disc wear track; and (3) the ball wear track.	140
Figure 7-17. Schematic showing the potential lubrication mechanism of the BN@C-B (1:1) melt lubricant at 880°C.....	142
Figure 8-1. (a) Cross-section of sodium borate-coated steel specimen; (b) Sodium borate-wetted steel specimen from (a) after in-situ heating at elevated temperatures.....	145
Figure 8-2. (a) Thermogravimetry (TGA) and Derivative thermogravimetry (DTA); (b) Differential scanning calorimetry (DSC) of the borate-capsule mixture (borate/capsule = 1:1 weight ratio).	146
Figure 8-3. (a) Schematic representing the in-situ thermo-responsive experiment of the hybrid microcapsules under borate melt conditions. SEM image showing the visualization of how the single microcapsule responses to the borate melt at different temperatures: (b) 500°C; (c) 600°C; (d) 700°C; (e)	

800°C; Side view at (f) 800°C and (g) 850°C.....	147
Figure 8-4. SEM and EDS analysis of the sodium borate (NBO) ((a)-(b)) and the capsule-added sodium borate (MC@NBO) ((c)-(d)) melt lubricants coated on the steel substrate after the static heating conditions at 930°C.....	148
Figure 8-5. XRD surface analysis of the coated steel after oxidation test at 930°C: (a) no coating; (b) sodium borate (NBO) coating; and (c) capsule-added sodium borate (MC@NBO) coating.	150
Figure 8-6. (a) Cross-section overview of the MC@NBO coated on the oxide-steel surfaces; (b) Aberration-corrected high-magnification bright field image of the single columnar oxide particle from the yellow square marked in (a); (c) EDS spectrum of the two distinct areas in the columnar oxide particle as spotted in (b).	151
Figure 8-7. SADP analysis of the compound formation at different regions in the specimen from the capsule-added sodium borate-coated steel sample under static heating conditions at 940°C.....	152
Figure 8-8. (a) Frictional behaviors of MC@NBO compared to NBO and dry sliding at 10 N, 930°C, 0.1 m/s; (b) Wear rate calculation of disc and ball for friction tests in (a); and (c) Mean friction coefficient of the MC@NBO melt lubricant at different temperatures.	154
Figure 8-9 (a) Frictional behaviors of capsule-added borate melt lubricant at different loadings at 940°C, 0.1 m/s; (b) Mean friction coefficient at different loadings from (a); and (c) Wear rate calculation of disc and ball for capsule-added borate melt lubricant at different loads.....	155
Figure 8-10. (a) SEM observation of disc worn surfaces; (b) corresponding EDS mapping; and (c) high-magnification SEM image of the disc worn surfaces after being lubricated by microcapsule-added sodium borate lubricant (MC@NBO). An inset image in (a) is the 3D profile of the disc wear track.	156
Figure 8-11. (a) SEM observation of ball worn surfaces; (b) corresponding EDS mapping; and (c) high-magnification SEM image of the ball worn surfaces after being lubricated by microcapsule-added sodium borate lubricant (MC@NBO). An inset image in (a) is the 3D profile of the ball wear track.....	156
Figure 8-12. (a) Cross-section overview of the disc's hierarchical tribofilm after being lubricated by MC@NBO melt at 10 N, 930°C, 0.1 m/s; (b) Elemental distribution within the cross-sectional tribofilm by EDS mapping; (c) Aberration-corrected high-magnification bright field image of the yellow square marked in (a); (d) SAPD analysis of the marked particle; and (e) EDS line scanning analysis of the oxide particle as indicated in (c).	157
Figure 8-13. SADP analysis of the thin glass layer (SADP1) and the oxide scale layer (SADP2) on the disc after friction test at 930°C.	158
Figure 8-14. (a) Cross-section overview of the ball's hierarchical tribofilm after being lubricated by MC@NBO melt at 10 N, 930°C, 0.1 m/s; (b) Elemental distribution within the cross-sectional tribofilm by EDS mapping; (c) Aberration-corrected high-magnification bright field image of the yellow square marked in (a); (d) SADP of the marked particles; and (e) EDS spectrum of the spotted particles in (c).	159

Figure 8-15. SADP analysis of the thin melt layer and the floated particles in the melt on the ball after friction test at 940°C.....	159
Figure 8-16. (a) HR-TEM image showing the presence of layered material within the melt; (b) Fast Fourier Transformation of (a) showing the hexagonal pattern of h-BN; and (c) EELS analysis of the white square marked in (a).	161
Figure 8-17. The structural transformation of the oxide surface on both counterparts at different frictional testing moments: Friction curve and microstructure of the oxide surfaces on (1) disc and (2) ball of the test stopped at 40 sec (a); 100 sec (b); and 600 sec (c).	162
Figure 8-18. EELS B K edge analysis of the glass tribofilm on the ball wear track, disc wear track, and outside the disc wear track.	163
Figure 8-19. Schematic representing the effect of friction on the corrosion of the MC@NBO melt and the reconstruction of the oxide microstructure.....	164

List of Tables

Table 2-1. Summarization of natural shell materials that are sensitive to pH change.	33
Table 2-2. Promising core-shell microcapsules with thermally stable materials for high-temperature lubricants.	39
Table 4-1. Physical characteristics of nanoparticles.	55
Table 4-2. Compositions of the steel counterparts.	56
Table 4-3. Summary of the lubrication and anti-oxidation performance of each lubricant and their possible mechanisms.	75
Table 7-1 Composition and lubricant naming convention.	123

Nomenclature

η	Viscosity of lubricant ($\text{N}\cdot\text{s}/\text{m}^2$)
N	Speed (m/s)
P	Load (N)
λ	Film thickness-to-composite roughness ratio
C	Concentration of chemical in solvent (M)
t	Time (s)
A	Exposed surface area of the shell (μm^2)
H	The partition coefficient
D	The diffusion coefficient
d or t	Thickness of the capsule's shell (μm)
θ	Three-phase contact angle ($^\circ$)
γ_{po}	Interfacial tension between particle and oil
γ_{ow}	Interfacial tension between oil and water
γ_{pw}	Interfacial tension between particle and water
r	Radius of particle
E^T	Young's modulus at temperature T (GPa)
E_{ox}^o	Young's modulus of oxide (GPa)
T	Temperature ($^\circ\text{C}$)
R and r	Ball radius (mm)
F	Applied force (N)
E^*	Reduced Young's modulus (GPa)
ν	Poisson's ratio
d	Wear scar diameter (mm)
σ_{max}	Compressive shell strength of the microcapsule (MPa)
P_{max}	The peak load in load-displacement curve (μN)
ε_f	The compressive strain of the microcapsule
h_f	The displacement in load-displacement curve (nm)
FeO	Wustite
Fe_3O_4	Magnetite
Fe_2O_3	Hematite
CuO	Copper oxide
TiO_2	Titanium oxide
ZrO_2	Zirconium oxide
SiO_2	Silicon oxide
Al_2O_3	Aluminum oxide
CeO_2	Cerium oxide

ZnO	Zinc oxide
CaCO ₃	Calcium carbonate
MoS ₂	Molybdenum disulfide
WS ₂	Tungsten disulfide
h-BN	Hexagonal boron nitride
a-ZrP	Zirconium phosphate
B ₂ O ₃	Boron oxide
ZDDPs	Zinc dialkyl dithiophosphates
GNPs	Graphite nanoplates
Na ₂ O	Sodium oxide
TEOS	Tetraethyl orthosilicate
CTAB	Cetyl trimethyl ammonium bromide
2D	Two dimensional
3D	Three dimensional
SEM	Scanning electron microscope
EDS	Energy dispersive X-ray spectroscopy
S/TEM	Scanning/Transmission electron microscope
BF	Bright field
HAADF	High angle annular dark-field
HR-STEM	High-resolution STEM
EELS	Electron energy loss spectroscopy
TGA	Thermogravimetric analysis
DSC	Differential scanning calorimetry
DTG	Derivative Thermogravimetry
XRD	X-ray diffraction analysis
XPS	X-ray photoelectron spectroscopy
FTIR	Fourier-transform infrared spectroscopy
FIB	Focus ion beam
TOF-SIMS	Time-of-flight secondary ion mass spectrometry
SADP	Selected area diffraction pattern
AC-STEM	Aberration-corrected STEM
DLS	Dynamic light scattering
MEMS	Microelectromechanical systems
BET	Brunauer–Emmett–Teller Absorption Analysis
NBO-Al	Sodium Borate + Aluminum oxide
NBO-Ti	Sodium Borate + Titanium oxide
NBO-Zr	Sodium Borate + Zirconium oxide
NBO-Si	Sodium Borate + Silicon oxide
NBO-Cal	Sodium Borate + Calcium carbonate

NBO-BN	Sodium Borate + Hexagonal boron nitride
NBO-Gr	Sodium Borate + Graphite nanoplates
Si-B-1	Mixture between Sodium Silicate and Sodium Borate with Silicate/Borate weight ratio = 9/1
Si-B-2	Mixture between Sodium Silicate and Sodium Borate with Silicate/Borate weight ratio = 1/1
NBO or B	Sodium Borate
NSiO or Si	Sodium Silicate
D-L	Dry friction test
C-L	Friction test with only microcapsule
B-L	Friction test with only Sodium Borate
C-B	Friction test with the mixture between capsule and Sodium Borate without Hexagonal boron nitride
BN@C-B	Friction test with the mixture between capsule and Sodium Borate with Hexagonal boron nitride
W/O	Water-in-oil
O/W	Oil-in-water
NBO in XPS	Non-bridging oxygen
BO in XPS	Bridging oxygen

Chapter 1

Introduction

Friction and wear are the ubiquitous phenomena that always emerge in the moving machinery components. While friction accounts for the loss of energy input to the system, wear affects significantly the material removal and the reliability of the working parts. Around 20% of the world's total energy consumption is used to only overcome the friction from the tribological contacts, while the estimated economic losses of around 815.6 trillion US dollars annually are due to wear failures in the US.¹ In particular, the manufacturing industry, which accounts for 20% of the share of annual total energy input, often experiences significant economic losses due to significant friction and wear evolution between the working components. For instance, excessive yield losses of 40% of production costs are often emerged in the hot metal forming industry that is due to the energy losses in friction, material losses in aggressive wear, and serious oxidation at elevated temperatures^{2,3}. Therefore, lubricants have always been required in the hot metal forming processes to reduce excessive friction and wear that in turn extends the service life of the working components and improves the product quality.

Researching in high-temperature lubricants for the advanced manufacturing industry has increased exponentially since the last decade following a high demand in the strict regulations and customer satisfaction. Recently, glass-like lubricants, comprising the derivatives of borate, silicate, phosphate, and the mixture thereof, have been observed to perform as excellent lubricants for high-temperature metal processing owing to their exceptional thermal stability, the ability to generate the viscous melt at elevated temperatures, and a tunable working temperature range by manipulating the compositions.^{4,5} The melts from these compounds behave as a Newtonian fluid⁶ that not only helps to lubricate the sliding contacts but also inhibits the growth of the oxide scale, thus, reducing the loss of material from oxidation.⁷ Since the use of glass-like lubricants in hot metal forming has been well documented in the technical notes, publications, and patents,⁸⁻¹¹ some efforts have been spent to understand insight into high-temperature lubrication of such compounds at elevated temperatures¹²⁻¹⁴. These in-depth fundamentals, including the complex interfacial structure evolution and material transportation between the melt and oxide surfaces, contribute extensively to the development of multifunctional lubricants for high-temperature lubrication under extreme conditions.

Since the glass-melt lubricants have by now reached their performance limits, the addition of the solid-lubricant (nanoparticles) to the glass melts can offer further improvements to the performance of high-temperature lubricants¹⁵. Advances in researching lubricant additives are not only driven by new materials and new developments in existing materials, but also by new approaches to combine the functional materials. In a conventional approach, solid-lubricant additives are often physically blended and mixed into a base lubricant to achieve the optimum friction and wear reduction for a lubricated system. However, such an approach has far-reaching

implications in a simultaneous achievement in either cost-effectiveness or lubricity enhancement. A key challenge in the emerging discipline of lubricant science is the uncontrolled competitive and antagonistic effects between different functional additives within the base fluid.^{16, 17} Due to an inevitable loss in effectiveness, additives are often formulated with a larger concentration than what is needed.¹⁶ It leads to the use of several organic surfactants or dispersants (potentially harmful to the environment) to prevent the agglomeration, and unexpected interactions at large concentrations, while ensuring the uniform dispersion of such functional additives in the based fluid.^{18, 19} Therefore, the development of integrated multifunctional additives that can provide multiple functions to boost the performances of melt lubricant at elevated temperatures is essential.

This dissertation focuses on the development of multifunctional lubricant additives for high-temperature lubrication of sodium-containing melt lubricants at steel/steel contacts. Since microencapsulation has been well-recognized as the smart approach to incorporate different materials in one body while providing the protection of sensitive additives²⁰, this study focuses on the utilization of microencapsulation techniques to develop newly multifunctional additives from well-known solid lubricant additives for high-temperature lubrication. The friction and wear behavior of the developed additives are thoroughly studied thereafter under the sodium-containing melt lubricant selected from the group of borate, phosphate, and silicate. In addition, the anti-oxidation capacity and the corrosion of sodium toward the oxide scale of the formulated lubricant are among the central subjects. Apart from the experimental works in fabricating and characterizing the novel microcapsules, another emphasis of this current work is on the interfacial chemistry between the lubricants and oxidized steel under static and friction conditions. These interactions predominantly determine the oxidation, corrosion, and lubrication of the applied lubricant on hot steel surfaces at high temperatures.

This dissertation starts with investigations on potential additives to construct the microcapsule which can synergistically boost the lubrication and anti-oxidation performance of the selected sodium-containing melt lubricant (e.g. sodium borate) at high temperatures. The synthesis and in-depth characterization of the customized microcapsules are conducted thereafter and the tribological performance of the microcapsule-added sodium-containing melt lubricant is evaluated at different temperatures, capsule/melt lubricant weight ratios, loadings, and sliding velocities. The microcapsule is originally intended for high-temperature lubrication in hot rolling of steel, but its relevance for a multitude of applications such as fire-retardant, heat insulation coating at high temperatures, and superhydrophobic coating, etc. is also emphasized. Furthermore, the author believes that this work will introduce a new effective strategy to develop and integrate multifunctional additives from existing materials rather than researching new materials for different engineering applications.

Chapter 2

Literature Review

2.1. Problems encountering at high-temperature steel/steel contacts

High-temperature steel manufacturing processes often involve different complex issues generated from the working components including severe friction, wear, serious oxidation, and thermomechanical failures. Such phenomena are found in most processes that require frequent contact between the tools and the workpiece at high temperatures such as metal sheet rolling, forging, stamping, and drawing... Apart from conventional friction and wear that cause significant energy and material losses^{2, 3}, high temperature working conditions approaching over 1000°C, spontaneously with mechanical deformation imposed by thermal cycles, load, and sliding velocity can lead to a degradation of the working components. Such thermomechanical deformation leads to microstructural evolution²¹, thermal softening²², and thermal fatigue^{23, 24} which are critical to the tribological performance of the tools. In addition, serious oxidation at elevated temperatures, heat conduction, and thermal diffusion play a pivotal role in the friction and wear behavior of the contact surfaces which should be taken into account. The complexity of the raised issues in high-temperature tribological processes is presented in **Figure 2-1**.

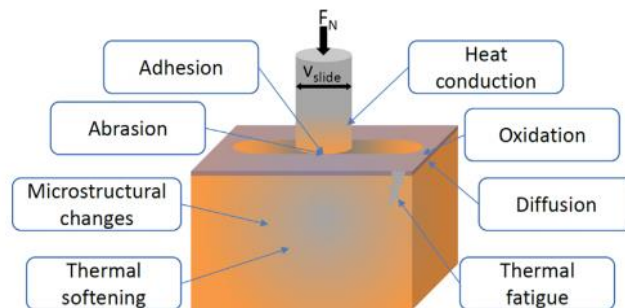


Figure 2-1. Schematic showing the complex phenomena that occurred in high-temperature tribological processes²⁵.

2.2. Oxidation, friction, and wear behavior under steel/steel contacts at elevated temperatures

One of the main problems which can be regarded as the most influential factor on the contact surfaces at elevated temperature is oxidation. The formation of the oxide layer and near-surface layer with a refined grain structure can cause a significant effect on the tribological performance^{26, 27}. For instance, the oxide scale can deform plastically or fracture that will have a considerable impact on the interaction between tool and workpiece and on the surface finish of the formed product²⁸. There are many investigations on the oxidation mechanism of metal and metal alloy by studying the morphological structures of the oxide scale. Under isothermal oxidation conditions, the oxide scale appears and adheres strongly to the surface of the metal. The microstructure,

thickness, and chemical compositions of this layer inherently depend on temperature, exposure time, and reactivity of oxidizing atmosphere²⁹. In addition, the size and shape of a metal substrate are also subjected to the oxidation stage. The formation of monolayer oxide thick films (>6000 Å) at the beginning could be fully explained by Wagner's theory that metallic oxide is mainly formed via diffusion of charged particles which is known as cations, anions, and electron³⁰. However, his theory is just used to explain and interpret the formation of the monolayer during the oxidation process. In fact, the results observed from the entire oxidation tests show the presence of multi-layer oxide on the metal surface.

Cabrera and Mott derived the formulae and theory of thin oxide film formation (<30 Å) at low temperatures in that they proposed the oxidation starts with the adsorption of gas into the metal surface³¹. After the formation of the first scale layer, the growth rate of the oxide scale depends on the ionic movement rate. The driving force for this movement is presumed from the oxygen ionic on the surface. Kofstad mentioned that the defect structure of oxides plays a vital role in the oxidation rate of metal³² as both metallic cations and oxygen anions can diffuse through these defects during the oxide formation. At high temperatures, the charge diffusion is mainly from the metal to the surface as can be seen on the right side of **Figure 2-2**. The good contact between the growing layer of the reaction product and the metal substrate is due to the plastic flow of the scale³³. In the next stage, the crack develops at the vicinity of the edge but will gradually spread out of the metal surface. At this stage, the rate of transport of metal from the metal substrate to the scale decreases due to an increase in the scale thickness. The secondary stage occurs thereafter that the oxidation reaction proceeds in terms of diffusion of oxygen molecules toward the metallic substrate. This process is highlighted on the left side of **Figure 2-2**. The secondary processes can help to partial filling of the crack with the reaction products and restrict the complete breaking of contact between the initial layer of the scale and the metallic substrate³³.

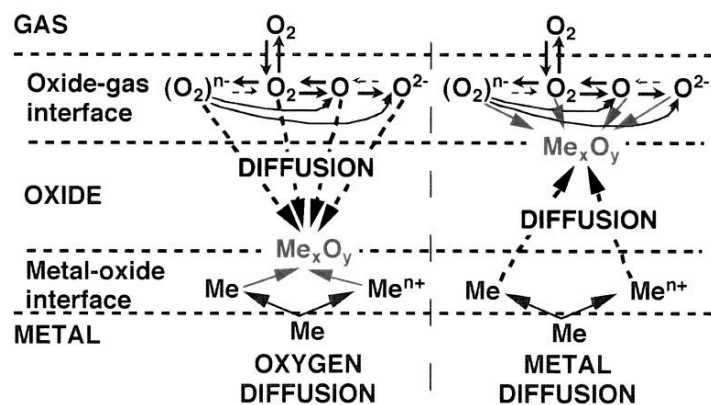


Figure 2-2. Elementary steps during metal oxidation³³.

Compared to other metallic elements in steel, the formation of the iron oxide scale is dominant and the scale is made up mostly from the mixture of iron oxides. The formation of iron oxides is a result of complex events and the structural hierarchy of the scale is inherently temperature-dependent. Under hot rolling conditions, the temperature often reaches 800-1150°C³⁴ and the oxide

scale generally consists of an innermost layer of FeO, a middle layer of Fe₃O₄, and an outermost layer of Fe₂O₃³⁵. Such a hierarchical layer of the oxide scale has been widely observed and reported under hot metal working conditions, especially in hot sheet rolling³⁶⁻³⁸. Since the oxide scale is directly exposed to the contact during the metal forming processes, e.g. hot rolling of steel sheet, its microstructure, and mechanical properties play a significant role in the tribological behaviors which will be discussed as following.

With loaded sliding contacts at elevated temperatures, wear and friction produce several critical issues such as loss of materials, premature failure of components, and poor product quality. The wear and oxidation processes behave differently with temperature. At ambient temperature, the wear formation in the sliding process follows mainly the delamination mechanism with the abrasive and adhesive wear occurring on the two sliding surfaces. The delamination theory which includes crack nucleation, crack propagation, and dislocation dynamic of two substrates was clearly discussed in the overview by Suh³⁹. According to this theory, the wear formation is generated mechanically instead of chemical effect. Thus, oxidation, in this case, is not as important compared to load, surface roughness, and sliding speed. However, at high temperatures, oxidation plays an important role in the wear development and wear rate of the sliding counterparts. It has been acknowledged that the formation of oxide layers occurs more easily in a sliding contact due to the significantly lower activation energy for oxidation⁴⁰. Therefore, the sliding surfaces are subjected not only to the stresses associated with frictional and contact forces but also to the oxidation by reaction with oxygen. Stott et al.⁴¹ have revealed that oxidation under sliding conditions can occur through surface oxidation, oxidation of the interacting asperities by friction-induced heat, and oxidation of the wear debris at the interface. The wear debris may consist of a mixture of oxide particles and partially oxidized metallic particles. In most cases, under the effect of temperature, load, and sliding speed, it has been found that there is the formation of the protective layer called “glaze layer” which is formed by the compaction and the sintering of the retained wear debris within the wear track.

Several studies of glaze layer or compact layer formation and its effects in various kinds of metallic alloy have been reported^{28, 42-48}. It is a notable phenomenon of oxidation in the hot rolling of metal⁴⁹. More research reveals that this layer acts as a prominent high-temperature lubricant that helps to reduce friction and wear rate²⁸ as can be seen in **Figure 2-3**. It is found that the development of the glaze layer is associated with the generation of a compacted oxide layer and partially oxidized alloy particles between the sliding counterparts. In the initial stage of sliding, there is the generation of metallic wear debris particles on the surfaces due to asperity contacts under sliding. Most of the debris is retained and they involve in the development of compact load-bearing layers⁴². Under subsequent shearing, these particles undergo deformation, fragmentation, and comminution and break down into smaller particles when they are moving randomly on the sliding surfaces. When they reach a sufficiently small size, a fraction of these finer particles is started to agglomerate on the wear surfaces, particularly in grooves formed in the early stages of sliding caused by the adhesion forces between solid surfaces arising from surface energy⁵⁰. As sliding continues, these agglomerated clusters of particles are sintered, to some extent, to form

more solid layers. The solid layer becomes hardened and is sufficient to protect the surface from wear damage. These are two competing processes that take place which is known as layers breakdown, resulting in the formation of further debris particles and consolidation of the layers by further sintering and welding of the particles. Thus, most metalworking processes operated at high temperatures increase the oxidation of residual particle formation and promote their sintering, resulting in the consolidation of the layer. Once the glaze is established, it reduced the wear rate. In contrast, if the particles are not well compacted and sintered, loose particles are removed easily from the contact area and the wear rate is significantly higher.

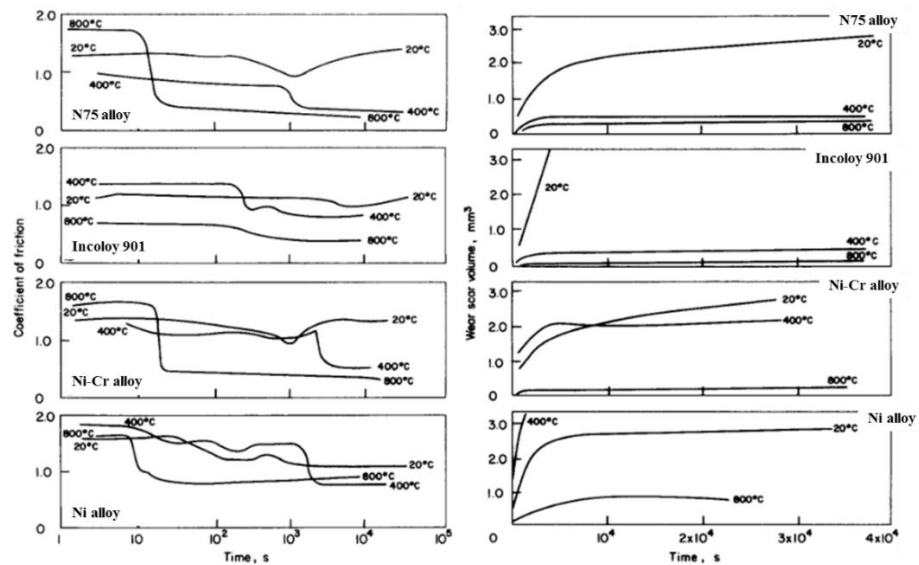


Figure 2-3. Coefficient of friction and wear scar volume as a function of time during like-on-like reciprocating sliding in the air (load-15 N; speed-8.3 Hz; amplitude-2.5 mm)⁴⁵.

As mentioned by Stott et al.^{28, 42, 44-49}, the formation of a glaze layer reduces wear and friction at the temperature range of 150-800°C. The combination between the operating temperature and frictional heating (hot-spot temperature) results in rapid transient oxidation which causes the thermal softening effect. When the glaze layer is completely formed, the average surface temperature remains fairly constant and the reduction in friction and wear is mainly associated with a low shear strength of the glaze and the relatively high strength of the underlying substrate⁴⁴. Moreover, the friction and wear relate partly to an intrinsic crystallite structure of oxides, whereby material with a cubic structure generally has higher friction than the hexagonal structure⁵¹. At different temperatures, the composition of the glaze changes leading to the different crystalline structures of oxides that may affect the lubricating behavior. The ionic potential of cations also known as the ratio between the oxidation number and ionic radius controls several physics and chemical properties of the oxides⁵².

Besides, the stable maintenance of the glaze layer during sliding is also an important factor that affects friction and wear at the steel/steel contacts⁵³. Wang et al. have found that the increase in load from 50 N to 200 N caused a transition of mild wear to severe wear. In this case, wear loss starts to increase significantly and reaches a relatively high level with a simultaneous observation

of significant plastic deformation in the oxide-substrate interface⁵⁴. Especially at a particularly high load, the glaze layer tends to break down into debris and results in a metal-metal contact leading to an increase in wear damages. Moreover, the hardness of tribo-pair materials in the development of scale layer plays a pivotal role⁵³. Comparing high-speed steel substrate and softer high-chrome steel substrate, the severe abrasion of the pin by hard oxide and/or oxide-containing debris has been observed in the high-speed steel/carbon steel combinations while wear-protective layers were established during the sliding high-chrome steel/carbon steel combinations⁵³. During sliding with a harder substrate, loose debris could not be entrapped and retained within the contact area due to the large size of the particles and the shallow wear grooves formed on the hard high-speed steel substrate. Meanwhile, the softer substrate can generate deeper grooves in the early stages, which is more effective in retaining debris, leading to a development of wear-protective glaze.

Several studies have also been conducted to investigate the effect of sliding speed on the severity of the wear rate and on the glaze layer at high loads and high temperatures^{42, 47, 48, 55}. Pauschitz et al. have verified that speed and temperature can affect the wear rate through the formation of three kinds of glaze layers⁴². However, the transfer layer formation on the harder counterpart resulted from the deposition of the wear material from the softer one tends to occur at ambient temperatures. At high temperatures, the formation of the mechanically mixed layer and composite layer is dominant. In other research, the term of mild-oxidational wear and severe-oxidation wear have also been introduced as it depends on the sliding speed above 1 m/s and 10 m/s respectively⁴⁸. The wear rate is often lower in the severe-oxidational wear regime because this film is thicker, continuous, and more plastic than the one in mild-oxidational wear⁵⁵.

2.3. Lubrication of steel/steel contacts at high temperatures

Although the generated glaze layers can lubricate the counterparts at high temperatures to some extent and reduce adhesion between surfaces, they often produce higher friction. To control the friction and wear under steel/steel contacts at elevated temperatures, major research efforts have been devoted to the development of specialty lubricants apart from the surface modification approaches⁵⁶. An application of lubricants between the moving contacts can result in different lubrication regimes depending on the load, speed, temperature, and properties of the lubricant, surface, and materials. According to the Stribeck curve (**Figure 2-4**)^{57, 58}, the friction coefficient is a function of the bearing parameter called the Hersey number ($\eta N/P$). There are three different lubrication regimes named boundary lubrication, mixed lubrication, and hydrodynamic lubrication as distinguished by different parts of the Stribeck curve (**Figure 2-4**) or by the calculation of the film thickness-to-composite roughness ratio (λ). It has been demonstrated that the hydrodynamic lubrication regime occurs when $\lambda > 3$. Under a hydrodynamic regime, the load is supported by the lubricant pressure generated by a taper flow between two surfaces under relative motion. On contrary, the boundary lubrication regime presents when the fluid film cannot separate the contacting surfaces resulting in a direct contact of surface asperities. The boundary lubrication regime appears when $\lambda < 1$ which causes high friction coefficient and wear. While high friction

coefficient induces significant energy losses, heat-induced from high rubbing can break off or wear down the asperities leading to simultaneous adhesive and abrasive that potentially can cause a seizure. Finally, the mixed lubrication regime is an intermediate regime between the boundary and hydrodynamic lubrication ($1 < \lambda < 3$) whereby the lubricant film and contacting asperities jointly support the applied load.

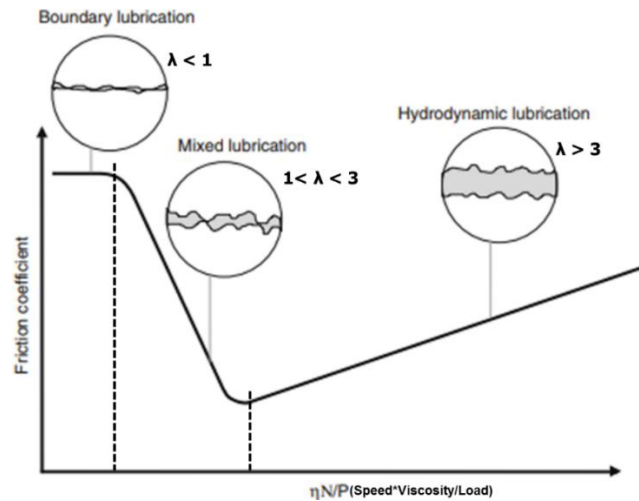


Figure 2-4. Schematic of a Stribeck curve where η is the dynamic viscosity of the lubricant, N is the rotational speed, and P is the applied pressure^{57, 58}.

Although the Stribeck curve was initially developed for the study of friction characteristics of materials in the journal bearings at room temperatures, it can be extended and have significant applications in high-temperature lubrication. It has been demonstrated that the hot rolling processes are often operated under the combination of lubrication regimes due to the non-conformity of the contacting surfaces (**Figure 2-5**)⁴. In the entry zone, there is often the hydrodynamic regime caused by the thick lubricant film boiling whereas the mixed/boundary lubrication regimes occur in the roll bite zone. Since the hot metal forming processes are often operated at elevated temperatures (800-1200°C), the significant heat from such conditions can cause the thermal decomposition/transition or boiling of the lubricant when they are in contact. The thermal diffusion, adsorption, and reactions between the lubricants and the oxide surface can be triggered thereafter that forms the tribofilm on the contacting surfaces. Unlike room or moderate temperatures at which the tribochemical process depends strongly on the stressed-shearing effect, the formation of tribofilm at elevated temperatures is governed by both the thermal effect and sliding shear. Under such arduous conditions, heat and an intermixing effect from stressed-shearing play an important role in the tribochemical reactions between the lubricants and oxide surfaces while pressure has been shown to have negligible effect⁵⁹. The lubrication under high-temperature conditions is a complex process that can be difficult to interpret fully.

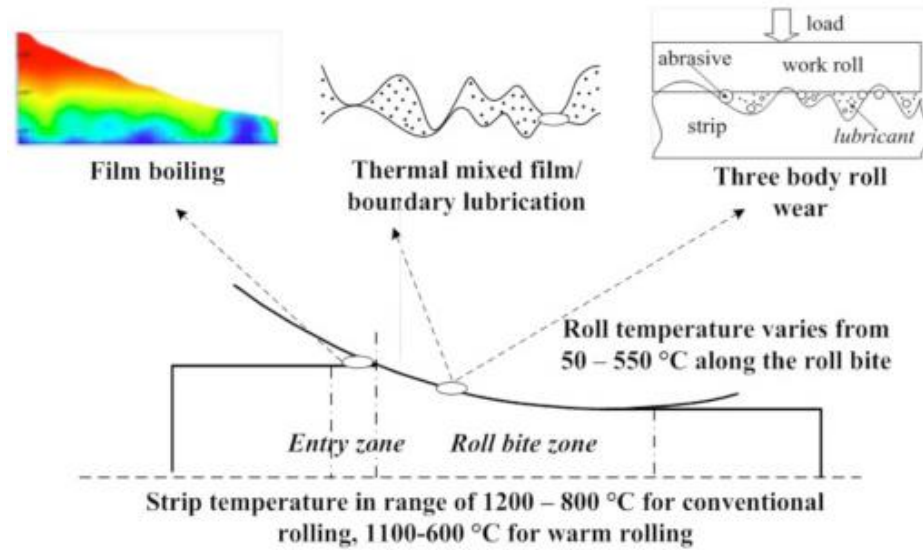


Figure 2-5. Schematic presenting the lubrication regimes of the hot rolling of steel processes⁴.

2.4. Solid lubricants for high-temperature lubrication processes

Under high load (>1GPa), elevated temperature (1100°C), and rapid velocity (it can be up to 10 m/s) in hot metal rolling of steel⁶⁰, the call for an effective lubricant, which exhibits outstanding performance, has become an attractive research topic. Various water- and oil-based lubricants have been widely applied to separate the rubbing members by a film of solid and/or liquid and to produce less secondary oxide scaling by lowering temperature as a result of heat dissipation by water or oils^{61, 62}. However, it is uncertain whether a uniform and stable tribofilm can be spontaneously formed on the rubbing surfaces to help reduce friction and wear while resisting oxidation. It is obvious that most oils and greases can rapidly decompose at temperatures well below 1000°C to produce some volatile toxic compounds and thus are not suited for high-temperature lubrication. An emerging approach comes from the application of the solid lubricants (oxide, carbide, nitride, boride, graphite compounds...) and glass lubricants (silicate, borate, phosphate...) which demonstrate an excellent performance at high temperatures by various mechanisms such as shearing and tribochemical reaction^{4, 63}. Moreover, environmental friendliness is an important factor when designing a new potential lubricant for high-temperature processes.

Solid lubricants have been used to solve some specific problems in which oil-base or grease cannot function effectively, especially under severe operating conditions. For a specific example, it has been used as an alternative method to replace the oil-based lubricant which is decomposed at high temperatures or frozen at low temperatures. Thus, it comes as no surprise that solid lubricants are the most suitable candidate for high-temperature working conditions⁶⁴. With the use of solid lubricants, friction coefficients up to 0.20 accompanied by wear are considered to be acceptable for severe boundary lubrication. The lubricating mechanism of these solid lubricants firstly requires good adhesion on the surfaces with low yield strength in the shear direction.

2.4.1. Inorganic metal oxide and ceramic nanoparticles

Nanoparticles as additives in lubricants have attracted significant interest for several years due to their excellent performance in both friction and wear reduction as well as their stability to adapt to high temperature and pressure. Many studies have focused on the lubrication behavior and the mechanism of solid nanoparticles in engine oil and lubricants for the machining and hot rolling⁶⁵⁻⁶⁷. For instance, Dai et al. show in their review that the addition of different nanoparticles to the oil lubricant can improve the thermodynamics, minimize mechanical losses in engines, and improve the fuel economy⁶⁷. Moreover, nanoparticles, in some cases, can react with the metal substrates to form a tribochemical lubricating film, which can reduce the shear stress of sliding surfaces⁶⁸. On the other hand, the formation of a protective layer generated by the interaction of solid nanoparticles and surfaces materials can reduce the direct contact between asperities, thus, preventing wear⁶⁹. It is generally accepted that spherical solid nanoparticles can also enable a rolling effect at the interfaces leading to a decrease in abrasive wear and friction⁷⁰. In most cases, the surface roughness is greater than the mean diameter of nanoparticles, and hence the nanoparticles can be deposited on the surfaces, forming the physical tribofilm, which compensates for the mass loss of substrates⁷¹. This phenomenon is one of the important mechanisms of nanoparticles in reducing friction and wear of the sliding contacts, the so-called “mending effect”. During friction, the micro-peaks on the sliding areas come into direct contact. The nanoparticles, with a mean diameter significantly smaller than the surface roughness, may also be squeezed into the gap between the contacting asperities and then be compressed into the grooves on the surface. The squeezing and compression will generate frictional heat which then leads to a localized increase of temperatures at the point of contact. The increase of temperature largely depends on experimental conditions, but the highest temperature can reach up to 1300 K at the contact point⁷². Under such conditions, it is reasonable to expect that nanoparticles start to diffuse and assemble onto the contact point surface. Along with the continual supply of the nanoparticle-containing lubricant in the engine, the nanoparticles can pile up and gradually fill the grooves and scars of the friction surface leading to the mending effect and resulting in a decrease of the friction. Furthermore, when the hard nanoparticles are introduced at the sliding contact, the roughness of the rubbing surfaces is reduced due to the abrasiveness of these particles, and concurrently, the roughness of the worn surfaces was found in agreement with the size of nanoparticles⁷³. All of these effects of nanoparticles on the contacting surfaces are classified as four mechanisms, which are known as a rolling effect, protective film effect, mending effect, and polishing effect as shown in **Figure 2-6**.

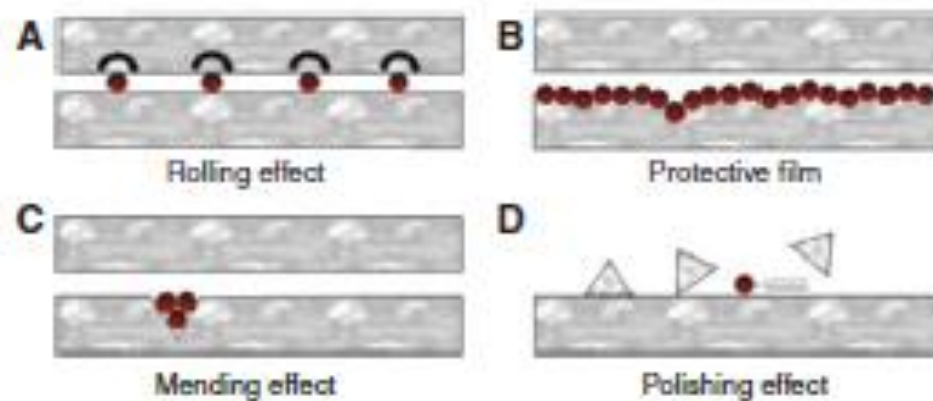


Figure 2-6. Possible lubrication mechanisms of nanoparticles with engine oils between the frictional surfaces^{66, 74}.

Several studies about the metal oxide nanoparticles were reported regarding their potential as lubricant additives such as CuO⁷⁵, TiO₂⁷⁶, ZrO₂⁷⁷, SiO₂⁷⁸, Al₂O₃⁷⁹, CeO₂⁸⁰, and ZnO⁸¹ and their relative composites. However, most of them are related to oil lubricant additives which are normally applied for room to moderate temperatures. Few articles investigated the application of these nanoparticles at elevated temperatures. Recently, these are some publications of high-temperature water-based TiO₂ nano-fluid lubricant regarding hot rolling process⁸²⁻⁸⁸. It has been demonstrated that TiO₂ nanoparticles can improve remarkably the load-carrying capacity, friction-reduction, and anti-wear abilities of pure water. TiO₂ nanoparticles often deposit on the rubbing surface during the friction process and improve the tribological properties of base lubricants. The anti-wear and friction reduction can be explained by the rolling effect of TiO₂ nanoparticles, which separates the direct contact between the asperities of the rubbing surfaces (**Figure 2-7a**).⁸⁹

Wenzhen et al. conducted the experiment of nano-TiO₂ additive oil-in-water lubricant for hot steel rolling at 1050°C.⁹⁰ An addition of TiO₂ nanoparticles at 4 wt.% can improve the adhesion of lubricant oil-in-water to the work rolls. Moreover, friction and the rolling force in both pin on disk test and hot rolling test are also reduced. However, the reduced friction appears only when the strip or testing disc is oxidized at high temperatures. At high temperatures, the surface of the oxidized disk has craters, which increases the space between ball and disk. Although the thickness of the oil film is reduced at high temperatures, the craters can retain the nanoparticles and allow the nanoparticles to enter the contact area, and then reduce the friction coefficient (**Figure 2-7b**). [In another research on the hot rolling of micro-alloyed steel, the polishing effect of TiO₂ nanoparticles was observed with smooth sliding surfaces while these nanoparticles were also compacted under sliding conditions to form a protective film that reduced friction and wear.](#)⁹¹ The film formation can isolate the air and hot surfaces of the rolled specimen, leading to a decrease in the oxide scale thickness (**Figure 2-7c**). Furthermore, when the nanoparticles are small enough (30-120 nm) to fill in the surface defects, a mending effect occurs and improves the surface finish⁷¹. Mending hereby is beneficial to alleviate the wear of work rolls in the subsequent hot rolling processes.

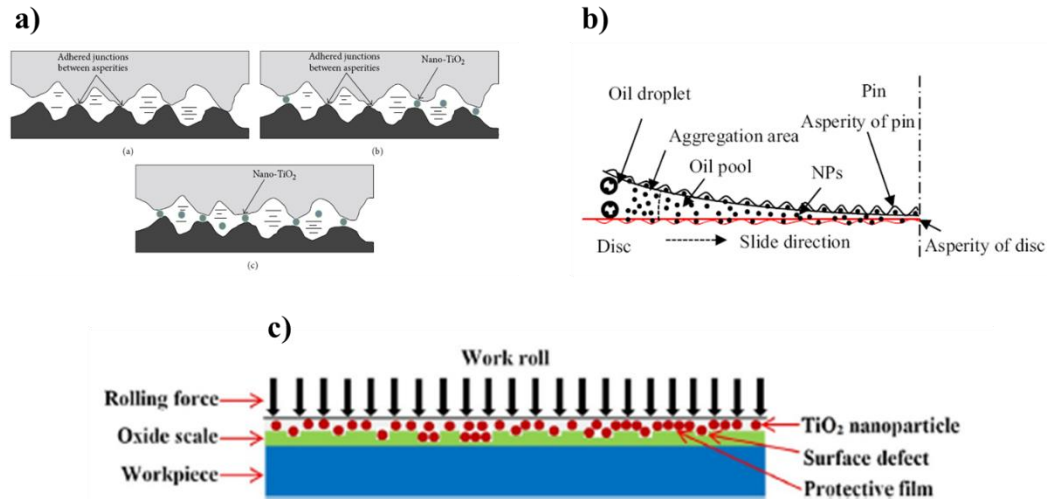


Figure 2-7. Schematic presenting the lubrication mechanism of TiO_2 nanoparticles at the rubbing interfaces.⁸⁹⁻⁹¹

Apart from TiO_2 nanoparticles, CaCO_3 submicron-particles have been studied as a lubricant additive in the oil lubricant for hot rolling. Shimotomai et al.⁹² conducted the hot rolling of stainless steel (SS440 and SUS444) at 900°C - 1000°C with the lubricant containing CaCO_3 nanoparticles. It has been found that an increase in CaCO_3 nanoparticles concentration in the base lubricant results in a significant drop (over 40%) in the rolling force (**Figure 2-8a**). The effect of CaCO_3 particles size has been investigated by testing two lubricants: a semi-fluid type (ST) with a particle size of $1\mu\text{m}$ and a fluid type (FT) with a particle size of 15 nm. From the obtained results, micron-scale particles outperform nano-scale particles in terms of rolling force reduction and anti-seizure performance (**Figure 2-8a**). The lubrication mechanism has been suggested as the rolling and mending effect as demonstrated in **Figure 2-8a**. Recently, Bao et al.⁹³ have investigated the effect of SiO_2 nanoparticles as water-based lubricant additive to enhance the surface qualities of the hot steel strips after rolling. In particular, the addition of less than 0.5 wt.% nanoparticles to the water lubricant refines the size of grains on the strip surface with an increase in the amount of pearlite. In addition, the oxide scale becomes thinner and denser with a maximum reduction of $\sim 7\mu\text{m}$ of the thickness when the concentration of nano- SiO_2 is at 0.3 wt%. The lubrication mechanism of the nano- SiO_2 has been attributed to micro-rolling, polishing, and self-repairing effect during hot rolling process (**Figure 2-8b**).

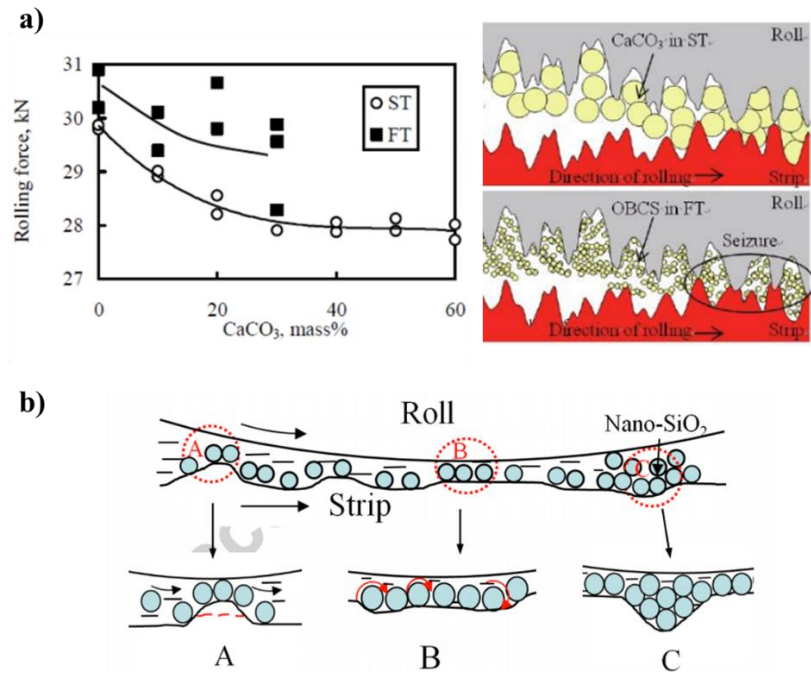


Figure 2-8. (a) Rolling force reduction from the hot rolling of stainless steel lubricated by CaCO₃-added oil lubricant and the lubrication mechanism at different sizes; (b) Mechanism of SiO₂ nanoparticles in enhancing the surface qualities of the hot strip rolling.^{92, 93}

2.4.2. Layered microparticles or nanosheets

Among nanoparticles, some materials which possess the hexagonal layered crystal structure have become an appealed topic for friction reduction additives. Due to this specific structure, they contribute to the anisotropic shear properties that reduce friction between contacting interfaces⁶⁴. Some of the compounds relating to this class are well-known such as MoS₂, WS₂, graphite, graphite fluoride. The most recent materials, which have attracted much attention, are graphene, graphene oxide, hexagonal boron nitride (h-BN), zirconium phosphate (α -ZrP), and quasi-layered compounds as shown in **Figure 2-9**. Although graphite and MoS₂ have been recognized as the conventional and predominant lubricant additives with the highest cost efficiency, they are inferior in oxygen resistance at elevated temperatures⁹⁴. Graphite, in particular, is easily oxidized above 500°C and is completely burned into CO₂ above 700°C.⁹⁵ Meanwhile, MoS₂ is usually oxidized into MoO₃ which has inferior lubricating performance compared to its precursor.⁹⁶ Due to such detrimental factors, graphite, and MoS₂ have been mainly employed as lubricant additives for medium-temperature metal forming processes such as casting, forging, cold rolling, and extrusion, etc.⁹⁷⁻⁹⁹

Among the layered materials, hexagonal boron nitride (h-BN) is known as a synthetic material, which possesses some interesting and unique properties at high-temperature conditions. h-BN is considered as a “clean” lubricant which can be an alternative to “dirty” graphite or MoS₂ in more general applications as a solid lubricant¹⁰⁰. A two-dimensional (2D) structure, which is analogous to graphite as can be seen in **Figure 2-9**, comes as a promising candidate for lubricant additive where the performance of graphite or MoS₂ is unacceptable. Thus, h-BN is expected to possess

excellent mechanical strength, which is beneficial for wear reduction and lubricating performance. As reported by Kostoglou et al.¹⁰¹, the high-temperature properties of boron nitride platelets (200-800 nm in width and 30-50 nm in thickness) were studied and the results reveal the thermal stability of h-BN platelets up to 1000°C before it is completely oxidized by oxygen. Moreover, h-BN is chemically stable and can act as a barrier in chemical protection similar to graphene. Due to the exceptional thermal and chemical stabilities, h-BN could become an ideal coating material against oxidation at high temperatures if a large area, high-quality, uniform atomic layers could be prepared on surfaces to be protected¹⁰². The good thermo-mechanical stability and the thermal shock resistance have enabled h-BN ceramics to be applied in high-temperature conditions.

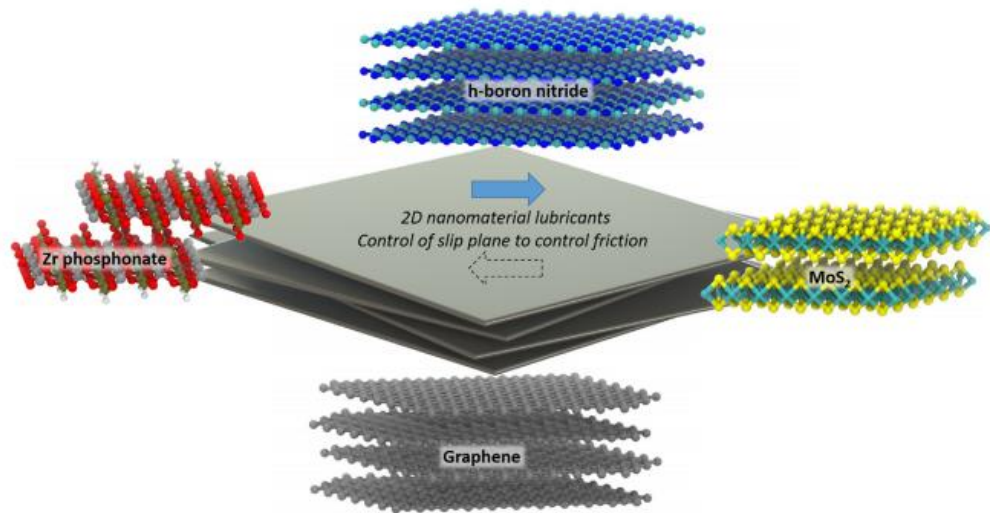


Figure 2-9. Various types of layered materials and friction reduction mechanisms. Picture courtesy of Spear and colleagues¹⁰³.

Several investigations have been conducted to identify and clarify the unique structure of h-BN relating to lubrication. It was believed that the lamella structure of h-BN might lead to the same tribological mechanism of graphite and MoS₂ when used as a lubricant additive. Nevertheless, the tribological performance of h-BN is slightly inferior to graphite and MoS₂ despite its excellent thermal stability and cleanliness. Several publications associated with the tribological behavior of h-BN as engine oil additives have been reported elsewhere^{100, 104-106}. The presence of h-BN on steel-steel and steel-iron contact leads to a decrease in wear, especially in the case of steel-steel contacts. During sliding, the h-BN is peeled off until it becomes monolayer and forms a protective film against friction and wear damage. Moreover, the addition of h-BN with an appropriate amount results in reducing friction and wear at contacting interfaces by the mending effect, which reduces the loss of mass of the substrate and prevents crack propagation during sliding. As claimed by Chen et al.¹⁰⁷, the tribological performance of h-BN in terms of reducing friction and wear is inferior to graphite for higher concentrations. The differences in this behavior were explained by a strong interaction between layers in h-BN, resulted from the dipole-dipole interaction (**Figure 2-10**) and partial ionicity in the layer lattice. However, in the case of cleanliness and environmental friendliness, h-BN is a promising candidate for a replacement of graphite in the aluminum forming

process, as stated by Podgornik et al.¹⁰⁸

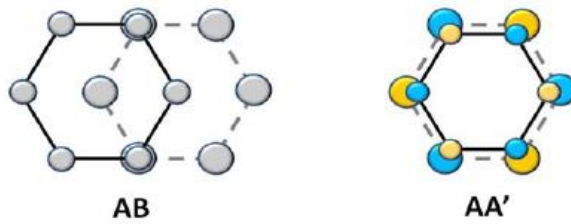


Figure 2-10. AB and AA' interaction between layers in graphene and h-BN, respectively¹⁰⁹.

Up to now, research on the tribological performance and mechanism of h-BN at elevated temperatures (800-1100°C) is still limited. Because of the high thermal stability up to 1000°C, its lubricating properties are expected to be similar to that at room and moderate temperatures including the interlayer sliding effect, protective tribofilm formation, filling concave effect, and viscosity regulation (**Figure 2-11**). In the paper from Zishan et al.¹¹⁰, they have studied the tribological performance of SiC/h-BN composite coating at up to 800°C. The composite sample containing h-BN as a filler shows an abrupt decrease in friction and wear, while the sample without h-BN shows a dramatic increase in friction and wear. Characterization of the worn surfaces showed that the tribological performances of h-BN on the one hand come from the natural structure of h-BN, which allows cleavage of a basal plane and provides the lubricious effect. On the other hand, some fine h-BN particles were oxidized and formed boron oxide (B_2O_3) during the wear test at high temperatures. This liquid not only protects the tribo-pairs but also is effective in lubricating the worn surfaces as well as reducing further oxidation as the coating^{63, 111}.

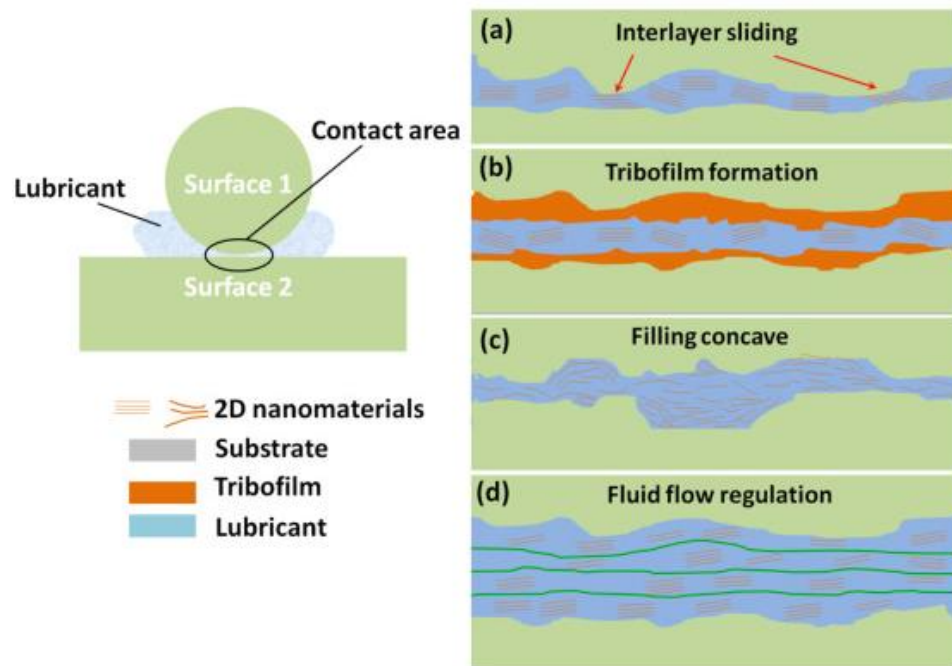


Figure 2-11. Common lubrication mechanism of 2D layered nanosheets as lubricant additive in the base lubricant¹¹².

2.4.3. Inorganic polymer glass melt lubricants

Phosphate compounds have been used as lubricant additives for a long period in automotive engines, hot metal forming, and manufacturing industries. It is well-known that the most important and common phosphate additive comes from zinc dialkyl dithiophosphates (ZDDPs). According to Barnes et al.¹¹³, ZDDP plays an important role as antioxidant and anti-wear additives in engine oil and other industrial lubricants. The mechanism behind its outstanding lubrication has been investigated by Martin and Pearson using the basis of the hard and soft acids & bases principle^{114, 115}. Due to the high thermal stability and excellent oxidation resistance, inorganic poly-phosphates have been applied widely in the hot metal forming industry as glass melt lubricants. As investigated by Kita et al.¹¹⁶, an addition of phosphate increases the oxidation resistance of graphite by almost 200°C. Meanwhile, the addition of magnesium-phosphate reduces the friction coefficient of graphite to less than 0.05 at 500°C. Recently, alkali phosphate glasses have been applied due to their excellent lubricating properties as well as oxidation protection¹¹⁷⁻¹²¹. From the literature, alkali phosphate glasses are very stable at elevated temperatures (up to 800°C) and their liquid melt possess high viscosity and good adhesion to the metal surface. The tribofilm formation from the tribochemical reactions between phosphate melts and metal surfaces creates a glass layer that can act as an oxidation protective barrier. The chemical nature hierarchical tribofilm layer of poly-phosphate has been reported as can be seen in **Figure 2-12** which reveals a polymerization of short-chain phosphate, formed by the reaction of iron oxide and poly-phosphate that shorten the chain length under sliding shear at high temperatures. This hierarchical structure is beneficial in improving the mechanical properties of the tribofilm and reducing friction and wear through the formation of a long chain-length polyphosphate sub-layer.

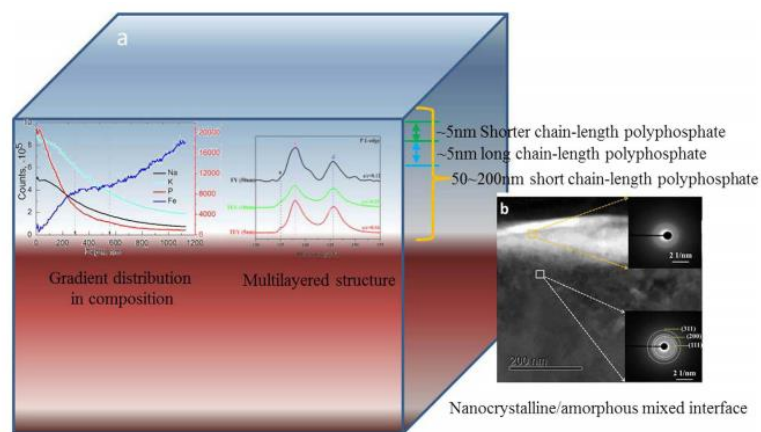


Figure 2-12. Schematic of phosphate-tribofilm induced at elevated temperature under tribological test.¹²⁰

Apart from phosphate melt, borate melt has also been considered as a possible candidate for elevated-temperature lubricant. Due to its inertness and thermal resistance, borate base inorganic polymer has been widely used as heat-resistant glass. The chemical reactions between borate compounds and steel substrates induce the formation of boron-containing films which can help to reduce friction and wear¹²². This tribofilm can support a high contact load and help to prevent

excessive wear. Commercial sodium tetraborate with the formulation of $\text{Na}_2\text{B}_4\text{O}_7 \cdot 10\text{H}_2\text{O}$ and several borate-base compounds have been applied as the additives components or lubricant base in industry¹²³. Several studies have reported that the use of alkali metal borates such as sodium tetraborate ($\text{Na}_2\text{B}_4\text{O}_7 \cdot 10\text{H}_2\text{O}$) and potassium tetraborate ($\text{K}_2\text{B}_4\text{O}_7 \cdot 10\text{H}_2\text{O}$) can dramatically reduce wear and display load-carrying capability at high temperatures^{124, 125}. In addition, several US patents show the excellent anti-wear properties and corrosion protection of a wide range of alkali metal borates at extreme pressure^{126, 127}. Boshui et al.¹²⁴ proposed that the anti-wear and friction reduction abilities of sodium borate and potassium borate come from the tribochemical reaction of these compounds and iron oxide. By utilizing XPS analysis, they found that there is a formation of B_2O_3 , Fe_2O_3 , and Fe_3O_4 within the wear track. Tran et al.¹³ have first characterized the tribofilm formation of sodium tetraborate at 800°C after the pin-on-disk testing. The authors found the formation of a bi-layered structure tribofilm assembled from sodium layer and boron oxide layer within the wear track. The diffusion layer of sodium above the scale may prohibit the movement of the metallic ions from the substrate to the interfaces and, thus, reduce the oxidation degree. Under friction at elevated temperatures, borate melt generates a complicated glass structure due to the unique properties of boron elements which can exist in tetrahedral or triangle hybridization with oxygen. During the friction process, tetrahedral hybridization can shift to triangle hybridization which can lead to an increase in the bridging oxygen bond that forms the highly-polymerized vitreous boron oxides at the sliding interfaces (**Figure 2-13**).

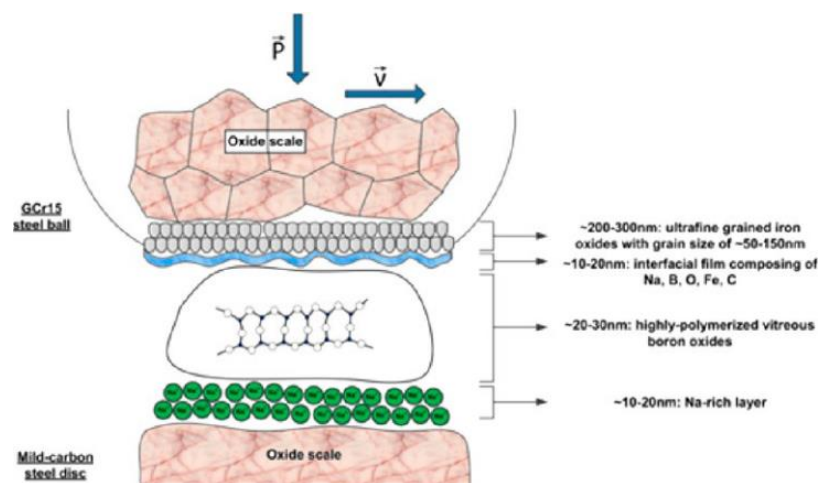


Figure 2-13. Schematic of phosphate-tribofilm induced at elevated temperature under tribological test.¹³

Besides the phosphate and borate melts, the silicate melts are another potential candidate for high-temperature lubricants due to their high thermal stability, high oxidation resistance as well as low cost, and environmental friendliness¹²⁸. Fundamentally, the silicate glass network composes the chain, cyclic, and larger polymeric structure of SiO_4^{4-} groups that are linked to each other through the covalent bridging oxygen atom. The addition of alkali cations at high concentration into the network can act as the network modifier or charge balance that can depolymerize the polymeric large chain into the shorter ones. This can be explained by the formation of non-bridging oxygen

to neutralize the excessive charge from alkali content. Therefore, the covalent bond of Si-O-Si is inevitably broken and the glassy network is destroyed continuously¹²⁹. The properties of alkali silicates are dependent on the ratio of SiO₂/Na₂O which can be adjusted. The first application of silicate melts in hot metal forming has been introduced in two publications from Japan^{11, 60} although the lubrication mechanism has not been interpreted. Recently, the lubrication mechanism of sodium metasilicate has been investigated by Wang et al.¹⁴ At 920°C, the sodium metasilicate melt separates the direct contact of the rubbing surfaces and generates a tribofilm which consists of a sodium-rich layer above a manganese-rich layer above the oxide scale (**Figure 2-14**). The manganese-rich and sodium-rich bi-layered tribolayer acts as a barrier to oxygen penetration and contributes to friction reduction. The amorphous sodium-rich layer is believed to contribute to the reduction of friction since the separation of the direct asperities contact by the amorphous sodium and sodium metasilicate layer can provide an easily shearing interface. In addition, the formation of the amorphous sodium-rich layer indicates the high activity of the sodium at high temperatures which can diffuse into the oxide scale area, migrating into vacant sites and filling interstitial defects. This process inhibits the outward diffusion of metallic cations and forms a barrier to prevent oxygen penetration, thus, reducing the oxidation degree. Meanwhile, the authors also identified the MnFe₂O₄ on the top surface with the dominant crystal plane (111) being parallel to the sliding surface, and they believe that this structure will behave like the typical layered nanoparticles which can contribute to the improvement of the tribological behavior of the rubbing counterparts.

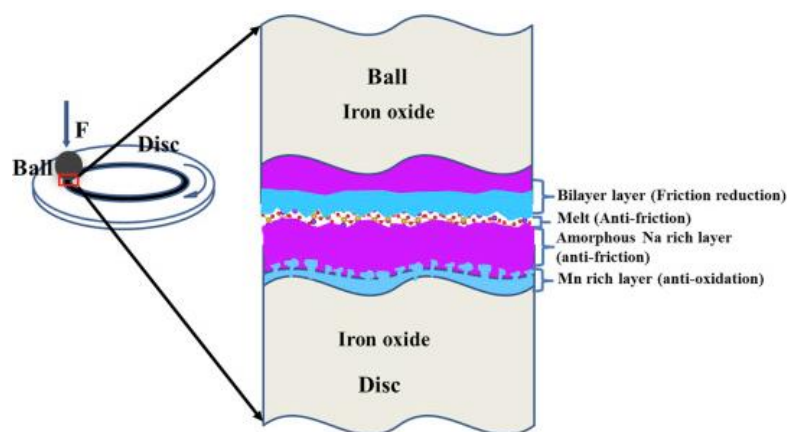


Figure 2-14. Schematic of the tribofilm formation on the counterparts after sodium metasilicate lubrication at elevated temperatures.¹⁴

2.5. Recent progress in high-temperature inorganic melt lubricants

2.5.1. Intrinsic effect of sodium oxide content on the lubrication and oxidation of melt lubricant

(This section content have been published in Langmuir, 2020, 36, 27, 7850–7860, <https://doi.org/10.1021/acs.langmuir.0c00895>)

At elevated temperatures, the formation of individual charged species (alkali cations and glass-

forming anions) has been shown to exist within the melts^{130, 131} that play an important role in the tribofilm formation during sliding⁵⁹. The contribution of sodium towards friction reduction and oxidation prevention has been previously addressed¹³², however, a comparison between B₂O₃ and Na₂O-2B₂O₃ in this study has a limitation since the structure of the latter binary system is significantly different from the structure of B₂O₃. The author has recently published the results on an intrinsic effect of sodium in lubricity and anti-oxidation of the sodium silicate melt to fortify the fundamental understanding of the lubrication mechanism of sodium-containing melt at elevated temperatures. In particular, the friction behavior and high-temperature oxidation of the sodium-containing silicate melts under steel/steel contacts have been investigated at different sodium oxide contents (Na₂O : SiO₂ = 1:3 (sodium trisilicate); 1:2 (sodium disilicate), and 1:1 (sodium metasilicate)).

Accordingly, sodium metasilicate, which has the highest sodium concentration, demonstrates the lowest friction coefficient of 0.14 under the steady-state regime (**Figure 2-15a**). The friction coefficients tend to increase as the sodium oxide content in the silicate lubricants decreases (**Figure 2-15a**). The highest friction coefficient is observed for sodium trisilicate (0.45), which is even higher than that of the dry sliding test (0.35). In addition, sodium metasilicate also results in the lowest disc and ball wear loss volumes (1.11 mm³ and 0.015 mm³ respectively) (**Figure 2-15b**) compared to other lubricants. The results of lubricated sliding show a general decrease of disc and ball wear loss with increasing concentration of sodium oxide. The inset 3D image in **Figure 2-15b** reveals the tendency of surface smoothening in both disc and ball wear track as the function of the sodium concentration in the silicate lubricants.

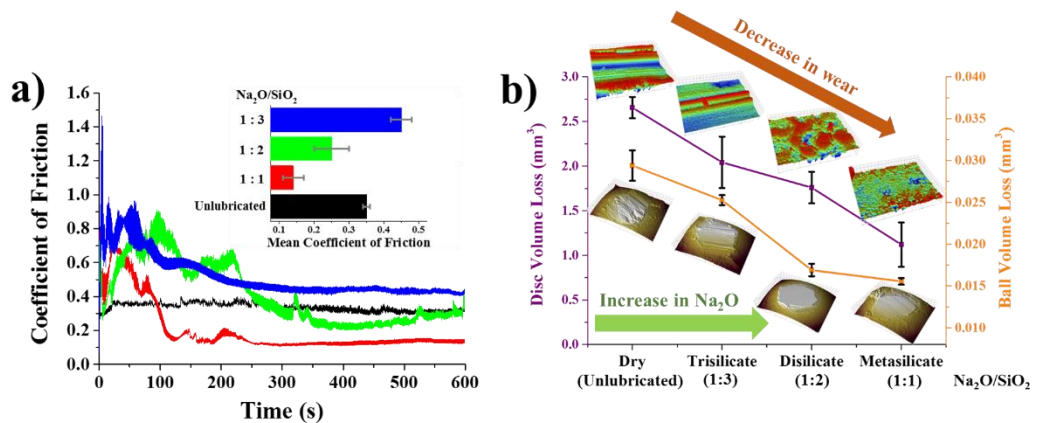


Figure 2-15. a) Dynamic coefficient of friction for sliding couples in unlubricated and lubricated (various silicate lubricants) conditions for 600 seconds at 950°C. The inset shows the average coefficient of friction at steady state; b) Corresponding disc and ball wear loss volumes after frictional tests using various lubricants at 950°C. The inset picture is the 2D wear depth image of the disc and ball after the friction test.

Under isothermal oxidation testing at 950°C, sodium-trisilicate (Na₂O : SiO₂ = 1:3) and –disilicate (Na₂O : SiO₂ = 1:2) delivers the excellent anti-oxidation by the fully melted coating on the steel substrate (SEM images, **Figure 2-16a-b**). Although several oxide particles nucleate inside the

trisilicate and disilicate melt (**Figure 2-16a-b**), the oxide layer in these cases is not fully developed. In contrast, sodium metasilicate ($\text{Na}_2\text{O} : \text{SiO}_2 = 1:1$) partially melts and it is intermingled with nucleated oxide particles to form a rigid composite layer ($\sim 100 \mu\text{m}$) above the steel substrate (**Figure 2-16c**). SEM/EDS mapping shows the formation of coarse discrete clumps of the Mn-rich phase, which are mainly concentrated on the surface and some within the coating. The oxidation reactivity of silicate melts increases significantly via an increase in sodium content. Sodium metasilicate with the highest concentration of sodium can react with Fe^{2+} through the charge exchange reaction (2-i). The free Na^+ ions resulted from (2-i) subsequently react to oxide species (Fe_2O_3 and Mn_2O_3), through (2-ii) and (2-iii), in the developed oxide layer. Such chemical reactions are thermodynamically favorable¹³³, which causes the formation of NaFeO_2 and NaMnO_2 in the coating. These reactions promote the formation of the individual charges from the steel base to fulfill the requirement of the reactants and thus accelerating the oxidation process. The reaction products from (2-i) to (2-iii) are intermingled to form the thick composite coating on the steel substrate.

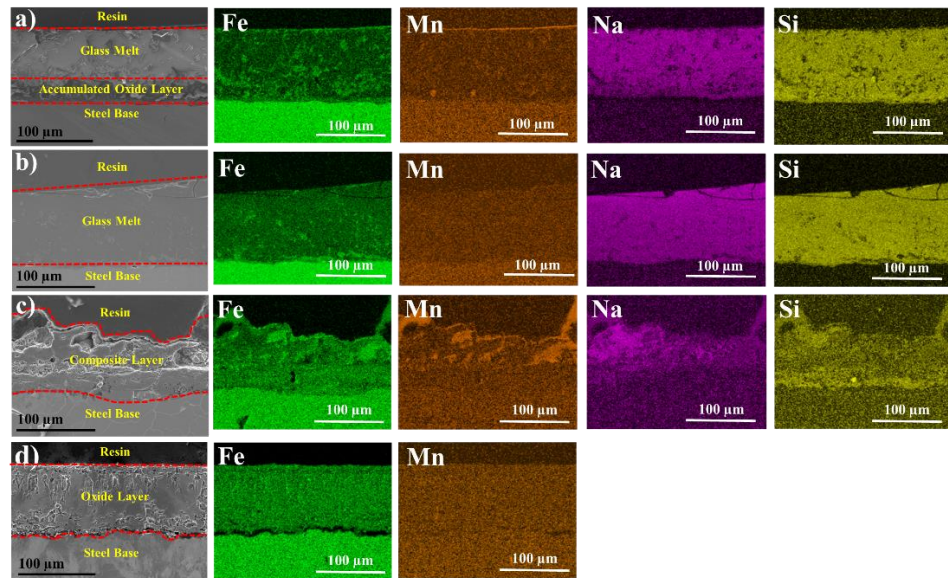
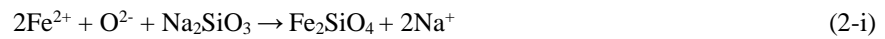


Figure 2-16. Cross-sectional SEM images and EDS maps of the oxide layer formed on the lubricant-coated steel disc following isothermal oxidation at 920°C for 600 seconds: a) Sodium trisilicate; b) Sodium disilicate; c) Sodium metasilicate; and d) No-lubricant.

Under the hot friction conditions, the tribofilm is developed resulting in the distinct tribological performance for each melt lubricant (**Figure 2-17**). In trisilicate melt, the segregation and cluster formation of sodium within the melt occurs due to a low sodium amount¹³⁸. Thus, the trisilicate

melt network behaves similarly to that of silica with an open network that favors the incorporation of M^{2+} and M^{3+} charged species ($M = Fe$ and Mn). The incorporation of transition metallic ions into the melt can cause the breakdown of the glassy matrix. This results in a significant drop in viscosity for trisilicate. In addition, the aggregation of sodium within the melt of trisilicate hinders the reactivity of Na^+ toward the oxide surface. Therefore, the trisilicate lubricant is easy to worn out as subjected to shearing. Such a phenomenon was confirmed by the formation of only a thin fine-grained oxide layer containing magnetite above the steel substrate (**Figure 2-17a, b**).

In contrast, the more uniform distribution of Na^+ within the glassy matrix appears at higher sodium content (disilicate and metasilicate)¹³⁸. The homogeneous distribution of Na^+ within the melt structure increases its mobility during the hot friction test. It is confirmed by the formation of a hierarchical tribofilm layer on the contact surfaces in both cases (**Figure 2-17c-f**). As the hot friction test progressed, the oxidation sequence induces an outward electron transfer¹³⁹, which saturates the oxide wear surfaces by high electron potential. Thus, the developing attraction field for cationic moieties (Na^+) movement is established. Even though the radius of Na^+ (0.095 nm) is higher than that of transition metal ions: Fe^{2+} (0.076 nm), Fe^{3+} (0.064 nm), Mn^{2+} (0.081 nm), and Mn^{3+} (0.072 nm)¹⁴⁰, its diffusivity in the amorphous glass is a low-energy process¹⁴¹, which is at least two orders of magnitude higher than that of O^{2-} . Therefore, a high concentration of sodium is developed on the oxide surface for both sodium disilicate and metasilicate. A deep reduction of friction in the case of metasilicate compared with disilicate (**Figure 2-15a**) is considered due to the presence of an amorphous sodium-rich layer (**Figure 2-17e, f**). This layer not only resulted in the electrostatic repulsion between the two positively charged surfaces that reduce the friction resistance^{142, 143} but also prevent the diffusion of M^{2+} and M^{3+} ($M = Fe$ and Mn) from steel to the silicate structure by reactions (2-ii) and (2-iii).

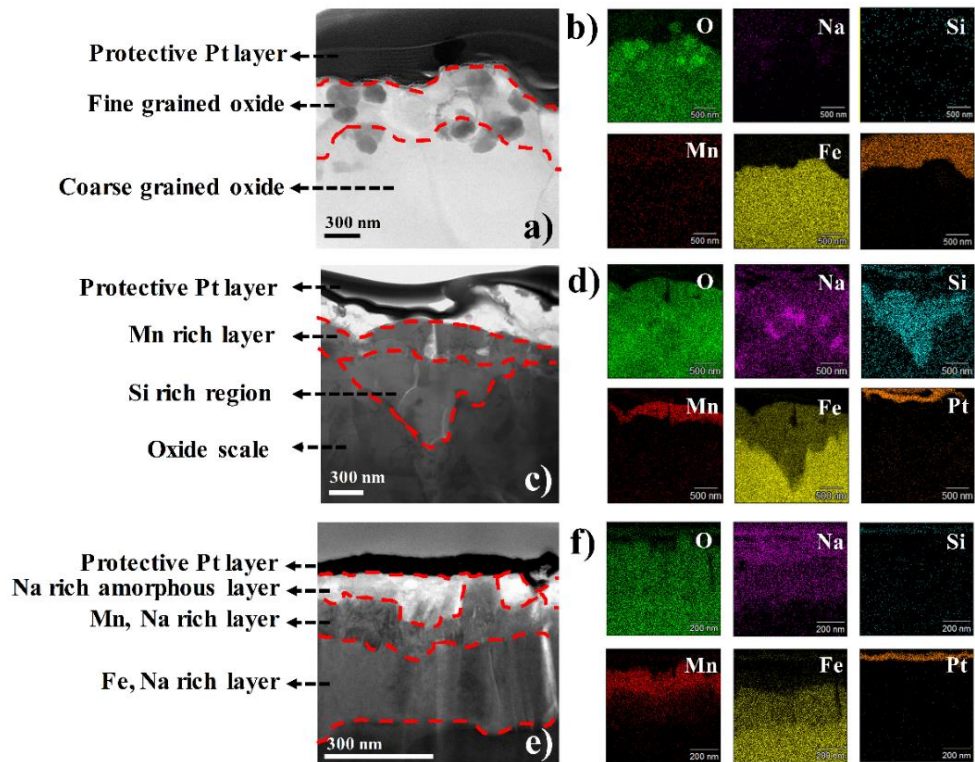


Figure 2-17. STEM-BF image of the cross-section taken from a disc wear track after sliding under trisilicate lubrication at 950°C. b) EDS maps of a) showing an elemental distribution; c) STEM-BF image of a cross-section taken from thick tribofilm region on the disc wear scar after being lubricated by disilicate at 950°C; d) EDS maps of (c) showing elemental distribution; e) STEM-BF image of a cross-section of a disc wear track following sliding under metasilicate lubrication at 950°C, and; f) EDS maps of e) showing elemental distribution in the tribofilm.

The characterization of the tribofilm on the ball for metasilicate is shown in **Figure 2-18** proving the diffusion of sodium from the melt to the oxide surfaces. There is the aggregation of sodium signal on the top and at the bottom of the silica-like layer on the ball (**Figure 2-18b**). The diffusion of sodium out of the metasilicate melt causes the polymerization of the disordered silicate network, resulting in a silica amorphous layer between the contact surfaces (**Figure 2-18a, c**). Since amorphous silica is a good boundary lubricant^{144, 145}, it can provide the easy shearing capability between the contacting components and reduce significantly friction with the presence of sodium ion¹⁴⁶. The finding of the silica layer in the present study fortifies the previous study of Wang et al.¹⁴, which did not show the presence of such layer on the ball to support the excellent friction reduction of metasilicate. In their study, only the composite layers of Na, Fe, and Mn were found as the topmost layer on the ball, which contains the spinel FeMn_2O_4 .

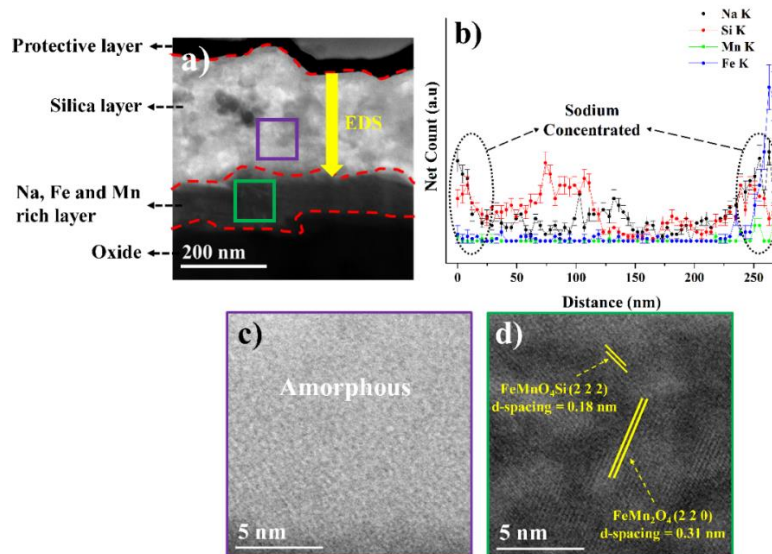


Figure 2-18. a) Magnified STEM-BF image of the tribofilm on the ball surface after being lubricated by sodium metasilicate; b) EDS line profile marked in a); c) HR-STEM image of silica-like layer, and; d) HR-STEM image of the reaction product layer.

It is believed that the lack of this NaFeO₂-Fe₂O₃ composite layer results in the destabilization of the whole tribofilm in the case of sodium disilicate, causing the large variation and increase of the friction as well as the inhomogeneous wear surface morphology. Therefore, the Na₂O : SiO₂ ratio is significantly important, which determines the oxidation prevention and tribological performances of the silicate melts. It was due to the critical role of sodium at different amounts that governs the different tribochemical reactivity of the silicate melts toward the oxide surface. Lowering the sodium content in the sodium silicate melt leads to the abundant volume space in the network¹⁴⁷, which can favor the incorporation of the cationic ions (Fe²⁺ and Mn²⁺) generated from the steel substrate at elevated temperatures. The entrapment of such ion species hinders oxidation progress. However, the low amount of sodium in the melt leads to the phase separation and cluster formation of sodium that reduces significantly the mobility of such charge individuals. Although increasing the amount of sodium can lead to oxidation promotion by reactions (2-ii) and (2-iii), it is responsible for accelerating and enhancing the tribochemical reaction between the silicate melt and oxide surfaces. These reactions govern the development of hierarchical tribofilm with multifunctional effects that can reduce friction significantly, maintain the stability of friction, and alleviate wear loss.

2.5.2. Combining sodium silicate and sodium borate melts for high-temperature lubricant

(This section content has been published in Industrial & Engineering Chemistry Research, 2020, 59, 7, 2921–2933, <https://doi.org/10.1021/acs.iecr.9b05767>).

Although the single sodium-containing melt lubricants have been received extensive considerations, few studies investigate the tribological performances of their mixture thereof. It is expected that the combination of an alkali-borate compound to an alkali-silicate can produce a better lubricity and less wear by the formation of borosilicate melt¹⁴⁸ with a stronger adherence on

the sliding contacts¹⁴⁹. The published results from the author are summarized below showing the investigation on the lubrication and anti-oxidation of the sodium borosilicate lubricant produced from the mixture between sodium borate and sodium silicate at elevated temperatures. This information not only paves a pathway for the utilization of sodium borosilicate melt in high-temperature lubrication but also provides a strong research background for the formulation of a high-temperature lubricant package.

Typically, two Silicate/Borax ratios were chosen in the study (Silicate/Borate weight ratio = 9/1 (Si-B-1) and 1/1 (Si-B-2)) according to the patent by Jennings et al.¹⁵⁰. Friction and wear evolution as a function of silicate/borate weight ratio and temperature are shown in **Figure 2-19**. Si-B-1 (silicate/borax = 9/1) result in a rapidly established steady-state friction response at 800°C, reducing the coefficient of friction from 0.5 (pure silicate) to approximately 0.17 (**Figure 2-19a**). The wear volume in the ball (over 0.02 mm³) (**Figure 2-19f**) is thought to be mainly associated with the initial running-in behavior. Compared to the steel coated by pure sodium silicate (Si), Si-B-1 (silicate/borax = 9/1) lubrication at 800°C results in a substantial reduction in disc wear by approximately 80% (**Figure 2-19e**). More sodium borate additions, Si-B-2 (silicate/borax = 1/1), leads to excellent wear resistance, with very low wear volumes for both the disc (0.8 mm³) and the ball (0.01 mm³) (**Figure 2-19e and Figure 2-19f**) when compared to that of the pure silicate system (6.0 and 0.03 mm³, respectively). However, a high friction value (0.5) prevails throughout the test (**Figure 2-19a**) at 800°C.

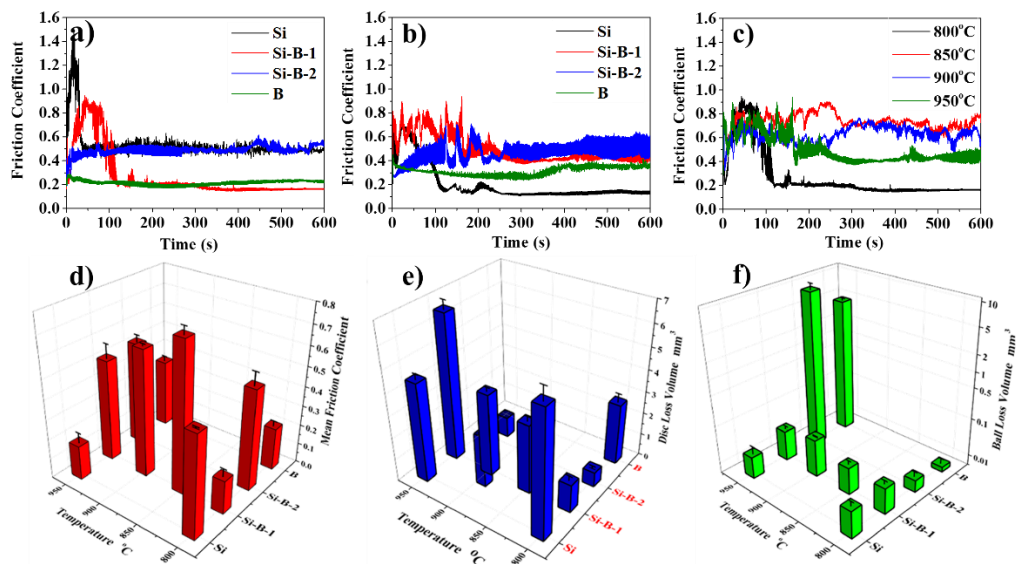


Figure 2-19 Tribological results for a) Compositional dependence of the coefficient of friction at 800°C; b) Compositional dependence of the coefficient of friction at 950°C; and c) Temperature-dependence of the coefficient of friction for sample Si-B-1; d) Mean steady-state friction coefficient as a function of temperature and composition; e) Disc wear loss volume and f) Ball wear loss volume after friction testing as a function of temperature and composition.

The key influencing factor of temperature on friction and wear of Si-B-1 is shown in **Figure 2-19c**, **Figure 2-19e**, and **Figure 2-19f**. Superior lubrication at 800°C attains other than the values from

higher temperatures with a friction coefficient of 0.17 (**Figure 2-19a**), disc wear volume of 1 mm³ (**Figure 2-19e**), and ball wear volume of more than 0.02 mm³ (**Figure 2-19f**). Particularly, the rise of temperature results in an increase and a high degree of instability in friction, particularly at 850°C and above (**Figure 2-19c**, **Figure 2-19e**, and **Figure 2-19f**). At 950°C, the addition of sodium borate (B) to sodium metasilicate (Si) at 950°C does not improve the tribological performance and the sliding stability deteriorates (**Figure 2-19b**, **Figure 2-19e** and **Figure 2-19f**). The lubricant Si-B-1 produces a heightened steady-state friction coefficient (0.4) (**Figure 2-19b**) compared with the lower temperature test (**Figure 2-19a**) with a modest ball wear loss of 0.04 mm³ (**Figure 2-19f**). These result from undesirable abrasive/adhesive wear and plastic deformation of the hot steel surfaces¹³. In marked contrast, the ball wear loss after being lubricated by Si-B-2 increases dramatically and reaches peak values of 9 and 5 mm³ respectively at 950°C (**Figure 2-19f**). Such massive wear loss in the ball is associated with the surface hardening effect that occurs on the steel disc due to the presence of boron¹⁵¹. Consequently, it leads to the formation of the iron boroferrite compounds in the boride layer on the steel substrate, and this process is called boriding surface hardening¹⁵². As investigated by Petrova et al.¹⁵³, the iron boroferrite coating improves the surface microhardness of the coated steel up to five times larger than the untreated steel.

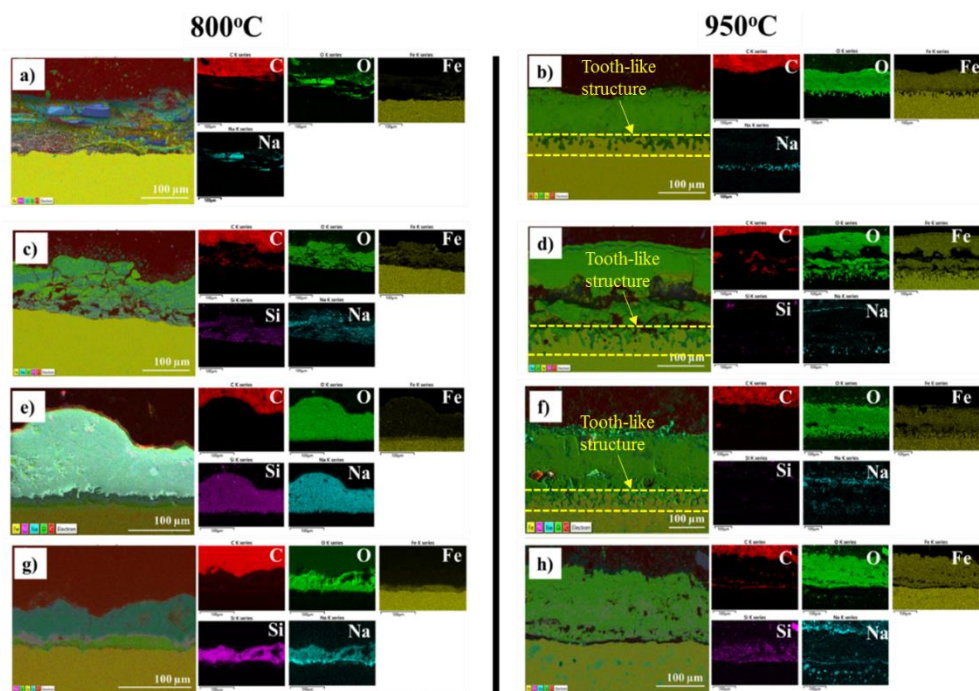


Figure 2-20. Elemental distribution between the coated lubricants and the oxide layers after oxidation test at 800°C and 950°C by ESD mapping: (a)-(b) B; (c)-(d) Si-B-2; (e)-(f) Si-B-1; and (g)-(h) Si.

Static oxidation behavior of borate, silicate, and the mixture thereof on mild steel are also considered at 800°C and 950°C. Compared to the results at 800°C, all the samples at 950°C display more severe oxidation of steel substrate (**Figure 2-20a-Figure 2-20h**). Intriguingly, all samples except for sodium silicate coating illustrate the diffusion and corrosion areas of sodium with an

anchored microstructure between the topcoat and the steel substrate (**Figure 2-20b, d, f, and h**). The formation of distinct tooth-like microstructure at 950°C for all boron-containing coatings (**Figure 2-20b, d, and f**) is the strong evidence for the boriding phenomena¹⁵⁴. In the previous studies of Tran et al.¹⁵⁵, sodium in the borate melt has high reactivity and mobility at 800°C that can significantly diffuse to the oxide scale even under static oxidation conditions and causes the fluxing action of the grown scale and promote the oxidation. The diffusion of sodium results in the polymerization of boron oxide in the borax melt network¹³ and this boron oxide phase intermingles and thermodynamically reacts to iron oxide to form the iron boroferrite at 950°C¹⁵¹. Therefore, it can be concluded that the lubricants containing sodium borate will likely cause the corrosion of the steel substrate above 900°C which is associated with the high reactivity and mobility of sodium in the sodium borate melt.

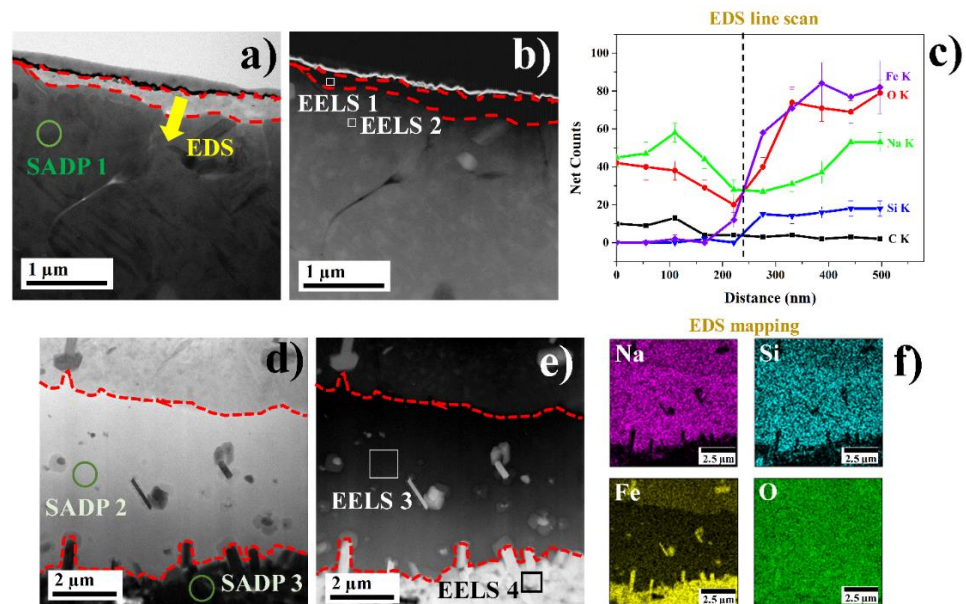


Figure 2-21. STEM-BF and STEM-HAADF images of the various layers produced in the disc wear scar after sliding under Si-B-1 lubrication at 800°C: a)-c) Details of the outermost carbon species layer and the adjacent reaction products layer; d)-f) Details of the mid-regions of the tribolayer showing the reaction products layer at the top; the amorphous glassy layer in the center and the iron oxide adjacent to the steel substrate at the bottom.

The lubrication mechanism of the best lubricant Si-B-1 at 800°C has been illustrated by the detailed views of the tribofilm on the disc wear surface. The uppermost (~500 nm deep) surface layer is an amorphous sodium carbonate layer with very low atomic number contrast (**Figure 2-21a and Figure 2-21b**) according to EDS line scans (**Figure 2-21c**) and EELS C-K edge (**Figure 2-22b**) analysis. The formation of this layer on the outer surface (**Figure 2-21a**) is due to the decarburization of [C] species in steel¹³ and the reactions between atmospheric carbon dioxide and sodium oxide during the cooling process. The second layer is structured by an agglomeration of large particles which are the reaction products between the melt and oxide components (**Figure 2-21b**). During sliding, the mechanical intermixing by shearing action favors the corrosion

reactions of iron oxide by the sodium-containing molten fluid. These particles then agglomerate and compact under stressed shearing and form the composite reaction product layer. Such resulting film is dense and protective, which is expected to suppress further scale development as it thickens.

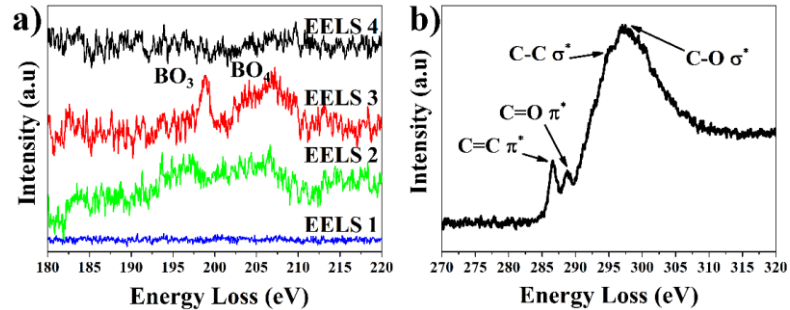


Figure 2-22. a) EELS B-K edge taken at the topmost layer (EELS 1); the adjacent reaction products layer (EELS 2); the mid amorphous glassy layer (EELS 3); and the oxide adjacent to the steel substrate (EELS 4). b) EELS C-K edge showing the distinct peaks of carbonate and amorphous carbon taken at the topmost layer.

The third layer is amorphous glass with few micro-oxide particles dispersed inside (**Figure 2-21d and Figure 2-21e**). According to EDS mapping (**Figure 2-21f**) and EELS analysis (**Figure 2-22a**), this amorphous glassy layer is essentially the molten sodium borosilicate lubricant, which is solidified during the cooling process after the sliding test. Under shearing conditions, the molten fluid is expected to be compressed into the underlying region. The friction results and tribofilm structure indicate that its presence has a significant beneficial effect in maintaining stable lubricity (**Figure 2-19a**). The strong attachment of the glass layer to the oxide surface ensures reliable tribological performance, even under applied stresses. Moreover, EELS analysis (EELS 3, **Figure 2-22a**) confirms the significant presence of trigonally configured boron in the glass layer which can favor the possibility of double bond switching phenomena¹⁴⁷. This bond switching is favorable for improving the shear capability of the molten fluid during friction (**Figure 2-23**).

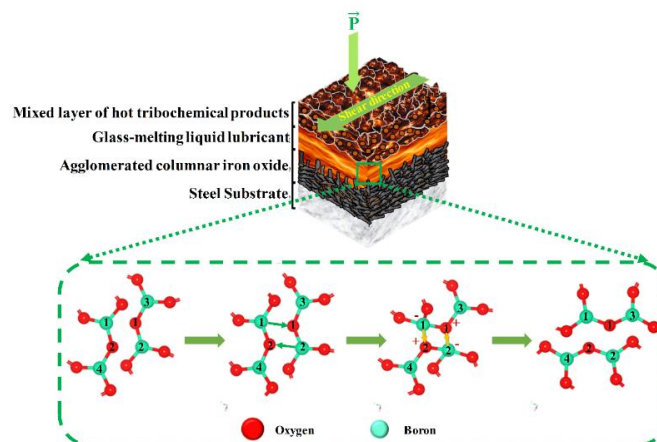


Figure 2-23 Schematic displaying the microstructure evolution on a disc surface after friction test under sodium borax-silicate (Si-B-1) lubricant at 800°C, with the double bond switching phenomena of trigonal boron oxide unit in the intermediate borosilicate melt layer.

On the ball specimens, the tribofilm comprises tightly aggregated large particles as the topmost layer, which is identical to the mixed reaction products on a disc (**Figure 2-24a**). Electron diffraction of this layer (**Figure 2-24b**) indicates the potential presence of Fe_2SiO_4 (1 3 0)¹⁵⁶. The crystallite phases of FeNaO_2 (0 0 2) are also observed¹³⁴. Between the uppermost region and the steel substrate is a second layer which is densely packed by the fine-grained oxide particles (**Figure 2-24c**). Electron diffraction of this region (**Figure 2-24d**) consisted of Fe_2O_3 ¹⁵⁷. The topmost layer on the ball is expected to limit the scale development while a second layer comprising ultra-fine-grained particles (average diameter 50-100 nm) with high yield strength, excellent impact toughness, and good fatigue strength^{158, 159} can enhance the mechanical strength of the sliding interface and improve its wear resistance^{159, 160}.

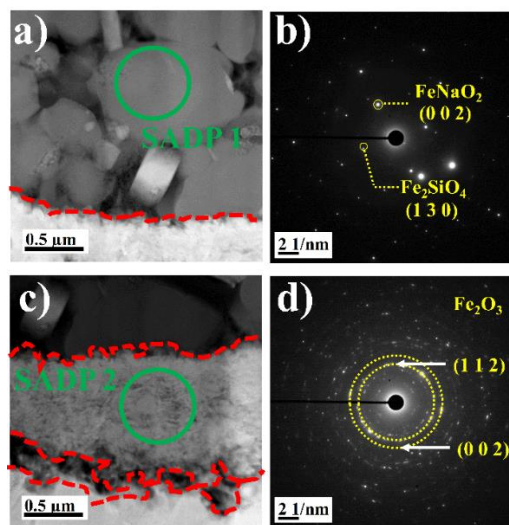


Figure 2-24 a) STEM-HAADF image of the outermost mixed reaction products layer on the ball under Si-B-1 lubrication at 800°C; b) STEM-HAADF image of the densely packed nanocrystalline layer between the outermost layer in a) and the steel substrate; c) SADP 1 captured from the region marked in a); d) SADP 2 captured from the region marked in b).

The results in this section demonstrate very good friction and wear reductions from the combination between sodium borate and sodium silicate melts at the silicate/borate = 9/1 weight ratio under hot friction test at 800°C. In addition, this mixture also provides good oxidation protection to the mild steel substrate which reduces the oxide thickness by 80% at 800°C by the formation of sodium borosilicate. However, the sodium borosilicate melt shows a deterioration of the lubrication and oxidation at above 850°C. It is closely related to the high mobility and reactivity of sodium in the melt toward the oxide scale as proven previously in section 2.5.1.

2.5.3. The lubricant formulation between sodium-containing melt and nanoparticles

Since the glass-melt lubricants by themselves have by now reached their performance limits, several attempts have been made to further reduce friction and wear by incorporating the solid lubricant into the glass melts. Graphite/Expanded graphite has been considered the most popular and it is still used in hot metal forming processes together with the melt lubricants.¹⁶¹ The addition

of expanded graphite in sodium metasilicate efficiently reduces the friction coefficient by ~79% at 851°C (**Figure 2-25**) and their lubrication mechanism has been investigated in-depth by Wang et al.¹⁶² At the testing temperature, expanded graphite oxidizes to form carbon dioxide (CO₂) which in turn react to sodium cations from the sodium metasilicate melt to form the sodium carbonate on the sliding surfaces. The formation of some grass-like debris containing both amorphous carbon and sodium carbonate nanocrystals within the wear track surface was observed and contributed to the friction reduction since sodium carbonate completely melts at 851°C. The viscous melt of sodium carbonate instead of sodium metasilicate is considered to be beneficial to friction reduction and anti-wear. In addition, the ordered MnFe₂O₄ layer with a thickness of 300 nm formed on the disc and the Na₅FeO₄ with (200) plane formed on the ball parallel to the sliding surface can be also the main reason for the friction reduction.

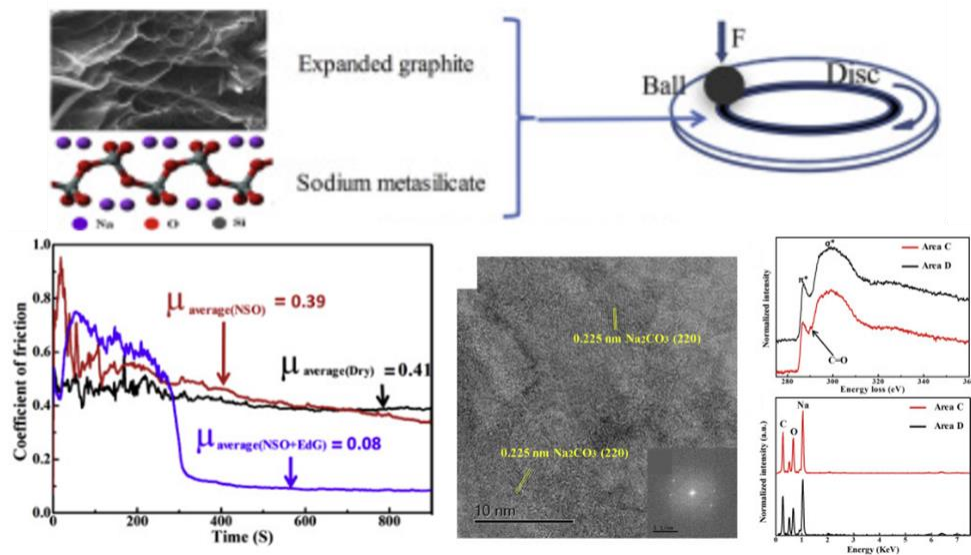


Figure 2-25. Lubrication performance and mechanism of the mixture between sodium metasilicate and expanded graphite.¹⁶²

However, graphite particles can be airborne and damage the electrical systems, and they accumulate as a black and dirty layer on the shop floor and increase the risk of slippage. Thus, its application has been restricted due to hygiene and environmental concerns.^{4, 163} In another research, Wang et al.¹⁵ blended the sodium polyphosphate with TiO₂ nanoparticles to formulate the water-based lubricant for hot strip rolling. It has been observed that the aqueous lubricant containing 2 wt.% TiO₂ nanoparticles and 20 wt.% sodium polyphosphate reduces the rolling force by 10% compared to pure water lubricant. It is believed that the lubrication mechanism of the mixture between sodium polyphosphate and TiO₂ nanoparticles is the combination of melt lubrication and nanoparticle lubrication. The semi-fluidic phosphate glass can deliver an easily shearing interface at the contact interfaces while nanoparticles can provide a protective film effect, sliding effect, and rotating effect or a combination between them during the rolling process. It is believed that the lubrication performance under hot rolling conditions can be further improved by the addition of other solid lubricants which can function synergistically with TiO₂ nanoparticles.

2.5.4. Research questions for high-temperature lubricants

The development of a functional additive package with an achievement in both the cost-effectiveness or lubricity efficiency has far-reaching implications, particularly in both transportation and hot metal forming processes, which often see the uncontrolled competitive and antagonistic effects between different solid lubricant additives within the based-fluid.^{16, 17} Because of the inevitable loss in effectiveness, solid lubricant additives are often formulated with a larger concentration than what is actually needed.¹⁶ It leads to the use of several organic surfactants or supporters (potentially harmful to the environment) to minimize the agglomeration, unexpected interactions between additives at large concentrations, and to ensure uniform dispersion of such functional additives within the based fluid.^{18, 19} To achieve the desired product with a better lubricating behavior than pure lubricant base, the number of additives, as well as the interaction between them, need to be calculated and considered carefully based on ASTM, API, or SAE¹⁶⁴. Either an excessive amount or an insufficient amount can decrease the tribological performance due to agglomeration and precipitation of these additives. In addition, the use of these surfactants or surface modifiers (mostly organic-based compounds) poses a risk to environment due to their decomposition at elevated temperatures that releases harmful gases. Therefore, a new approach or strategy should be considered to replace the traditional blending of the lubricant additives in the base lubricant by physical mixing.

2.6. Microencapsulation in the development of lubricant additives

Microencapsulation, which is a well-recognized technique, is commonly applied in the food and pharmaceutical industry, comes as a promising approach for formulating the lubricant. The reasons behind the purpose of using this technique start with the protected effect from the shell material, which acts as a shield inhibiting the unexpected interaction of components including chemical reaction, oxidation, or degradation when subjected to harsh environments. Moreover, by microencapsulating chemical additives inside the shell, it is possible to control the release of substances from the core to the outside environment by adjusting pH, temperature, or time. These benefits have been used and applied in various industrial fields regarding the delivery of the drug, protect oil fragrance, slow-release medicine, etc... Due to its desirable benefits, microencapsulation has recently become an innovative trend in lubricating industrial applications. Microencapsulation has been applied for the multi-additive system in engine lubricant to optimize the tribological functioning of the oil. In reality, several studies were conducted and their results show undoubted evidence to support this idea¹⁶⁴⁻¹⁶⁷.

2.6.1. Triggered release of the core active ingredient from the microcapsules

According to Hsu et al.¹⁶⁴, the following benefits of the micro and nano-capsules containing chemical lubricant additives basically come from long-term protection of engines by a slow release of additives over a period of time, an avoidance of the deleterious additive-additive interaction, and a reduction in the effective dosage of additive. In addition, the presence of multi desirable chemical additives in one package can result in a synergistic effect of each component, which can

enhance the lubricating properties. Moreover, the capsules are available to be triggered to release the core materials by several remedies such as chemical triggers (pH, disulfide bonds cleavage), thermally induced release (temperature change, phase transition), magnetically initiated release, electrical triggering, and mechanical triggering (shear)^{164, 165}.

The chemical-induced release includes two approaches, which come from adjusting the pH of the suspension and cleavage of the disulfide bonds by chemical reaction. These remedies have been applied in drug delivery triggering, focusing on the interaction of the outside environment to the capsules. The main mechanisms of releasing additives by adjusting pH come from several reasons, which relate mostly to the nature of the shell components and the interaction between the shell materials and the pH of surrounding environments (**Figure 2-26**). **Table 2-1** shows a few examples of an experiment regarding chemical trigger release, which comes from the natural and chemical structure of polymer shell materials.

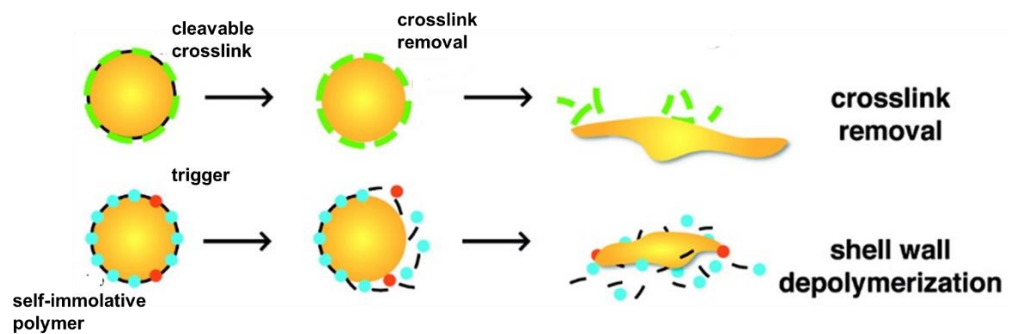


Figure 2-26. Schematic presenting the idea behind the chemical-triggered release of the core ingredients.¹⁶⁸

In addition to chemical-induced triggering, the thermal treatment which induces the release of the additive core is also an important factor for a controlled release during a period of time. Changing in temperature may result in the melting of a microcapsule or microsphere polymer or causing a phase change transition, transforming a swollen, hydrated state to a shrunken, dehydrated state. Temperature increases can also result in the purposeful disassembly of polymers. There are some examples of phase transitions of low melting point shell materials, which create pores in the shell wall, leading to core release. Several food additives and fragrances have been shown to release more quickly upon shell wall melting. According to Dabbagh et al.¹⁶⁹, by increasing the temperature of core-shell nanostructures comprising of mesoporous silica core and low melting point polyethylene glycol (PEG), the shell undergoes the phase transition from solid to liquid, leading to a release of the additives inside. As mentioned from Esser-Kahn et al.¹⁶⁸, the lower critical solution temperature of NIPAAm (derivatives of poly(N-isopropyl acrylamide) can result in a pore formation when biphasic capsule walls are heated, leading to increased permeability. Also, NIPAAm microcapsules can burst from increased internal pressure upon contraction of the capsule shell wall due to temperature increase according to Latnikova et al.¹⁷⁰. In summary, the principal mechanism of thermal-induced release, thermally induced degradation of the shell, and diffusion of the core material through the polymeric shell can be boosted by the increased inner

pressure. This statement was also claimed in the research of Latnikova et al.¹⁷¹ which demonstrated the thermal-triggered release of the liquid core.

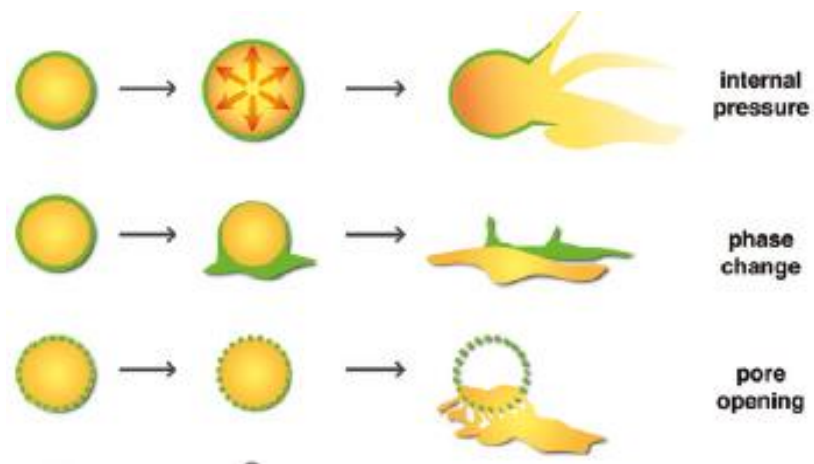
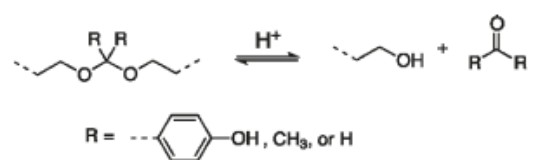
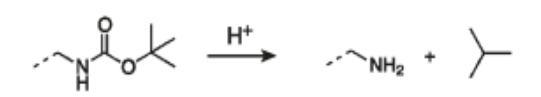
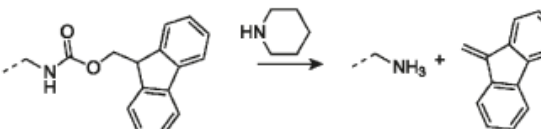


Figure 2-27. Schematic presenting the idea behind the thermal-triggered release of the core ingredients.¹⁶⁸

Another approach for the chemical additives to burst out from the microcapsule's core comes from the mechanical-induced release. This method is not common in pharmaceutical and food applications, thus its mechanism is rarely mentioned and investigated. However, the recent popularity of the microencapsulation technique in the lubrication industry leads to a quest to provide an insight into the mechanical triggers. As the lubricant contains additive-comprising microcapsules, in a specific case: engine oil, is subjected to slide and shear at high pressure, loading, and high temperatures, the mechanism of rupturing microcapsules by asperities shearing and sliding may become more important in releasing additives and reducing wear and friction. Several studies in the past have illustrated different types of microcapsules on the surfaces. In the thesis of Mitchell¹⁶⁵, the author concluded that there are three types of microcapsules on the surfaces including microcapsules that are rested or embedded either partially or fully on a surface. Further details will be discussed in the following part of the lubricant-containing micro-capsules application review, which introduces some of the published studies regarding microencapsulation in the lubricating area.

Table 2-1. Summarization of natural shell materials that are sensitive to pH change.

References	Polymer shell material	pH-induced release	Mechanism
172	Polyurethanes and Polyureas containing dimethyl ketal moiety	$\text{pH} \leq 5$	<p>In these experiments, the authors used ketals, also known as acetal chemistry, as acid-degradable chemical cross-linkers. At $\text{pH} < 5$, each ketal is converted to a ketone and two alcohols providing the chemical disassembly needed for triggered release.</p> 
173	Polyketals and Polyacetals	$\text{pH} < 5$	
174	Amphiphilic Polymethacrylate with a lialal-derived acetal moiety as hydrophobic side and poly(ethylene glycol) as a hydrophilic side.	$\text{pH} < 5$ (in this research is 3)	
175	Poly(hydroxyethyl acrylate)-block-Poly(n-butyl acrylate) (PHEA-PBA) cross-linked by a phenolic acetal.	$\text{pH} \leq 5$	
176	Various polyelectrolytes including poly-(acrylic acid) (PAA), poly(allylamine hydrochloride) (PAH)	Acidic	<p>The mechanism of rupturing in these polymer shell materials relies on charge switching inside the capsule shell walls mediated by the addition of protons to disrupt ionic or hydrogen-bonding interactions.</p> 
177	Polyelectrolytes consists Poly(acrylic acid-co-styrene) and Benzylated Poly(ethylenimine).	Acidic	
178	Poly(styrene) microcapsules coated with a synthesized polyelectrolyte	$\text{pH} = 4.5-5.5$	
179	Tannic acid assembled with a range of neutral polymers, poly(N-vinylpyrrolidone) (PVPON), poly(N-vinylcaprolactam) (PVCL) or poly(N-isopropylacrylamide) (PNIPAM).	pH out of range 2-10	
180	poly(2-vinylpyridine-b-ethylene oxide) (P2VP-PEO) block copolymer	$\text{pH} < 5$	

2.6.2. A brief review of the application of microencapsulation in tribology

In the patent by Williamson et al.¹⁸¹, the application of encapsulated lubricous materials on the surface of orthopedic cast iron is beneficial for easy handling because some approaches in the past have disadvantages due to the tape being too sticky or too slippery (**Figure 2-28**). As shown, the microcapsules were stuck onto the surface of the iron substrate by some chemical mixtures such as nylon or rayon. The microcapsules were formed of the water-insoluble polymer known as perylene and contain an ethoxylated surfactant, with the size ranging from 100 μm to 300 μm . The use of microencapsulation here prevents the surface from becoming too slippery to handle but, after rupturing by shearing from the contact interfaces between the tape and the roll-particles with light pressure the cast can be kept pliable for long enough to mold tightly to the limb. A downside to this approach however is that the microcapsules at the surface can be easily ruptured in transit thus making the material unusable.

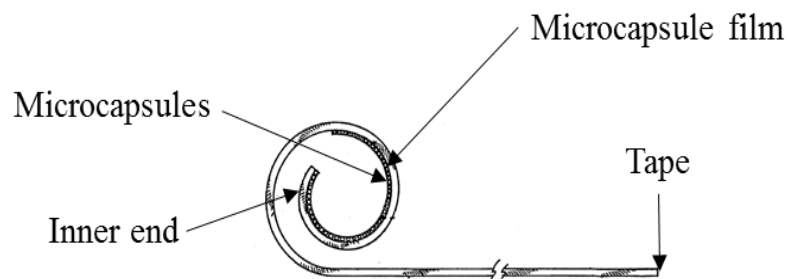


Figure 2-28. Microcapsules coated on the inner end of the tape-referenced steel.¹⁸¹

In the studies investigated by Guo et al.^{182, 183}, the partially or fully embedded microcapsules show a significant improvement in reducing friction and wear when the substrate slides over the surfaces of testing species. While the friction coefficient of loaded microcapsules epoxy is low compared to unloaded epoxy, the worn surfaces of loaded epoxy become smoother with less debris than the unloaded one. The mechanism was explained by the behavior coming from the mechanical triggered release of the lubricant inside the capsules, thus the sliding surfaces were lubricated during the testing, as shown in **Figure 2-29**. Moreover, the cavity formed after the capsules were broken by sliding and the core release, in turn, generated the void spaces which trap the debris inside, thus lowering the wear damage. It is important to mention that the mechanisms of fully embedded microcapsules inside the epoxy matrix are also the same as the partially embedded, which comes from the releasing of core lubricant and debris trapping during sliding. Several studies have been conducted based on such an idea about embedding the microcapsule in a various epoxy matrix and the results are consistent with the mechanisms presented above¹⁸⁴⁻¹⁸⁷.

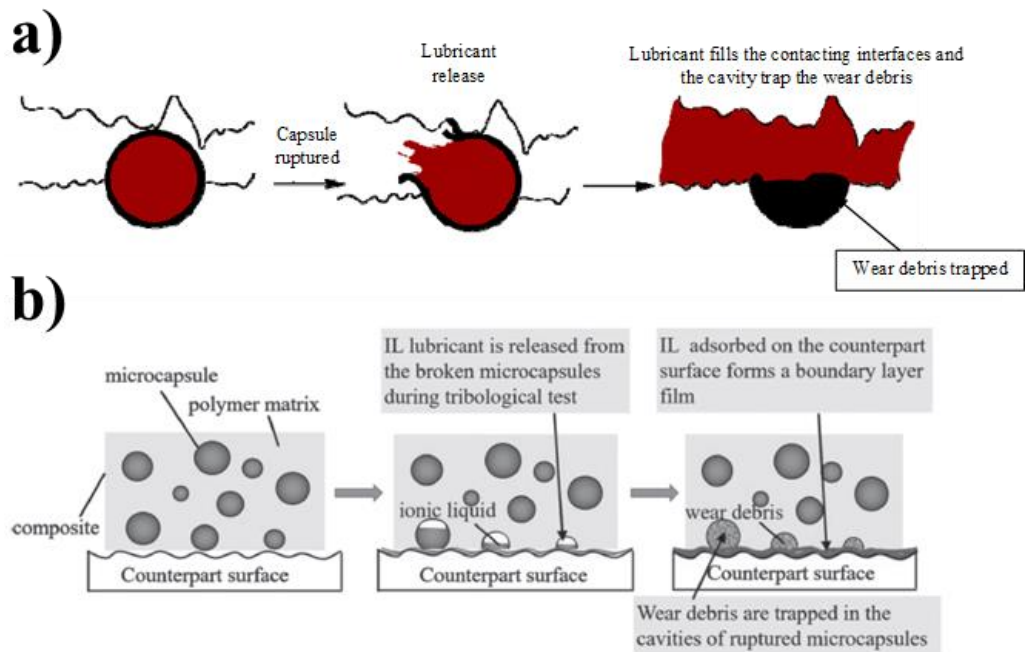


Figure 2-29. (a) Partially embedded and (b) Fully embedded microcapsules inside the epoxy matrix.^{165, 187}

On the other hand, microencapsulation has also been applied in another way, whereby encapsulating chemical additives can enhance the lubricating properties of the oil lubricant. Because this is a relatively new topic, there are not many published research papers and reports. The earliest introduction of this technique in formulating lubricant additives is from the doctoral thesis of Mitchell whereby the friction modifier was encapsulated by the poly(methyl methacrylate) (PMMA) shell.¹⁶⁵ The paper generated from this thesis shows a moderate effect in reducing the friction and wear of the dodecane lubricant compared to dodecane containing a saturated friction modifier.¹⁸⁸ The lubrication mechanism has been proposed by the authors as presented in **Figure 2-30**. In particular, it is anticipated that the PMMA shell is first squeezed through a contact to form the polymeric tribofilm on the wear surface. During the squeezing and crumbling of the shell, the bursting of microcapsules occurs which can release quickly the friction modifier to where and when it is needed within the contacting interfaces. In the next stage, a fraction of the friction modifier is anticipated to self-assemble on the polymeric tribofilm of PMMA through hydrogen bonding. Other friction modifier molecules may align perpendicularly on the wear surfaces depending on the polarities of the adsorbed monolayer of friction modifiers on the PMMA tribofilm. During sliding, the authors believe that this multi-layer of adsorbing friction modifiers and PMMA polymeric film can protect the wear surface and reduce friction by acting as the sacrificial layer similar to the mechanism of the friction modifiers.

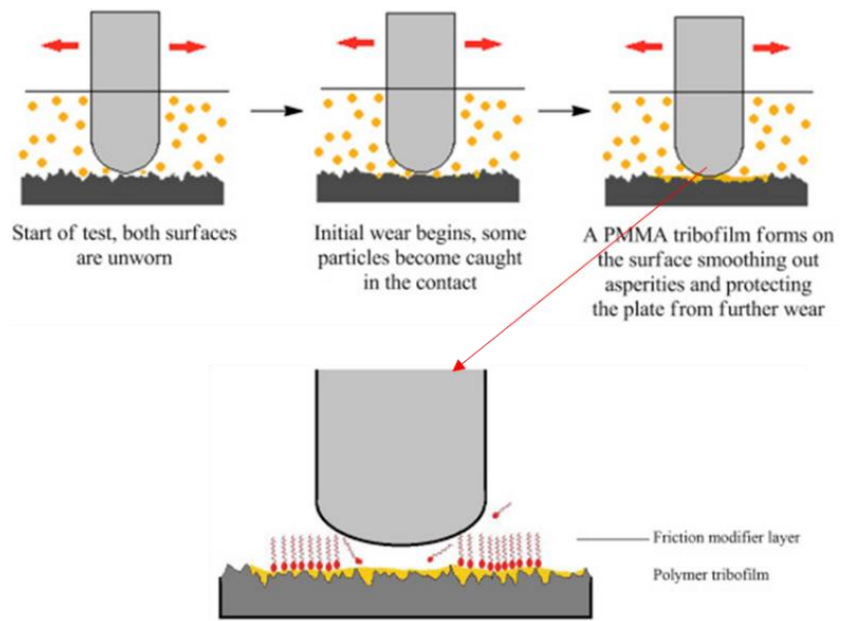


Figure 2-30. Proposed lubrication mechanism of the lubricant containing friction modifier loaded in the PMMA microcapsules.¹⁸⁸

Later, the application of this technique in engine oil has been reported in the patents of Hsu et al.^{164, 166, 167}, in which the benefits of microcapsules containing chemical additives in engine oil come from a controlled release of the core materials to decrease the oil consumption or increase the time intervals between oil changes. The concept of this idea is demonstrated in (Figure 2-31). The release control of core additives, as mentioned above, relates to several localized events and parameters. In this assembly, the change of environment (temperature, pH, mechanical shear) and the nature of polymer shells (cross-linking agents, lower critical solution temperature compounds) act as the main important factors for triggering the release of lubricant additives. The mechanisms associated with chemical triggers, thermal-induced release, and mechanical triggers are important in the automotive engine and metal forming industry. As mentioned by Hsu et al.¹⁸⁹, the testing of encapsulated additives depends on the intended use. For example, the released rate needs to be taken into account if the slow-release through the porous shell is the main purpose.

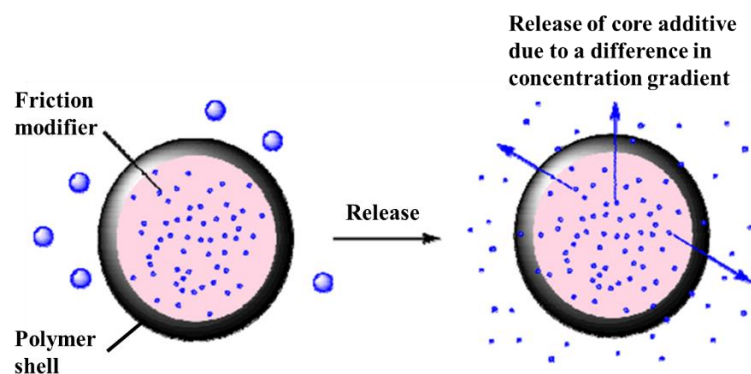


Figure 2-31. Concept of the controlled release of friction modifiers or chemical additives from the microcapsules.¹⁶⁵

From the controlled release concept, the requirement of improving the tribological performances, increasing the time interval before an oil change, and reducing the number of additives used for economic reasons is crucial. Therefore, microcapsules containing lubricant additives with a slow-release rate offer a potential solution. The release rate of the core depends on several parameters, which can be explained and described by Fick's Laws of diffusion¹⁶⁵:

$$\frac{dC}{dt} = A.H.D. \frac{C_{in}-C_{ext}}{d} \quad (2-1)$$

In this formula, A is the exposed surface area of the shell, H is the partition coefficient which is dependent on the natural properties of two immiscible solvents (continuous phases and dispersed phases). On the other hand, D is the diffusion coefficient of core additives which relates to the temperature, viscosity of the solution, and molecular weight of core additives. In addition, the thickness of the shell formation also affects the release rate, which is derived by d in the equation. The difference in concentration of core materials in continuous solvent outside and dispersed solvent inside also plays an important role in driving the movement of additives, which is also known as the gradient concentration. As A, H, D, and d can be controlled and manipulated through the preparation of core-shell materials and the selection of suitable solvents, the only reason which can influence the release rate comes from the gradient concentration between inside and outside. As the additives outside the capsules are consumed with time, the gradient concentration is either constant or increase (in case of fast consumption), thus driving the movement of materials outside and increase the release rate. As mentioned above, the release rate is remarkably important to improve lubrication by this mechanism. Therefore, the method to determine this parameter is essential to modify and control the amount of additives diffusing through the capsule walls.

In a patent by Hsu¹⁶⁴, different tests were conducted to examine the tribological performances regarding shear stability, wear reduction, and oxidation stability of the lubricant containing microcapsules. The results show that after 60 minutes exposed to the ring-on-liner test, only 30% of microcapsules remained intact in the oil lubricant, indicating the significant rupture of the microcapsules under shearing conditions. Meanwhile, the wear test of microcapsules containing anti-wear agents dispersed in oil was evaluated by a four-ball wear tester. It was found that both the samples show a significant reduction in wear scar comparing to pure oil. The wear test conducted by four-ball exhibits the lower wear scar of pure oil-containing microcapsules than with a dispersed anti-wear agent. However, in the ball-three-flats wear testing module, the results are contradicted in which oil-containing microcapsules with different amounts show higher wear scar than oil containing dispersed anti-wear agents. The latest study of Xu¹⁹⁰ has also found negligible improvements in friction and wear of the PAO4 containing PMMA microcapsules encapsulating friction modifier compared to the oil with friction modifiers. In this study, the author only discussed the benefit of using microcapsules with the perspective of the controlled release concept and the protection of core materials by the shell rather than any significant improvement in friction and wear of the counterparts.

2.6.3. Summary of potential core and shell materials for high-temperature lubricant formulation

The microencapsulation technique seems to be a promising method for preparing the next generation of high-temperature lubricant additives although an original concept of microencapsulation should be modified to be applicable under hot metal forming lubrications. Accordingly, a major roadblock to this new application in lubricant formulation is the majority breakage of the microcapsules (~70%) under the boundary/mixed lubrication regimes where friction and wear are the most severe. While the shell fragments/debris often deteriorate the function of the encapsulated additives and, in some cases, increase wear of the moving counterpart, the crumbling of the microcapsules challenges the achievement of the control-release objective. Since the crumbling of the microcapsules is inevitable under the boundary/mixed lubrication regime, the control-release concept shows a limitation in ongoing research of microencapsulation in lubricant science. Thus, an alternative, yet effective strategy for the utilization of microencapsulation in high-temperature lubrication is required.

A new design strategy for the microencapsulation technique is, thus, required in this thesis focusing on the synergistic interactions between the shell materials, the functional core, and the base lubricant. It breaks away from the traditional utilization of microencapsulation. In this strategy, the shell of the colloidal capsule should either contribute to the lubricating function or react synergistically with the high-temperature- lubricants. The core additives will be released when the shell is crumbled, thermally triggered, or mechanically triggered under severe conditions during a frictional event that in turn additionally delivers a lubrication improvement to the based fluid. In this aspect, all materials in the designed microcapsules work synergistically along with the base lubricants to reduce friction, wear, and oxidation. From this perspective of synergy under friction conditions, the hybrid colloidal capsule is considered to be “smart responsive”. Since all materials are incorporated in one formula, an important aspect to note on the novelty of this strategy is that both the shell and the core materials can be fully utilized under severe tribological operations with much reduced material losses and wastes as they are applied where needed.

To achieve the goals of the proposed strategy, the selection of both shell and core materials plays an important role. At elevated temperatures, such as hot metal forming (can be up to 800-1000°C), the traditional polymeric shell will be quickly burned off. If the core is not thermally stable, both shell and core will be decomposed and their functions lost. The decomposition of polymer shells can also produce some harmful volatile compounds and unexpected components, which can affect both environment and final products. Among all materials, inorganic materials should be the potential candidates for structuring the shell and core materials. Currently, there are several studies reported about the inorganic shell materials for encapsulating phase-change materials to be used for energy storage in building materials and civil engineering applications. Several promising studies with materials are summarized in **Table 2-2**.

Table 2-2. Promising core-shell microcapsules with thermally stable materials for high-temperature lubricants.

References	Core	Shell	Temperature (°C)	Note
191, 192	n-octadecane, paraffin	CaCO ₃	The shell structure can be stable over 650°C.	Synthesis by emulsion technique. The average size of particles is 5 µm. Tween 80 and Span 80 were used as the surfactants.
193	Polystyrene (PS)	PEOS (a precursor of silica).	The decomposition temperature of PS increases up to 400°C	Synthesis by emulsification method. The average size of particles is 150 nm. No surfactant, dispersed by ultrasonication.
194, 195	n-Eicosane, paraffin	Silica derives (from TEOS or sodium silicate)	Thermal stability increase from 60°C (pure n-Eicosane) to 270°C (50 wt/wt SiO ₂ /n-Eicosane).	Synthesis by sol-gel method. The average size of particles is ranging from 250 nm to 550 nm. The emulsifier used here is triblock copolymer PEO-PPO-PEO (P123).
196	Silica (SiO ₂)	Zinc Borate (Zn ₅ B ₄ O ₁₁)	---	Self-assembly technique. The average size of particles is 40 nm diameters with the thickness of the shell of 5 nm.
197	MoS ₂ , graphite, and a graphite fluoride	Alkali metal silicate (preferably sodium or potassium silicate)	1000°C.	Spray drying technique. 92.2%, 58%, and 68% residual weight in case of MoS ₂ , graphite, and graphite fluoride encapsulated respectively.

198	Copper	Chromium-Nickel	The core-shell structure can be stable from 1050°C to 1150°C.	Synthesis by electroplating. The average size of particles is more than 2 μm. Suitable for high-temperature thermal energy storage such as solar thermal power generation and industrial waste heat recovery.
199	Sodium nitrate	Silica	This core-shell material can be stable from 300-500°C (testing temperature)	The encapsulation techniques such as electroless and electrochemical coatings, and coating using silicates were used to produce the core-shell materials in thermal energy storage systems.
200	The molten salt from the group of sodium nitrate, potassium nitrate, inorganic salt, and combination thereof.	The materials from the group of sodium chloride, bonded metal particles, sintered metal particles, clay, and a mixture of clay and metal.	Thermal stability can go up to 300-800°C	Core-shell phase change material was produced by suspending phase change material in an air stream and exposed to a solution of a mixture comprising a binder and metal particles. Upon drying, a coating of one or more layers, of the mixture is formed around the particle of the phase change material. Applied in the thermal energy storage system.
201	Copper balls	Nickel film with/without insertion of carbon or ruthenium as an inhibition layer	Thermal stability can reach over 927°C	Capsule material is synthesized by electro-plating method with the thickness controlled by operating time. Used for recovering high-temperature waste heat in hydrogen production by reforming reaction.

2.6.4. Research questions for microencapsulation in tribology

As highlighted above, microencapsulation is the traditional approach in creating the core-shell structure materials. The core-shell materials, which are thermally stable and can be applied in high temperatures, should come from the inorganic compounds. Such materials have recently been utilized and investigated in the thermal energy storage industry to preserve and use the heat waste in many industrial fields such as chemical engineering, civil engineering, and solar power plant... Although the encapsulation is an old idea from the previous century, it can still be an innovative method that has currently been extended and applied in many areas. The most recent encapsulation materials in tribology come from the micro-encapsulated chemical and lubricant additives used in improving the lubricating performance of engine oil²⁰². However, the literature only shows the benefit of microencapsulation in the long-term storage and effective controlled dosage of the lubricant additives by the controlled release strategy. In addition, there is no publication or investigation of micro-encapsulation materials used in high-temperature lubricants which can be employed in the metal forming industry including hot-rolling, hot-forging, etc where the controlled release cannot be utilized. Furthermore, it is essential to explore and examine the new environmentally friendly lubricants to implement and replace the traditional lubricant in the metal manufacturing industry. Therefore, microencapsulation by an inorganic shell with thermally lubricious compounds and easily dispersed in water can potentially offer a promising new generation of eco-friendly lubricant for harsh operation conditions at elevated temperatures.

2.7. Designing a strategy for novel high-temperature lubricant additives based on microencapsulation

As mentioned above, several lubricant additives can functionalize at high temperatures including solid nanoparticles and inorganic polymeric materials. Apart from the utilization of inorganic polymeric solid lubricants (borates, silicates, and phosphates) as the base lubricant for high-temperature lubrication, an application of solid nanoparticles such as 2D materials and ceramic/ceramic oxides is another feasible choice for further friction and wear reduction while inhibiting the oxidation and heat transfer from the hot strip to the work rolls. Therefore, solid nanoparticles from the 2D and ceramic/ceramic oxide materials are selected for the fabrication of the novel microcapsule. To combine these materials effectively with the possibility of more than three materials in the microcapsule, there are several strategies²⁰³, including: Pickering emulsion templated assembly, layer-by-layer self-assembly, and the amphiphilicity-driven self-assembly of polymer-brush grafted nanoparticles. Among them, the Pickering emulsion templated assembly is considered the most facile and efficient approach²⁰³⁻²⁰⁵.

Pickering emulsion was first proposed by Ramsden and Pickering but it was not considered for a long period of time until further advanced development of material science. It possesses many unique features that classical emulsions stabilized by surfactants cannot function, such as superior stability and low toxicity due to its free surfactant. In general, Pickering emulsion focuses on the nano- or micro-particles with a suitable three-phase contact angle (oil-water-solid). The three-

phase contact angle (θ) measured into the water phase of the stabilizing particles at the water-oil interface is described mathematically by Young's equation²⁰⁶ and it represents the wettability of the stabilizing particles:

$$\cos \theta = \frac{\gamma_{po} - \gamma_{pw}}{\gamma_{ow}} \quad (2-2)$$

where γ represents the interfacial tension between oil (o), water (w), and particle (p). This equation (2-2) has been well established for particles with different morphologies such as cube, sphere, and peanut^{207, 208}.

These micro-/nanoparticles are favorable to anchor at the water-oil interface and reduce surface tension. Recently, several publications relating to the use of Pickering emulsions and their fundamentals are well established and explained²⁰⁹. The natural stability of Pickering emulsion derives from the wettability of nano- or micro-particles subjected to use. As mentioned by Chevalier et al.²⁰⁹, the three phases contact angle between particles, oil, and water should be lower or higher than 90° to form the oil-in-water (o/w) or water-in-oil (w/o) emulsion respectively. In particular, studies by Kaptay²¹⁰ suggested that the optimum θ for stabilizing o/w emulsions is 70-86° and 94-110° for stabilizing w/o emulsions. At appropriate concentration and three-phase contact angle, the micro-/nanoparticles can lower the surface tension of water-oil interfaces and prevent the emulsion from coalescence. The following equation (2-3) from Binks²¹¹ shows the dependence of the energy (ΔE) required to remove a solid spherical particle of radius r from the oil/water interface which is applicable to the small particles (less than 2 μm) at which the gravitational effects may be neglected:

$$\Delta E = \pi r^2 \gamma_{ow} (1 \pm \cos \theta)^2 \quad (2-3)$$

It has been demonstrated from this equation that the energy of adsorption of a particle at an interface is always greater than the particle's thermal energy, even in the case of very small solid particles²¹². Thus, the adsorption of the solid particles attached to the oil/water interface is irreversible which requires a large amount of energy to destabilize the emulsion systems. For this reason, amphiphilic substances can also be used together with particles to improve the wettability of desired particles^{209, 213}. Because of the small number of amphiphilic substances used, which is commonly lower than critical micelle concentration (CMC), the Pickering emulsion approach is accepted and used widely to construct new shells.

Pickering emulsion can be utilized to form the new type of capsules which is always named colloidosomes or colloidal capsules (**Figure 2-32**)²¹⁴. Colloidosomes are the capsule formed by the accumulation of particles at the water-oil interfaces. As this aggregation can create a shell with a porous structure, it is used in targeted delivery and control the release of a drug. Due to the high energy of desorption of these particles from soft interfaces, colloidosomes are remarkably stable. The combination of the sol-gel microencapsulation route with colloidosomes to form the silica shell with anchored particles has been introduced in several studies²¹⁵⁻²¹⁷. In these articles, the

authors used the combination of micro- or nano-particles and amphiphilic components to improve the wettability of particles applied. Especially, in the case of the patent US9017706B2²¹⁷, the use of crystallizable oil or water as core material can be an approach to entrap some chemical additives inside during the microencapsulation process. Thus, the crystallizable oil core from liquid paraffin may be chosen as a carrier to localize other additives. Besides, water is also good as a carrier that can maintain the dispersion of covalently functionalized 2D materials or nanoparticles uniformly.

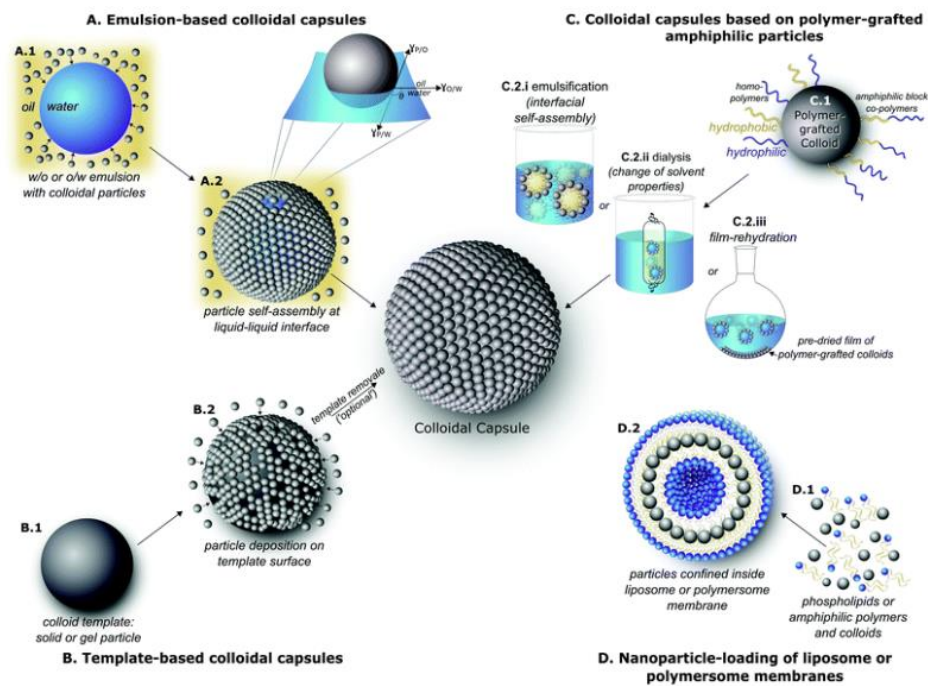


Figure 2-32. Overview of the colloidal capsules and the approaches to fabricate them.²⁰³

2.8. Summary and proposed research scopes

The current work sets to provide a new strategy for the application of microencapsulation in customizing the novel high-temperature lubricant additives. In addition, a fundamental understanding of the tribological behavior of the novel microcapsule under lubrication with sodium borate melts in the hot metal forming conditions is explored in this thesis for the first time. Sodium borate melt has been chosen as the base lubricant in this study due to its popularity in the hot metal forming industry with excellent performance in anti-oxidation, friction reduction, and wear resistance under high-temperature conditions, however, the boriding effect of the oxide scale is commonly occurred at above 850°C which negatively impacts the lubricity of this melt as demonstrated previously in section 2.5.2. Improving the lubricity, minimizing the boriding effect of sodium borate, and corrosion attack of sodium toward the oxide scale by the novel microcapsules would also be a worthwhile consideration in this study.

It should be noted that the requirement of most metal forming processes is to optimize the friction not to minimize the friction. The use of a proper friction coefficient is essential in the hot metal forming industry, especially in hot rolling of steel, to ensure the operating components work efficiently and economically to produce high product dimensional accuracy and surface functional

quality. Since there are many different forms of metalworking in the hot metal forming industry, the optimal friction coefficient in hot metal forming largely depends on the characteristics of the individual process²¹⁸. A friction coefficient of 0.1 is often considered as a reasonable value in a dome stretch-formed from a piece of flat steel sheet²¹⁹, however, the friction coefficient of 0.07 is considered as the minimum value required for a stable hot aluminum-alloy strip rolling process²²⁰. Due to different requirements in friction for different hot metalworking processes, the candidate attempts to propose a new strategy to design the new solid lubricant additives for hot metalworking with the main focus on a tunable capability and wide selection of components to freely control the friction and wear for hot metal forming lubrication. Not only friction reduction, but the new additives are also aimed for a significant decrease in the wear losses and the oxidation degree of the steel which are the pivotal requirements for the most high-temperature manufacturing processes. The candidate believes that the proposed strategy is practically effective in controlling the friction and wear to adapt to the specific requirements of different metalworking processes.

In this dissertation, the combination of the sol-gel process and Pickering emulsion to make the novel inorganic-based microcapsule for high-temperature lubrication is proposed. Generally speaking, this capsule comprises a shell of silica decorated with ceramic/ceramic oxide nanoparticles (e.g. CaCO_3 , ZrO_2 , TiO_2 ,...) and the core of 2D nanosheets (e.g. h-BN, graphene oxide,...) entrapped within the water core (**Figure 2-33**). In this formula, the hybrid shell of silica and nanoparticles is expected to melt or break at elevated temperatures under the presence of sodium borate melt and in turn releases other 2D additives during sliding to assemble the novel tribofilm structure. It is expected that the formation of the sodium borosilicate will occur at the sliding interfaces. The combination of boron oxide network and silicon dioxide network in the borosilicate melt can render the weakness in the lubrication of sodium borate and sodium silicate alone according to section 2.5.2. Wan et al.⁴ also confirm that a combination of borate and silicate networks can eliminate the drawbacks of poor adhesion and toxicity at high temperatures from each compound separately.



Figure 2-33. The schematic presenting the structure of the proposed colloidal capsule for this research.

To achieve a complete fundamental understanding of tribofilm structure, tribochemical reaction as well as friction reduction, wear-resistant and oxidation inhibition under extreme pressure and elevated temperatures in hot rolling, the following tasks listed in **Figure 2-34** need to be carried out. Each of these tasks combined with the updated fundamental understanding about the lubrication of the melt lubricants in sections 2.5.1 and 2.5.2 is necessary not only to find an appropriate route for microencapsulation synthesis but also to evaluate the tribofilm formation and to perform advanced characterization to clarify tribological behavior.

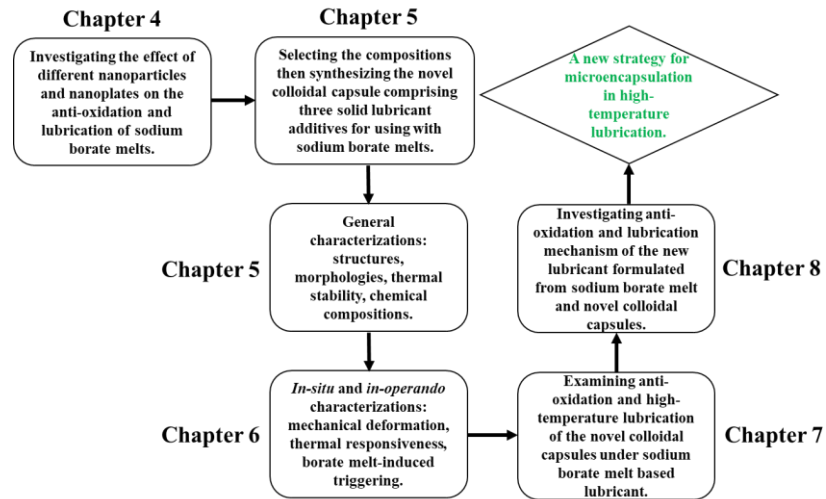


Figure 2-34. Schematic presenting the flowchart of the intended works for the proposed study.

Chapter 3

Experimental methodology and characterization techniques

This chapter describes the experimental apparatus and analytical instruments which **are** used throughout the study. In this chapter, a brief overview of working principles and technical specifications are presented.

3.1. High-temperature friction and wear experiments

High-temperature friction tests are extensively conducted on a Bruker UMT3 tribometer (**Figure 3-1**) which is capable of operating up to the maximum temperature of 1000°C. The tribometer has two set-up configurations including ball-on-disc rotation and ball-on-plate reciprocation which can both be operated at elevated temperatures. In this study, the ball-on-disc rotation is mainly used to simulate the hot rolling working conditions²²¹ while the ball-on-plate reciprocation is partly used to evaluate the high-temperature lubrication of the formulated lubricants.²⁸ A two-dimensional DFH load cell is installed in the carriage which has a minimum force resolution of 10 mN and the maximum normal load of 200 N. The upper linear stage can provide the accurate positioning of the pin up to 1 μm while the lower rotary spindle/reciprocating motor can operate in the range of 0.1 to 5000 rpm and 0.1 to 60 Hz respectively. In the case of the reciprocating motion, the stroke length can be modified in the range of 0.1 to 25 mm. During hot friction tests, both normal and lateral forces are simultaneously recorded by an integrated program (UMT) which can be used later to obtain the friction coefficient. The hot friction tests are performed according to the designed scripts which allow a highly precise acquisition of friction force with good repeatability. For the high-temperature lubrication testing, the lubricant is drop-coated on the disc yielding a lubricant concentration of 0.83 ml/cm² before the pin and the disc are engaged.

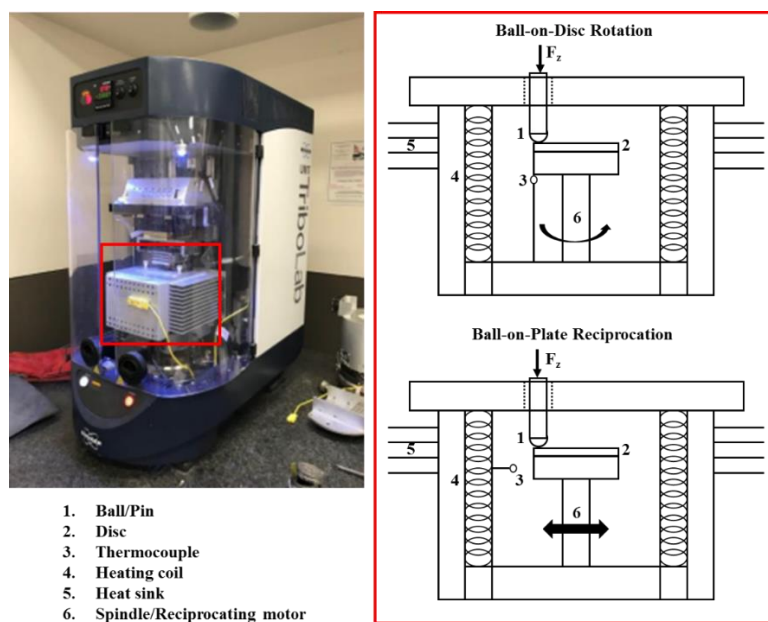


Figure 3-1. Digital image and simplified schematic of the high-temperature tribometer UMT3.

The maximum contact pressure is calculated according to the reduced young modulus of the oxide scales at testing temperature (equation 3-1)²²². The maximum contact pressure is calculated by the Hertzian stress theory (equations 3-2 to 3-4)²²³:

$$E^T = E_{ox}^0 (1 + n(T-25)) \quad (3-1)$$

$$a = \sqrt[3]{\frac{3RF}{4E^*}} \quad (3-2)$$

$$\frac{1}{E^*} = \frac{1-\nu_1^2}{E_1} + \frac{1-\nu_2^2}{E_2} \quad (3-3)$$

$$P_{max} = \frac{3}{2} \frac{F}{\pi a^2} \quad (3-4)$$

where a is the radius of contact area; R is ball radius (mm); F is applied force (N); E_1 and E_2 are Young's modulus of contact bodies (GPa); ν_1 and ν_2 are Poisson's ratio of contact bodies (chosen as 0.3); E^T is Young's modulus of oxide scale at temperature T (°C); $n = -4.7 \cdot 10^{-4}$; and $E_{ox}^0 = 240$ GPa. These calculations are conducted based on the mentioned equations throughout this study to calculate maximum contact pressure unless stated otherwise.

High-temperature testing is carried out in ambient air with 20% relative humidity (recorded at room temperature) for 10 minutes. Such enough time exposure is applied to ensure the full development of the tribofilm and to investigate the adherence capability of the melt lubricant in hot rolling simulation. At the end of a test, both steel counterparts are brought out of the furnace immediately to minimize further oxidation. The friction tests are conducted in triplicate to ensure the repeatability of the results.

Ball wear loss volumes are derived from the measurement of the wear scar diameter while the corresponding groove volume on the wear track of the plate is measured using a ContourGT-K 3D Optical Microscope. In the disc wear track, the wear profiles at four different positions along the wear tracks are recorded, and then the data is exported for wear area calculation. The cross-sectional wear area is calculated by using an integrated function in the Vision64 software to obtain a mean wear area. The value is then multiplied by the circumference of the wear track to determine the wear volume. In the case of the ball, the diameter of the wear scar following testing is recorded and used for calculating the wear loss volume based on equations 3-5 and 3-6 according to ASME standard for ball-on-disc wear testing²²⁴, where d is the wear scar diameter and r is the ball radius:

$$\text{Ball volume loss} = \left(\frac{\pi h}{6}\right) * \left[\frac{3d^2}{4} + h^2\right] \quad (3-5)$$

$$h = r - \left(r^2 - \frac{d^2}{4}\right)^{\frac{1}{2}} \quad (3-6)$$

3.2. Analytical methodology

This section describes the application of the main advanced characterizing and analytical methods which have been used throughout this study. Other details about the working parameters and the specific testing methodologies, procedures, or techniques that are used for a particular purpose will be mentioned when needed in each following chapter.

3.2.1. Thermal analysis

In this study, a NETZSCH STA 449F5 unit operating under the nitrogen atmosphere with a flow rate of 10 ml/min has been used to study the melting, oxidation, and recrystallization due to the mass change and heat flow that is associated with the chemical processes.²²⁵ One standard platinum crucible is used for the TGA measurement whereas another empty platinum crucible was used as a reference for the DSC measurement. The temperature range is set from 30 to 1000°C at a heating rate of 10°C/min.

3.2.2. X-ray diffraction analysis

X-ray diffraction analysis has been performed in this study by using a GBC MMA Diffractometer with a Cu K α source and a step size of 0.05°. The operating voltage and current of X-ray are constantly set at 35 kV and 28.6 mA, respectively. The XRD pattern is analyzed by HighScore Plus and Match! with a database of Powder Diffraction Files (PDF) 4+ 2020.

3.2.3. X-ray photoelectron spectroscopy (XPS)

XPS is well-recognized as one of the surface-sensitive quantitative spectroscopic techniques which can provide a wealth of information about the surface chemistry of the material. In this study, XPS has been conducted by Nexsa Surface Analysis System of ThermoFisher Scientific. The spot size of 400 μm diameter is used for the tested area and the power of the X-ray gun is about 70W by using Al K α ($h\nu = 1486.6\text{eV}$) radiation. A flood gun is used on the samples for charge compensation during the analysis. For survey spectra, pass energy of 200 eV and step size of 1 eV are used. For higher energy resolution, narrow scan spectra pass energy of 50 eV with a step size of 0.1 eV is used. Scan times for each spectrum are about 20-30 times. Prior to XPS scanning, the surface samples are subjected to ion-gun etching at low voltage to remove the probably adsorbed air on the surface. All procedures are conducted in analysis ultra-high vacuum chamber which has the pressure of 2.8×10^{-10} mbar.

3.2.4. Fourier-transform infrared spectroscopy (FTIR)

Prior to the measurement, the powders are dried at 70°C overnight to remove the moisture. FT-IR spectra were then recorded on a Perkin-Elmer Spectrum 100 apparatus in ATR mode from 4000 to 650 cm^{-1} , with a resolution of 0.5 cm^{-1} , using the KBr pellet technique.

3.2.5. Raman spectroscopy

Raman spectroscopy is the common non-destructive spectroscopic technique that is often used to

determine the structural fingerprint by which molecules can be identified. In this study, inVia Renishaw Raman microscope operated at a wavelength of 539 nm with a spot size of 3 μm is used to analyze the powder and bulk samples. Prior to the characterization, the spectrometer calibration protocol is conducted based on the calibration routine proposed by Bocklitz et al.²²⁶ This method ensures only Raman information of the sample is utilized by a chemometric model and excludes a contribution from artifacts from small shifts in the excitation wavelength.

3.2.6. 3D interferometer

Non-contact surface topography analysis has been performed by 3D Interferometer Optical Microscope (ContourGT-K 3D Optical Profiler from Bruker). In this study, the system has been used to quantitatively measure the volume wear losses of the counterparts after the hot friction test. Moreover, wear surface characteristics including surface roughness parameters are recorded and analyzed to understand the tribological behavior of the designed lubricant.

3.2.7. Scanning electron microscopy (SEM)

SEM is a type of electron microscope that provides a detailed image of the sample by scanning the sample surface with the focused electron beam which is scanned in a raster scan pattern. In this study, SEM has been performed by using high-performance JEOL JSM-6490LA which is equipped with a 30 keV conventional tungsten filament and adjustable operating pressure. The instrument has a maximum resolution of 3.5 nm at 30 keV which can be switched between the secondary electron (SE) and backscattered secondary electron (BSE) detectors to suit specific imaging purposes. Moreover, the 80x80 mm² SSD energy dispersive X-ray detector has been installed in the instrument which allows a rapid quantitative chemical analysis with high accuracy of the imaged samples by an integrated Aztec Oxford software suit. Field-emission SEM has also been performed in this study by the use of FEI Helios Nanolab G3 CX to image the sample down to nanoscale thanks to the field emission gun which produces a smaller diameter, more coherent, and greater current density and brightness compared to the traditional filaments.

3.2.8. Focus ion beam microscopy (FIB)

In this study, FIB is mainly used to prepare high-quality electron-transparent specimens by cross-sectioning the bulk materials or deposition of the micro-/nano-particles for further analysis with Transmission Electron Microscope (TEM) or *in-situ* TEM experiments. The FIB microscope works on the SEM principle by using an ion beam (commonly Gallium ion) instead of an electron beam. Since the ions have a much larger mass than electrons, they can sputter away atoms interacting with the beam which allows the milling of the specimen when high currents are employed. FEI Helios Nanolab G3 CX, a dual-beam FIB-SEM, has been extensively used to conduct the FIB routine for both TEM/STEM specimen preparation and *in-situ* sample preparations (**Figure 3-2**).

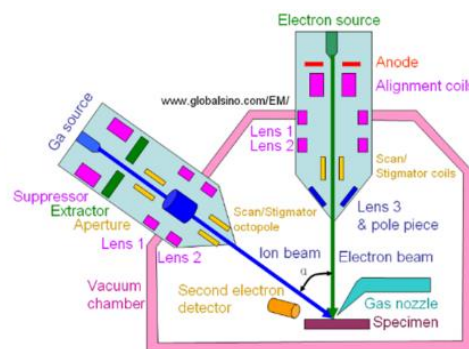


Figure 3-2. Digital image and simplified schematic of dual-beam FIB-SEM instrument^{227, 228}.

3.2.9. Time-of-flight secondary ion mass spectrometry (TOF-SIMS)

High-resolution TOF-SIMS emerges as a powerful analytical methodology for imaging and recording elements and compounds in the near-surface region of solid materials. In principle, the surface of the sample is bombarded by a primary ion beam which sputters off material and produces mostly neutrals species but also positive or negative charged ions (i.e. secondary ions). These secondary ions are detected and separated by their time-of-flight in the SIMS detector, which is linearly linked to the square root of the m/z ratio. The current recent development of TOF detectors which can be coupled to a high-resolution Ga-FIB has shown that it is possible to capture images and extract chemical data at 10's of nm spatial resolution in a minimally invasive manner. In this study, Ga-TOF-SIMS has been used not only to study the surface chemistry of the material but also to conduct the new *in-situ* heating experiment.

3.2.10. (Scanning) Transmission Electron Microscope (STEM)

Transmission Electron Microscope has been a paramount technique in material research that enables material characterization at the nanometer length scale. In this study, extensive works have been done with the TEM analysis regarding the characterization of the structured micro-/nano-particles and the thin tribofilm on surfaces. JEOL JEM-2011 and JEOL JEM-ARM200F have been extensively utilized to study the varied ranges of material. While the JEOL JEM-2011 provides routine TEM characterization of simple materials such as nano-/micro-particles with a capability to obtain the high-resolution TEM images and selected area diffraction pattern (SADP), JEOL JEM-ARM200F has been usually used to acquire the information at the atomic resolution with the ability to generate simultaneously High Angle Annular Dark Field (HAADF) and Bright Field (BF) images. Moreover, JEOL JEM-ARM200F is capable to conduct electron energy loss spectroscopy (EELS) analysis which is a powerful technique to study bonding, electronic states, surface plasmons, etc. down to atomic scale by measuring the energy transferred from the main electron beam to the specimen when the beam passes through the analyzed sample²²⁹. In JEOL JEM-ARM200F, where the cold field emission gun is installed, the resolution of EELS can range from 0.7 eV down to 9 meV with an aid of the monochromators²³⁰. The superior performance of JEOL JEM-ARM200F compared to JEOL JEM-2011 comes from the aberration corrector which can correct either the probe-forming lens for STEM or the imaging-forming lens for the TEM

mode. In conventional TEM, the resolution of the image is limited by the positive spherical aberration introduced by round lenses, but, the aberration correctors can negate the spherical aberration coefficient²³¹. Due to such advantages, aberration-corrected STEM (AC-STEM) has been commonly applied to study the thin tribofilm formation generated on the surfaces after hot friction test or the interfacial bonding configuration at the nanoscale in this study.

An *in-situ* TEM compression experiment is conducted on a JEOL JEM-2010 TEM at 200 kV using a PI 95 TEM PicoIndenter holder. The diamond tip is modified by FIB to produce a circular flat-punch surface of around 3 μm diameter. The load function is set as displacement control with Q-control mode. The compression tests are performed at a constant displacement rate of 16.67 $\text{nm}\cdot\text{s}^{-1}$, and the entire process is recorded by using a digital video recorder built in the microscope. The applied force and displacement of the punch are recorded simultaneously during the deformation process. The rupture strength and compressive strain of the microcapsules are obtained from the Force–Displacement curve.

For the *in-situ* TEM heating observation, Gatan 652 *In-situ* Heating Holder in JEOL JEM-ARM200F) is capable to study the structural changes at the submicron-/nano-scale from the prepared specimens ranging from the nanoparticles to the bulk foils. However, EDS analysis/mapping cannot be done during heating by this holder due to infrared radiation blinding the detector. It can only be done after cooling the specimen to room temperature. Due to thermal drift, high-resolution studies are not also practical with this type of holder. Prior to the experiment, two microcapsules, which were inter-connected by a weak van der Waals force, were manipulated and mounted on the molybdenum M-grid. The prepared specimen is placed on the MEMS chip that was installed in the *in-situ* heating holder. A heating rate is commonly set at 1°C/s and each temperature is held for 30 s to record the picture of microstructural transformation.

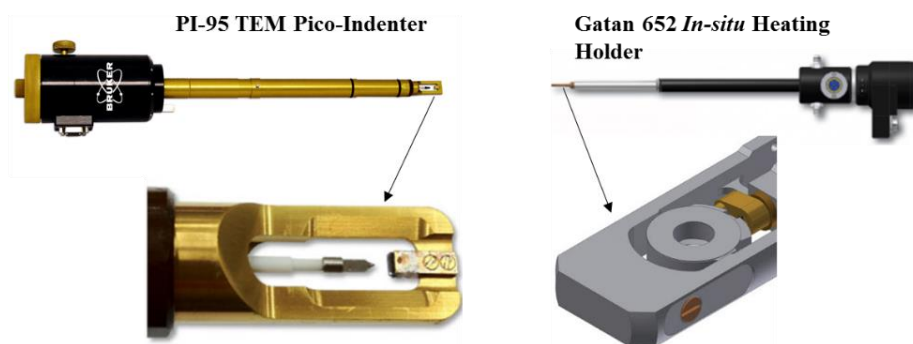


Figure 3-3. Digital images of the *in-situ* facilities used in this study.

Chapter 4

A study on the tribological performances of nanoparticles under sodium borate melt lubrication

*This chapter content belongs to a manuscript currently under review by the journal Tribology International.

Recent work suggests that glass melt lubricants can significantly improve the friction reduction and wear alleviation as well as oxidation inhibition between the sliding counterparts at elevated temperatures, however, they have by now reached their performance limits. From the previous studies, it has been demonstrated that sodium borate delivers desirable lubrication up to 800°C while sodium silicate starts to perform at 920°C. Considering the potential application for high-temperature rolling processes which are commonly operated at 900-1000°C,³⁴ sodium silicate comes as a promising base lubricant. However, the lubrication efficiency of sodium silicate depends strongly on the high concentration of sodium in the melt network which can cause significant corrosion of the protective oxide scale, thus, leading to an increase in oxidation level. To further reduce friction and wear while maintaining desirable anti-oxidation performance, it is necessary to formulate the melt lubricants with several solid lubricant additives that are thermally stable and can function at elevated temperatures.

Recently, several attempts have been made to incorporate solid nanoparticles into the glass melts when formulating high-temperature lubricants.^{4, 15} In this chapter, different solid nanoparticles, including SiO₂, TiO₂, Al₂O₃, ZrO₂, CaCO₃, h-BN nanosheets, and graphite nanoplates (GrNPs), have been studied as lubricant additives for high-temperature rolling processes at 930°C. Sodium borate melt has been applied as the melt lubricant due to its outstanding lubrication and anti-oxidation performances although its performance has been only reported up to 800°C from the previous studies of Tran et al.²³² Since sodium borate has lesser corrosion attack and is more environmentally friendly than sodium silicate and sodium phosphate,⁴ the aim of this chapter is to investigate the lubricity and further improve the lubrication performance and anti-oxidation of sodium borate at higher temperatures (900-1000°C).

As suggested by previous studies of Tran et al.²³³, oxide growth from stainless steel provides a better foundation for lubricant adsorption than mild-carbon steel, thus, the sodium borate melt shows superior lubrication performance on stainless steel than mild steel. Moreover, it is believed that the high-oxidation degree of mild-carbon steel compared to stainless steel can interfere significantly with the lubricant performance of the melt lubricants, thus, leading to difficulty in interpreting and investigating the true performance and lubricity of the melt lubricants.^{149, 233} For instance, a high-oxidation degree of the mild-carbon steel causes the rapid growth of oxide during sliding which can not only result in higher surface roughness but also large-grained single-crystalline oxides on the surfaces.^{37, 234} These processes disturb the formation of the boundary

tribofilm and destroy the melt network that deteriorates the performances, especially at significantly high temperatures (900-1000°C). In addition, oxide scale grew on the mild-carbon steel often shows weak adhesion to the steel substrate compared to the Cr-containing steel (e.g. stainless steel), thus, delivering poor support to the melt lubricant and the resulted tribofilm.^{139, 235} When formulating the melt lubricant with nanoparticles, these occurrences can result in more complex phenomena which make it difficult to understand the true behavior of the lubricant. Therefore, the lubrication and anti-oxidation performance of sodium borate formulated with solid lubricant additives will be performed on stainless steel in this chapter and other following chapters unless otherwise noticed.

4.1. Experimental details

4.1.1. Materials

Sodium tetraborate ($\text{Na}_2\text{B}_4\text{O}_7 \cdot 10\text{H}_2\text{O}$) (Borax) is chosen as the base lubricant which was purchased from Sigma-Aldrich. SiO_2 , TiO_2 , Al_2O_3 , and ZrO_2 nanoparticles were provided by Shanghai Xinglu Chemical Technology for this study. Precipitated CaCO_3 nanoparticles were purchased from US Research Nanomaterials. h-BN nanosheets were provided by HWNANO (Hongwu International Group Ltd). Graphite nanoplates were purchased from Sixth Element Materials Technology Co. Ltd (Changzhou, China). All materials are used without further purification unless otherwise noted.

XRD analysis of the given chemicals and nanoparticles is indicated in **Figure 4-1** which shows the representative crystallite diffraction peaks. Accordingly, **Figure 4-1a** shows the crystalline diffraction peaks of sodium tetraborate decahydrate with the strong diffraction peaks at 15.55° and 31.58° which correspond to (200) and (132) planes according to the referenced XRD analysis of JCPDS No. 75-1078. Meanwhile, the crystalline systems of ceramic oxide nanoparticles are presented in **Figure 4-1b-Figure 4-1d**. In particular, Al_2O_3 nanoparticles display the significant presence of $\alpha\text{-Al}_2\text{O}_3$ crystallinity with the typical reflection peaks of (012), (104), (116) at 25.5° , 35.1° , and 57.5° respectively (**Figure 4-1b**) according to the JCPDS No. 46-1212. Meanwhile, TiO_2 nanoparticles are composed dominantly by the anatase phase which can be identified by the distinct emergence of the reflection planes of (101) and (200) at 25.0° and 48.0° according to JCPDS No. 21-1272. ZrO_2 nanoparticles comprise the phases of t- ZrO_2 (JCPDS No. 70-1769) as identified by the peaks at 30.5° , 34.5° , 50.3° and 60.1° corresponding to the (101), (110), (200) and (211). In addition, m- ZrO_2 is detected within the ZrO_2 nanoparticles according to the representative peaks at 28.4° and 31.6° for (111) reflection (JCPDS No. 37-1484). CaCO_3 nanoparticles show a significant presence of the calcite phases with a strong crystallinity at 29.5° which corresponds to a reflection plane of (211) according to JCPDS No. 05-586. Different from other ceramic oxide nanoparticles, SiO_2 nanoparticles are characterized by the broad hump with an equivalent Bragg angle at 21.8° which is typical for an amorphous structure (**Figure 4-1c**). On the other hand, two-dimensional (2D) nanoplates of h-BN and graphite reveal the most intense and sharp peak at 26.8° (**Figure 4-1d**) which corresponds to the (002) diffraction plane of the layered

structure according to JCPDS No. 75-2078 and JCPDS No. 85-1068.

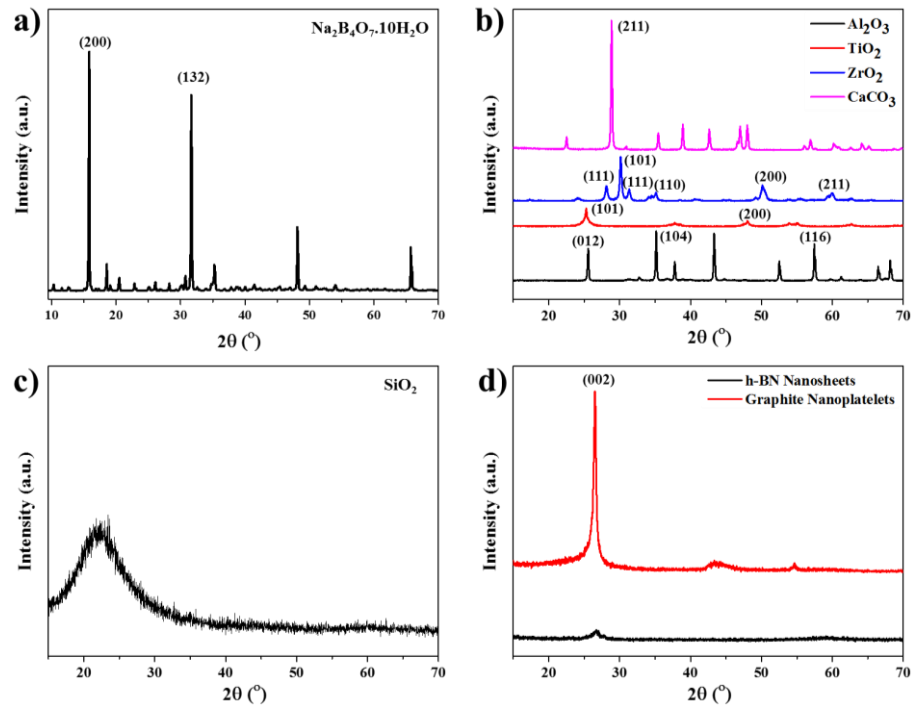


Figure 4-1. X-ray diffraction (XRD) analysis of the lubricant and as-received nanoparticles: (a) sodium tetraborate; (b) ceramic crystallite oxide nanoparticles; (c) ceramic amorphous oxide nanoparticles; and (d) layered nanoparticles.

To examine the morphology and size distribution of the as-received nanoparticles, a transmission electron microscope (TEM) is applied to image the nanoparticles as indicated in **Figure 4-2**. It can be seen that Al_2O_3 , TiO_2 , and SiO_2 nanoparticles show the nearly spheroid morphology which ranges between the spherical and elliptical shapes (**Figure 4-2a**, **Figure 4-2c**, and **Figure 4-2d**). The size distribution of these nanoparticles is calculated by counting at least three hundred particles for each material from the TEM images which shows the range of 20-40 nm for Al_2O_3 , 50-100 nm for SiO_2 , and 15-20 nm for TiO_2 . Meanwhile, CaCO_3 and ZrO_2 nanoparticles reveal the cuboidal shape (**Figure 4-2b** and **Figure 4-2e**) with the size distribution ranging from 50 to 100 nm. Shown in **Figure 4-2f** and **Figure 4-2g** are the TEM images of the layered nanoparticles (h-BN nanoflakes and graphite nanoplates) which exhibit clear lattice fringes from a wrinkled sheet with crumpling and scrolling presence. **Table 4-1** summarizes the physical characteristics of different nanoparticles in terms of size, crystal systems, and hardness.

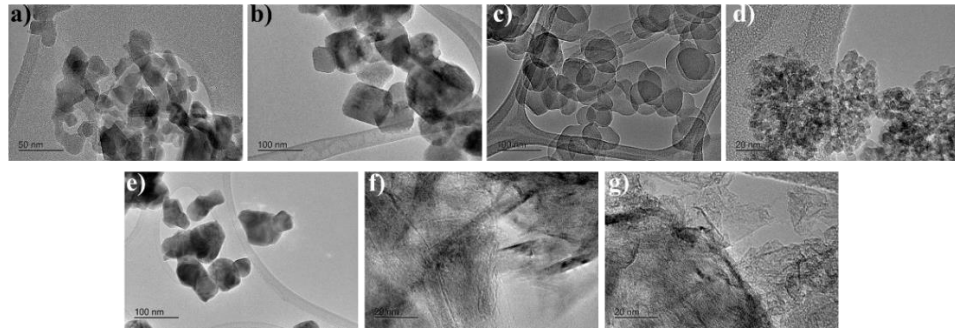


Figure 4-2. TEM images of different nanoparticles used in this study: (a) Al₂O₃; (b) CaCO₃; (c) SiO₂; (d) TiO₂; (e) ZrO₂; (f) h-BN nanosheets; (g) graphite nanoplates.

Table 4-1. Physical characteristics of nanoparticles.

Materials	Size (nm)	Morphology	Crystal systems	Hardness (GPa)
SiO ₂	100-150	Spherical	Amorphous	10.00 ²³⁶
TiO ₂	15-20	Spherical	Tetragonal	3.50 ²³⁷
Al ₂ O ₃	20-40	Spherical	Trigonal	26.20 ²³⁸
ZrO ₂	80-100	Cuboidal	Monoclinic	11.77 ²³⁹
CaCO ₃	50-100	Cuboidal	Trigonal	5.00 ²⁴⁰
h-BN	~200	Layered	Hexagonal	24.6 (Theoretical) ²⁴¹
graphite	200-300	Layered	Hexagonal	37.4 (Theoretical) ²⁴¹

4.1.2. Lubricant formulation and tribopairs preparation

The water-based lubricant is formulated by dissolving a certain amount of sodium borate into water that forms the 0.5 wt.% salt solution. Subsequently, different nanoparticles are added and dispersed uniformly into the salt solutions by ultrasonication for 30 mins at 40 W. The weight ratio between nanoparticles and sodium borate is kept at 1:1. To limit the agglomeration effect, a certain amount of non-ionic surfactant (Tween 80) has been added resulting in 0.5 wt.% concentration. The selection of non-ionic surfactants is due to their low thermal stability which can be decomposed into fumes at elevated temperatures and leave no traces on the sliding surfaces. In this case, any interferences on the tribological performance of the nanoparticles can be minimized. The formulated lubricants are named NBO for sodium borate, NBO-Al for the addition of Al₂O₃ nanoparticles, NBO-Ti for the addition of TiO₂ nanoparticles, NBO-Zr for the addition of ZrO₂ nanoparticles, NBO-Si for the addition of SiO₂ nanoparticles, NBO-Cal for the addition of CaCO₃ nanoparticles, NBO-BN for the addition of h-BN nanoplates, and NBO-Gr for the addition of graphite nanoplates. **Figure 4-3** shows the dynamic light scattering measurement of the nanoparticle dispersions in sodium borate water-based lubricant after ultrasonication and 24h-after ultrasonication. It can be seen that Tween 80 surfactant provides good dispersion of nanoparticles within the water-based fluid. Dynamic light scattering (DLS) measurement indicates the good

agreement between the measured Z-average size distribution from each nanoparticle after ultrasonication compared to that from **Table 4-1** and **Figure 4-2**. However, the agglomeration takes place 24h-after ultrasonication (**Figure 4-3**) for all nanoparticles. Therefore, the lubricants are immediately subjected to a hot friction test after ultrasonication to minimize the aggregation effect that can interfere with the tribological performance.

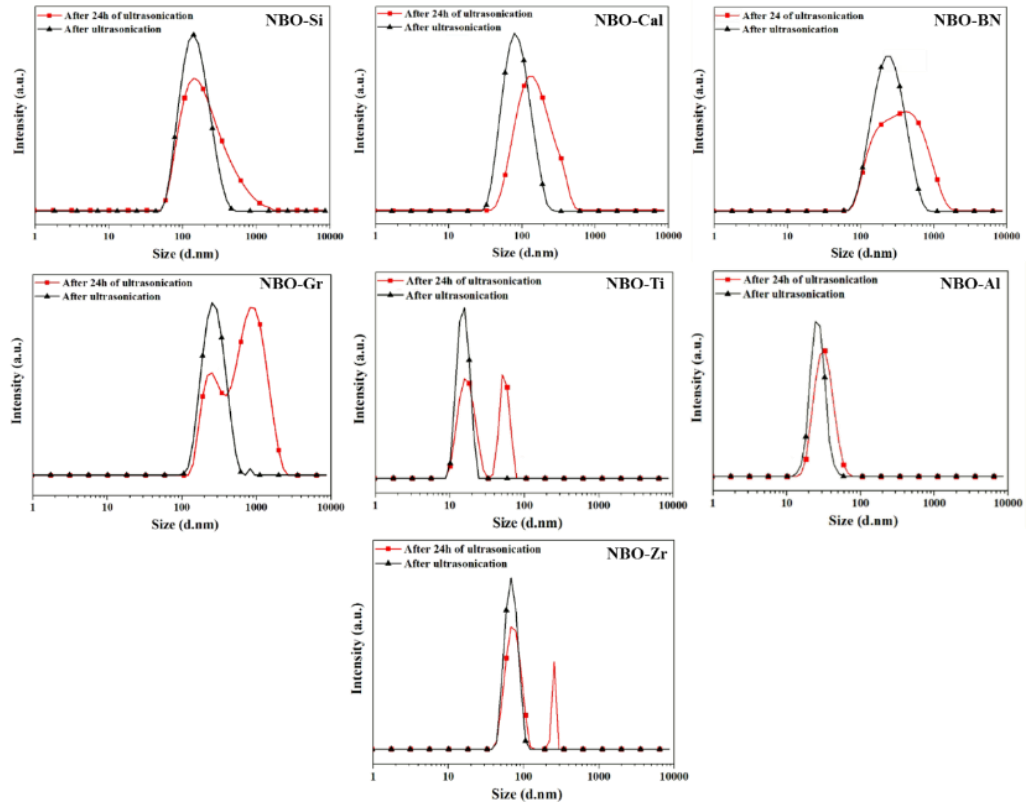


Figure 4-3. Z-average measurement by dynamic light scattering (DLS) showing the size distribution of the nanoparticles within the formulated water-based lubricants after ultrasonication and 24h-after ultrasonication.

In the case of tribotest at elevated temperatures, the stationary contact is chosen as a GCr15 chromium steel ball (6.35 mm diameter, $R_a = 20$ nm), while stainless steel disc (30 mm diameter, 3 mm thickness, and $R_a = 500$ nm) is selected as the moving part. The tribopairs are rinsed with solvents to remove contaminants before conducting the friction test. The composition of the tribopairs is displayed in **Table 4-2**. The formulated lubricants are then uniformly drop-coated on the steel disc surface as indicated in the experimental methods in **Chapter 3**.

Table 4-2. Compositions of the steel counterparts.

Materials	Composition (wt.%)								
	C	Mn	Si	P	S	Cr	Ni	Mo	Fe
Steel Disc	0.02	1.71	0.5	0.03	0.02	16.2	11	2.18	rest
Steel Ball	0.95-1.05	0.35	0.25	0.025	0.025	1.4-1.65	-	-	rest

4.1.3. High-temperature tribological testing

The friction tests are performed in a Bruker Universal Mechanical Tester (UMT) using the rotation module equipped in a furnace. The set temperature of the furnace for the friction test was 940°C, resulting in the actual temperature of the disc being 930°C. This testing module has been verified by Zhu et al.²²¹ as suitable to simulate the friction-wear behavior of hot metal rolling conditions.

4.2. Results and Discussion

4.2.1. Friction and wear behavior of the nanoparticles under sodium borate melt lubrication at elevated temperatures

Figure 4-4 shows the friction and wear performance of the formulated lubricants comprising sodium borate and nanoparticles compared to dry and sodium borate friction tests. It can be seen in **Figure 4-4a-Figure 4-4d** that the dry friction test produces the highest friction coefficient and wear losses. An application of sodium borate (NBO) reduces significantly friction coefficient (by ~ 41%) and wear losses (by over 70%) which can be associated with the formation of the hierarchical tribofilm on the sliding surfaces.¹³ Intriguingly, the addition of different nanoparticles results in different friction outcomes. Among the applied nanoparticles, SiO₂ nanoparticles improve significantly the lubrication performance of sodium borate (NBO) which reduces the friction coefficient by two times and wear losses by ~50% (NBO-Si, **Figure 4-4a-Figure 4-4d**). It can be seen in **Figure 4-4a** that the NBO-Si lubricant results in a gradual decrease of friction coefficient with less fluctuation until reaching the steady-state at below 0.2. In contrast, Al₂O₃ nanoparticles increase the friction coefficient and wear of NBO by 46% and over 50% respectively (**Figure 4-4b-Figure 4-4d**) with a dramatic variation in friction behavior (**Figure 4-4a**). Compared to other nanoparticles, NBO-Al shows the worst friction performance.

In the case of other nanoparticles, the addition of TiO₂ (NBO-Ti) and ZrO₂ (NBO-Zr) nanoparticles substantially decreases the friction coefficient and wear of sodium borate (**Figure 4-4a-Figure 4-4d**). The tribological improvement of TiO₂ nanoparticles at elevated temperatures has been well-recognized from the previous studies,^{15, 88, 242, 243} however, the tribological enhancement from ZrO₂ nanoparticles that outperforms TiO₂ nanoparticles has been observed in this study for the first time. In particular, ZrO₂ nanoparticles decrease the friction coefficient of sodium borate by 18% compared to 10% from TiO₂ nanoparticles. Moreover, the ball and disc wear losses from NBO-Zr reduce by 50% and 23% respectively compared to NBO which are greater than TiO₂ nanoparticles (NBO-Ti) (**Figure 4-4c-Figure 4-4d**). Other nanoparticles and nanoplates including CaCO₃ (NBO-Cal), h-BN (NBO-BN), and graphite (NBO-Gr) show negligible improvements in the friction performance of sodium borate (NBO). In particular, CaCO₃ nanoparticles (NBO-Cal) show almost no changes in the friction curve and the mean friction coefficient of sodium borate (**Figure 4-4a-Figure 4-4b**), but, the disc and ball wear losses, in this case, increase significantly by 190% and 55% respectively compared to NBO which are higher than even NBO-Al.

Meanwhile, the nanoplates of h-BN and graphite cause the fluctuation in friction behavior from

the running-in stage to the steady-state. The addition of h-BN nanoplates (NBO-BN) reduces the friction coefficient substantially in the first 100s (**Figure 4-4a**), however, the friction increase thereafter followed by significant variation after 400s of sliding. This phenomenon indicates the deterioration of lubricity from the applied lubricant. It has been demonstrated that the decomposition rate of h-BN nanoplates increases via a decrease in the number of the h-BN layer at above 800°C.^{110, 244} At the first 100s, the h-BN nanoplates reduce friction by the interlayer shearing effect which can exfoliate the nanosheets and reduce the number of layers. Subsequently, the exfoliated sheets and the reduced-layer h-BN decompose into the B₂O₃ melt at the sliding surfaces which can interfere with the sodium borate and cause the fluctuation in friction. The significant fluctuation after 400s of sliding from the friction test of NBO-BN resembles the friction behavior of the B₂O₃ melt as observed in the previous study of Tran et al.¹³² As a result, the disc and ball wear losses are moderately higher than NBO under the same testing conditions (**Figure 4-4c-Figure 4-4d**).

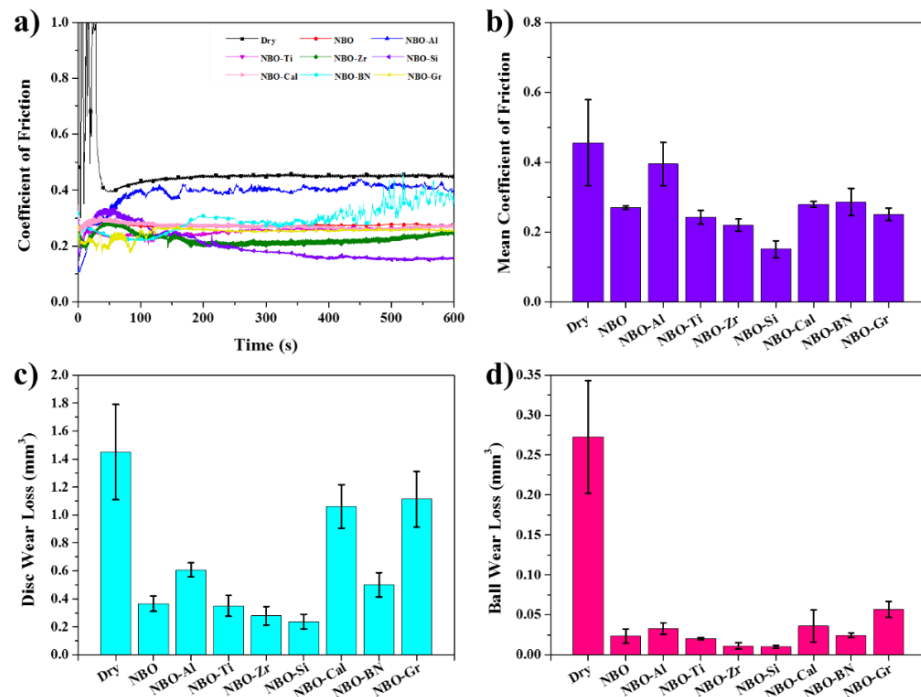


Figure 4-4. (a) Dynamic friction behavior of dry friction, sodium borate lubrication, and sodium borate + nanoparticles lubrication tests; (b) Mean friction coefficient; (c) Disc wear loss volume; and, (d) Ball wear loss volume from different friction tests.

In the case of graphite nanoplates, the NBO-Gr results in a significant variation in the running-in stage before reaching a steady-state after 150 s. Such behavior is consistent with that observed in the previous study of Wang et al.²⁴⁵ when graphite nanoplates were added to sodium metasilicate melt at elevated temperatures. The significant variation is due to the intense deformation and material removal from the sliding counterparts which generates the debris particles and surface delamination at elevated temperatures. However, the graphite nanoplates not only fail to reduce the friction coefficient but also increase significantly the wear losses (**Figure 4-4c-Figure 4-4d**). Since graphite is decomposed at elevated temperatures that leave the unstable carbon product on

the sliding surfaces,²⁴⁶ it is believed that these products act as third body abrasive particles that cause the fluctuation in the running-in stage. Such fluctuation can result in a significant increase in disc and ball wear losses compared to NBO (**Figure 4-4c-Figure 4-4d**). A significant increase in disc and ball wear losses can be attributed to the grinding and polishing effects of these abrasive particles which increase the contacting surface areas between the counterparts. Although the increased real contact area may lead to an increase in friction due to an increase in the asperities contact, it can also reduce the applied pressure. It is believed that fraction of GNPs still retains the lamellar shape among the unstable carbon products which can prevent the direct asperity contact between the sliding counterpart. The reduced applied pressure and the presence of small fraction of GNPs on the sliding surfaces can be the reason for the slight decrease in the mean friction coefficient of NBO-Gr compared to NBO (**Figure 4-4b**).

4.2.2. Wear track observation after hot friction tests under Dry and NBO lubrication

To understand the friction and wear performance of the formulated lubricants, the wear surface morphologies of the disc and ball are investigated. Shown in **Figure 4-5** are the SEM images of the disc wear morphologies after the hot friction tests of un-lubricated and NBO-lubricated conditions. The dry friction test produces a severe wear on the disc surface with the presence of holes, delamination, and smearing which is characteristic of the removal of materials due to abrasive and adhesive wear (**Figure 4-5a-Figure 4-5b**). EDS analysis at the worn surface shows the presence of different metallic elements (Cr, Fe, Mn, and Ni) from the steel with a significant intensity of oxygen confirming the high oxidation rate (**Figure 4-5c**). Meanwhile, SEM images of the worn surface after the lubrication test of NBO reveals a smoother pattern with several particles of the recrystallized sodium borate after cooling to room temperature (**Figure 4-5d-Figure 4-5e**). EDS analysis confirms a strong presence of sodium borate elements at the dark gray areas compared to the brighter areas of the worn surfaces (**Figure 4-5f**). The dark gray areas have a significant agglomeration of the sodium borate crystalline particles due to the recrystallization of the sodium borate melt during the cooling process. In general terms, when the friction test ceased, the sodium borate melt could flow into the sliding contacts and covered part of the sliding surfaces. During the cooling process, the sodium borate melt recrystallized and formed the solid particles in these areas. These crystallite particles have a lower contrast, thus appearing darker, than the steel/oxide surfaces, thus, resulting in the different areas on the SEM images.

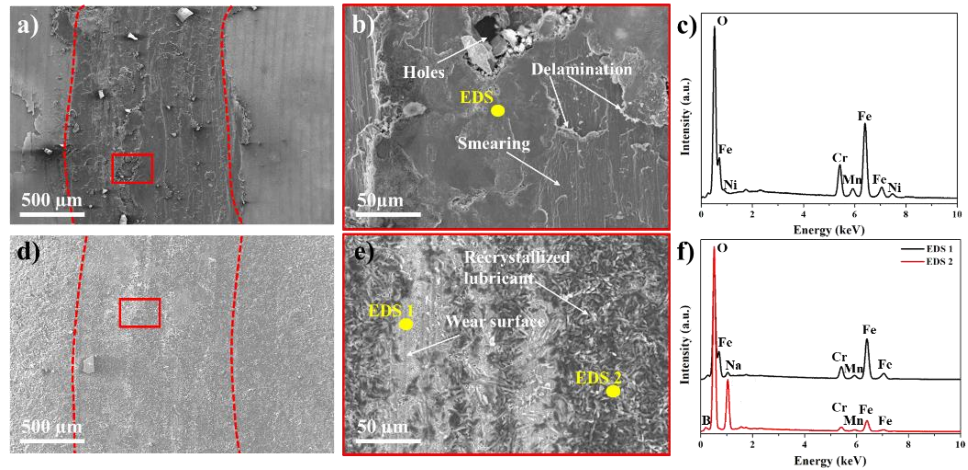


Figure 4-5. Disc wear track analysis by SEM and EDS from (a)-(c) Dry friction test and (d)-(f) NBO friction test.

For the ball-worn surface, the dry sliding resulted in a significantly large ball wear scar with the characteristic of adhesive wear (**Figure 4-6a**). High magnification observation reveals the ploughing and smearing patterns with the smooth areas representing the compacted material transfer which are all characteristic for both abrasive and adhesive wear (**Figure 4-6b**). EDS analysis at the wear surface shows the dominant presence of Fe and O which indicates the formation of iron oxide. An application of NBO lubricant reduces the ball wear scar significantly (**Figure 4-6d**), however, the smearing patterns of the abrasive wear still appear across the wear surface (**Figure 4-6e**). There are some areas covered by the black particles which can be the recrystallized sodium borate as demonstrated by EDS analysis (**Figure 4-6f**). It is similar to the observation on the disc wear surface since the sodium borate melt in the liquid state could infiltrate into the sliding interfaces when the friction test stopped and thermodynamically recrystallized during the cooling process.

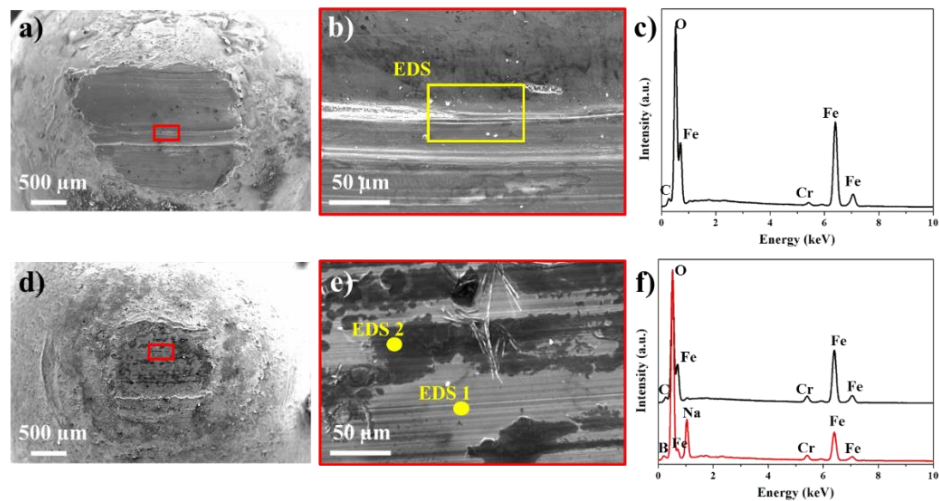


Figure 4-6. Ball wear track analysis by SEM and EDS from (a)-(c) Dry friction test and (d)-(f) NBO friction test.

4.2.3. Wear track observation after hot friction tests under NBO lubrication with ceramic oxide nanoparticles

The effect of different ceramic oxide nanoparticles on the disc wear surface morphologies of NBO is shown in **Figure 4-7**. Accordingly, the disc worn surface from NBO-Cal is relatively rough and the wear track width is broad compared to other formulated lubricants (**Figure 4-7a**). High magnification reveals the two distinct patterns including the smooth pad-like areas and the densely aggregated particle areas (**Figure 4-7b**). Elemental analysis by EDS at the densely aggregated particle areas shows the sharp signals of Na and Ca compared to the pad-like areas which may demonstrate the presence of recrystallized borate lubricant containing both Na and Ca (**Figure 4-7c**). It is believed that the large calcium oxide clusters exist within the melt that plays as the third-body abrasive particles. Meanwhile, silica (SiO_2) exhibits a superior performance which results in smooth and uniform wear disc surfaces (**Figure 4-7d**). There are some small flake particles on the sliding surface which could be the recrystallized lubricants during the cooling down process (**Figure 4-7e**). Apart from such particles, there is no distinct abrasive or adhesive wear on the disc wear surface lubricated by NBO-Si. EDS analysis on the wear surface reveals a strong presence of the chemical elements from the lubricants (e.g. Na, Si, and B) on the wear surfaces indicating the formation of the tribofilm from the synergy between the NBO melt and SiO_2 nanoparticles.

On the hands, the disc wear surface after being lubricated by NBO-Al reveals the presence of many ploughing patterns along the wear track indicating severe abrasive wear (**Figure 4-7g**). Besides, high magnification observation reveals several cracks and pits which roughen the surfaces (**Figure 4-7h**). EDS analysis detects a slight intensity of the Al at the ploughing and grooving lines which might come from the Al_2O_3 nanoparticles (**Figure 4-7i**). The lubrication test with NBO-Ti and NBO-Zr, on contrary, reveals the formation of smooth wear surfaces, although the disc wear surface appears granular (**Figure 4-7j and Figure 4-7m**). High magnification analysis shows the uniform and smooth surface patterns for NBO-Ti but the NBO-Zr exhibits a simultaneous presence of granular and flattened areas (**Figure 4-7k and Figure 4-7n**). From elemental analysis, the wear surface after being lubricated by NBO-Ti shows the strong presence of Ti apart from the steel oxide elements (e.g. Fe, Cr, Mn) (**Figure 4-7l**). There was also a slight detection of Na on the worn surface implying that the tribofilm between the melt, TiO_2 nanoparticles, and oxide is formed. In the case of NBO-Zr, the significant intensity of Zr and Na presents at the granular areas while the flattened areas show strong detection of elements from the stainless steel oxides (**Figure 4-7o**). It could mean that the tribofilm between the melt lubricant and the ZrO_2 nanoparticles does not form fully.

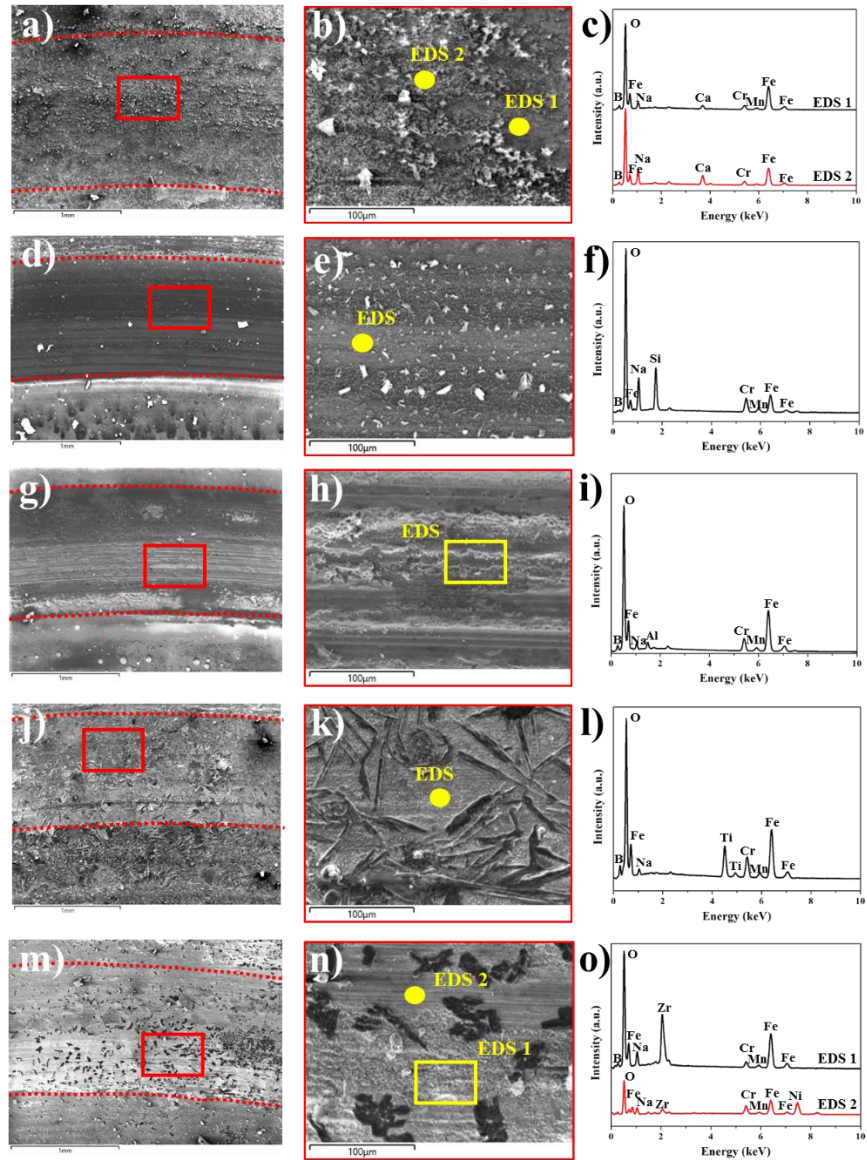


Figure 4-7. Disc wear track analysis by SEM and EDS from (a)-(c) NBO-Cal; (d)-(f) NBO-Si; (g)-(i) NBO-Al; (j)-(l) NBO-Ti; and (m)-(o) NBO-Zr friction tests.

For the ball wear scar, a similar trend is observed for the formulated lubricants containing ceramic oxide nanoparticles. For instance, the lubrication test of NBO-Cal results in the largest ball wear scar among the ceramic oxide nanoparticles (**Figure 4-8a**). The wear ball surface is partially covered by the big lumps (**Figure 4-8b**) which has a strong intensity signal of sodium and calcium (**Figure 4-8c**). Apart from the big lumps, the remaining surfaces are relatively smooth with the detection of sodium and iron oxide which indicates the tribochemical reactions between the sodium borate melt and the oxide surfaces. In contrast, the ball lubricated by NBO-Si shows the smallest wear scar diameter (**Figure 4-8d**) among other lubricants formulated with ceramic oxide particles. The ball wear surfaces are homogeneous and smooth with a strong intensity signal of Na and Si (**Figure 4-8e-Figure 4-8f**) similar to the disc wear surface.

For the NBO-Al, the wear morphology on the ball shows a similar pattern to the disc with the

appearance of ploughing and smearing on the transferred material on the ball (**Figure 4-8g**). There is the delamination and cracking observed from a high-magnified image (**Figure 4-8h**) with the detection of high intensity of Na and Al at the ploughing areas (**Figure 4-8i**). Meanwhile, the ball lubricated by NBO-Ti shows the distinct material transfer adhered around the wear scar (**Figure 4-8j**). Detailed analysis reveals the strong presence of Na and Ti covered the surface (**Figure 4-8l**). There is also the presence of several smearing patterns with some agglomerated particles through the sliding direction (**Figure 4-8k**). Intriguingly, the ball lubricated by NBO-Zr shows less material transfer from the disc compared to NBO-Al and NBO-Ti (**Figure 4-8m**) and the wear surface is more uniform compared to the disc with the presence of densely smearing streaks (**Figure 4-8n**). This indicates the occurrence of mainly abrasive wear compared to the simultaneous occurrence of abrasive and adhesive wear from NBO-Ti and NBO-Al. The EDS analysis on the wear surface shows the weak detection of Zr while Na and Fe were strongly observed. It is quite different from the observed results of the corresponding disc which will be discussed in the discussion section.

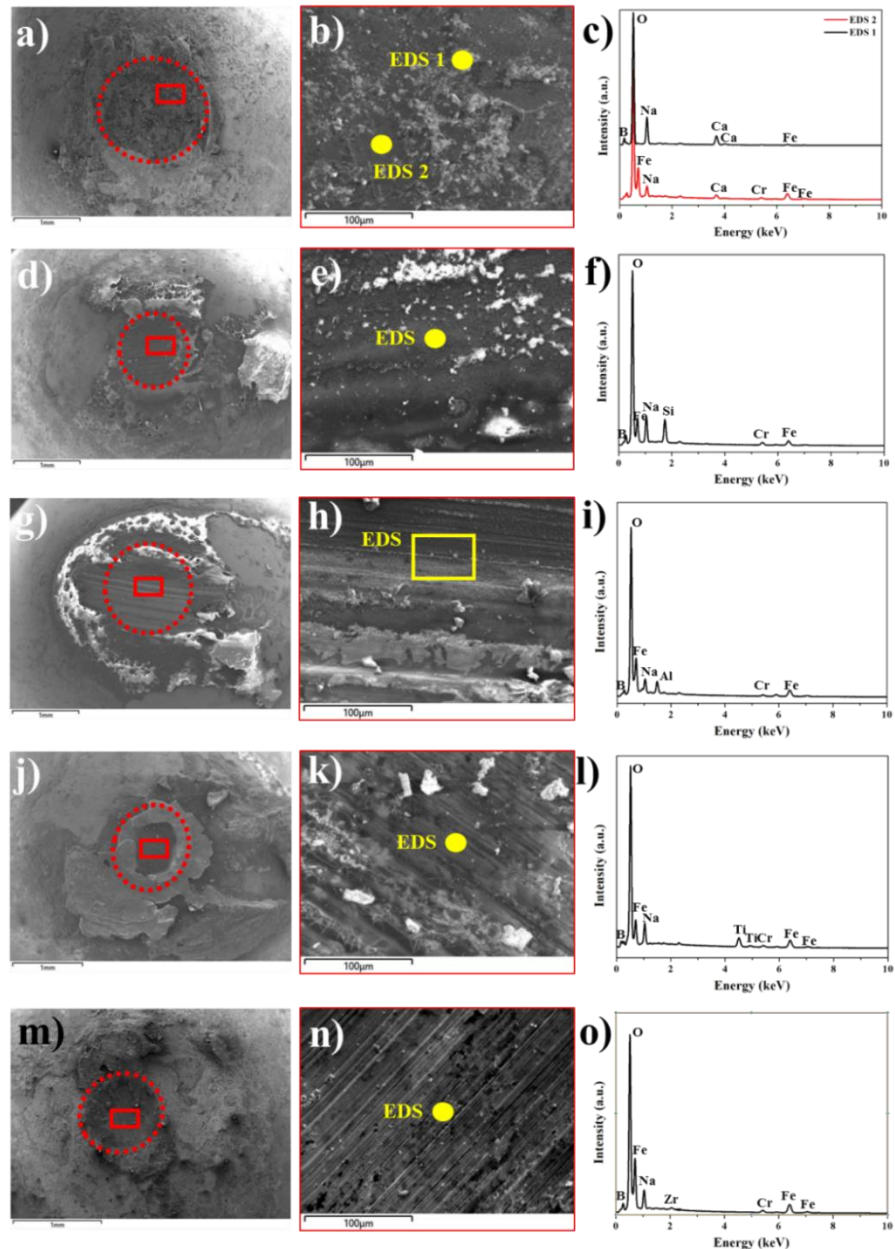


Figure 4-8. Ball wear track analysis by SEM and EDS from (a)-(c) NBO-Cal; (d)-(f) NBO-Si; (g)-(i) NBO-Al; (j)-(l) NBO-Ti; and (m)-(o) NBO-Zr friction tests.

4.2.4. Wear track observation after hot friction tests under NBO lubrication with layered nanoparticles

Figure 4-9 and **Figure 4-10** show the wear surface analysis on the disc and ball from the hot friction test of the lubricant formulated with h-BN nanosheets (NBO-BN) and graphite nanoplates (NBO-Gr). Compared to ceramic oxide nanoparticles, the nanoflakes of h-BN and graphite produces a larger disc wear width (**Figure 4-9a** and **Figure 4-9d**). While a high magnification examination of the disc shows the scaly pattern on the smeared wear surfaces for NBO-BN (**Figure 4-9b**), the disc wear surface after being lubricated by NBO-Gr are granular and inhomogenous with the presence of various pits and scars on smoothly compacted surfaces (**Figure 4-9e**). In the

case of NBO-BN, EDS analysis confirms the scaly pattern has a strong signal intensity of Na and B and less Fe than the smeared areas (**Figure 4-9c**). Thus, the scaly pattern may be the solidified sodium borate melt, however, it is not similar to what is observed from other friction tests with ceramic oxide nanoparticles. For the EDS analysis of the wear surface from NBO-Gr, a strong intensity signal of Na is detected while the metallic elements from the oxide are weakly presented (**Figure 4-9f**).

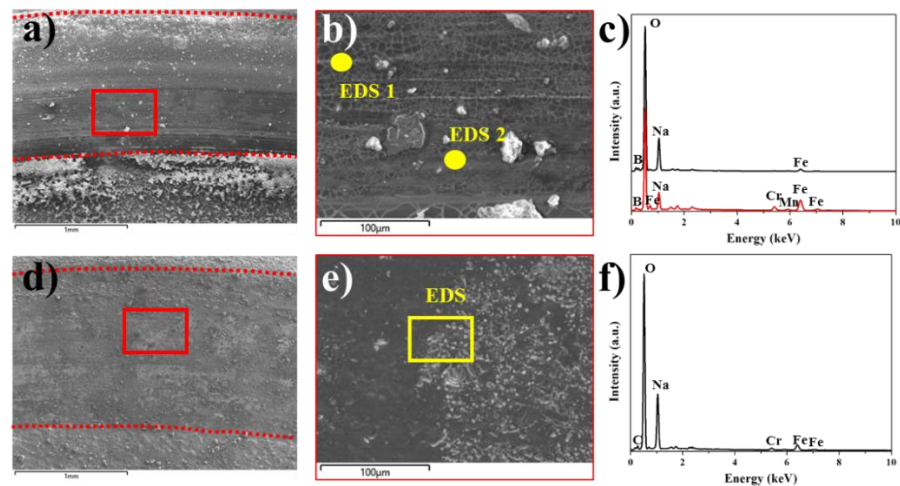


Figure 4-9. Disc wear track analysis by SEM and EDS from (a)-(c) NBO-BN; and (d)-(f) NBO-Gr friction tests.

For the ball wear surface, the NBO-Gr results in a larger ball wear scar than the NBO-BN, and both the balls experience significant adhesive wear and material transfer from the disc (**Figure 4-10a** and **Figure 4-10d**). The detailed observation of the ball wear morphology from NBO-BN shows the rough surface with the ploughing and scaly patterns with some delamination (**Figure 4-10b**). The ploughing and delamination indicate the occurrence of abrasive wear that roughen the worn surface. The scaly pattern could be the solidified sodium borate melt as demonstrated in **Figure 4-9**. EDS analysis in the ploughing and delamination areas shows the presence of metallic elemental from the oxide compounds with less sodium. It can be seen that the metallic elements are Cr, Fe, and Ni. Since the Cr and Ni contents in the GCr15 ball are relatively low, they can not be detected in the oxide scale, thus, proving the material transfer from the disc to the ball. Meanwhile, NBO-Gr results in a severe ball wear surface with the streak-line pattern of smearing and ploughing (**Figure 4-10e**). However, EDS analysis from the ball wear surface shows a strong presence of Na and C but no detection of metallic compounds. While the Na can come from the lubricant residue, the high intensity of C indicates a relatively thick carbon coating that covered the whole wear surface.

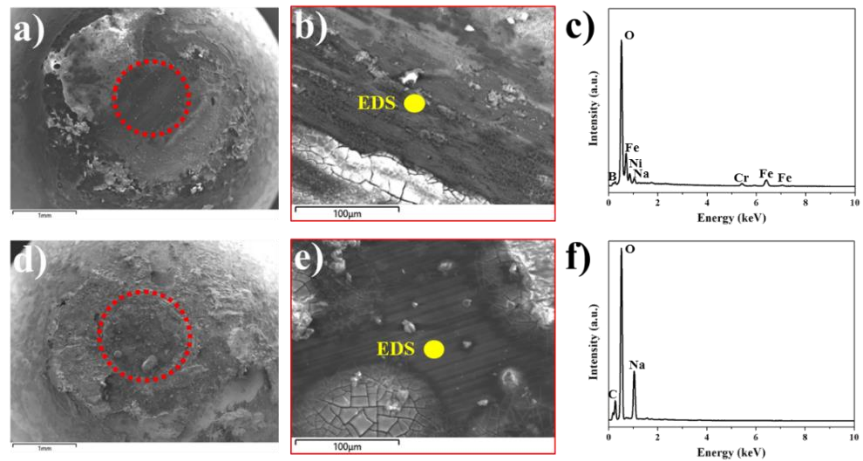


Figure 4-10. Ball wear track analysis by SEM and EDS from (a)-(c) NBO-BN; and (d)-(f) NBO-Gr friction tests.

4.2.5. Oxidation performance of the coated lubricants on the steel disc surfaces at 930°C

Apart from the tribological performances, the anti-oxidation performances of the formulated lubricants under static isothermal conditions are important for high-temperature manufacturing processes. Prior to hot rolling or hot forging of steel, the steel plate is commonly preheated at 850-1000°C³⁴ in the furnace which can cause serious oxidation and induce material losses through the formation of the oxide scale. As can be seen, **Figure 4-11a** shows the formation of the thick (~ 65 µm) oxide scale containing dominantly Fe-Cr oxides for the stainless steel after heat-treatment processes at 930°C for an hour. The application of the sodium borate (NBO) coating significantly reduces the oxide formation. According to the EDS analysis (**Figure 4-11b**), there is the Cr-rich oxide layer beneath the NBO coating while the coating shows the moderate intensity of Fe within the coating. Since sodium borate can react with iron oxide to form the iron boroferrite at elevated temperatures, the incorporation of Fe within the coating can be due to such occurrences. Although sodium borate shows good anti-oxidation at below 800°C¹⁵⁵, this ability deteriorates at above 850°C due to its high reactivity toward the oxide scale that causes the formation of boroferrite and other sodium-metallic oxides²³⁴. Therefore, it is expected that the NBO coating on the steel in this study comprises these reaction products after being treated at 930°C. The total oxide formation is, thus, measured from the Cr-rich oxide to the coating which is around 20 µm (**Figure 4-11b**).

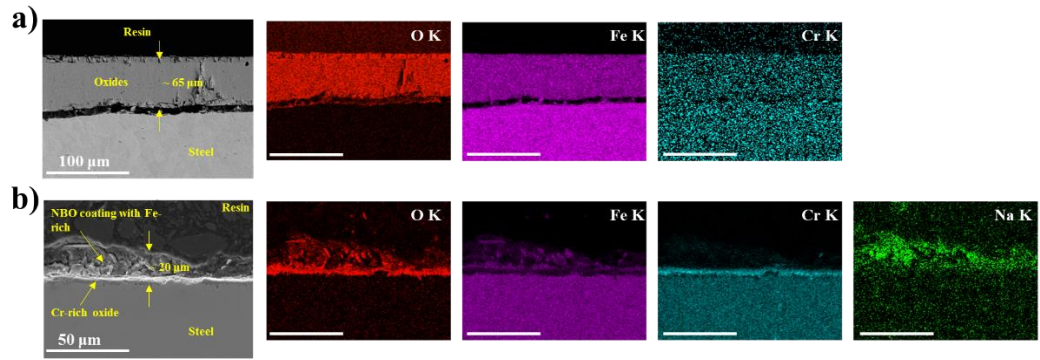


Figure 4-11. Cross-sectional analysis of the (a) non-coated steel and (b) NBO-coated steel after isothermal oxidation at 930°C.

The addition of ceramic oxide nanoparticles to the sodium borate glass melt can change the melt physicochemical properties which results in different anti-oxidation behavior. For instance, the addition of CaCO_3 nanoparticles to the NBO (NBO-Ca) reduces the oxide thickness to 17 μm (**Figure 4-12a**). From EDS analysis, the formation of the Fe-rich oxide layer above the Cr-rich oxide layer is evident. Meanwhile, the coating above the Fe-rich oxide layer contains a significant amount of Na and Ca. It can be seen that Ca stayed mainly at the coating/Fe-rich oxide interfaces while Na is distributed evenly within the coating. Besides, there is less Fe signal intensity within the coating compared to the case of NBO coating (**Figure 4-12a** and **Figure 4-11b**) which demonstrates the beneficial effect of Ca from the CaCO_3 nanoparticles to the oxidation inhibition of Fe. For NBO-Si lubricant coating, only the formation of a Cr-rich oxide layer ($\sim 4 \mu\text{m}$) is found beneath the melt layer (**Figure 4-12b**) which contains a slight signal of Fe. The coating, in this case, is the melt layer containing a uniform distribution of Na and Si with negligible Fe. Among other lubricants, NBO-Si performs the best anti-oxidation which is due to the reaction between the sodium borate and SiO_2 that formed sodium borosilicate.

Meanwhile, the addition of Al_2O_3 nanoparticles to the sodium borate (NBO-Al) also results in the melt layer with a uniform distribution of Al and Na (**Figure 4-12c**). However, the signal intensity signal is slightly stronger near the oxide layer ($\sim 8 \mu\text{m}$) which has a strong signal of Fe and Cr. There is also significant Fe coming from the floating particles within the melt layer. Compared to the NBO, the addition of Al_2O_3 can substantially reduce the oxidation of the steel due to the incorporation of Al_2O_3 nanoparticles into the sodium borate melt. On the other hand, there is a thin oxide layer ($\sim 7 \mu\text{m}$) under the coating of NBO-Ti which has a strong signal of Cr and Fe with the moderate presence of Ti (**Figure 4-12d**). In the coating, Na is uniformly distributed with no aggregation at the oxide layer whereas the Ti signal intensity appears locally within the coating. From the EDS analysis, TiO_2 nanoparticles can incorporate into the oxide layer to reduce the oxidation degree. However, the NBO-Zr containing ZrO_2 nanoparticles show little improvement in the oxidation inhibition compared to NBO with the oxide layer of $\sim 14 \mu\text{m}$ (**Figure 4-12e**). From the EDS analysis, ZrO_2 nanoparticles seem to incorporate within the melt layer due to the uniform distribution of Zr with the coating. The oxide layer in this case is the Cr-rich layer beneath the coating plus the aggregated Fe-rich particles above the Cr-rich oxide layer.

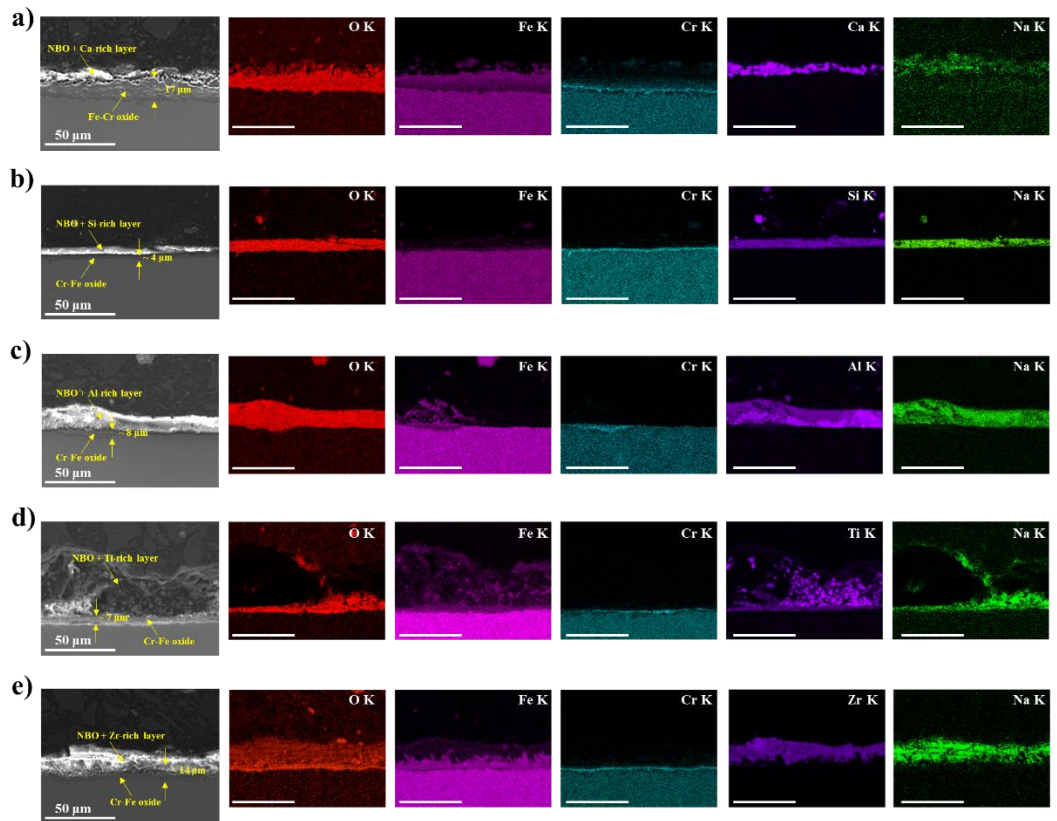


Figure 4-12. Cross-sectional analysis of the (a) NBO-Cal-coated steel; (b) NBO-Si-coated steel; (c) NBO-Al-coated steel; (d) NBO-Ti-coated steel; and (e) NBO-Zr-coated steel after isothermal oxidation at 930°C.

For the layered nanoparticles, NBO-BN containing h-BN nanosheets shows the formation of the melt above the oxide layer **Figure 4-13a**. The oxide layer (~ 14 μm) is rich in Fe and Cr and there is a slight presence of Fe within the melt. Compared to NBO, there is no much improvement in the oxidation inhibition of the resulted melt. Meanwhile, the addition of graphite nanoplates to the sodium borate (NBO-Gr) reduces the oxide scale thickness to 8 μm although there is also the incorporation of Fe within the melt (**Figure 4-13b**). From the EDS mapping, a slight signal of C is also detected within the melt which may come from the randomly distributed graphite nanoplates.

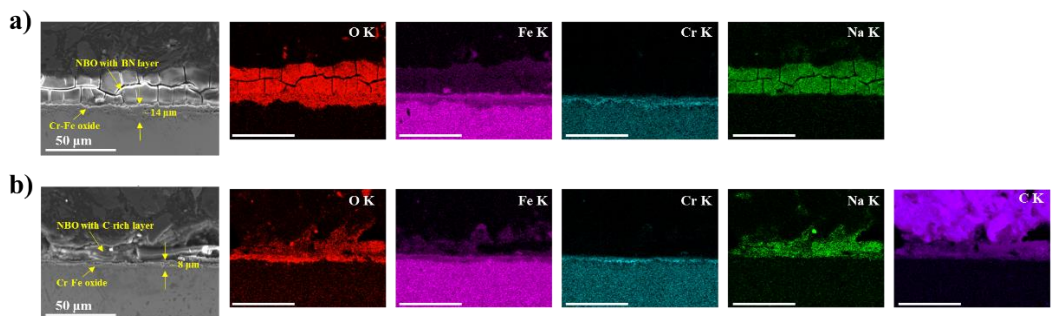


Figure 4-13. Cross-sectional analysis of the (a) NBO-BN-coated steel and (b) NBO-Gr-coated steel after isothermal oxidation at 930°C.

4.2.6. Proposed anti-oxidation and lubrication mechanisms of different nanoparticles under sodium borate melt at 930°C

Oxidation of steel at elevated temperatures initially occurs via Wagner's mechanism whereby the metallic oxide is formed through the outward diffusion of charged particles from the steel (e.g. Cr^{2+} , Fe^{2+} , Mn^{2+} , etc.) to the steel/air interface³⁰. The glass-melt coating can act as a protective barrier which not only reduces the adsorption of oxygen to the steel substrate but also isolates the oxide/metal surface from the surrounding environments. Sodium borate has previously been demonstrated as a good melt lubricant that can deliver outstanding anti-oxidation and reduce friction and wear up to 800°C.¹⁵⁵ However, at higher temperatures, sodium borate gradually lost its anti-oxidation and lubrication abilities due to its vigorous reactions toward oxide compounds. In particular, sodium in the borate melt is particularly mobile at above 850°C which can react with the oxide compounds or metallic cations to form the reaction products²³⁴. From XRD analysis (**Figure 4-14**, NBO), it can be seen that NaFeO_2 and Na_2CrO_4 were detected in addition to the dominant presence of Cr_2O_3 and FeCr_2O_4 from the oxide scale. Although NBO reduces the oxide scale thickness by ~69% compared to the non-coated steel, the highly mobile sodium can cause corrosion to the oxide scale as evidenced by the formation of sodium-containing reaction products. The sodium corrosion induces the cation vacancies within the protective oxide that loosen this layer and facilitate infiltration of the sodium to the metallic substrate¹⁵⁵. When these reactions reach equilibrium, the metallic cations from the steel combine with the glass network (e.g. B_2O_3) to form other reaction products. The resulted reaction products from this stage can be Fe_3BO_6 , $4\text{FeO}\cdot\text{Fe}_2\text{O}_3\cdot\text{B}_2\text{O}_3$, and $\text{Fe}_3(\text{BO}_3)\text{O}_2$ (**Figure 4-14**, NBO) that are intermixed and combined into an aggregated rigid layer that gradually replaces the liquid melt (**Figure 4-11b**). These compounds are known as iron boroferrite which causes wear to the ball counterpart.

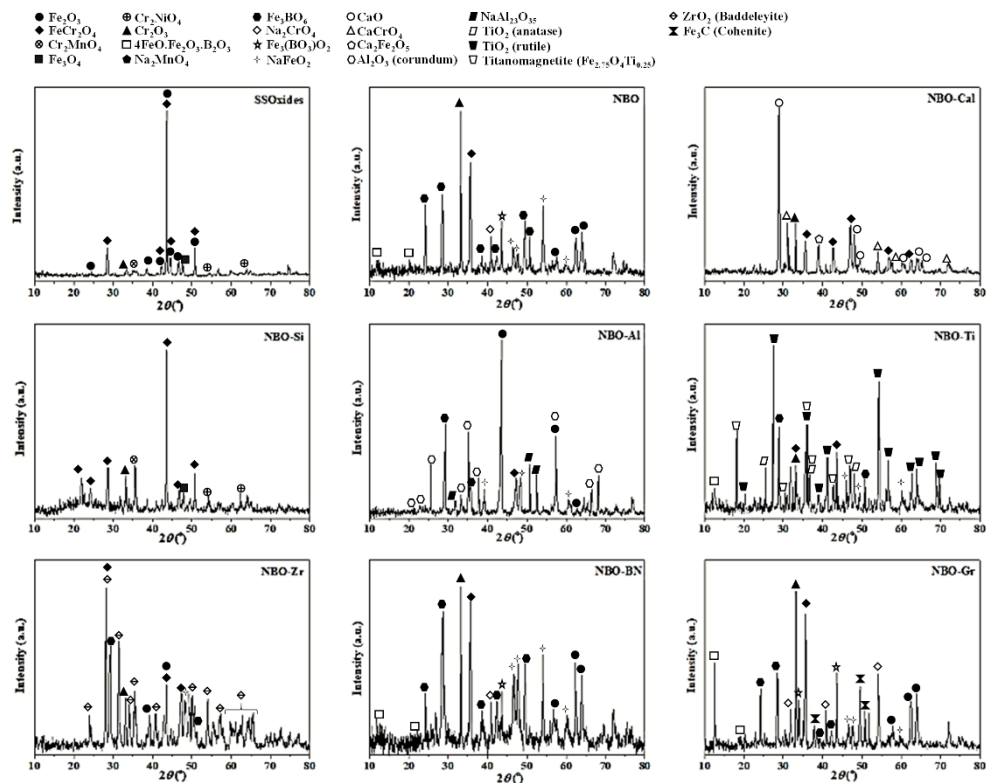


Figure 4-14. XRD analysis of the phases in the non-coated steel and lubricant-coated steel after isothermal oxidation test at 930°C.

In the case of CaCO_3 nanoparticles, it is believed that the calcium oxide forms at the sliding interfaces since CaCO_3 starts to decompose at 800°C ²⁴⁷. The XRD analysis of NBO-Cal coating shows a distinct detection of CaO after oxidation test at 930°C (**Figure 4-14**, NBO-Cal). Although CaO can act as a network modifier in the glass network, it can not incorporate into the sodium tetraborate melt network since the concentration of sodium (network modifier) in sodium tetraborate melt is at the eutectic²⁴⁸. Instead, the CaO phase reacts to iron oxide and chromium oxide to form the CaCrO_4 and $\text{Ca}_2\text{Fe}_2\text{O}_5$ phases along with the Fe-Cr oxides (**Figure 4-14**, NBO-Cal). With CaO, there is no observation of iron boroferrite or sodium-metallic oxide formation after the oxidation test, thus, indicating the inhibition of the boriding effect on the oxide scale. From the SEM/EDS analysis of the NBO-Cal coating cross-section (**Figure 4-12a**), the oxide scale of Fe and Cr is densely compacted while the Ca-rich layer stays above the scale. This Ca-rich layer acts as the protective barrier that limits the infiltration of sodium borate melt to the oxide scale, thus, reducing the reactions between the melt and oxide layer or steel. However, such a Ca-rich aggregated layer may increase wear and friction (**Figure 4-4**). The SEM/EDS of the cross-section from the disc wear track after lubrication by NBO-Cal shows the compacted oxide beneath the loosely aggregated large Ca-rich particles. This Ca-rich layer has a strong signal of Fe with a moderate presence of Cr and a weak intensity of sodium (**Figure 4-15a**). It is believed that sodium borate cannot provide effective lubrication due to the presence of this Ca-rich layer. Although the anti-oxidation and tribological performance are not much improved compared to NBO, CaCO_3 nanoparticles can be used to limit the boriding effect and the reactions between sodium and oxide.

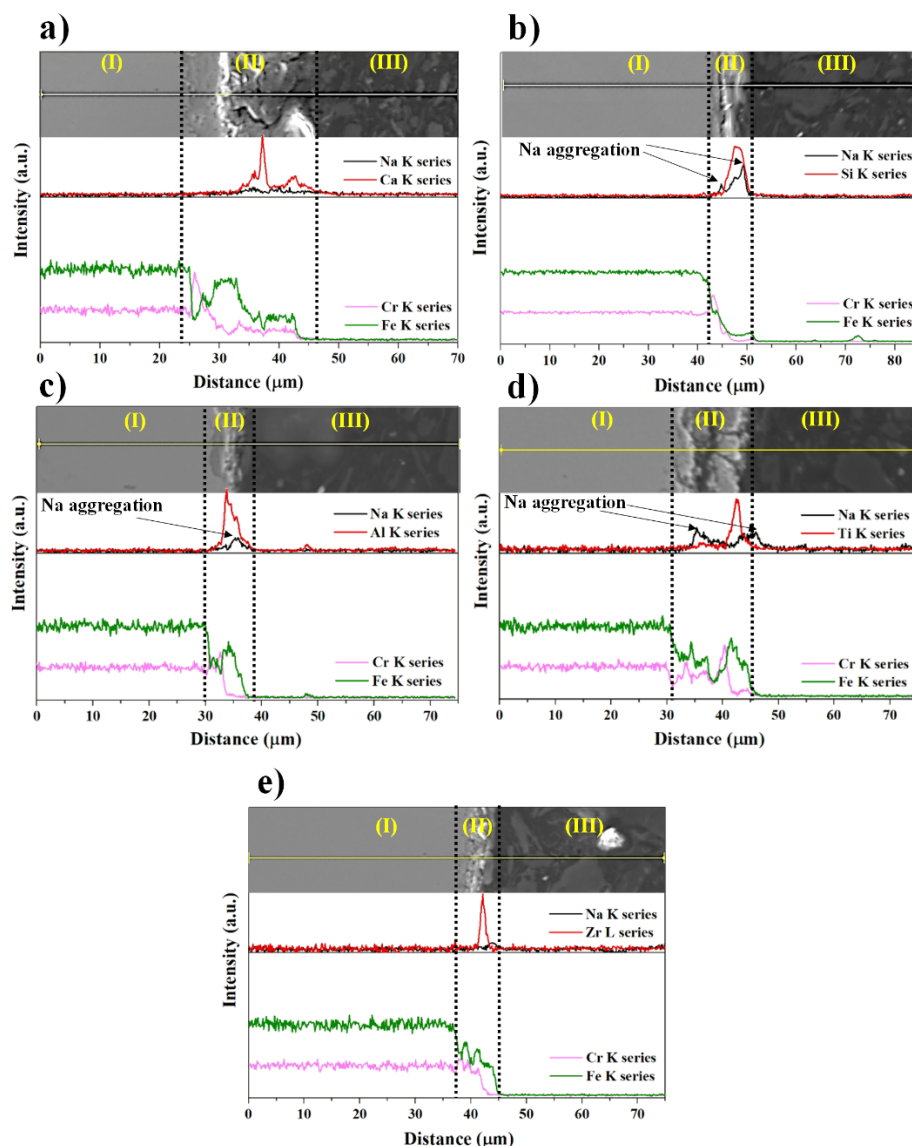


Figure 4-15. Cross-sectional analysis of the disc wear track after being lubricated by: (a) NBO-Cal; (b) NBO-Si; (c) NBO-Al₂O₃; (d) NBO-Ti; and (e) NBO-Zr. As marked in the images, region (I) is the steel base; region (II) is the tribofilm, and; region (III) is the mounting resin.

Among nanoparticles, SiO₂ nanoparticles perform the best lubrication and anti-oxidation as determined by friction coefficient, wear losses, and oxide scale thickness (**Figure 4-4** and **Figure 4-12b**). As previously reported^{66, 74}, the lubrication mechanisms of nanoparticles include the rolling effect, mending effect, protective film formation, and polishing effect. However, these mechanisms are only applicable in the case that the nanoparticles do not react or are consumed by the base lubricants. At elevated temperatures, the excellent performance of SiO₂ nanoparticles is due to the dissolution reaction between amorphous SiO₂ particles and sodium borate melt that results in the formation of sodium borosilicate melt. The formation of sodium borosilicate glass-melt on the steel is shown by EDS mapping analysis (**Figure 4-12b**). In addition, XRD analysis of the NBO-Si coating on steel after oxidation test reveals a prominent appearance of the broad hump peak which is characteristic for the amorphous glass (**Figure 4-14**, NBO-Si). Apart from the

broad hump peak, there is a detection of only Cr-oxide, Fe-Cr oxide, and other spinel oxides of Cr-Ni and Cr-Mn (**Figure 4-14**, NBO-Si) with no detection of sodium-containing reaction products. It can be due to the difference in the structural chemistry of the sodium borosilicate melt compared to sodium borate. The presence of the silica phase in the borosilicate network can slow down the ionic mobility of sodium due to an increase in the coordination number with more local constraints around sodium molecules²⁴⁹. Eventually, the formation of iron boroferrite is restricted and the sodium borosilicate melt acts as an efficient barrier to hinder the scale growth (**Figure 4-12b**). Apart from excellent anti-oxidation, the sodium borosilicate delivers outstanding friction and wear reduction which can be related to the formation of the thin glass tribofilm on the surface as demonstrated in **Figure 4-15**. During shearing, friction-induced heating can trigger the diffusion of sodium from the borosilicate melt to the oxide scale in the tribo-pair. EDS line scanning of the cross-section on the disc wear (**Figure 4-15b**) reveals an increase in the sodium intensity at the Cr-rich oxide/glass interface and on top of the glass film. This observation indicates the outward diffusion of sodium from the glass matrix which has been demonstrated previously²⁵⁰. Due to the diffusion of sodium, the borosilicate melt undergoes polymerization to form a densely rigid tribofilm above the oxide scale that limits the direct contact between the two sliding pairs (**Figure 4-15b**). The glass tribofilm with soft and easy-shearing characteristics can lower friction and wear (**Figure 4-4**)¹¹⁹.

Similar to SiO₂ nanoparticles, Al₂O₃ and ZrO₂ nanoparticles can incorporate with sodium borate melt to form the new melt with improved anti-oxidation performance. NBO-Al results in the formation of the melt with uniform distribution of Al (**Figure 4-12c**). However, there are some local areas at the coating/oxide interfaces with a strong intensity of Al which indicates the partial retention of the Al₂O₃ nanoparticles. It is believed that a fraction of Al₂O₃ nanoparticles are dissolved by sodium borate melt to form the sodium aluminoborate since Al₂O₃ can act as a network former²⁵¹. The incorporation of Al₂O₃ into the borate network increased the connectivity of the melt network²⁵² which reduces the oxygen diffusion to the metallic substrate. It thus improves the anti-oxidation performance. However, the presence of Al₂O₃ causes the transformation of tetrahedral ^[4]B (BO₄) into trigonal ^[3]B (BO₃) as a result of a decrease of the coordination number of O around Na atoms which leads to the separation of Na₂O phase^{253, 254}. Meanwhile, aluminum has a higher net formal charge compared to boron which is difficult to compensate with the remaining large and single valence Na⁺²⁵¹. Therefore, the sodium aluminoborate melt can preferably receive other smaller metallic cations with high valence from steel (e.g. Fe²⁺, Fe³⁺...) to compensate for the charge. Simultaneously, the Na₂O phase can combine with these metallic charges to form the reaction product floated within the melt (**Figure 4-12c**) and these particles can be NaFeO₂ as evidenced by the XRD analysis (**Figure 4-14**). Apart from the sodium-iron oxides, there is the presence of undissolved Al₂O₃, Fe₂O₃, and other reaction products. Since Al₂O₃ has very high hardness (**Table 4-1**), it acts as a third-body abrasive particle which increases friction and wear (**Figure 4-4**). During subsequent sliding, it is believed that the Al₂O₃ particles, Fe₂O₃ particles, and reaction products are locally compacted into the glaze above the chromium oxide scale which roughens the wear scar and results in the ploughing features

(**Figure 4-7g-h, Figure 4-8g-h**). The cross-sectional analysis of the disc wear track after being lubricated by NBO-Al (**Figure 4-15c**) proves the statement that shows a strong intensity signal of Al, Na, and Fe from the tribolayer above the Cr-rich oxide scale.

For ZrO₂ nanoparticles, a similar occurrence is observed with the formation of the melt containing a uniform distribution of Zr above the oxide scale (**Figure 4-12e**). The oxide scale is comprised of a Cr-rich oxide layer above the steel substrate and an aggregated layer of Fe-rich oxide particles at the bottom of the melt. It has been demonstrated that ZrO₂ is dissolved by the sodium-containing melt with the amount of dissolved ZrO₂ being proportional to the alkali content²⁵⁵. The presence of octahedral ⁶Zr (ZrO₆) species is dominant within the glass network as evidenced for silicate, borate, and borosilicate^{256, 257}. Similar to ⁴Al, the ⁶Zr preferably bonds to the ³B rather than ⁴B which can cause the shift between ⁴B and ³B during dissolution. Since octahedral ⁶Zr requires a small and high valent cation to completely charge balance the 6 bridging oxygen²⁵⁵, the presence of alkali (e.g. sodium) in sodium tetraborate is not sufficient that causes the diffusion of metallic cations (e.g. Fe²⁺ and Fe³⁺ ...) from the steel to the melt (**Figure 4-12e**). As a result, the nucleation of Fe-rich oxide particles is observed. However, XRD analysis indicates the presence of a dominant ZrO₂ phase from the coating after the oxidation test implying that only a fraction of ZrO₂ is dissolved in the sodium borate melt (**Figure 4-14**). Apart from the ZrO₂ phase, several phases of iron oxide, chromium oxide, iron-chromium oxide are also observed. Specifically, the Fe₃BO₆ phase is observed indicating the boriding effect. The boriding effect can cause the nucleation of the iron borate/iron boroferrite from the oxide toward the melt to form the loose layer as observed in **Figure 4-12e**.²⁵⁰ The oxide layer, in this case, is 14 μm thick which shows no significant improvement in anti-oxidation compared to NBO. However, from the analysis, it is also believed that the sodium cations in the sodium zircoborate are less mobile compared to sodium borate since all the sodium may be subjected to stabilize and balance the charge of ⁶Zr within the melt network. Therefore, no sodium-metallic oxides are found by XRD analysis, thus, showing less corrosion of sodium to the oxide scale. For the lubrication performance, NBO-Zr can substantially reduce the friction and wear compared to NBO. The lubrication mechanism can be closely related to the mending and rolling action of the remained nanoparticles at the sliding interfaces. The mending effect can be recognized by a formation of the compacted tribolayer above the steel substrate containing ZrO₂ nanoparticles and oxides (**Figure 4-15e**). It can be seen that a strong detection of Zr is observed within the Fe and Cr rich oxide layer. Only a little presence of sodium is detected above the Zr-rich layer which indicates the low reactivity of sodium in the melt. Meanwhile, the rolling action can be attributed to the presence of some areas with the aggregation of particles on the disc wear surface (**Figure 4-7n**). Since ZrO₂ nanoparticles have the moderate hardness (**Table 4-1**) which is harder than oxides (6.7 GPa)²⁵⁸, it can cause some smearing and micro-ploughing on the wear surface as evidenced clearly in **Figure 4-8n**.

On the other hand, NBO-Ti shows a different performance compared to other oxide nanoparticles. There is no dissolution of the TiO₂ nanoparticles to the sodium borate melt (**Figure 4-12d**) and the nanoparticles are clumped into the submicron-particles that were distributed locally within the melt. From the oxidation test, the oxide scale is found only ~7 μm below the coating, however,

there is a significant presence of Fe within the coating (**Figure 4-12d**). Since TiO₂ nanoparticles are not dissolved in the borate melt, it is believed that the oxidation process of the steel under the NBO-Ti coating is nearly similar to NBO-coated steel. In particular, XRD analysis of the NBO-Ti coating after oxidation at 930°C shows the presence of TiO₂ (anatase) and TiO₂ (rutile) phases with other iron borates/iron boroferrites (e.g. Fe₃BO₆, 4FeO.Fe₂O₃.B₂O₃, and Fe₃(BO₃)O₂) (**Figure 4-14**). There is also the existence of iron oxide, chromium oxide, iron-chromium spinel oxide, and sodium-iron oxide. Apart from the transformation of anatase to rutile which is common at above 600°C²⁵⁹, almost all the phase formations are similar to NBO coating. However, there is an additional presence of titanomagnetite (Fe_{2.75}O₄Ti_{0.25}) which can come from the thin layer of Fe and Ti above the Cr-rich oxide scale (**Figure 4-12d**). From the analysis, it can be concluded that the NBO-Ti shows no improvement in anti-oxidation and sodium-corrosion inhibition compared to NBO. However, the addition of TiO₂ nanoparticles can slightly improve the friction and wear of NBO (**Figure 4-4**) which can be due to the rolling action and mending effect⁸⁸. From the cross-sectional analysis of the disc wear track, the formation of a thick tribolayer (II) above the steel substrate is observed (**Figure 4-15d**). EDS line scanning analysis reveals the incorporation of TiO₂ nanoparticles within the iron-oxide and sodium-iron oxide layer to form the top layer. However, such top layer is not compacted and dense which can be evidenced by the detection of sodium near the iron-chromium oxide layer above the substrate (**Figure 4-15d**).

For the layered nanoparticles (h-BN and graphite nanoplates), the anti-oxidation and corrosion inhibition of NBO-BN and NBO-Gr were not much improved compared to NBO. Although the main oxide layer thicknesses are ~14 μm and ~8 μm for NBO-BN and NBO-Gr respectively, there is a significant presence of Fe within the coating. According to XRD analysis (**Figure 4-14**), these coatings show the formation of iron borate/iron boroferrite phases (e.g. Fe₃BO₆, 4FeO.Fe₂O₃.B₂O₃, and Fe₃(BO₃)O₂) together with the iron oxide, chromium oxide, iron-chromium spinel oxide, and sodium-iron oxide. Apart from the oxides which come from the natural oxidation of the steel, other reaction products between the melt and oxides are due to the high mobility of sodium and the boriding effect. It should be noted that there is no peak in the XRD analysis that shows the presence of (0 0 2) plane from the h-BN and graphite crystal structures. The non-existence of this peak implies that the h-BN and graphite are decomposed and no longer maintained their layered structure at 930°C. It is consistent with the thermal stability of graphite nanoplates which decompose from 800 to 900°C to produce the carbon residue²⁶⁰. Meanwhile, the decrease in size (to submicron/nanometer) of h-BN nanosheets can lead to lower thermal stability. A previous study by Zishan et al.¹¹⁰ has revealed that fine h-BN nanosheets can undergo oxidation to form boron oxide when conducting tribological testing at 800°C. It is further supported by Li et al.²⁴⁴ which shows the oxidation of the h-BN nanosheets starts at 800°C at which an intensity of the G band, representing the hexagonal layer, starts to decrease. At 850°C, severe oxidation of h-BN nanosheets to boron oxide is observed. Due to the decomposition of the nanoplates, the tribological performance is not improved.

A summary of the lubrication and anti-oxidation as well as the possible mechanisms of each lubricant additive at elevated temperature are shown in **Table 4-3**.

Table 4-3. Summary of the lubrication and anti-oxidation performance of each lubricant and their possible mechanisms.

Lubricant	Average COF	Wear disc (mm ³)	Wear ball (mm ³)	Oxide layer (μm)	Notes on oxidation	Mechanism of nanoparticles in lubrication improvement
No lub	0.46 ± 0.12	1.450 ± 0.340	0.273 ± 0.070	~ 65.0	-	-
NBO	0.27 ± 0.01	0.365 ± 0.055	0.023 ± 0.008	~ 20.0	Showing boriding effect and corrosion reactions between Na and oxides	-
NBO-Ca	0.280 ± 0.01	1.062 ± 0.155	0.036 ± 0.002	~ 17.0	No boriding effect and no corrosion reactions between Na and oxides due to the presence of a Ca-rich layer between the oxide scale and the melt	No improvement in friction and wear increment due to the presence of Ca-rich clumps from the reaction products of Ca and oxides on the sliding surfaces.
NBO-Si	0.151 ± 0.02	0.237 ± 0.052	0.010 ± 0.002	~ 4.0	No boriding effect and no corrosion reactions between Na and oxides due to the formation of sodium borosilicate melt	Significant improvement in friction and wear due to the formation of sodium borosilicate melt which has excellent lubricity.
NBO-Al	0.395 ± 0.06	0.608 ± 0.050	0.033 ± 0.007	~ 8.0	No boriding effect but showing the corrosion reactions between Na and oxides due to the formation of Na ₂ O phase by the presence of Al ₂ O ₃ phase.	Significant increase in friction and wear due to the presence of the remaining hard abrasive Al ₂ O ₃ nanoparticles that were sintered into large clumps at high temperatures.
NBO-Ti	0.243 ± 0.02	0.349 ± 0.074	0.020 ± 0.002	~ 7.0	Showing boriding effect and corrosion reactions between Na and oxides that alter the melt coating since TiO ₂ cannot be dissolved by sodium borate melt or cannot formed the	Slight improvement in friction and wear decrease moderately due to the rolling and mending effect of nano-size.

					protective layer.	
NBO-Zr	0.220 ± 0.02	0.279 ± 0.066	0.011 ± 0.004	~ 14.0	No boriding effect but showing corrosion reactions between Na and oxides due to the partial dissolution of ZrO ₂ in sodium borate that reduced the mobility of Na cations.	Moderate improvement in friction and wear decrease dramatically due to the rolling and mending effect of nano-size as well as the polishing effect from the ZrO ₂ phase.
NBO-hBN	0.286 ± 0.04	0.500 ± 0.087	0.024 ± 0.003	~14.0	Significant boriding effect and corrosion reactions between Na and oxides due to the decomposition of h-BN into B ₂ O ₃ .	Significant fluctuation in friction and wear increase moderately due to decomposition of h-BN into B ₂ O ₃ .
NBO-GnP	0.251 ± 0.02	1.125 ± 0.199	0.057 ± 0.010	~ 8.0	Significant boriding effect and corrosion reactions between Na and oxides due to the decomposition of GnP into carbon products.	Significant fluctuation in friction and wear increase dramatically due to the decomposition of GnP into carbon residues on the sliding surfaces.

4.3. Conclusions

A comprehensive study on the effect of nanoparticles and nanoplates on the high-temperature lubrication and anti-oxidation of sodium borate has been conducted at 930°C. Under testing conditions, the boriding effect occurred on the oxide scale under the presence of sodium borate melt that caused undesirable lubrication and anti-oxidation. The addition of nanoparticles can affect this process and result in different lubrication and anti-oxidation behavior. Several concluding remarks have been listed below:

- SiO₂ nanoparticles deliver the best anti-oxidation and lubrication performance among other nanoparticles and nanoplates which is due to the dissolution reaction between SiO₂ and sodium borate to form sodium borosilicate at the sliding interfaces. The boriding effect and the sodium corrosion under oxidation conditions are also inhibited.
- CaCO₃ nanoparticles show no much improvement in anti-oxidation and lubrication of the sodium borate melt, however, it can reduce the corrosion attack of the sodium to the oxide scale and the boriding effect of the iron oxide by the formation of the Ca-rich layer between the melt and the oxide.
- Al₂O₃ nanoparticles show good anti-oxidation performance due to the formation of sodium aluminoborate melt at high temperatures. However, the formation of this melt promotes the separation of Na₂O phase which causes the corrosion reaction to the oxides. In addition, the undissolved Al₂O₃ nanoparticles have a detrimental effect on the lubrication performance due to their high hardness.
- TiO₂ nanoparticles can not be dissolved into the sodium borate melt, thus, the oxidation processes of the steel under sodium borate + TiO₂ nanoparticles are not much different compared to sodium borate. The formation of iron boroferrite/iron borate and the sodium corrosion of oxides are still observed, although the lubrication performance is slightly improved in terms of wear and friction reduction.
- Fraction of ZrO₂ nanoparticles can be dissolved by sodium borate to form the zirconium-containing sodium borate melt under isothermal oxidation at 930°C. The resulted melt shows no much improvement in reducing the oxide scale thickness and the boriding effect of iron oxide but the corrosion of sodium to the oxide is limited due to the presence of octahedral ^[6]Zr species within the glass network. The lubrication of sodium borate is moderately improved by the rolling action and mending effect of the small size ZrO₂ nanoparticles.
- The layered nanoparticles including h-BN nanosheets and graphite nanoplates show no improvement in the anti-oxidation and lubrication performance of sodium borate which is due to the decomposition of these materials at elevated temperatures.

Chapter 5

Synthesis of the hybrid shell structure for the smart microcapsule from potential additives

*Part of this chapter content has been published in Small, 2020, 16, 2001978, <https://doi.org/10.1002/sml.202001978> and another part is under review by ACS Applied Nano Materials.

As demonstrated in the previous chapter (**Chapter 4**), achieving better performances in terms of friction, wear, and oxidation for the glass melt lubricants requires the addition of solid lubricant additives (e.g. nanoparticles) which are thermally stable to function at elevated temperatures. Typically, the formulation of the high-temperature lubricants is often carried out within the water-based fluid. The nanoparticles will be blended in the water-based lubricant which contains the melt precursor by the physical mixing approaches. However, such a formulation by this approach shows a challenge in the uncontrolled competitive and antagonistic interactions between different functional additives in the base fluid.^{16, 17} These interactions often reduce the functions of the additives while producing a large agglomeration and precipitation of the solid lubricant additives in the water-based fluid. Therefore, an addition of several surfactants and dispersants is often demanded, which are commonly synthetic organic compounds (potentially harmful to the environment), to ensure the dispersion stability and prevent the agglomeration of the nanoparticles.^{18, 19}

To resolve such issues, combining several additives into one formula is a promising approach since it can not only reduce the usage of surfactants or dispersants but also deliver all the functional additives to where they are needed²⁶¹. In this chapter, the fabrication of the thermally and mechanically stable shell for the smart microcapsules was conducted. In particular, the chemistry underpinning the formation of the hierarchical hybrid shell was investigated systematically. Additionally, the responsiveness and the thermal robustness of the hybrid shell were evaluated at elevated temperatures. Pickering emulsion-templated assembly, which is considered a simple and efficient approach^{203, 204}, was utilized to construct the micro-/nano-hierarchical shell with thermo-responsive characteristics. In this configuration, the nanoparticles are externally decorated on the shell wall. The incorporation of nanoparticles on the shell creates the densely packed layer making up the outer shell that contributes significantly to the enhanced strength, excellent impermeability, thermal stability, and chemical inertness of the so-called “colloidal capsule”^{203, 204}.

For potential applications of the microcapsule at elevated temperatures, silica (SiO₂) is a promising shell component because of its excellent thermomechanical stability and low permeability^{262, 263}. In addition, CaCO₃ nanoparticles, which are commonly used in conjunction with silica in high-temperature applications^{264, 265}, can be applied as the building blocks for the formation of the densely packed external shell. Such a combination can bring the thermo-responsive aspect to the designed colloidal capsule since CaCO₃ commonly reacts to SiO₂ at high temperatures to form the

calcium silicate compounds with interesting properties²⁶⁶. Furthermore, from the previous chapters (**Chapter 4**), the silica (SiO₂) phase shows great improvement in friction and wear reductions and anti-oxidation of sodium borate melt by the *in-situ* formation of sodium borosilicate. Meanwhile, CaCO₃ nanoparticles can inhibit the boriding effect while preventing the high-temperature reactions between sodium and oxide layer (**Chapter 4**). Such performance of CaCO₃ nanoparticles is expected to limit the corrosion of sodium and the formation of iron boroferrite when incorporated with sodium borosilicate. Therefore, the combination between SiO₂ and CaCO₃ is expected to deliver the multifunction to sodium borate melt in terms of improving the oxidation-inhibition, friction-reduction, and wear-alleviation at high temperatures.

5.1. Experimental details

5.1.1. Reagents

Tetraethyl orthosilicate (TEOS) (98%) (CAS [78-10-4]), anhydrous ethanol (100%) (CAS [64-17-5]), toluene (99.8%) (CAS [108-88-3]), and hexylamine (99%) (CAS [111-26-2]) were purchased from Sigma-Aldrich. Stearic acid-modified calcium carbonate nanoparticles (98%, 50 nm) were supplied from US Research Nanomaterials. All reagents were used without further purification unless otherwise noted.

5.1.2. Colloidal capsules synthesis

The synthesis process is described in **Figure 5-1**. In a typical procedure, stearic acid-coated calcium carbonate is suspended in toluene (10 ml) by ultrasonication for 10 minutes (Bandelin Ultrashall 1955, 6.5 mm tapered-tip, 100 W output) to ensure the uniform dispersion of nanoparticles within the continuous phase. To be able to stabilize the water-in-oil (W/O) emulsion system, the CaCO₃ nanoparticles with the stearic acid-modified surfaces is used since the high hydrophobicity of the as-obtained nanoparticles makes them preferable to stay at the water-oil interfaces²⁶⁷. Typically, particles with a contact angle in the range of 15° < θ < 90° can stabilize (oil-in-water) O/W emulsions, whilst particles with a contact angle in the range of 90° < θ < 165° can stabilize W/O emulsions²¹⁰. In addition, stearic acid is a common and inexpensive modifier that shows strong adsorption on the CaCO₃ surfaces by the formation of the chemisorbed monolayer followed by the several physisorbed connected with the initial monolayer through a weak interface link between the hydrocarbon chains in a tail-to-tail arrangement²⁶⁷. Subsequently, to form the water-in-oil emulsion, a certain volume of distilled water is added to the particle dispersion in toluene under high-shearing emulsification for 3 minutes (Ultra Turrax T-25, 22000 rpm). Next, 0.6 ml hexylamine (yielding the concentration in toluene of 50 mg/ml) is added to the emulsion under continuous magnetic stirring as the catalytic agent to assist in the formation of the silica shell at the water-toluene interface²¹⁵. The solution is then stirred gently at 300 rpm to facilitate the deposition of hexylamine at the water-oil interface. After 30 minutes, TEOS is added multiple times in dropwise fashion to the emulsion over 24 h periods, under constant stirring. Different synthesis conditions are conducted in this study by varying the CaCO₃ nanoparticle concentration (0.25g, 0.5g, 1g), the water-oil-ratio (0.25/10, 0.5/10, 1/10), the total amount of TEOS addition

(0.5ml, 1ml, 1.5ml), and the reaction duration (12 h, 24 h, 48 h). The resulting microcapsules are washed by acetone, then ethanol, and finally distilled water, before they are isolated by centrifugation.

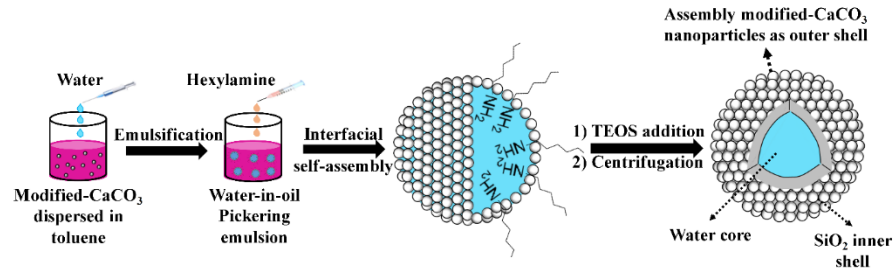


Figure 5-1. The synthesis process of colloidal capsules by Pickering emulsion-templated assembly using stearic acid-modified calcium carbonate nanoparticles.

5.1.3. Characterization methods

Light optical microscopy: Light optical microscopy was performed using Novel NMM-800/820 Universal Microscope to characterize the Pickering emulsion droplet formation. Typically, a drop of W/O Pickering emulsion is placed on a glass slide before placing it on the specimen stage. Transmitted light was used for droplet observation.

Thermal analysis: The laser flash method (LINSEIS LFA 1000) is used to evaluate the thermal insulation of the colloidal capsules. Typically, the thermal diffusivity of the mild carbon steel and capsule-coated mild carbon steel are measured in the 30-550°C temperature range under vacuum conditions. The mild carbon steel disc used in the measurement has a diameter of 11.2 mm and a thickness of 1.2 mm. Prior to the measurement, a certain amount of colloidal capsule is coated on the steel disc. **Figure 5-2a** shows the initial thickness of the coating was 0.25 ± 0.05 mm. Since the thickness of the coating remains approximately the same after heating at 550°C (**Figure 5-2b**), the thermal diffusivity is directly fitted by the combined model developed by Dusza et al.²⁶⁸ All measurements are repeated at least three times to confirm their reproducibility.

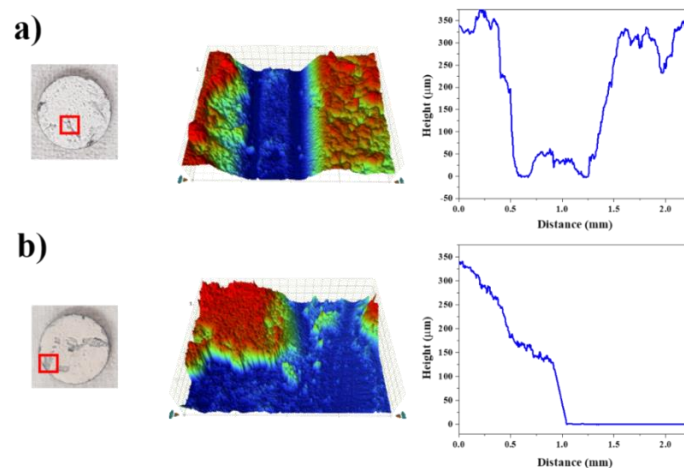


Figure 5-2. Capsule coating prepared on the mild carbon steel disc for thermal diffusivity measurement: a) Before thermal diffusivity test; and, b) After the thermal diffusivity test at 550°C.

5.2. Results and discussion

5.2.1. Characterization of stearic acid-modified CaCO₃ nanoparticles

TEM-BF (**Figure 5-3a**) reveals the cuboidal shape with the average size of 50 ± 10 nm of the stearic acid-modified CaCO₃ nanoparticles. High-resolution TEM is conducted to identify the crystalline pattern of the as-received nanoparticles which shows the main presence of the (2 1 1) plane from calcite with the *d*-spacing of 0.303 nm (**Figure 5-3b**). The identification of such phase is in agreement with the results obtained from the X-ray diffraction (XRD) spectrum (**Figure 5-3c**) which reveals the presence of several crystalline phases from the precipitated stearic acid-modified CaCO₃ nanoparticles. In particular, the modified CaCO₃ nanoparticles show the main characteristic planes of (1 1 0), (2 1 1), (2 2 2), (1 0 -1), (2 1 0), (2 0 0), (2 2 0), (3 3 2), (2 0 -1) and (2 1 -1), corresponding to 2θ value of 23.2° , 29.5° , 31.5° , 36.1° , 39.3° , 43.2° , 47.5° , 48.4° , 56.5° and 57.3° respectively. These peaks are assigned to the crystalline structure of calcite (JCPDS No. 05-586), which is a dominant phase in the structure of CaCO₃ nanoparticles. According to the chemistry analysis by Fourier-transform infrared spectroscopy (FTIR) (**Figure 5-3d**), the characteristic absorption band of ion carbonate (CO₃²⁻) asymmetric stretching (~ 1400 cm⁻¹) and the calcium stearate (COO⁻) (1575 cm⁻¹) are identified for the modified CaCO₃ nanoparticles, which is consistent with previous studies^{267, 269}. Besides, the absorption band at 885 cm⁻¹ can be related to the combination of the ion carbonate stretching and the vibration of the C-C bond from the stearic acid^{267, 269}.

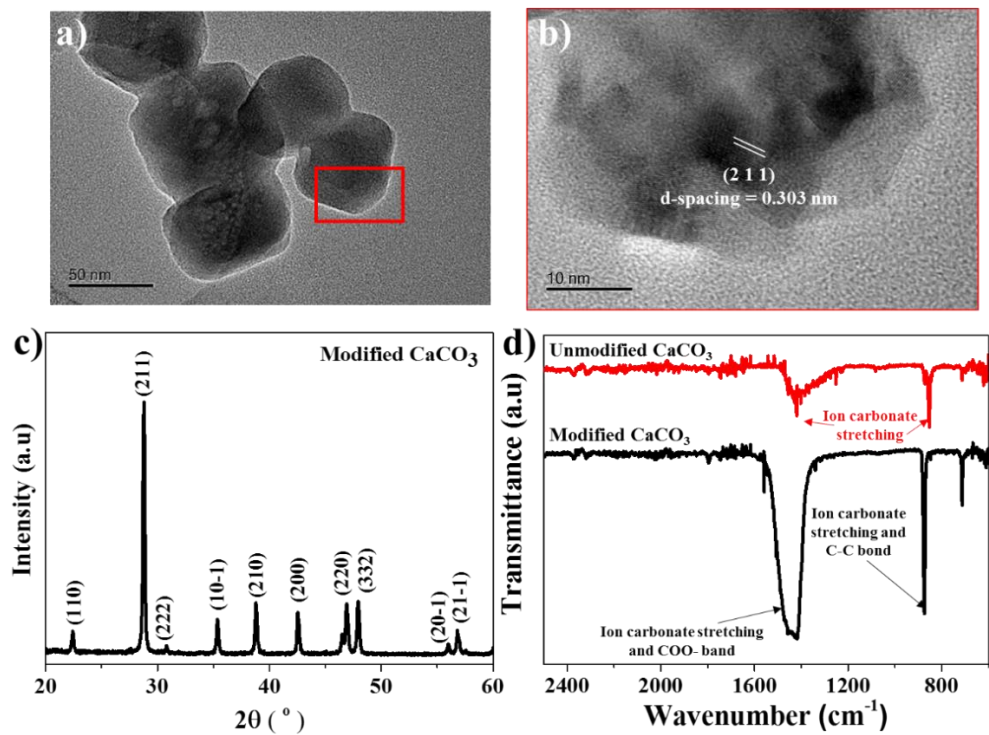


Figure 5-3. (a) Bright-field TEM image showing the CaCO₃ nanoparticles morphology; (b) High-resolution TEM image at high magnifications; (c) XRD analysis; and (d) FTIR analysis of the CaCO₃ nanoparticles.

5.2.2. Stability and droplet size distribution of W/O Pickering emulsion at different conditions

It has been well known that the amount of nanoparticles as stabilizing agents plays a pivotal role in determining the mean diameter, size distributions, and stability of the Pickering emulsion^{204, 208}. In this study, the size of the emulsion is adjusted by varying the amount of stearic-acid-coated CaCO₃ nanoparticles. As shown in **Figure 5-4a-Figure 5-4c**, the obtained droplets in W/O Pickering emulsions with varying concentrations of CaCO₃ nanoparticles exhibit a spherical shape with no coalescence occurs. The mean diameter and size distribution decrease slightly in response to the increase in the number of nanoparticles (**Figure 5-4a-Figure 5-4c**). In particular, the mean diameter of emulsion droplet increases from $5.15 \pm 2.68 \mu\text{m}$ to $7.50 \pm 2.10 \mu\text{m}$ when the amount of CaCO₃ nanoparticles decreases from 1 g to 0.25 g. The size distribution shifts to a smaller size when the number of nanoparticles increases from 0.25 g to 1 g (inset image in **Figure 5-4a-Figure 5-4c**) at a constant water-in-oil ratio of 1/10. It can be explained due to the large interfacial areas of emulsion droplets being adsorbed by a high amount of nanoparticles. The number of particles adsorbed at the droplet surface forms a densely packed monolayer, thus promoting the stabilization of the emulsion²⁷⁰.

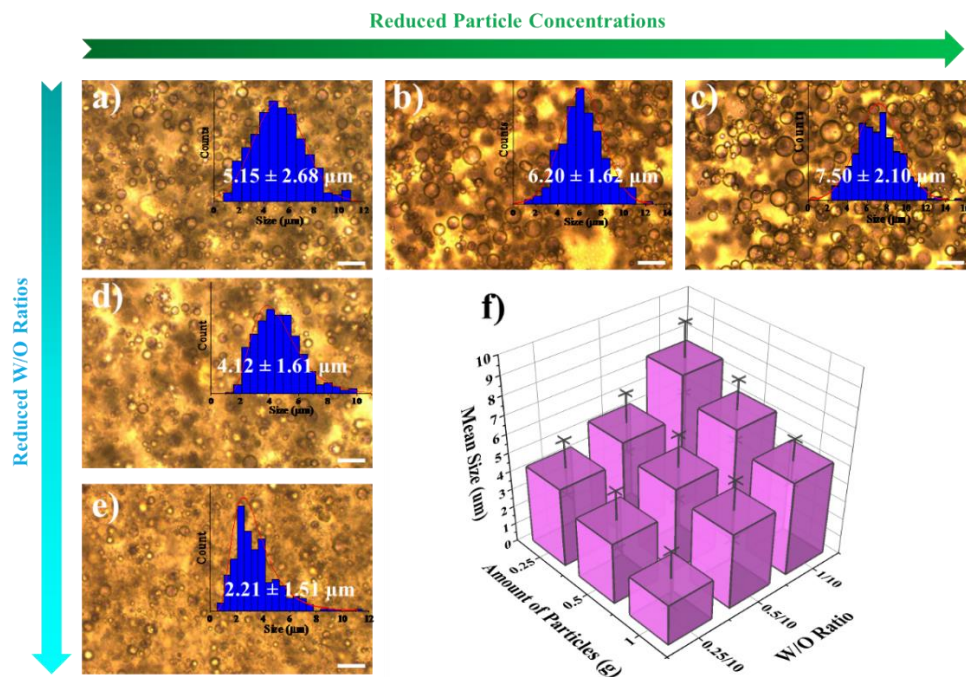


Figure 5-4. Optical observation of Pickering emulsion and droplet size distribution via the adjustment of the synthesized conditions. Variation of nanoparticles concentration with a W/O ratio of 1/10: (a) 1 g, (b) 0.5 g, and (c) 0.25 g CaCO₃ nanoparticles. Variation of W/O ratio with 1 g CaCO₃ nanoparticles: (d) 0.5/10, and (e) 0.25/10. (f) Summary of mean size of Pickering emulsion droplets via the adjustment of the amount of CaCO₃ nanoparticles and water-oil-ratio (W/O ratio).

Apart from the effect of nanoparticle concentration, the size distribution and mean diameter of emulsion droplets are also influenced by the volume fraction of the dispersed phase water or

termed as W/O ratio, as shown in **Figure 5-4a, Figure 5-4d, and Figure 5-4e**. It can be observed that the size of the water droplets rises from $2.21 \pm 1.51 \mu\text{m}$ to $5.15 \pm 2.68 \mu\text{m}$ with an increase in the volume fraction of the dispersed water phase from the W/O ratio of 0.25/10 to 1/10. The obtained results are consistent with other reports for Pickering emulsion²⁷¹. As previously demonstrated, the volume fraction of the droplets is an important factor in determining the close packing of the nanoparticles at the interfaces²⁷². When the volume fraction increases to a certain critical value with a constant nanoparticle concentration, droplets will coalesce together due to the close-packed layer of nanoparticles being distorted²⁷³. The summary of the resulted W/O droplet size distribution at different nanoparticle concentrations and W/O ratios is presented in **Figure 5-4f**.

5.2.3. The chemistry underpinning the formation of CaCO₃-decorated SiO₂ doubled-shell colloidal capsules

According to the mean diameter and the light optical analysis of the emulsion droplets (**Figure 5-4**), the coalescence does not occur and the emulsion droplets keep the original spheroid shape even at the lowest concentration of nanoparticles (0.25 g) and the highest water-oil-ratio (1/10), which indicates the excellent stability nature of Pickering emulsion. After the addition of *n*-hexylamine and TEOS as the catalyst and shell precursor, the sol-gel reaction takes place at the interface²¹⁵, generating the inner SiO₂ shell layer. In this study, the allowed hexylamine concentration is chosen at the optimum point (50 mg/ml) for the water-in-toluene emulsion system, which is favorable for both catalytic effect and emulsion stability requirements²⁷⁴.

The effects of nanoparticle concentrations and water-oil (w/o) ratios on the formation of the colloidal capsule are shown in **Figure 5-5a-Figure 5-5f**. The TEOS is added dropwise and kept constant at 1 ml for all synthesis conditions. As observed in **Figure 5-5a**, almost no capsule is formed and only fractured components are obtained when 0.25 g CaCO₃ nanoparticles are used (1/10 w/o ratio), despite a stable Pickering emulsion has been established (**Figure 5-5c**). This behavior is probably due to the generation of ethanol as a side-product of the sol-gel reaction. The presence of the junctions caused by the bridging effect of ethanol to the dispersed phase induces an effective inter-aggregate attraction. This junction-induced attraction is strong enough to drive phase separation between a dense network and a dilute micellar phase²⁷⁵, which detaches the stabilizing nanoparticles out of the interfacial areas (**Figure 5-5b**). The intact spherical shape of the colloidal capsule is observed when the amount of the nanoparticles reached 0.5 g (**Figure 5-5c**) and there is a trivial fracture in the case of 1g nanoparticles (**Figure 5-5e**). The concentration of nanoparticles has a strong influence on the size distribution of the water droplets in the toluene continuous phase (**Figure 5-4a-Figure 5-4c**), which is consistent with a previous study²⁰⁴. A further increase in the concentration of CaCO₃ nanoparticles can lead to the formation of a three-dimensional network of nanoparticles surrounding the droplets apart from the number of nanoparticles attached at the water-oil interfaces²⁷⁶, thereby promoting emulsion stabilization. It can be seen from the SEM observation in **Figure 5-5d and f** for the densely packed nanoparticles. The thickness of the external shell varies from 255.4 ± 20.8 to 460.2 ± 40.1 nm with an increase

of the CaCO_3 nanoparticles concentration in the Pickering emulsion. Such phenomena favorably prevent the coalescence between the emulsion droplets due to the presence of ethanol and result in the spheroid colloidal capsule being kept intact. Meanwhile, the silica inner shell thickness shows no change with varying the CaCO_3 nanoparticles concentration.

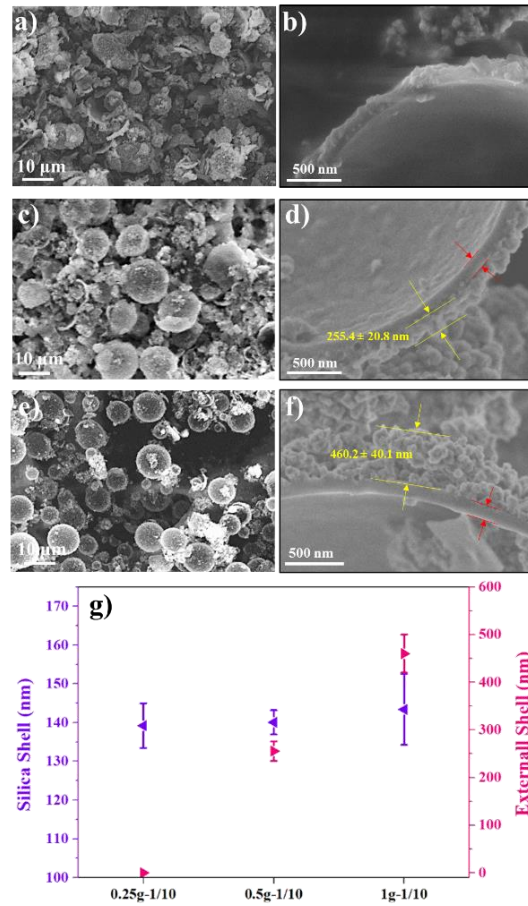


Figure 5-5. SEM images showing the effect of CaCO_3 nanoparticle concentration on the formation of the colloidal capsules: (a)-(b) 0.25 g, (c)-(d) 0.5 g, and (e)-(f) 1 g with a constant water-in-oil (w/o) ratio of 1/10 and TEOS addition of 1 ml; (g) Summary of the SiO_2 and densely external CaCO_3 nanoparticles shell thickness.

The w/o ratio shows an adverse influence on the colloidal capsule formation (**Figure 5-6a-Figure 5-6f**) with 1 g CaCO_3 nanoparticles. The intact spherical colloidal capsules are only obtained at the highest w/o ratio (1/10) (**Figure 5-6e**) although this condition shows the highest emulsion droplet size distribution compared with other w/o ratios (**Figure 5-4a, d, and e**). The w/o ratio of 0.25/10 can lead to the formation of the smaller size capsule although they are agglomerated with the presence of the tiny nanoparticle clusters and several shell-fractures (**Figure 5-6a**). Nevertheless, the formation of well-separated and larger size colloidal capsules appears in the case of a 0.5/10 w/o ratio (**Figure 5-6c**). During the shell formation, the hydrolysis of TEOS results in the formation of silicic acid that diffused and dissolved into the water core²¹⁵. At high water volume fraction, the silicic acid stays mainly at the water-oil interface, due to the attraction of the base n-hexylamine²¹⁶. However, the decrease of water volume fraction leads to a local increase in the

concentration of silicic acid in the reduced-size water droplet. The collision between these molecules by Brownian movements results in the nucleation of silica agglomerates and can potentially disturb the stability of the Pickering emulsion. The silica shell thickness of the different w/o ratios is presented in **Figure 5-6g** which is measured from **Figure 5-6b, d, and f**. It remains unchanged at ~140 nm which implies a negligible effect of the w/o ratio on the formation of the silica shell.

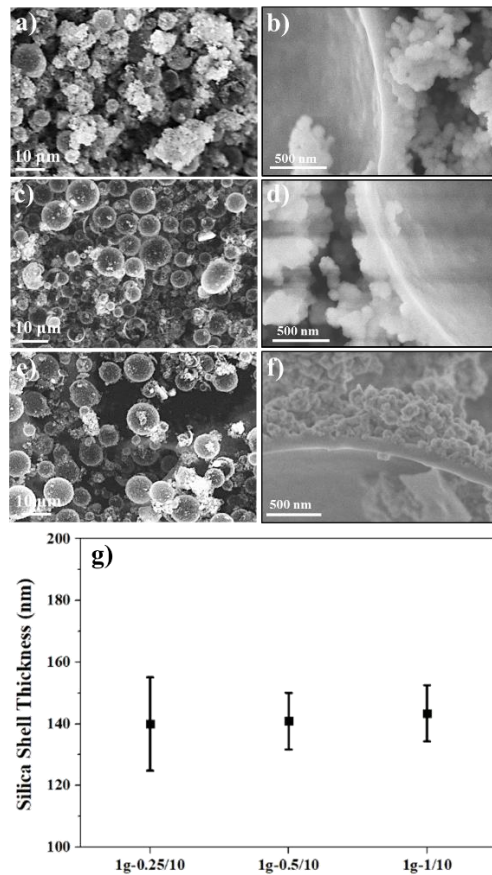


Figure 5-6. SEM images showing the effect of CaCO₃ nanoparticle concentration on the formation of the colloidal capsules: (a)-(b) 0.25 g, (c)-(d) 0.5 g, and (e)-(f) 1 g with a constant water-in-oil (w/o) ratio of 1/10 and TEOS addition of 1 ml; (g) Summary of the SiO₂ and densely external CaCO₃ nanoparticles shell thickness.

As shown in **Figure 5-7**, the concentration of TEOS plays an indispensable role in the successful formation of the colloidal capsule. In view of the mechanical properties, the fraction of broken capsules increases when the silica shell thickness decreases. Low TEOS amounts (0.5 ml, **Figure 5-7a**) results in significant fractures and only a small number of intact capsules remain. By increasing the TEOS volume to 1 ml, it results in fewer fractures and less capsule defect (**Figure 5-7c**). However, excessive TEOS addition (1.5 ml) causes more fractures to the obtained capsules (**Figure 5-7e**). The resulted silica shell thickness at different TEOS volumes is presented in **Figure 5-7g** which is measured from **Figure 5-7b, d, and f**. The poor particle formation at low TEOS addition is probably due to the reduced silica shell thickness (98 ± 4 nm) (**Figure 5-7g**), which is vulnerable to breakage during capsule collection under stirring and centrifugation. Meanwhile, the

highest amount of the TEOS addition (1.5 ml) leads to more fractures despite the thickest shell formation (180 ± 8 nm, **Figure 5-7g**) which is due to an increase in ethanol generated during the sol-gel reaction. Since ethanol acts as a co-solvent, it preferably co-solubilizes water, partially hydrolyzed TEOS, and non-hydrolyzed TEOS at W/O interfaces. This can cause the formation of the silica agglomerates and non-uniform shell morphology due to an increasing amount of solubilized water in the toluene²¹⁶. The results indicate controllability over the shell thickness of the colloidal capsules by changing the concentration of the TEOS.

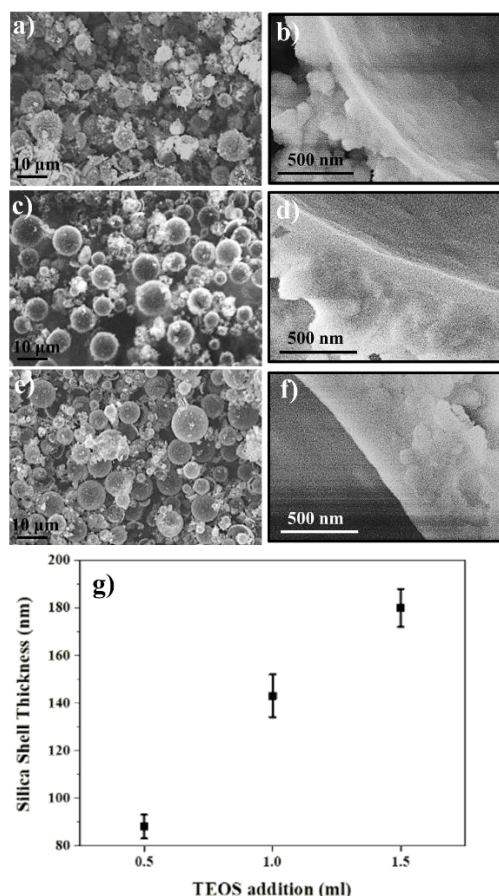


Figure 5-7. SEM images showing the effect of TEOS concentration on the formation of the colloidal capsule: (a)-(b) 0.5 ml; (c)-(d) 1 ml; (e)-(f) 1.5 ml with 1 g of CaCO_3 and a w/o ratio of 1/10; (g) The variation of silica shell thickness under different TEOS additions.

Shown in **Figure 5-8a** are the colloidal capsules obtained after 12 h of sol-gel reaction. They appear non-rigid and not fully developed. This indicates that the water droplet is not fully enveloped by the silica at this stage of the reaction with the shell thickness is around 105 ± 6 nm (**Figure 5-8b**). In contrast, the colloidal capsules, which are isolated after a longer period (24 h), show a complete shell formation after drying (**Figure 5-8c**). The silica shell thickness measurement (**Figure 5-8g**), calculated from **Figure 5-8b, d, and f**, shows a gradual increase to 140 ± 10 nm in this case (**Figure 5-8g**) which can be related to an increase in TEOS conversion. However, further increase of the reaction duration to 48 h shows no change in the colloidal capsule

formation (**Figure 5-8e**), and the shell thickness (145 ± 8 nm) is approximately equal to the results obtained after 24 h reaction (**Figure 5-8g**).

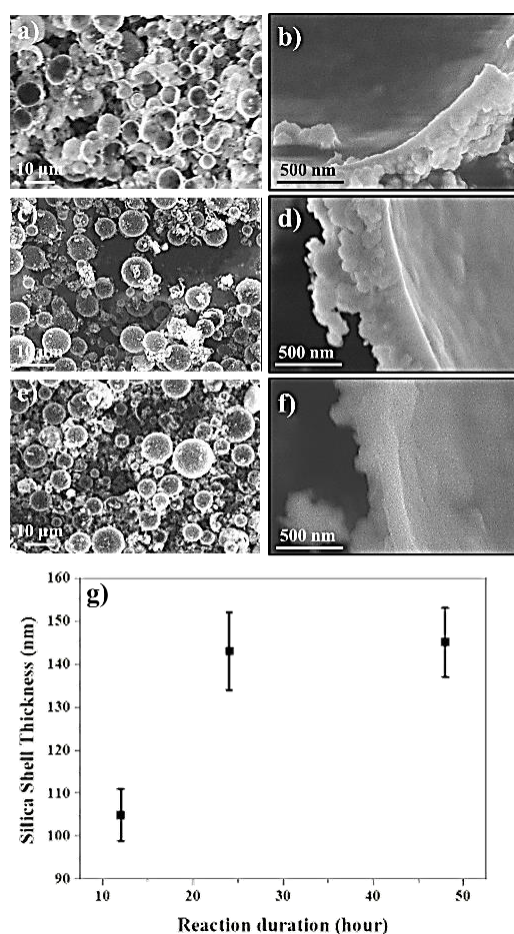


Figure 5-8. SEM images showing the effect of the reaction duration on the formation of the colloidal capsule: (a)-(b) 12 h; (c)-(d) 24 h; (e)-(f) 48 h with 1 g of CaCO_3 , 1/10 w/o ratio, and 1 ml TEOS addition; (g) The silica shell thickness under different reaction durations.

During the shell formation, the silica shell grows from the inside (water phase) to the outside (toluene phase)²¹⁵. As a consequence, the water has to diffuse through the growing shell to participate in the hydrolyzed reactions of TEOS. Initially, all the reactants are in contact with each other at the w/o interface and the hydrolysis and condensation of TEOS occur rapidly to form the thin silica shell. Ethanol, as a side product of such reactions, promotes the diffusion of water from the water phase through the thin silica shell to the toluene phase due to its co-solubilizing effect²⁷⁷. It thus results in the thicker silica shell formation and the complete colloidal capsule formation over a certain period. When the silica shell reaches a certain thickness, the shell growth rate decreases with time and stops as the time constant since the diffusion of water and ethanol to the locus of the reaction increases significantly upon increasing shell thickness.

Based on the obtained results, the optimum condition for the intact formation and defect-free colloidal capsules is 1 g CaCO_3 nanoparticles, 1/10 w/o ratio, a total addition of 1 ml TEOS, and the reaction duration of 24 h. From the electron microscopy examination, a mean colloidal capsule

diameter obtained at such optimum conditions is $7.5 \pm 1.8 \mu\text{m}$ (**Figure 5-9**). This is slightly larger than the water droplets observed in the inverse Pickering emulsion system of the synthesized conditions ($5.15 \pm 2.68 \mu\text{m}$, **Figure 5-4a**). The slight increase of the colloidal capsule size compared to the Pickering emulsion droplets under the same conditions can be due to the presence of *n*-hexylamine.

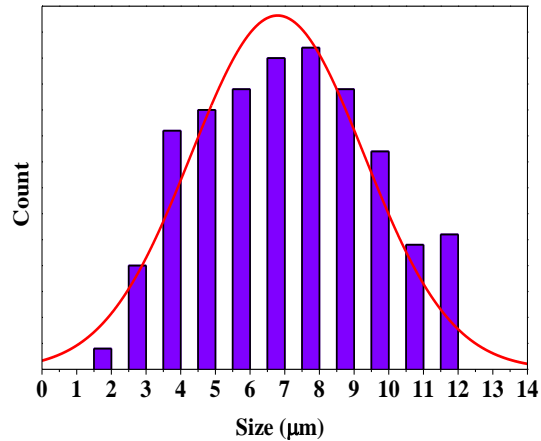


Figure 5-9. Size distribution of the hybrid $\text{CaCO}_3\text{-SiO}_2$ colloidal capsules obtained at the optimum synthesizing conditions.

Hexylamine can affect the wettability of stabilizing particles and in turn the stability of the Pickering emulsion. The three-phase contact angle (θ) of the stabilizing particles (**Figure 5-10**) at the water-oil interface is described mathematically by Young's equation²⁰⁶ and it represents the wettability of the stabilizing particles:

$$\cos \theta = \frac{\gamma_{po} - \gamma_{pw}}{\gamma_{ow}} \quad (7-1)$$

In equation (i), γ represents the interfacial tension between oil (o), water (w), and particle (p). The addition of hexylamine can decrease the interfacial tension between the water and toluene since it plays a similar role as a surfactant due to its amphiphilic effect²¹⁵. As the interfacial tension between water and toluene (γ_{ow}) decreases, the $\cos \theta$ in equation (7-1) increases accordingly which leads to an increase in the three-phase contact angle (θ). It may affect negatively the Pickering emulsion stability at an excessive concentration of *n*-hexylamine due to the formation of a stable colloidal CaCO_3 in toluene. In that case, the particles prefer to stay in the toluene phase rather than at the water-oil interface, thus it is not suited to stabilize the Pickering emulsion.

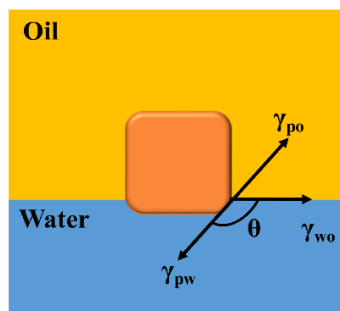


Figure 5-10. Schematic representation of the stearic acid-modified CaCO_3 nanoparticles at the water-oil interface.

5.2.4. Chemistry characterization of the CaCO_3 -decorated SiO_2 doubled-shell colloidal capsules

The optimized synthesis conditions of Figure 2c are chosen to prepare the intact colloidal capsules for further evaluation. Fourier-transform infrared spectroscopy (FTIR) reveals the presence of both SiO_2 and stearic acid-modified CaCO_3 in the colloidal capsule (**Figure 5-11a**). The FTIR spectrum shows the characteristic absorption band of carbonate (CO_3^{2-}) asymmetric stretching at 1400 cm^{-1} and the stearate (COO^-) at 1575 cm^{-1} .^{267, 269} The presence of an absorption band at 1085 cm^{-1} for the Si-O bond stretching in the colloidal capsules, reveals the existence of stoichiometric silicon dioxide.²⁷⁸ X-ray diffraction (XRD) spectrum reveals the dominant of calcite phases (COD ID 1010928) in CaCO_3 , while silica hollow sphere exhibits the amorphous nature (**Figure 5-11b**). For the colloidal capsule, there is the dominant presence of the calcite phases, while the broad hump of amorphous silica is quite ambiguous (**Figure 5-11b**). However, apart from the indications of calcite and silica, there are three new peaks at 2θ of 32.6° , 37.7° and 44.1° which may correspond to (3 0 2), (4 0 0) and (1 4 2) reflections in the crystalline structure of dicalcium silicate Ca_2SiO_5 (COD ID 9011376), which suggests the formation of a new compound within the shell (**Figure 5-11b**).

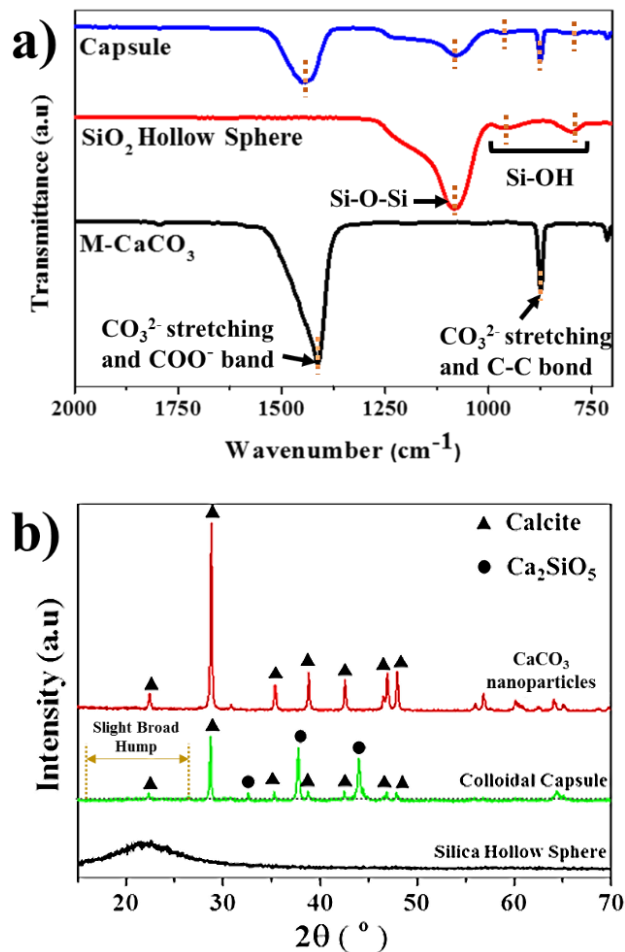


Figure 5-11. (a) FT-IR spectra and (b) XRD analysis of stearic acid-modified CaCO₃ nanoparticles, SiO₂, and as-obtained colloidal capsule.

The obtained colloidal capsules at the optimal conditions are intact with negligible fractures. The external morphology investigation by SEM shows that these colloidal capsules are spherical with a rough outer shell surface due to the agglomeration of numerous 50 nm nanoparticles (Figure **Figure 5-12f**). TEM analysis in **Figure 5-12g** reveals the close-packed assembly of the dense multilayer of nanoparticles on the inner shell with domains that display the main packing of the cubic shape of Λ_0 lattice to form the outer shell. It is quite different from the common packing at the w/o interface of cuboidal nanoparticles that favors both hexagonal and cubic packing of Λ_1 and Λ_0 lattice.^{207, 279} This is probably due to the number of nanoparticles that favor the multi-stacked layer on the shell and make it difficult to observe the Λ_1 lattice. The cross-sectional observation in **Figure 5-12c** reveals the distinct formation of the two shell layers and the hollow spherical structure of the hybrid colloidal capsules. It can be seen that the inner surface of the shell is quite rough **Figure 5-12c** which was attributed to the presence of numerous CaCO₃ nanoparticles at the w/o interfaces that formed the multilayer self-assembly.²⁸⁰ EDS mapping analysis confirms that the thin inner shell is silica and the densely packed external shell comprises mainly CaCO₃.

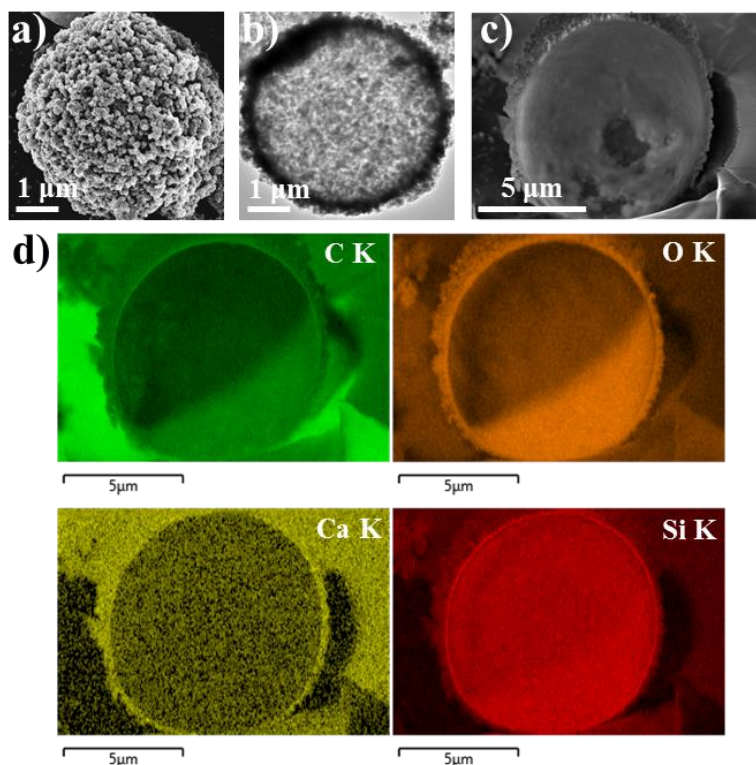


Figure 5-12. (a) Secondary electron (SE) image of the external morphology of the colloidal capsule; (b) TEM-BF image showing the hollow interior structure and the packing assembly of the nanoparticles on the inner shell; (c) SE image of a sectioned colloidal capsule; and (d) EDS mapping analysis of the elemental distribution within the hybrid shell structure.

To investigate the chemistry between the compounds within the hybrid colloidal capsules, XPS is utilized to identify the bonding configurations. Prior to the XPS analysis, the capsule powder is ground into fine grains to ensure there are a fraction of shell fragments with their cross-section aligned perpendicular to the beam analysis. From the deconvolution of Si 2p, Ca 2p, and C 1s (**Figure 5-13**), there are no new peaks or the shifting of the deconvoluted peaks which indicates that there may be no chemical reactions occurred, and the CaCO_3 nanoparticles are physically adsorbed or attached to the SiO_2 inner shell. Further analysis of the O 1s spectra is conducted to examine the bonding formation since the O 1s from the XPS analysis often possess a wealth of information on the bonding formation between the compounds. The deconvolution of O 1s in **Figure 5-13** suggests the dominant presence of the peak at 531-532 eV, which is due to the Si-O-Si bond.²⁸¹ Another peak at 531.9 eV relates to the CO_3^{2-} , COO^- and the water from moisture (**Figure 5-13**).^{282, 283} However, there is a slight emergence of the peak at 530 eV after the deconvolution of the O 1s spectrum (**Figure 5-13**). This peak corresponds to the Ca-O-Si bonding configuration²⁸⁴ which suggests the chemical bonding formation between CaCO_3 nanoparticles and SiO_2 shell.

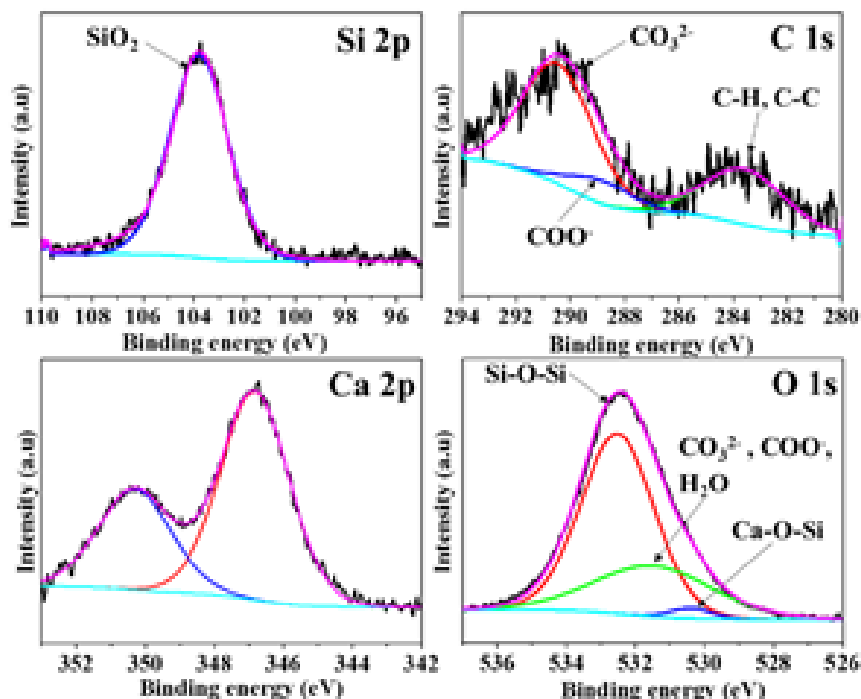


Figure 5-13. XPS survey spectrum of SiO₂, CaCO₃ nanoparticles, and the hybrid CaCO₃-SiO₂ colloidal capsules; (d) XPS detail analysis and the deconvolution of these spectra of Si 2p, C 1s, Ca 2p, and O 1s from the hybrid colloidal capsule.

5.2.5. Thermal analysis of the hybrid CaCO₃-decorated SiO₂ doubled-shell colloidal capsules at elevated temperatures

Thermogravimetric Analysis (TGA) and Derivative Thermogravimetry (DTG) analysis of the capsule are performed under nitrogen atmosphere and the results are shown in **Figure 5-14a-Figure 5-14b** as a function of temperature. There is a gradual decrease of the mass in the temperature range of 100-500°C in the TGA curve (**Figure 5-14a**). It corresponds to the first two peaks in the derivative thermogravimetry (TDG) at 209°C and 400-480°C (**Figure 5-14b**). The first peak at 209°C in DTG may be due to the complete water evaporation from the core of the capsules, while the second peak at 400-480°C indicates the decomposition of the stearic acid at the outer shell. Differential Scanning Calorimetry (DSC) curve (**Figure 5-14c**) confirms the stearic acid degradation by the presence of an exothermic hump at 405°C.²⁸⁵ The significant mass changes are observed from 500°C and 750°C (TGA in Figure 3a). As stated by Gabal et al.²⁸⁶, pure calcite (CaCO₃) starts to decompose at 750°C. However, DTG confirms the two significant mass losses at 566°C and 710°C (Figure 3a). These peaks can probably be due to the decarbonization from CaCO₃ nanoparticles although they appeared at much lower temperatures than that of pure calcite decompositions.

From the previous literature, the appearance of the SiO₂ phase accelerates the process of CaCO₃ decomposition at a lower temperature due to the spacing effect²⁸⁷ from SiO₂. Significantly, the presence of SiO₂ in the decomposition process of CaCO₃ can cause the formation of silicate phases even at temperatures below 1000°C²⁸⁸. Therefore, the first significant decomposition peak at 566°C

(Figure 5-14b) is due to the reaction between CaCO₃ and SiO₂, while another sharp and distinct peak at 710°C (Figure 5-14b) is related to the decomposition of an excess of CaCO₃ nanoparticles. These reactions occur as suggested by the continuous decrease of the heat flow in DSC until reaching a dip at 720°C (Figure 5-14c)²⁶⁶. Following these occurrences, the fusion between the remaining CaO phase (from the decomposition of excessive CaCO₃ at 710°C) and the remaining SiO₂ phase is also suggested by causing the sharp increase in heat flow which indicates the emergence of exothermic reactions from 750°C to 900°C (Figure 5-14c).²⁸⁹

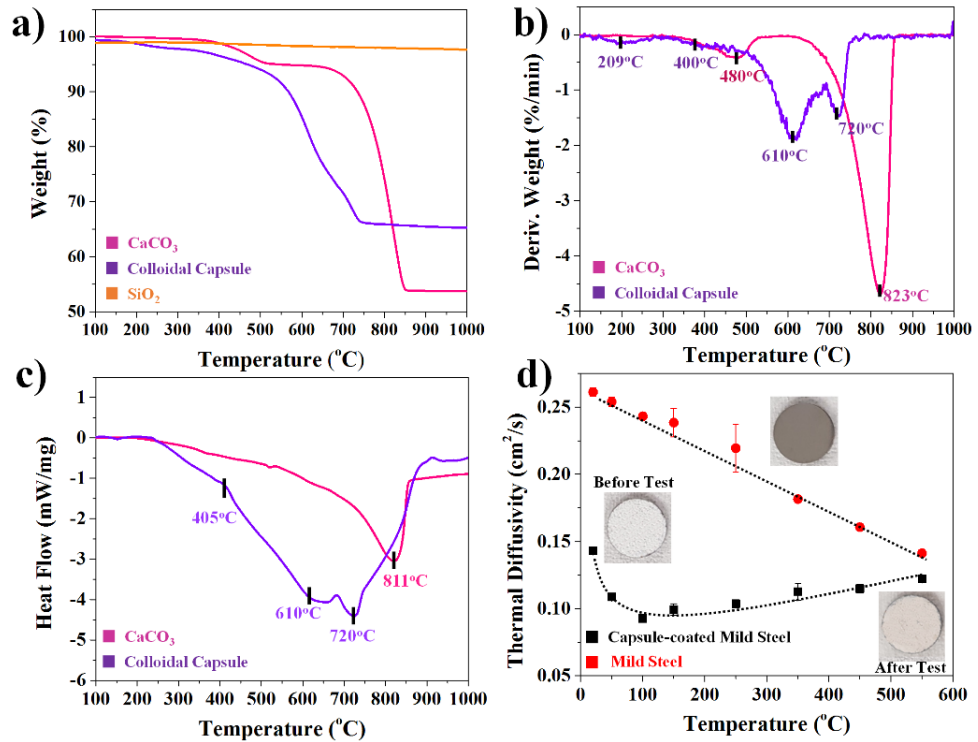
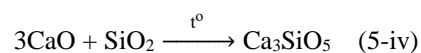
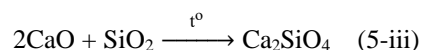
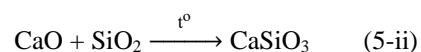


Figure 5-14. (a) Thermogravimetric Analysis (TGA) of the colloidal capsule, CaCO₃ nanoparticles, and SiO₂; (b) Derivative Thermogravimetry (DTG) of the colloidal capsule and CaCO₃ nanoparticles; (c) Differential Scanning Calorimetry (DSC) of the colloidal capsule and CaCO₃ nanoparticles; and (d) Thermal diffusivity measurement of the mild carbon steel and capsule-coated mild carbon steel.

The formation of several types of calcium silicate can be referred to the equations (5-i), (5-ii), (5-iii), and (5-iv)²⁶⁶. Since the decomposition of CaCO₃ is a highly endothermic reaction, the overall formation process of calcium silicate compounds from CaCO₃ and SiO₂ remains endothermic (Figure 5-14c, 550-750°C)²⁶⁶. Another distinct peak of the decomposition in DTG at 710°C (Figure 5-14b) with the associated endothermic peak at 728°C in DSC (Figure 5-14c) is related to the decarbonization of the excessive CaCO₃ nanoparticles that adhere to the outer shell. The exothermic peak at 973°C suggests the complete fusion between the formed CaO and the SiO₂ shell to form calcium silicate compounds²⁸⁹.





To evaluate the insulation effect of the colloidal capsule, thermal diffusivity is measured (**Figure 5-14d**). From room temperature to 100°C, the thermal diffusivity of capsule-coated mild steel decreased sharply (0.15-0.1 cm²/s) and is significantly lower than that of mild steel (0.26-0.24 cm²/s) (**Figure 5-14d**). It can be due to the evaporation of the water core at these temperatures that results in the hollow interior structure with a significant decrease in thermal conductivity. When the temperature increases, the thermal diffusivity of mild steel declines dramatically which is consistent with other reports.²⁹⁰ Meanwhile, the capsule-coated mild steel shows the opposite trend of a steady increase but the diffusivity is still significantly lower than the mild steel between 350 and 550°C (**Figure 5-14d**). Therefore, the colloidal capsules with hollow interior structures after water evaporation are expected to have an insulative effect.

5.3. Conclusions

A robust means of synthesizing the hybrid CaCO₃-decorated SiO₂ doubled-shell colloidal capsules is proposed via Pickering emulsion-templated assembly followed by interfacial sol-gel microencapsulation process. The aim of this chapter focuses on optimizing the synthesis conditions and investigating the formation mechanism of the hybrid colloidal capsules. Moreover, comprehensive characterizations have been conducted to elucidate the chemistry underpinning the formation processes and to evaluate the thermal robustness of the hybrid microcapsules. Several concluding remarks are pointed out as follow:

- The concentration of CaCO₃ nanoparticles, water to oil (w/o) ratio, TEOS addition, and the reaction duration play a pivotal role in the successful formation of CaCO₃-hybridized SiO₂ doubled-shell colloidal capsules.
- The concentration of CaCO₃ and the w/o ratio contribute significantly to the emulsion stability.
- The formation of the mechanically strong doubled-shell, which prevents the colloidal capsules from premature rupture, depends mainly on the TEOS addition and the reaction duration.
- The presence of the dicalcium silicate (Ca₂SiO₅) phase within the as-prepared microcapsule indicates the chemical reactions between CaCO₃ nanoparticles and SiO₂ during the sol-gel processes. The underlying mechanism of this phase formation and its role will be elucidated in the next chapter.

Chapter 6

Thermo-mechanical properties of the hybrid shell structure elucidated by novel *in-situ* analytical techniques

*Part of this chapter content has been published in Small, 2020, 16, 2001978, <https://doi.org/10.1002/sml.202001978>, and another part published in The Journal of Physical Chemistry C, 2021 125 (31), 17462-17473, <https://doi.org/10.1021/acs.jpcc.1c04680>.

The focus of this chapter aims to explore the mechanical and thermo-mechanical behavior of the well-defined hybrid CaCO₃-decorated SiO₂ doubled-shell colloidal capsules obtained from **Chapter 5**.

Firstly, the mechanical properties of the individual hybrid CaCO₃-decorated SiO₂ doubled-shell colloidal capsules will be characterized in comparison with SiO₂ single-shell hollow sphere to evaluate the effect of incorporating nanoparticles on the SiO₂ shell. In addition, the underlying mechanism by which nanoparticles modify the inner shell properties will be explored through a nanoparticles/shell interfacial analysis at the nanoscale. Despite a large number of study reports on the contribution of nanoparticles to the improved mechanical properties of the colloidal capsule,^{203, 204} the intrinsic interfacial structure between the modified nanoparticle building blocks and the inner shell has not been investigated in detail. No previous study provides a deep insight into the bonding formation between the nanoparticles and the inner shell surface to understand how nanoparticles modify the shell properties during the shell forming process. This information is significantly important to understand the binding nature of the densely packed nanoparticles onto the inner shell, which determines the distinct mechanical properties of the whole colloidal capsule.

To achieve the first goal of studying the intrinsic effect of nanoparticles on the mechanical properties of the developed colloidal capsule, *in-situ* mechanical compression on Transmission Electron Microscope (TEM) and Aberration-Corrected Scanning Transmission Microscope (AC-STEM) has been combined. *In-situ* transmission electron microscope (TEM) mechanical compression has been well-recognized as a high spatial resolution method to determine the mechanical deformation of the single micro-/nano-particle. Such a technique allows direct internal observation of the deformation of the sub-micrometer thin shells with quantitative recordings of nano/micro-mechanical properties²³¹. Meanwhile, Aberration Corrected Scanning Transmission Microscopy (AC-STEM) is a powerful technique for studying the interfacial chemistry between different phases in the hierarchical nano-/micro-structure with atomic resolution²⁹¹. The combination between these techniques has not been conducted before in studying the hybrid multi-shell microcapsule systems and it will be implemented in this chapter for the first time.

Secondly, the thermo-mechanical properties of the individual hybrid CaCO₃-decorated SiO₂ doubled-shell colloidal capsules will also be investigated after annealed the colloidal capsule at different temperatures. In particular, how the hybrid CaCO₃-SiO₂ doubled-shell adjusts its

mechanical properties at different temperatures will be elucidated. Moreover, the underlying mechanism by which the hybrid microcapsule modifies their mechanical properties and their morphologies via temperature will be demonstrated simultaneously.

It is hypothesized that the migration of the elements between the shell interfaces may result in the formation of new compounds and the structural transformation that can modify significantly the shell properties at high temperatures.²⁹² Tracking such elemental movement at a small length scale (micro-/nano-metre) is significantly important since it enlightens the fundamentals behind the high-temperature reactions and structural transformations in the hybrid multi-shell microcapsules. This information can advance the fabrication of unusual nanoscale systems and novel hybrid/composite solid-state materials for harsh heating conditions.^{293, 294}

Therefore, to achieve the second goal, the author has initially developed a new multi-modal correlative microscopy that combines focused ion beam and scanning electron microscopy (FIB-SEM), time-of-flight-secondary ion mass spectrometry (TOF-SIMS), and microelectromechanical systems (MEMS)-based microheater to directly visualize real-time the solid-state chemical reactions at submicron-length scale. To the best of our knowledge, such a multi-modal correlative system has not been reported and utilized before. The main purposes of utilizing TOF-SIMS are due to their inherent working mechanism that avoids the interference of infrared radiation at elevated temperatures.²⁹⁵⁻²⁹⁷ Besides, the interaction volume, and the plural scattering effect issues that affect traditional EDS and energy-filtered electron loss analysis at high voltages in SEM/TEM are also avoided.^{298, 299}

Specifically, the thermo-mechanical properties of the individual hybrid colloidal capsule after annealed at different temperatures will be firstly evaluated by *in-situ* TEM mechanical compression. Subsequently, the underlying mechanism of the changes in the mechanical behavior after annealed at different temperatures will be unraveled by utilizing the proposed methodology. Other *in-situ* analytical techniques will also be applied to validate the efficiency and reliability of the proposed technique to visualize in-operando the solid-state chemical reactions at elevated temperatures.

6.1. Experimental details

6.1.1. Reagents

Cetyl trimethyl ammonium bromide (CTAB) (100%) (CAS [57-09-0]), octadecane (99 + %) (CAS [593-45-3]) and ammonia solution (25 wt.%) (CAS [1336-21-6]) were obtained from Chem-Supply. All reagents were used without further purification unless otherwise noted.

6.1.2. Preparation of SiO₂ hollow sphere as a reference

Silica hollow spheres are prepared according to the method developed by Liang et al³⁰⁰ and used as the reference material. In a typical procedure, 3ml of TEOS + 3 ml of octadecane are placed in a 100 ml beaker under gentle stirring. Subsequently, CTAB (0.123 g), deionized water (25 ml),

and anhydrous ethanol (17.7 ml) are added to the beaker in turn. The mixture is then stirred at 700 rpm for 30 minutes before it is homogenized (Ultra Turrax T-25 at a rate of 11000 rpm) for 3 minutes at room temperature. After emulsification, 0.52 ml of aqueous ammonia is added to initiate the interfacial hydrolysis and poly-condensation reaction of TEOS. The mixture is then stirred at 300 rpm for over 24 h. Finally, the resulting silica hollow sphere is washed with acetone followed by ethanol. It is then isolated by centrifugation, followed by calcination in air at 600°C for 6 hours to remove volatile and oxidizable residues.

6.1.3. Preparation of annealed CaCO₃-decorated SiO₂ hybrid colloidal capsules

The well-defined and intact colloidal capsules are prepared following the approach in Chapter 5 at the optimum condition of 1 g CaCO₃ nanoparticles, water/oil ratio of 1:10, the *n*-hexylamine concentration of 50 mg/ml, total TEOS volume of 1 ml, and the reaction duration of 24 h. After washing and drying, the as-prepared colloidal capsules are annealed at different temperatures including 555°C, 650°C, 720°C, 900°C, and 1000°C for an hour. The annealed capsules are collected and prepared by FIB for *in-situ* TEM mechanical compression experiments.

6.1.4. Characterizations

N₂ adsorption/desorption experiment: The isotherm, specific surface area, average pore size width, and average pore volume of the annealed microcapsules are characterized by the N₂ adsorption/desorption experiment at temperature 77K using Autosorb (Quantachrome Instruments). While the specific surface area of the annealed microcapsules is determined by Brunauer–Emmett–Teller (BET) equation, the pore properties were obtained by Barrett–Joyner–Halenda (BJH) method. The measurements are performed on the annealed microcapsules after degassing the samples in a vacuum at 150°C for 4h.

Structural transformation via temperature: The *in-situ* heating experiment is performed inside the SEM chamber (FEI Helios G3 CX) to visualize the structural transformation of the colloidal capsule in real-time. A single capsule is picked and placed on the microelectromechanical system (MEMS) chip and the *in-situ* heating is conducted between 500-1000°C with a heating rate of 5°C/s.

6.1.5. *In-situ* TEM mechanical compression testing

The setup conditions for *in-situ* TEM mechanical compression are described in Chapter 3. Prior to the *in-situ* experiment, the individual capsule is mounted on a copper grid that has been ion milled to produce a flat surface. The calibration by air indentation is performed prior to each test to eliminate the possible errors from the former tests. The compression test is repeated four times with the approximate size of the particles. According to Yang et al.³⁰¹ and Sun et al.³⁰², the normalized shell strength, σ_{\max} , and the compressive strain, ϵ_f , can be calculated from the load-displacement curves following the equation (6-1) and (6-2):

$$\sigma_{\max} = \frac{P_{\max}}{\pi \left[\left(\frac{D_o}{2} \right)^2 - \left(\frac{D_i}{2} \right)^2 \right]} = \frac{P_{\max}}{\pi t (D_o - t)} \quad (6-1)$$

$$\varepsilon_f = \frac{h_f}{D_o} \quad (6-2)$$

where P_{\max} represents the peak load and D_o , D_i , t , and h_f are the outer diameter, inner diameter, shell thickness, and compressive displacement, respectively.

6.1.6. *In-situ* heating TOF-SIMS experiment

Prior to conduct the *in-operando* heating experiment, the cross-sectional specimen from the single colloidal capsule is prepared. Typically, the obtained colloidal capsules are deposited on the silicon wafer and a single capsule is manipulated in the dual-beam FIB-SEM chamber (FEI Helios NanoLab G3 CX) (Figure 6-1). After lifting and hanging in space, the microcapsule, mounted on the tungsten tip, is cross-sectioned into the ring under the voltage of 30 keV and the beam current of 80 pA to limit the material pre-deposition between the two shells. Subsequently, the tungsten tip is rotated 180° to align the ring parallel to the MEMS-heating chip surface. The ring is then gently deposited on the chip surface and fixed by platinum welding at the sides. TOF-SIMS post-analysis of the prepared ring is conducted at the voltage of 16 keV and the beam current of 50 pA with the horizontal field width (HFW) of 7.5 μm.

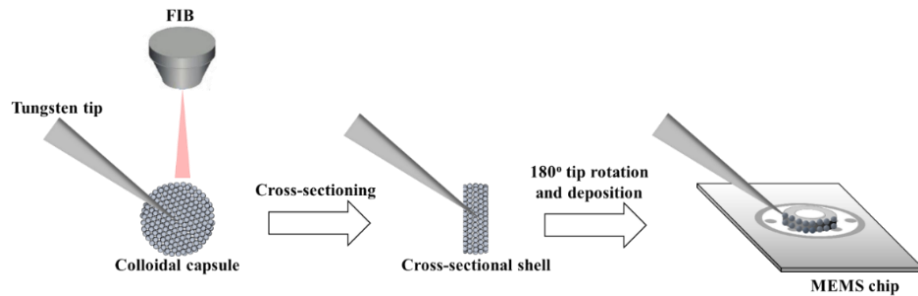


Figure 6-1. Cross-sectional specimen preparation in dual FIB-SEM before the *in-situ* heating TOF-SIMS experiment.

The *in-situ* heating TOF-SIMS experiments are subsequently conducted in the dual-beam FIB-SEM vacuum chamber (FEI Helios NanoLab G3 CX) with the aid of a Thermo Scientific™ μHeater holder. The small MEMS-based chip, as a heater, is installed in the holder before the experiment which can rapidly heat a sample at a rate of 0.01 to 104°C/sec with temperature settling to within 1°C. In this study, the chip is heated to 200°C directly before the *in-situ* heating experiment coupled with TOF-SIMS analysis. The dynamic heating is conducted from 200 to 1000°C with a heating rate of 1°C/sec. During the heating period, the TOF-SIMS is performed dynamically under 16 keV voltage and 50 pA current with horizontal field width (HFW) of 7.5 μm that results in the acquisition time for each frame of 9 sec and a flight time was 10 μs. Such low acquisition time compared with other reported *in-situ* heating mapping techniques^{303, 304} allows better real-time recording of elemental diffusion. An initial group delay before detection is set to 1500 ns to eliminate ringing artifacts unique to this detector which prevents detection of species below 5 m/z. The ion optics are optimized for sensitivity which produces the mass resolution for calcium (Ca) of ~888 in imaging mode which is more than sufficient to achieve isotope mass

separation. However, an effective dosage from the analysis is impossible to determine due to the continuous illumination of the Ga ion source and the short pulse duration of the acquisition leading to a significant disparity in the acquired dosage window and the true illumination dosage. The *in-situ* heating TOF-SIMS experiment is immediately stopped when the temperature reached 1000°C. The results are exported by the TofSimsExplorer software from TOFWerk and they are further processed by Fiji-ImageJ to produce a video of the elemental movement via temperature.

6.1.7. *In-situ* heating XRD experiment

The temperature-induced crystallographic phase changes are investigated using a PANalytical Empyrean (Malvern Panalytical) X-ray Diffraction (XRD) Goniometer equipped with an Anton Paar HTK16N heating stage, including a Pt heating strip with a thickness of 0.5 mm. The Pt strip height alignment is performed while observing an alignment tunnel in the direct X-ray beam. After alignment, a thin layer of a well-ground sample is placed into the middle of the Pt strip, wetted with few drops of ethanol for better adhesion and creation of a flat surface profile, and then left to dry. The measurements are performed in a standard Bragg-Brentano reflection geometry using Cu K α radiation ($\lambda = 1.5406 \text{ \AA}$) and operating conditions of an accelerating voltage of 45 kV and a current of 40 mA. All scans are performed in a 2θ angle range of 20° to 80° and a speed of 6°/min in a vacuum. The heating rate during temperature ramps was set to 25°/min. To ensure uniform temperature distribution in the samples, the measurement program was set to wait for 60 sec at each target temperature prior to exposing a sample to the XRD beam.

6.1.8. *In-situ* heating TEM observation

The thermal-induced doubled-shell transformation at elevated temperatures was initially observed by conducting the heating experiment in the TEM chamber (Gatan 652 *In-situ* Heating Holder in JEOL JEM-ARM200F). The setup conditions for an *in-situ* heating experiment in TEM are based on the description in Chapter 3.

6.2. Results and Discussion

6.2.1. Formation of CaCO₃-decorated SiO₂ colloidal capsules and SiO₂ hollow sphere

A sol-gel method combined with a typical cetyl trimethyl ammonium bromide (CTAB) surfactant is used to prepare the silica hollow spheres as the reference material for the *in-situ* TEM experiment. The influence of various synthesis conditions on the formation of silica hollow spheres has been investigated extensively³⁰⁵⁻³⁰⁷ and will not be discussed here. To reduce the porosity in the silica shell, the final product is annealed at 600°C. The annealing process not only removes the core material (octadecane) but also improves the mechanical strength of the silica shell due to a sintering effect.³⁰⁸ The mean sphere size of the silica hollow sphere is $3.5 \pm 0.7 \mu\text{m}$ (inset picture in **Figure 6-2a**). After calcination, the spheres have smooth exteriors (**Figure 6-2c**) and are hollow in structure (**Figure 6-2d**). A cross-section examination of the calcined silica hollow sphere shows the interior surfaces to be much rougher than the exterior with a shell thickness of $310 \pm 70 \text{ nm}$ (**Figure 6-2e**). The obtained colloidal capsules at the optimal conditions are intact with negligible

fractures (**Figure 6-2b**). They are spherical with a rough outer shell surface due to the agglomeration of many 50 nm nanoparticles (**Figure 6-2f**). As demonstrated in **Chapter 5**, the obtained colloidal capsules have a mean particle diameter of $7.5 \pm 1.8 \mu\text{m}$. The total thickness of the doubled-shell from the colloidal capsule is $460 \pm 20 \text{ nm}$, which comprises the silica inner shell thickness of $166 \pm 14 \text{ nm}$ (**Figure 6-2h**).

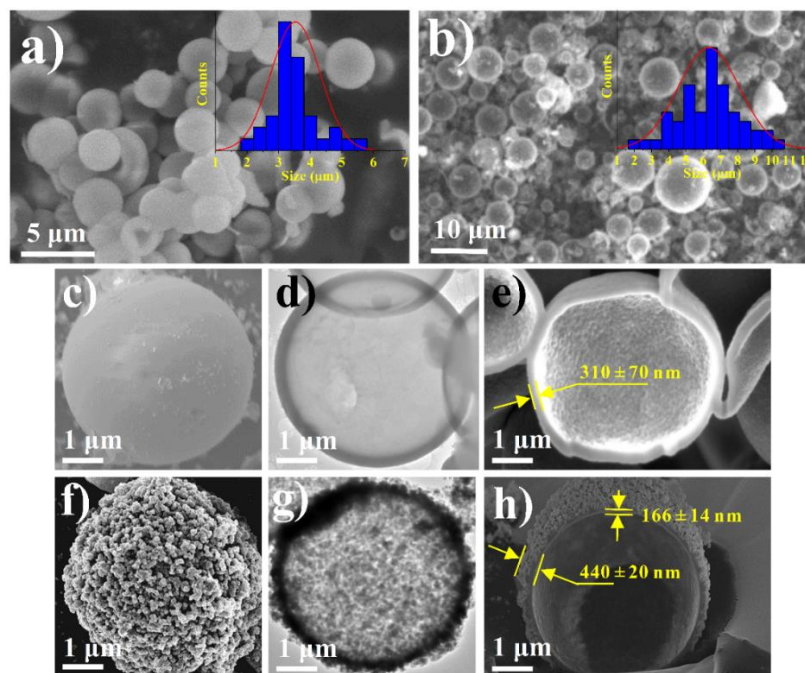


Figure 6-2. (a) SEM images of silica hollow spheres. Inset is the particle size distribution (mean diameter = $3.5 \pm 0.7 \mu\text{m}$); (b) SEM images of the colloidal capsule. Inset is the particle size distribution (mean diameter = $6.3 \pm 1.8 \mu\text{m}$); (c) SEM images showing smooth shell surface of silica hollow sphere; (d) TEM image showing the hollow structure and shell wall; (e) SEM image of a fractured sphere showing rough internal surface from silica hollow sphere; (f) SEM image showing a rough colloidal capsule surface; (g) TEM image showing the hollow structure, shell thickness and particle assembly in the shell; and (h) SEM image of a sectioned colloidal capsule.

It is well known that the use of a soft-templating method for the preparation of a silica-based hollow sphere is considered a simple and efficient approach. Water-in-oil (w/o) and oil-in-water (o/w) are the most common emulsion systems that have been used for the fabrication of silica hollow spheres with a wide range of diameters. In both systems, conventional synthetic emulsifiers are often utilized to stabilize the emulsion systems. In a water-in-oil emulsion, the hydrolysis/condensation rate of silane precursors can be adjusted by the pH value of the aqueous dispersed phase and the viscosity of the external oil phase.³⁰⁹ Meanwhile, in an oil-in-water emulsion system, the size and shell thickness of the silica hollow sphere can be tuned via ethanol-to-water ratio and surfactant concentration apart from the pH of the aqueous phase and the amount of the silane precursor in the oil phase.³¹⁰ Comparing to the w/o emulsion system, the synthesis of silica hollow sphere by o/w emulsion shows better performance as it produces a better scaffold to support the silica shell due to the relative stability of oil droplets.³¹¹ The silica hollow sphere

obtained from the w/o emulsion shows a severe agglomeration and particle fusion is a complex issue that often occurs.³⁰⁷ Considering such problems, it is decided to select the o/w approach to fabricate a silica hollow sphere and control the shell thickness and the size based on the previous references.

6.2.2. Mechanical evaluation of the CaCO₃-decorated SiO₂ colloidal capsule compared to SiO₂ hollow sphere

To examine the mechanical behaviors of the doubled-shell colloidal capsule compared to the singled-shell silica hollow sphere, *in-situ* TEM mechanical compression is utilized. The individual microcapsule is picked and manipulated in a dual FIB-SEM chamber (**Figure 6-3a**). Four individual capsules are mounted on the ion-milled copper holder for each type of tested particle before the *in-situ* TEM compression (**Figure 6-3b**-**Figure 6-3c**).

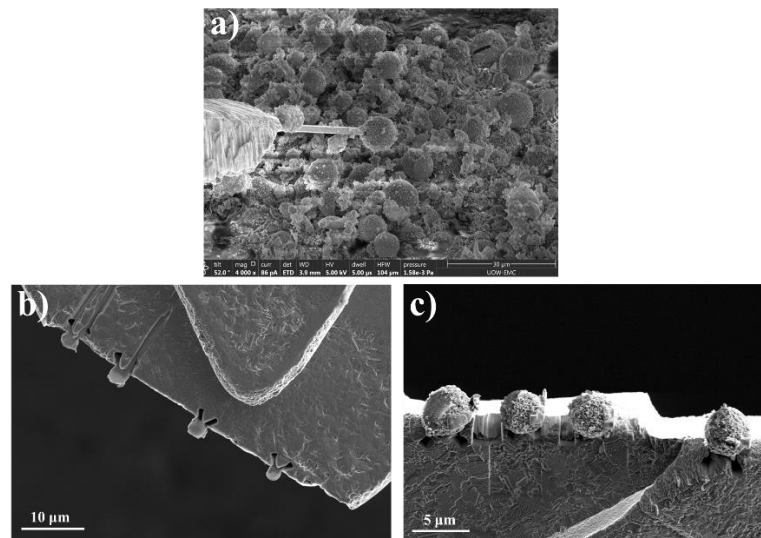


Figure 6-3. FE-SEM images and the mechanical properties of the prepared silica hollow sphere and the colloidal capsule picked for *in-situ* TEM compression. (a) FE-SEM image of the silica hollow sphere; (b) FE-SEM images of the colloidal capsule.

The representative load-displacement curve of a typical silica hollow sphere ($D_o = 3.4 \mu\text{m}$, $t = 360 \text{ nm}$) is shown in **Figure 6-4a**. In addition, a representative load-displacement curve from the colloidal capsule ($D_o = 3.3 \mu\text{m}$, $t = 448 \text{ nm}$) is displayed in **Figure 6-4b**. The results shown in **Figure 6-4a**-**Figure 6-4b** can be considered representative of the batch for each investigated material. They are either true for certain particles, or statistically significant averages for the investigated particles. The tested individuals respond similarly to external forces with the load increases linearly with displacement until the peak value when the particles are fractured. However, there is a significant difference in the compressive behavior of the silica hollow sphere, the non-heat treated and heat treated colloidal capsule, which is related mainly to the structural characteristics of the shell.

The silica hollow sphere experiences an elastic deformation during a displacement of 150 nm (Stage I) followed by an elastic-plastic deformation (Stage I*) in the next 220 nm (**Figure 6-4a**).

The rupture of the silica hollow sphere is determined when a crack on the shell appeared at the peak load of 550 μN (**Figure 6-4a**), but the whole particle does not collapse completely. Coupled with the load-displacement curve and TEM images, the compressive behavior indicates a partial ductility of the silica hollow sphere.^{312, 313}

In contrast, the doubled-shell of non-heat treated colloidal capsule deforms elastically in the first 280 nm (Stage I), before it experiences an elastic-plastic deformation (Stage I*) of 180 nm (**Figure 6-4b**). The longer elastic deformation of the colloidal capsule indicates higher stiffness and brittleness behaviors compared with the silica hollow sphere.³¹³ Surprisingly, the colloidal capsule demonstrated a complete breakage of the shell structure at the peak load of 675 μN rather than the appearance of the crack (**Figure 6-4b**). Compared to silica amorphous particles, the calcite particle is stiffer and more brittle (**Figure 6-4c**). It has been demonstrated that under high stresses, amorphous silica with a glassy structure can deform plastically and results in a ductile behavior that mediates the rotation and migration of atomic clusters.³¹⁴ Therefore, the brittle and high stiffness of CaCO_3 nanoparticles packed as the outer shell (calcite, **Figure 6-4c**) could be the main reason that affects the shell properties of the whole colloidal capsule, which is different from the single hollow silica sphere.

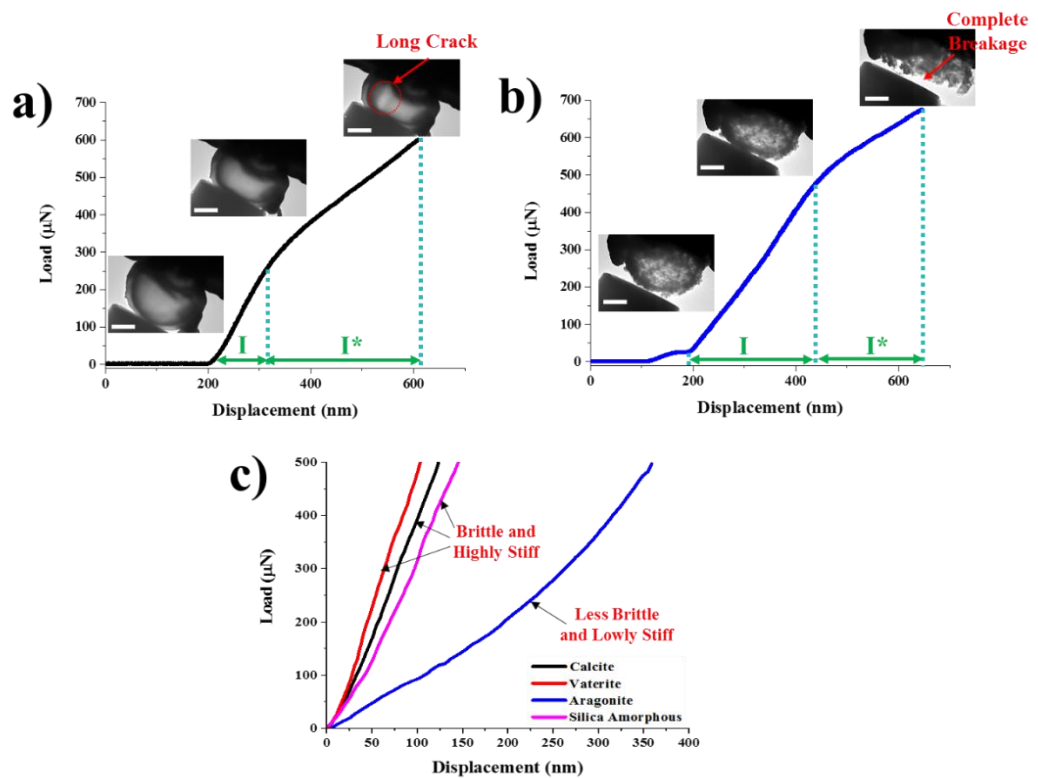


Figure 6-4. Representative load-displacement curves of: (a) a single silica hollow sphere; (b) non-heat treated colloidal capsule; (c) different crystalline polymorphs of calcium carbonate³¹⁵ and silica amorphous³¹⁶ particles. The inset pictures are the TEM image showing the dynamic change of the tested particle during the compression. The scale bar is 1 μm .

The calculated normalized strength (σ_{max}) and compressive strain (ϵ_f) for the tested individuals are

shown in **Figure 6-5a-Figure 6-5f**, which shows the distribution of the rupture properties for silica hollow sphere and the colloidal capsule. Four particles for each material are subjected to mechanical compression, and the results show a variation in the normalized strength and the compressive strain for a narrow range, 3-4 μm , of the particle's diameter (**Figure 6-5a-Figure 6-5d**). Since it is difficult to collect the particles with the exact size and geometry for each tested material, the averages of normalized strength and compressive strain for silica hollow sphere and the colloidal capsule are displayed in **Figure 6-5e-Figure 6-5f**. These results are representative of the particles with a diameter in the range of 3-4 μm and are necessarily tentative.

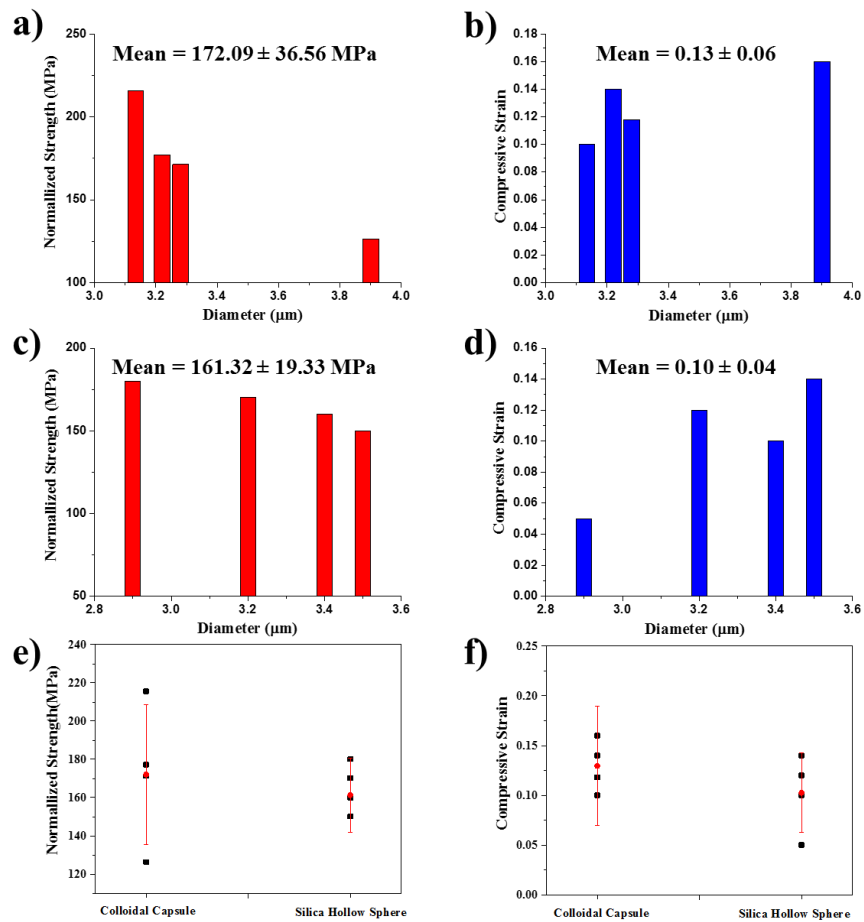


Figure 6-5. The calculated normalized strength and compressive strain via a slight variation in the tested particle's diameter (3-4 μm) of: (a)-(b) the doubled-shell colloidal capsule; (c)-(d) silica hollow sphere. Distribution of the normalized strength (e) and compressive strain (f) of the doubled-shell colloidal capsule and silica hollow sphere. The averages of the rupture properties for each tested individual are displayed in the red dot.

As can be seen, the statistical significant averages of the normalized strength and compressive strain from the annealed silica hollow sphere are 161.32 ± 19.33 MPa and 0.10 ± 0.04 respectively (**Figure 6-5e**). Meanwhile, the colloidal capsule in this study shows the strength of 172.09 ± 36.56 MPa and the compressive strain is in the range of $\epsilon_f = 0.13 \pm 0.06$ (**Figure 6-5f**). It is originally predicted that the mechanical strength of the obtained colloidal capsule ($D_o = 3.3$ μm , $t_{\text{total}} = 448$ nm with $t_{\text{SiO}_2} = 170$ nm) should be weaker than that of the annealed silica hollow sphere at the

same diameter ($D_0 = 3.4 \mu\text{m}$, $t = 360 \text{ nm}$) due to the much thinner internal silica shell. In the case of simply physical absorption, the CaCO_3 nanoparticles will not act as a building block and modify the nature of the SiO_2 shell. However, the shell strength of the silica hollow sphere ($161.32 \pm 19.33 \text{ MPa}$) is slightly lower than the obtained colloidal capsule ($172.09 \pm 36.56 \text{ MPa}$) (**Figure 6-5e-Figure 6-5f**), and their compressive behaviors are significantly different. These observations demonstrate the distinct mechanical modification of the SiO_2 shell by the CaCO_3 nanoparticles. The chemical interaction between them may modify the physicochemical nature of the silica inner shell, and it will be discussed in the next section.

6.2.3. Intrinsic effect of CaCO_3 nanoparticles in the mechanical behavior of the SiO_2 shell

To gain an insight into the effect of CaCO_3 nanoparticles on the SiO_2 shell, the interfacial structure between these materials is examined by using Scanning Transmission Electron Microscope (STEM). A non-annealed single colloidal capsule is sectioned by ion milling using Focus-ion-beam (FIB) milling (**Figure 6-6**), and the thin ring specimen is then examined by STEM.

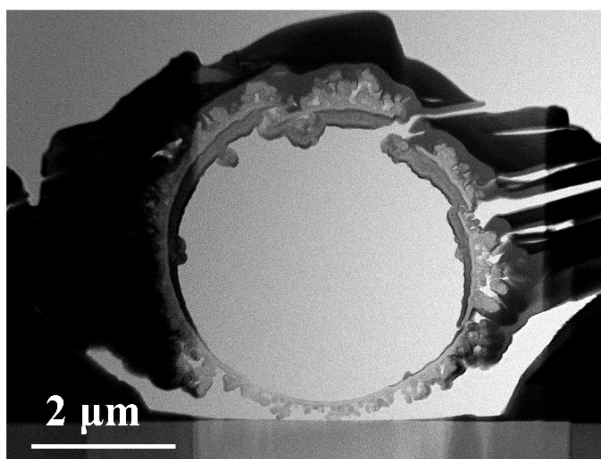


Figure 6-6. Preparation of the thin ring from the picked colloidal capsule for STEM observation.

High-Angle Annular Dark-Field (HAADF) imaging in Figure 5a shows the wall of the sectioned ring. The carbonate phase with a high mean atomic number appears brighter than the silica in this imaging mode (**Figure 6-7a**). STEM-Electron Dispersive X-ray Spectroscopy (EDX) mapping (**Figure 6-7b**, Si K) reveals a dense internal silica shell and a thin skin of silica coating embedded with carbonate nanoparticles in the external shell. It is believed that this skin plays an important role in connecting all the nanoparticles and results in an enhanced aggregation on the outer shell. In addition, many of the carbonate nanoparticles are embedded in the silica shell which may support the bonding between the external and the internal shells (**Figure 6-7a**). Selected Area Electron Diffraction Patterns (SADPs) are obtained from the silica inner layer and the nanoparticles to verify the formation of the dicalcium silicate phase from **Figure 5-11b**. However, the spacings due to dicalcium silicate are not detected. It can be seen from **Figure 6-7c-Figure 6-7d** that only the presence of single-crystalline from calcite in the nanoparticles and the diffused ring of the amorphous structure from the silica shell are observed. XRD suggests that some compound formation has occurred in the shell (**Figure 5-11b**), and the mechanical behavior

(**Figure 6-4a-Figure 6-4b**) proves that such interactions modify the shell properties.

To find the underlying mechanism, the interfacial structure between the silica layer and the CaCO₃ nanoparticles (marked in **Figure 6-7a**) is examined by Aberration Corrected-STEM (AC-STEM). AC-STEM Bright Field (BF) image at the boundary area (**Figure 6-7e**) shows an indistinct boundary between the amorphous and crystalline phases. A diffraction contrast in **Figure 6-7e** illustrates the presence of different fringes at the interface compared to that at the crystalline particles. Apart from the presence of CaCO₃ (1 1 0) *d*-spacing = 0.37 nm in the crystalline regions, there is a small existence of Ca₂SiO₅ (4 0 0) *d*-spacing = 0.23 nm adjacent to the boundary areas. The corresponding HAADF image (**Figure 6-7f**) reveals the existence of a low atomic layer (~ 1 nm), which is identified as a stearic acid layer at the boundary regions.

Electron Energy Loss Spectroscopy (EELS) line scanning is subsequently conducted, as marked in **Figure 6-7f**, to inspect the elemental distribution and bonding formation across the three different phases. The EELS spectrum in **Figure 6-7g** is extracted from different areas including: CaCO₃ nanoparticles (3), interfacial area (2), and SiO₂ shell (1). CaCO₃ nanoparticles (3) present the distinct peaks of C-K, Ca-L, and O-K edges from calcite³¹⁷ (**Figure 6-7g**), with no distinct peak shifting for the new phase formation. In addition, the EELS spectrum in silica shell (1) shows no existence of calcium and carbon elements (C-K and Ca-L edges, **Figure 6-7g**), and the distinct peaks from silica³¹⁸ (Si-L and O-K edges, **Figure 6-7g**) suggests no new phase formed in this layer. However, it is interesting to note that there is a presence of a small calcium element at the interface (**Figure 6-7g**, Ca-L edge of (2)), and an increase of carbon signal to produce a broad hump edge of amorphous carbon has been detected at this region (**Figure 6-7g**, C-K edge of (2)). The existence of calcium in this organic layer confirms the formation of calcium stearate, which has been demonstrated by FTIR (**Figure 5-11a**). However, a lack of the functional groups of C-O and C=O from calcium stearate in the EELS C-K edge (**Figure 6-7g**) can be due to the large hydrocarbon backbone of stearic acid molecules. There is only one carbon in the chain of eighteen that represents the carboxylate group in the molecular structure. Thus, the carbon signal only shows the strong signal of an amorphous structure, which represents the domination of seventeen hydrocarbon backbones. Apart from the existence of calcium at the interface (2), the Si-L edge at this area also reveals the presence of an additional peak at 102 eV comparing to the SiO₂ shell (1) (Si-L edge, **Figure 6-7g**). This peak represents the formation of [O=SiO₂]²⁻Ca²⁺, which suggests the formation of the chemical bonding at the interfacial areas³¹⁹, and this is consistent with the XPS results (**Figure 5-13**).

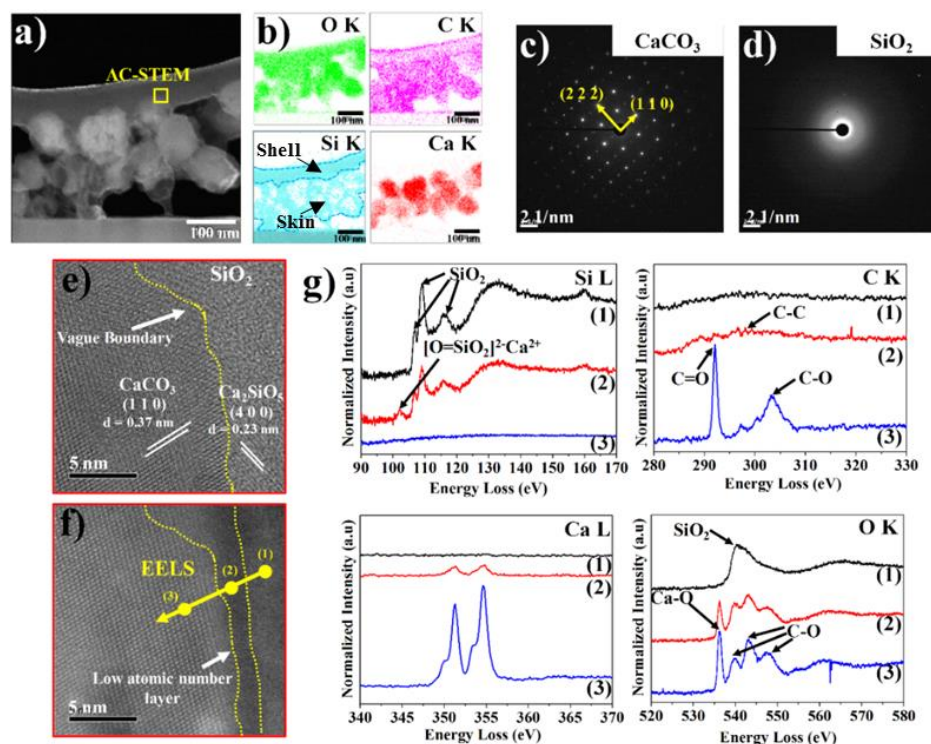


Figure 6-7 (a) STEM-HAADF image of the thinned ring; (b) EDS mapping images of elemental distribution; (c) SADP of the nanoparticles; (d) SADP of the silica shell; (e) the inner shell BF imaging of the interfacial structure at very high magnification marked in (a); (f) Corresponding HAADF imaging of the interfacial structure from (e); (g) EELS analysis of Si-L, C-K, Ca-L, and O-K edges from the silica inner shell to the nanoparticles marked in (f).

Based on the obtained results, the formation of such dicalcium silicate phase and the chemical bonding at the interfacial areas can be due to the chemical reaction between the reactive calcium stearate (COO^-Ca^+) in the stearic acid layer and the silicic acid ($\text{Si}(\text{OH})_4$) hydrolyzed from TEOS. The chemical bonding between the embedded carbonate nanoparticles and the silica shell at the interfacial areas proves that these nanoparticles are firmly anchored to the inner shell. Such interfacial structure not only binds the SiO_2 amorphous shell and CaCO_3 nanoparticles together but also secures the aggregation of a vast number of nanoparticles to form the outer shell. Consequently, it results in distinct compressive behavior and the enhanced strength of the colloidal capsule compared to the silica hollow sphere. In addition, this interfacial structure can also explain the significant mass loss of the colloidal capsule at 566°C (DTG in **Error! Reference source not found.b**), being significantly lower than that of pure calcite (CaCO_3) (750°C).²⁸⁶ The presence of a thin silica layer enveloping CaCO_3 nanoparticles on the outer shell and the chemical bonding formation between these two phases can accelerate the process of CaCO_3 decomposition by the formation of silicate phases even at a temperature below 1000°C .^{287, 288}

6.2.4. Mechanical evaluation of the CaCO_3 -decorated SiO_2 colloidal capsule with different diameters

For comparison, the compression experiment is performed with different sizes of the colloidal

capsules to investigate the effect of size on the mechanical responses. **Figure 6-8a** shows the representative load-displacement curve of the 7.5 μm colloidal capsule under the same testing conditions as the smaller ones (3.3 μm) in **Figure 6-4b**. For the tested individual, it can be seen that the load rises linearly with displacement until a peak value at which point the particles ruptured. Under compression of the capsule with a 7.5 μm diameter (**Figure 6-8a**), the densely packed external shell experiences a small elastic deformation of 300 nm (Stage I') before the whole doubled-shell elastically deforms in the next 600 nm (Stage I). A short elastic-plastic deformation of 200 nm (Stage I*) occurred, and a peak load of 475 μN is reached before the rupture of the capsules (**Figure 6-8a**). The inset TEM images in **Figure 6-8a** show the characteristic appearance of a brittle fracture in the inner shell. Similar to 3.3 μm colloidal capsule (**Figure 6-4b**), the 7.5 μm particle shows a brittle response during the mechanical compression (**Figure 6-8a**). However, the shape of the load-displacement curve in the case of a 7.5 μm tested colloidal capsule indicates a lower stiffness for the larger capsule compared with the smaller one (**Figure 6-4b** and **Figure 6-8a**).

Quantitative changes in mechanical properties related to the size of microcapsules are shown in **Figure 6-8b**, which depicts the calculated compressive strength and strain of the colloidal capsules with different diameters. According to **Figure 6-8b** the compressive strength rises sharply from 88.8 ± 7.9 to 260.4 ± 14.4 MPa when the capsule's diameter reduced from 5.5 to 2.2 μm , but the compressive strain decreased dramatically from 0.16 ± 0.04 down to 0.09 ± 0.03 . It is worth noting that the compressive strain remains similar for all the tested capsules with a size above 5.5 μm , despite a slight increase of normalized strength when the particle size is reduced from 10.2 μm to 5.5 μm . This size effect on the strength of microcapsules is similar to that described in the literature reported previously.³²⁰⁻³²²

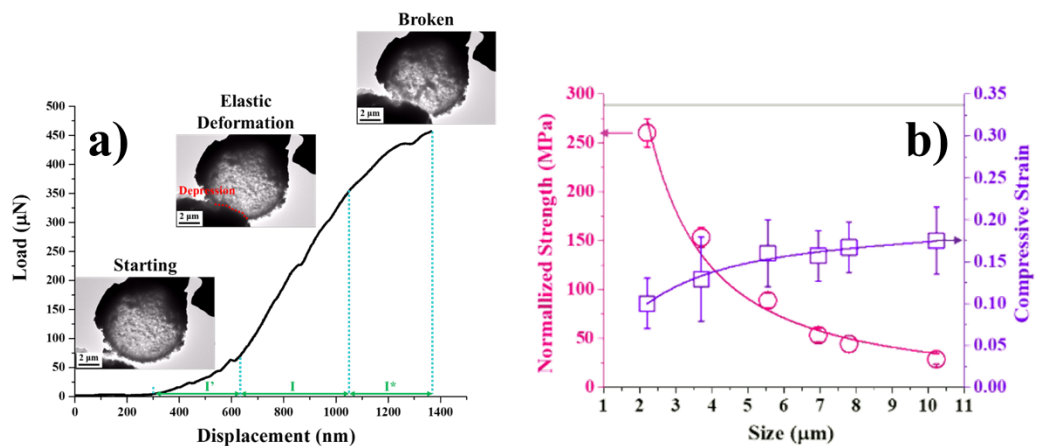


Figure 6-8. (a) Load-displacement curve of the mechanical compression of the representative 7.5 μm individual colloidal capsule; (b) Normalized strength and compressive strain of the colloidal capsule via diameter.

Such differences in the mechanical behavior between the large and small colloidal capsules can be explained by observing the structure and the mechanical deformation of the thin rings prepared from the colloidal capsules with different sizes (**Figure 6-9**). Two colloidal capsules with different

diameters ($\sim 7 \mu\text{m}$ and $\sim 3 \mu\text{m}$) are picked and mounted on the copper grid before being cross-sectioned into the thin specimens by a Ga ion beam. To preserve the characteristics of the doubled-shell, the thinning process is conducted at a low voltage of 16 keV and a current of 80 pA to avoid the deposition of the materials from the two shells to each other. As can be seen, the observation of two shells is distinct in the case of the larger ring (**Figure 6-9a**), while the smaller ring shows an ambiguous boundary between the external and internal shells (**Figure 6-9b**). In addition, the external shell of the small capsule is denser and appears more rigid than the large capsule (**Figure 6-9a-Figure 6-9b**). During the mechanical compression, the small ring exhibits the direct deformation of the doubled-shell in Stage 1 (**Figure 6-9b**), whereas the large ring reveals the small displacement of the external shell (Stage 1, **Figure 6-9a**). The large ring appears ductile and flexible in the second stage and the presence of a breakage in the inner shell is observed in Stage 3, **Figure 6-9a**). In contrast, the small ring reveals high rigidity and non-flexible performance during the deformation in Stage 2 (**Figure 6-9b**). The presence of tearing is observed before the total breakage of the whole ring (**Figure 6-9b**). Comparing the results, it can be seen that the double-shell from the small capsule behaves as a single composite shell rather than the separated hybrid-shell from the large capsule (**Figure 6-9c**). It can be the underlying reason for the changes in the shell strength and strain of the colloidal capsules with different diameters.

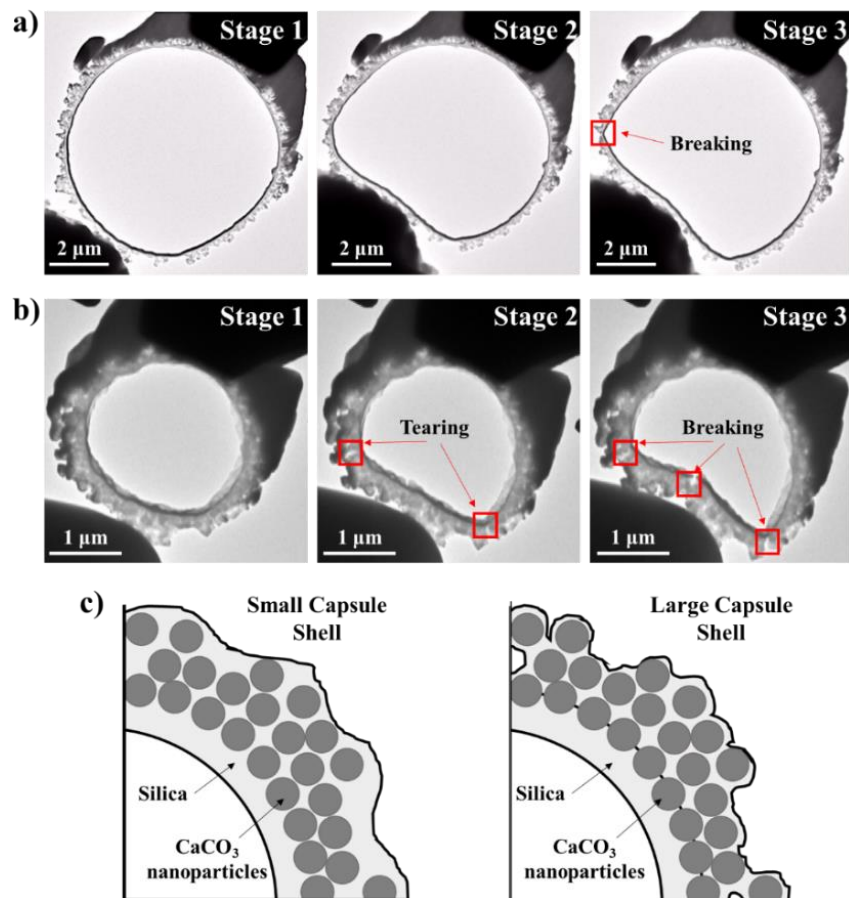


Figure 6-9 Mechanical deformations of the thin-rings prepared from the large (a) and small (b) colloidal capsules; (c) Schematic representing the possible mechanisms of different mechanical behavior from the large and small colloidal capsules.

6.2.5. Mechanical evaluation of the CaCO₃-decorated SiO₂ colloidal capsule after annealed at elevated temperatures

The thermal robustness of the obtained colloidal capsules has been demonstrated by *in-situ* SEM heating observation. At elevated temperatures, the colloidal capsule changes its morphology significantly and probably shrinks into a smaller sphere (**Figure 6-10**). According to **Figure 6-10**, the colloidal capsules exhibit superior thermal stability up to 1000°C with no distinct damages. The external shell of the colloidal capsules transforms from a granular feature to a rambutan-like structure when the temperature is increased from room temperature to 1000°C (**Figure 6-10**). From 500-700°C, the colloidal capsules start to shrink from 5.75 μm to 5.25 μm. The surface morphology of the colloidal capsules changes with the appearance of the pliable spines. The formation of the pliable spines can be due to the sintering and agglomeration of the resulted CaO phase from the decomposition of CaCO₃ nanoparticles in the external shell. These spines become larger and the distinct shrinkage of the whole colloidal capsule structure is observed at 900°C that produced 4.5 μm rambutan-like colloidal capsule at 1000°C. Since the nanoparticles at the outer shell are anchored on the silica shell,³²³ the shrinkage of the colloidal capsule system can be explained by the classical thermodynamics proposed by Bogdan et al. for immobilized nanoparticles that are evenly distributed on the shell.³²⁴ During an increase of temperature, the internal forces, led by a significant diffusion of the CaO phase to the SiO₂ shell, results in a shrinkage of the colloidal capsule to ensure a minimum energy configuration. It thus results in a smaller microcapsule. Moreover, this behavior may be closely associated with the liquid sintering effect at significantly high temperatures that plays an important role in the reduction of the shell thickness and the shrinkage of the capsules.³⁰⁸

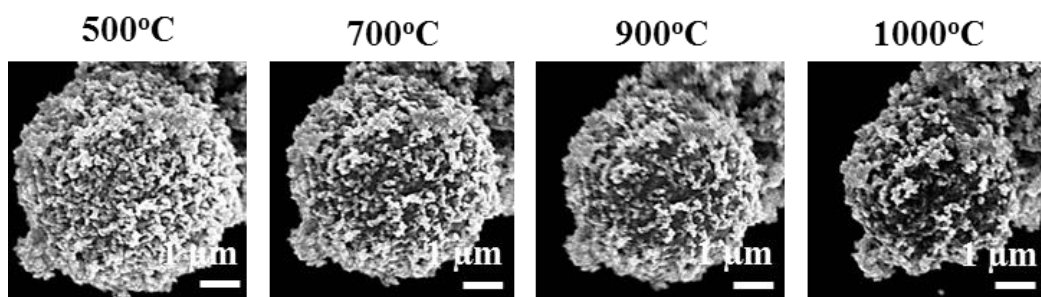


Figure 6-10 In-situ observation of the capsule's shell morphology transformation at elevated temperatures.

Apart from the changes in morphology and diameter, a significant change of the mechanical properties is observed for the colloidal capsule after annealed at elevated temperatures which are significantly different from the reported results of the silica hollow sphere. Zhang et al.³⁰⁸ did the AFM mechanical testing in the non-annealed and annealed silica hollow sphere and they show an increase in the compressive strength and stiffness for the annealed silica hollow sphere, albeit with a significant decrease in the ductility. In the present study, according to the TEM observation, the distinct switch from highly stiff and brittle (non-annealed microcapsule) (**Figure 6-4b**) to lowly stiff and ductile characteristics (1000°C-annealed microcapsule) (**Figure 6-11a**) is evident. The

sample annealed at 1000°C experiences two stages of elastic deformation as shown in the load-displacement curve (**Figure 6-11b**). The first one can be related to artifacts caused by the take-up of slack, and alignment or seating of the specimen, while the latter, with the pop-in occurrence, is attributed to the elastic deformation of the total capsule shell structure before the plastic deformation ensues (**Figure 6-11b**). The pop-in phenomenon at the second stage of elastic deformation can probably be due to the sudden breakage of the small pliable spines on the shell after annealed at 1000°C. The normalized compressive strength (σ_{\max}) and strain (ϵ_f) can be calculated based on the obtained load-displacement curve and the microcapsule geometry (diameter (D_{particle})) and total shell thickness (t) of the investigated colloidal capsules.³²³ According to **Figure 6-11c**, a slight drop from 201.5 ± 45.7 to 154.1 ± 11.6 MPa in the compressive strength is observed from non-annealed to 720°C annealed-microcapsules, while the compressive strain of these tested particles is similar. The compressive strength starts to increase significantly at 900°C, and it reaches a maximum of 278.9 ± 48.3 MPa for the particles annealed at 1000°C (**Figure 6-11c**) despite the thinner single-shell (210 ± 20 nm) formed at 1000°C (**Figure 6-11a**) compared with a thicker doubled-shell (440 ± 20 nm) of the non-annealed microcapsule (**Figure 6-2h**). In addition, the compressive strain of the 1000°C-annealed colloidal capsule is approximately doubled compared to the non-annealed one (**Figure 6-11c**).

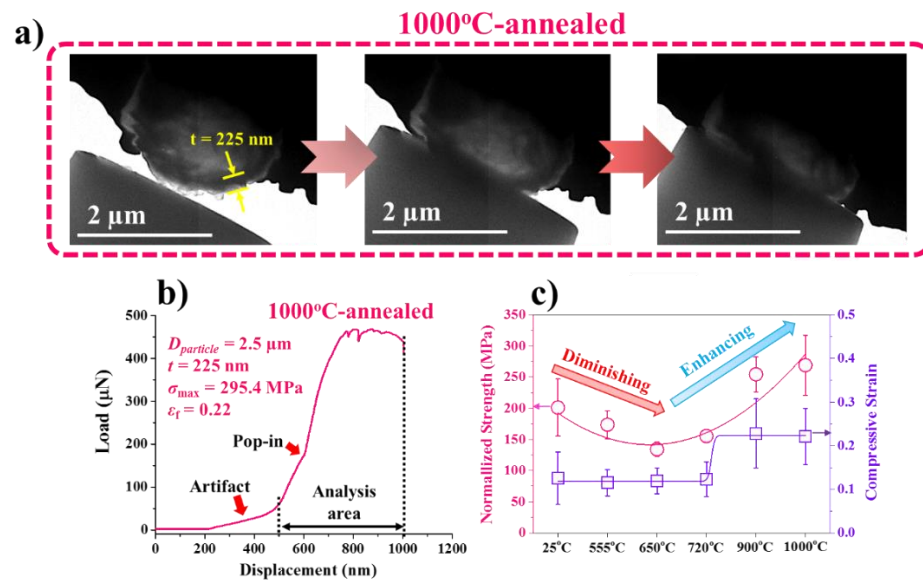


Figure 6-11 (a) Dynamic observation of the in-situ TEM mechanical compression of 1000°C-annealed hybrid microcapsules; (b) Corresponding load-displacement curve of the 1000°C-annealed colloidal microcapsule; and (c) Changes in compressive strength and strain of the colloidal microcapsules after heat treatment at different temperatures.

The presented normalized compressive strength and strain at each annealing temperature are statistically significant averages from four tests for a narrow distribution of the capsule's diameter (2.8-4.0 μm). **Figure 6-12** shows the distribution of the normalized compressive strength and strain from the *in-situ* compression of a single colloidal capsule. The average values (red dot with error bar), which are used to reveal the trend in **Figure 6-11c**. The results in **Figure 6-11c** are statistical

averages for four tested individuals in **Figure 6-12a** and **Figure 6-12b**. As it is impossible to collect the tested particles which have the same size, geometry, and morphology, the results can be considered representative of the batch which are significant averages for tested individuals after annealing at different temperatures. Thus, although these results are necessarily tentative, they can reveal a clear trend in the microcapsule mechanics via temperature. Such information has not been reported in the previous study and is significantly important when combined with other *in-situ* results that not only unveil the behavior of the materials at elevated temperatures but also open an opportunity to *in-operando* manipulate their properties via temperature.

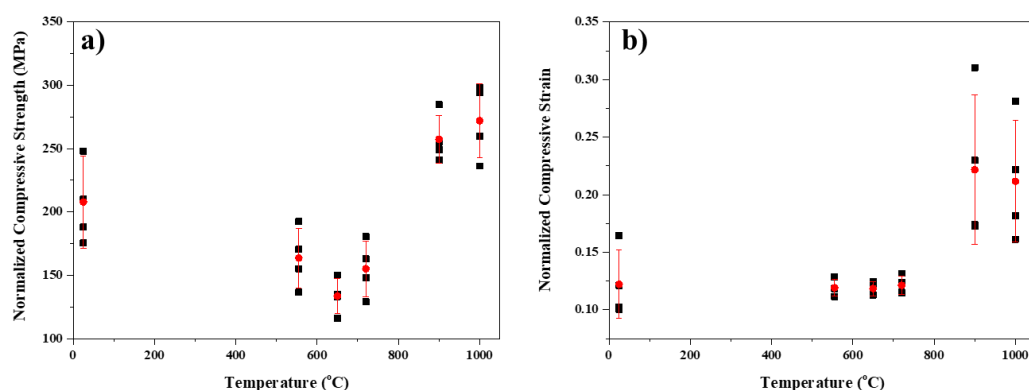


Figure 6-12. Statistical distribution of the normalized compressive strength (a) and compressive strain (b) of the individual colloidal capsules after annealed at different temperatures. The red dot with the error bar is the average from at least three *in-situ* compression tests of each individual.

6.2.6. Chemistry underpinning the significant changes in the morphologies and mechanical properties of the annealed-colloidal capsule

At elevated temperatures, it is hypothesized that high-temperature solid-state reactions occur in the hybrid doubled-shell colloidal capsule that results in significant modifications to the material properties.^{325, 326} In particular, the chemical transport between two shells may determine these changes which often include complex chemical processes such as: high-temperature diffusion, temperature-induced stresses, thermal-induced elastic/plastic deformations, and phase-transformation.²⁹² Although the TGA/DTG/DSC characterizations have proven the occurrences of the high-temperature solid-state reactions in the colloidal capsule system (**Error! Reference source not found.**), the lack of spatial information in terms of chemical diffusion and phase formation at different temperatures limits the understanding of the true nature that governed such changes in hybrid colloidal capsule properties. In this section, the combination between TOF-SIMS imaging and MEMS-based microheater has been introduced to track the chemical diffusion in our developed CaCO₃-SiO₂ hybrid microcapsule during heating.

Figure 6-13a shows the preparation of the ring sample on the MEMS-based microheater by the approach in **Figure 6-1** before the heating experiments. According to the TOF-SIMS mapping analysis, ²⁸Si⁺ and ⁴⁰Ca²⁺ are dominantly detected from the ring sample. While ²⁸Si⁺ mainly comes from the inner shell structure, the ⁴⁰Ca²⁺ is mostly generated from the external densely-packed

nanoparticles shell (**Figure 6-13a**). In this study, the Ga-FIB has been used along with TOF-SIMS detectors to capture images and extract chemical data of the analyzed sample during heating. While these systems are capable of obtaining high spatial resolution data, they compromise both mass resolution and sensitivity by pulsing the acquisition rather than the source. Hence, although collection efficiency is somewhat reduced, however, within the context of this experiment, both sensitivity and mass resolution is more than sufficient to resolve the features of interest. **Figure 6-13b** reveals the good mass separation in the positive ion spectra (m/z 0-60) with a distinct detection of several positive ions from the ring sample that are related to the bombardment of the SiO_2 and CaCO_3 phases by the primary ions.^{327, 328}

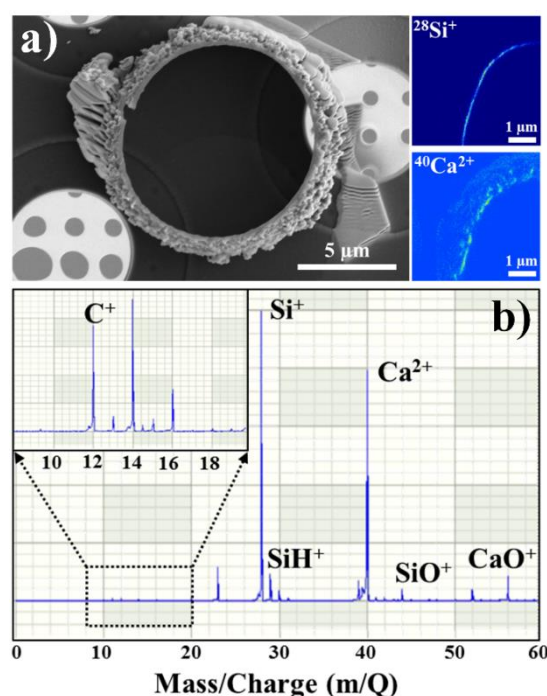


Figure 6-13 (a) SEM image of the sample on the heating chip and high-resolution TOF-SIMS elemental mapping of $^{28}\text{Si}^+$ and $^{40}\text{Ca}^{2+}$ from the ring sample; (b) TOF-SIMS positive ion spectra (m/z 0-60) of the cross-sectioned ring sample.

The experimental setting conditions of an *in-situ* heating TOF-SIMS analysis are presented in **Figure 6-14a**. The experiment is operated from 200 to 1000°C with a heating rate of 1°C/sec. During heating, the high-resolution TOF-SIMS is conducted on the ring sample with the Ga^+ primary ion source at an angle of 52°. A low-energy electron flood gun is activated to avoid the charging effect. Typically, 16 keV voltage and 50 pA current with a horizontal field width (HFW) of 7.5 μm are applied in imaging mode which resulted in the acquisition time for each frame of 9s and a flight time of 10 μs. Such low acquisition time compared to other reported *in-situ* heating mapping techniques^{303, 304} allows a better real-time recording of elemental diffusion. The ion optics are optimized for sensitivity which produced the mass resolution for calcium (Ca) of ~888 in imaging mode. However, an effective dosage from the analysis is impossible to determine due to the continuous illumination of the Ga ion source and the short pulse duration of the acquisition leading to a significant disparity in the acquired dosage window and the true illumination dosage.

Figure 6-14b shows the intensity variation thermogram of the $^{28}\text{Si}^+$ and $^{40}\text{Ca}^{2+}$ ions from the *in-situ* TOF-SIMS analysis as a function of temperature. The obtained results are stable even at elevated temperatures ($\sim 1000^\circ\text{C}$) despite the significant infrared radiation (**Figure A-1**). While the intensity signal of $^{28}\text{Si}^+$ increases gradually from 800 to 1000°C , there is a sharp rise of $^{40}\text{Ca}^{2+}$ in the same temperature range. This behavior can be related to the high mobility of the Ca^{2+} at high temperatures compared to the Si^+ which allows a higher potential to be ionized by Ga^+ primary beam.³²⁹

Figure 6-14c-Figure 6-14g shows the distribution of $^{40}\text{Ca}^{2+}$ (green color) and $^{28}\text{Si}^+$ (red color) via temperature in the ring sample. During an increase in temperature, $^{40}\text{Ca}^{2+}$ becomes mobile and the movement of such ion between the shell layers is recorded. Meanwhile, $^{28}\text{Si}^+$ is considerably stable and stays mainly at the internal shell layer. The diffusion of Ca^{2+} to the amorphous silica glass is thermodynamically favorable at high temperatures which is due to the significant mobility and high affinity of Ca^{2+} ion³³⁰ compared to the highly polymerized SiO_2 glass network. Therefore, it is reasonable to observe the diffusion of $^{40}\text{Ca}^{2+}$ to the SiO_2 shell with no migration of $^{28}\text{Si}^+$ during the *in-situ* TOF-SIMS analysis (**Figure 6-14c-Figure 6-14g**). Upon heating at 200°C , there is no movement of $^{40}\text{Ca}^{2+}$ and $^{28}\text{Si}^+$ in both shell layers (**Figure 6-14c**). However, the diffusion of $^{40}\text{Ca}^{2+}$ to $^{28}\text{Si}^+$ -containing layer (SiO_2 shell) starts to occur at 555°C that turns the fraction of the red layer into yellow (**Figure 6-14d**). It can be seen that the majority of $^{40}\text{Ca}^{2+}$ proximity to external/internal shell interfaces diffuse to the SiO_2 layer from 555 to 720°C (**Figure 6-14d-Figure 6-14e**). Above 720°C , the remaining $^{40}\text{Ca}^{2+}$ from the external shell (far away from the external shell/internal shell interfaces) begin to diffuse to the SiO_2 layer (**Figure 6-14e-Figure 6-14f**). This migration of $^{40}\text{Ca}^{2+}$ is completed at 1000°C (**Figure 6-14g**) that indicates the entire dissolution of the external shell to the inner shell. Despite the thermal drifting that occurs during the visualization of the elemental movement (**Figure 6-14c-Figure 6-14g**), a coupling between TOF-SIMS analysis and MEMS-based heating has demonstrated a significant potential for real-time tracking the micro-/nano-scale high-temperature elemental migration with high spatial resolution.

It is well-known that SIMS is appropriate when studying the phenomenon that occurs extremely close to the surface. In this study, the phenomenon is surface-mediated, but the surface is steeply inclined (ostensibly orthogonal) to the incoming ion beam, therefore, the arising concern is whether the examples presented here are representative of what occurs in the bulk. To check the reliability of the results, the interpretation of the data as being equivalent to a cross-section through the reaction layer has therefore been validated by an EDS post-mortem examination of the cross-sectioned thin rings used in *in-situ* TEM heating after cooled down to room temperature (**Figure A-3, Appendix A**). The direct observation of the chemical diffusion in **Figure 6-14c-Figure 6-14g** has proven the occurrence of the solid-state reactions between the shells in the hybrid doubled-shell microcapsules during heating apart from TGA/DTG/DSC. To validate the spatial observation in *in-situ* heating TOF-SIMS while obtaining an insight into the compound formation as a consequence of such chemical diffusion, additional *in-situ* XRD heating is also performed under vacuum conditions as shown in **Figure A-2 (Appendix A)**.

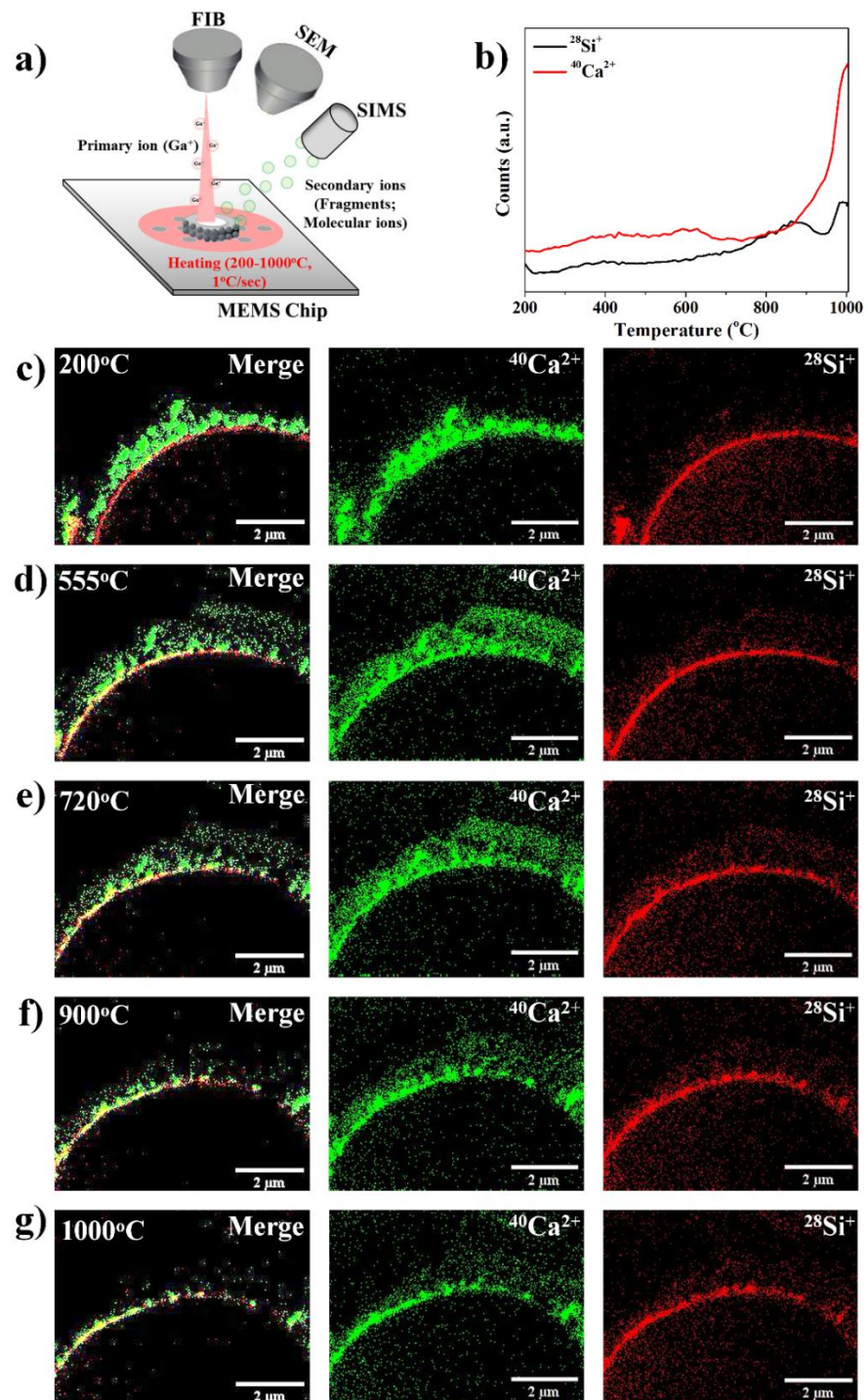


Figure 6-14 (a) Schematic showing the conditions for the TOF-SIMS analysis at elevated temperatures; (b) Intensity variation thermogram of $^{28}\text{Si}^+$ and $^{40}\text{Ca}^{2+}$ ions as a function of temperature. Elemental mapping of $^{28}\text{Si}^+$, $^{40}\text{Ca}^{2+}$, and the merging of these two ions corresponds to different temperatures, including: (c) 200°C; (d) 555°C; (e) 720°C; (f) 900°C; and (g) 1000°C.

From the TGA/DTG, DSC, *in-situ* TOF-SIMS, and *in-situ* XRD heating results (**Figure 5-14**, **Figure 6-14** and **Figure A-2b**), it is hypothesized that a drop in the strength of the hybrid microcapsules from 555 to 720°C (**Figure 6-11c**) can be due to the reactions between CaCO_3 nanoparticles (proximity to the external shell/internal shell interfaces) and SiO_2 inner shell. These

processes generate CO₂ that diffuses outward from the external shell/ internal shell interfaces to the surrounding environment. This process in turn induces the formation of not only the pliable spines on the capsule's surfaces but also the significant porosity in the external shell. Thus, the porosity can eventually weaken the mechanical strength of the doubled-shell³⁰⁸ and results in a decrease in the compressive strength (**Figure 6-11c**).

An *in-situ* TEM heating experiment is conducted on the two interconnected rings (**Figure 6-15a-Figure 6-15f**) to validate our hypothesis by visualizing the structural changes at a nano/sub-micron scale during the heating of the hybrid shell. The red square marked area in **Figure 6-15a-Figure 6-15f** indicates the examining area of the interconnected external shells. High-resolution bright-field images at 555-720°C (**Figure 6-15b2-Figure 6-15d2**) indicate the brighter diffraction contrast at the external shell (red arrow marked) of the two cross-sectioned shell specimens compared with the image obtained at room temperature (**Figure 6-15a2**). This occurrence indicates the lateral thickness of the specimen decreases with temperature due to an increase in porosity that reduces the traveling pathway of the electron through the specimens.³³¹ The external shell area changes from dense packing to sparse agglomeration of the nanoparticles during the temperature increase (**Figure 6-15a2-Figure 6-15d2**). Although the liquid sintering effect of SiO₂ phase at above 600°C may occur that fills the voids, wet, and connect the CaCO₃ nanoparticles leading to a reduction of pores within the shells³³², it is believed that the solid-state reactions between the CaCO₃ nanoparticles and SiO₂ are dominant at 555-720°C. Such vigorous reactions induce the dissolution of CaCO₃ nanoparticles in the SiO₂ matrix and generate significant CO₂ which increases the porosity of the shell structure. The TEM results are also supported by the N₂ adsorption and desorption experiment which shows an increase in the total BET surface area and average pore diameter of the capsule powders after annealed at different temperatures (**Figure A-4 and Table A-1, Appendix A**).

As the temperature progressed to 900°C-1000°C, the shrinkage appeared at the external shell area that reduces the gap between the two cross-sectioned specimens (**Figure 6-15e2**). It could probably include both the liquid sintering effect^{332, 333} and the complete dissolution of the CaO phase to the SiO₂ phase. At 900-1000°C, CaCO₃ nanoparticles on the external shell are all decomposed leaving the presence of only CaO phase on the capsule surface (**Figure A-2b**). At this temperature range, the dissolution of CaO phase into the SiO₂ phase takes place simultaneously with the liquid sintering effect of SiO₂ phase. It is believed that the dissolution of CaO phase into SiO₂ phase at this temperature range decreases the connectivity of the SiO₂ matrix since CaO phase can act as a glass network modifier³³⁴. A decrease in connectivity, in turn, reduces the softening point and transitioning point of the glass network thus favors the liquid sintering effect of SiO₂ phase. The occurrence of liquid sintering can fill the pores and merge the two ring specimens as evidenced by the merging between the cross-sectioned specimens at 1000°C (**Figure 6-15f2**). The interfacial area between two specimens at 1000°C appears ambiguous and darker in the bright-field image compared to that at 720°C (**Figure 6-15d2**) and 900°C (**Figure 6-15e2**). This phenomenon at 1000°C indicates the sintering of the shell that significantly reduces the porosity which is in agreement with the BET surface area and average pore diameter results (**Figure A-4 and Table**

A-1, Appendix A).

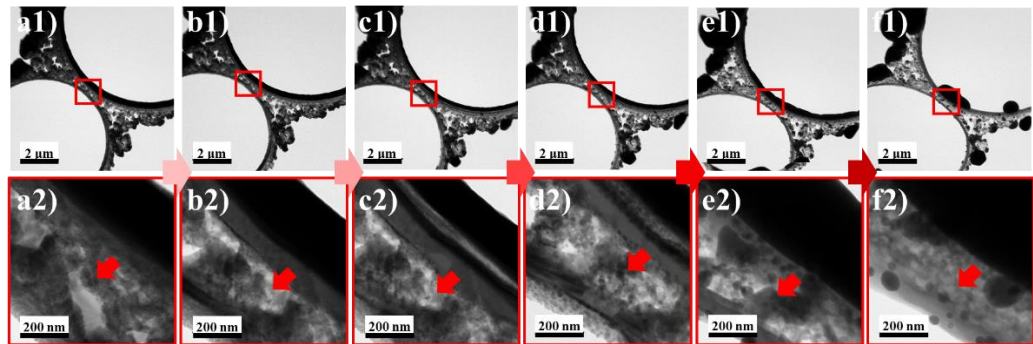


Figure 6-15. The structural transformation of the doubled-shell at different temperatures conducted by *in-situ* TEM heating observation, including: (a1-a2) room temperature; (b1-b2) 555°C; (c1-c2) 650°C; (d1-d2) 720°C; (e1-e2) 900°C; and (f1-f2) 1000°C.

Combining the results from *in-situ* XRD heating, *in-situ* TOF-SIMS, and *in-situ* TEM heating (**Figure A-2**, **Figure 6-14**, and **Figure 6-15**), a drop in the strength of the hybrid colloidal capsules from 555 to 720°C (**Figure 6-11c**) is due to the solid-state reaction between CaCO₃ nanoparticles (proximity to the external shell/internal shell interfaces) and SiO₂ inner shell (**Figure 6-14d-Figure 6-14e**). As evidenced by TGA/DTG/DSC, this reaction generates significant carbon dioxide gas (CO₂) and induces partial incorporation of calcium into the silica phase at the external shell/internal shell interfaces. During this solid-state reaction, the generated CO₂ gases diffuse outward from the external shell/internal shell interfaces to the surrounding environment. This process in turn induces the formation of not only the sparsely connected pliable spines on the capsule's surfaces but also the significant porosity in the external shell (**Figure 6-15c2-Figure 6-15e2**). In the original hybrid CaCO₃-decorated SiO₂ doubled-shell structure, with the increasing compressive strain, the discretely packed nanoparticles can form the cluster effect at the external shell, which causes an energy dissipation by the inter-particle contacts³³⁵ thus improving compressive resistance to the whole microcapsule structure³²³. However, the changes from the densely packed nanoparticles to the sparsely connected pliable spines diminish such effects and reduce compressive resistance. In addition, the presence of submicron-/nano-pores formed in the doubled-shell structure (evidenced by the shape of the N₂ adsorption-desorption curve in **Error! Reference source not found., Appendix A**) plays as the defect and reduces the integrity of the structured shell³⁰⁸. Therefore, an increase in porosity and the disappearance of the densely packed nanoparticles shell in this temperature range can eventually weaken the mechanical strength of the doubled-shell and results in a decrease in the compressive strength (**Figure 6-11c**) which is consistent with the mechanical behavior of the ceramic refractory materials³³⁶.

Meanwhile, the strain at failure remains nearly constant for the tested colloidal capsules at this temperature range compared to the non-annealed microcapsule. According to Shan et al.³³⁷, the strain at failure of the hierarchically structured hollow sphere is related to the deformation behavior of the homogenous and continuous phases, thus, the characteristics of the silica inner shell determine the strain at failure of the hybrid microcapsule in the presented study. From the *in-situ*

TEM heating observation (**Figure 6-15b-Figure 6-15e**), there are negligible changes in the structure of the silica inner shell and it is amorphous from 555 to 720°C (**Figure 6-15c-Figure 6-15e**). Although TOF-SIMS analysis (**Figure 6-14d-Figure 6-14e**) evidences the incorporation of $^{40}\text{Ca}^{2+}$ into the silica inner shell at this temperature range, *in-situ* XRD heating shows negligible phase formations and crystallization (**Figure A-2**). It has been demonstrated that the fracture failure, toughness, and brittleness of the amorphous glasses correspond to the concentration of the network modifier³³⁸ while their strain at failure depends on the strain rate and the structural characteristic of materials³³⁹. Since the inner shell remains amorphous from 555 to 720°C and the *in-situ* compression testing is all conducted in the same procedure, it is reasonable to obtain the constant strain at failure of the hybrid shell in this annealing temperature range.

On the other hand, a sudden increase in strength and strain of the colloidal capsule after annealed at 900°C and 1000°C (**Figure 6-11c**) can be attributed to both the sintering effect (**Figure 6-15b2-Figure 6-15g2**), the complete migration of calcium (**Figure 6-14f-Figure 6-14g**), and the recrystallization of amorphous calcium silicate in the inner shell (**Figure A-2, Appendix A**). While the sintering effect reduces dramatically the porosity within the shell structure and reduces the shell thickness, the formation of the tricalcium silicate crystallite phase within the amorphous shell is responsible for increased strength and strain. The significant incorporation of calcium in the silica shell network at 1000°C (**Figure 6-14g**) can reduce rigidity³⁴⁰ and improve fracture strength³⁴¹ by the formation of the calcium silicate shell. Meanwhile, the excellent ductility with a distinct plastic deformation of the 1000°C-annealed colloidal capsule can be associated with the presence of crystalline tricalcium silicate dispersed phases within the amorphous silicate shell matrix. Under mechanical compression of amorphous materials, local deformation under a high shear stress of static compression often creates adiabatic heating when the fracture propagates along the fracture plane³⁴². Such adiabatic heating creates the viscous flow within the amorphous network during compression before a complete fracture which determines the ductility of the material³⁴³. The dispersed crystalline tricalcium silicate phases within the amorphous silicate shell matrix can act as a resistance to shear deformation and enhance the degree of local adiabatic heating, thus, leading to a more significant viscous flow of the silica amorphous shell.^{342, 344} Therefore, an excellent ductility with superior fracture strength is achieved in the CaCO_3 -decorated SiO_2 doubled-shell colloidal capsule after being annealed at 1000°C.

6.2.7. Mechanical properties of the developed CaCO_3 - SiO_2 hybrid doubled-shell compared to other state-of-the-art shells

The normalized strength from our tested particles is significantly higher than those in reported literature (**Figure 6-16**) which include: traditional polyurethane (PU)³⁴⁵, Ni-P (composite of nickel and phosphorus) metallic shell³⁰², SiO_2 -PU composite shell³⁴⁶, and poly urea-formaldehyde (PUF)³⁴⁷ microcapsules. By comparison, the shell strength of 1000°C heat-treated colloidal capsules from our study is two times higher than the up-to-date metallic shell and is more than 15 times higher than the traditional polymeric and polymeric-ceramic composite shells of all published results. This mechanical enhancement can be partially attributed to the different

chemical compositions of the shell materials used to produce the colloidal capsules when compared to the ones in the literature. Besides, the small diameter of the tested individual particles ($D_o = \sim 3 \mu\text{m}$) compared to previous literature reports ($D_o > 100 \mu\text{m}$) can be another reason for such mechanical improvement. It has been reported that the mechanical properties are enhanced when the geometry of the particles decreases,³²⁰⁻³²² whereby the smaller is the capsule diameter, the higher the mechanical strength. The low porosity and the composite crystalline-amorphous microstructure of the calcium silicate shell could also be the reason for such a higher strength. For the compressive strain, the traditional polymeric (PUF) and polymeric-ceramic ($\text{SiO}_2\text{-PU}$) shells show the highest performances which are common for polymeric materials. The compressive strain of our heat-treated colloidal capsule is comparable to that of metallic shell and is double that of PU shell.

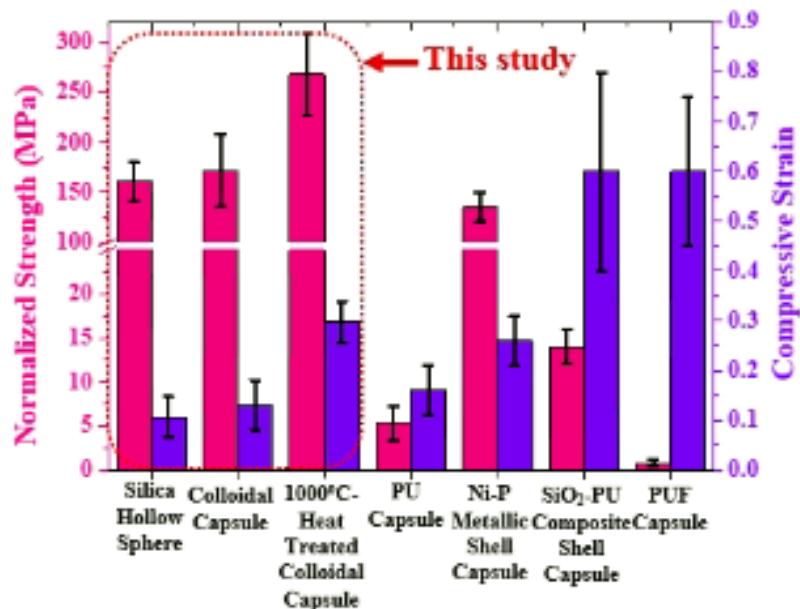


Figure 6-16. Normalized strength and compressive strain of silica hollow sphere, non-heat treated, and heat-treated colloidal capsule, compared with other reported capsule systems.

6.3. Conclusions

In this chapter, the thermomechanical properties of the designed hybrid doubled-shell $\text{CaCO}_3\text{-SiO}_2$ colloidal capsule have been investigated comprehensively. In particular, we have initially utilized several *in-situ* analytical techniques to investigate the mechanical properties of our developed colloidal capsule and the underlying mechanism by which its mechanical properties behave differently compared to the single silica shell hollow sphere. The effect of annealing temperature in modifying the mechanical behavior of the hybrid doubled-shell has also been elucidated by the newly developed technique and validated by other complementary analytical *in-situ* techniques. Several concluding remarks are pointed out as follow:

- The nanoparticles (CaCO_3) modify considerably the mechanical nature of the silica shell from semi-ductility to brittleness.

- AC-STEM has firstly been applied to reveal the intrinsic effect of nanoparticles that is due to the formation of the dispersed phase of dicalcium silicate adjacent to the interfacial areas between the shells, and the chemical bonding at the nanoparticles/silica shell interfaces.
- The significant changes in the shell strength and strain at different sizes of the colloidal capsules are closely related to the differences in the shell microstructures.
- The designed colloidal capsule can self-adjust its mechanical properties via temperature. In particular, after annealed at above 900°C, the colloidal capsule retains an intact spherical shape with a significant improvement in ductility and mechanical strength.
- Such superior characteristics can be utilized in designing the desirable smart thermo-responsive colloidal capsule for a wide range of high-temperature applications such as thermal energy storage, fire-resistant, and thermal-insulation.^{348, 349}
- The chemistry underpinning the changes in the mechanical properties of the colloidal capsule at different annealing temperatures has been unveiled by the newly developed multimodal correlative microscopy combining TOF-SIMS analysis and MEMS-based microheater in the FIB-SEM chamber.
- The results obtained by the *in-situ* TOF-SIMS heating analysis showed a strong correlation to those obtained from other complementary analytical techniques.
- Since this is the first study, to the best of our knowledge, on utilizing such a highly efficient technique, it is anticipated that several research directions now exist and also that the potential applications are not limited to the study of hybrid microcapsule mechanics at high temperatures.

Chapter 7

Lubrication and anti-oxidation of colloidal capsule encapsulating h-BN nanosheets under sodium borate melt at elevated temperatures

* This chapter content has been published in ACS Applied Materials & Interfaces 2021, 13, 6, 7714–7724, <https://doi.org/10.1021/acsami.0c20759>

Herein, the author envisages a new strategy for the application of microencapsulation technology in lubricant science. In particular, a compact hybrid colloidal capsule has been tailored that draws a series of “best in category” materials together into a single, monolithically integrated, micro-/nano-hierarchical structure with strong prospects for high-temperature lubrication. The designed hybrid colloidal capsules will be applied directly as a multifunctional additive added to a base lubricant to enhance the system efficiency with minimal harmful emissions and environmental impact. To develop such a capable capsule, the shell of the colloidal capsule should either contribute to the lubricating function or react synergistically with the base lubricant. From this perspective, we choose the designed hybrid doubled-shell $\text{CaCO}_3\text{-SiO}_2$ from the previous chapters (**Chapter 5** and **Chapter 6**) as the shell materials for the hybrid colloidal capsule.

The hybrid doubled-shell $\text{CaCO}_3\text{-SiO}_2$ colloidal capsule has been developed and characterized systematically in the previous chapters (Chapter 5 and Chapter 6). Interestingly, the hybrid shell shows excellent thermomechanical robustness with thermo-responsive characteristics at elevated temperatures. It is hypothesized that the designed hybrid shell will provide excellent protection to the encapsulated materials at high temperatures by the formation of the dense calcium silicate shell with superior strength. While the high strength of the resulted calcium silicate shell prevents the premature breakage that causes the unwanted release of the core ingredients, the dense shell network inhibits the diffusion of oxidizing components (e.g. oxygen) from the surrounding environment to the encapsulated core. These advantages inhibit the unexpected decomposition of the encapsulated core at elevated temperatures, thus, preserving the original function of the thermally unstable active materials during heating in air. Moreover, it is expected that the resulted calcium silicate shell can react to sodium borate to form the borosilicate melt containing both sodium and calcium. It has been demonstrated from the results in Chapter 4 that sodium borosilicate melt provides outstanding lubrication compared to sodium borate and the existence of calcium can reduce the boriding effect and the sodium corrosion towards the oxide scale of sodium borate melt.

We choose h-BN nanosheets as the encapsulated core material based on the results obtained in **Chapter 4**. It has been demonstrated that the oxidation of the h-BN nanosheets at elevated temperatures can cause a deterioration in lubrication performances. Although the thermal stability of the bulk h-BN is reported to be at around 1000°C, the decrease in size (to submicron/nanometer) of h-BN nanosheets leads to lower thermal stability. A previous study by Zishan et al.¹¹⁰ has

revealed that fine h-BN nanosheets can undergo oxidation to form boron oxide when conducting tribological testing at 800°C. It is further supported by Li et al.²⁴⁴ which shows the oxidation of the h-BN nanosheets starts at 800°C at which an intensity of the G band, representing the hexagonal layer, starts to decrease. At 850°C, severe oxidation of h-BN nanosheets to boron oxide is observed. Therefore, we would expect that with a mixture of (h-BN nanosheets + CaCO₃-SiO₂ doubled-shell microcapsules without h-BN + sodium borate) at elevated temperatures, a certain amount of h-BN nanosheets presented on the top coating will be oxidized in an open-air to form boron oxide and will no longer provide the friction reduction effect. In the case of h-BN-containing CaCO₃-SiO₂ microcapsules, all h-BN nanosheets are encapsulated within the CaCO₃-SiO₂ hybrid shell. When the shell is dissolved into the sodium borate melt (**Figure 7-1**), all the h-BN nanosheets will be immediately covered by the sodium-calcium borosilicate melt and be protected from oxidation. The visualization of the demonstrated concepts is shown below:

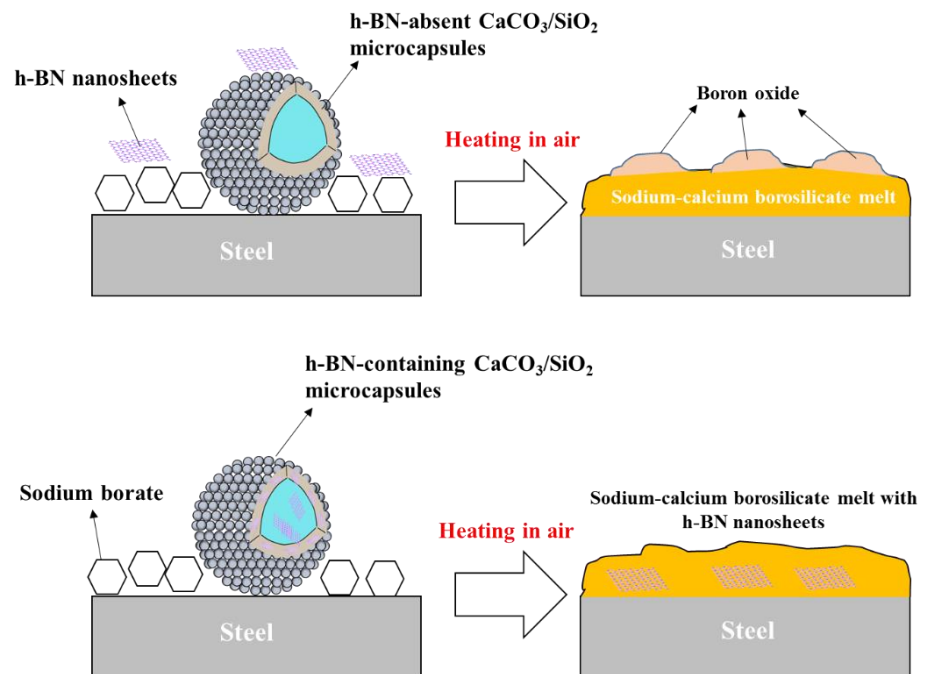


Figure 7-1. Schematic representing the advantages of encapsulating h-BN nanosheets inside the designed CaCO₃-SiO₂ doubled-shell for high-temperature lubrication application.

7.1. Experimental details

7.1.1. Reagents

Hexagonal boron nitride bulk is purchased from Momentive Performance Materials Inc and used without further purification unless otherwise noted.

7.1.2. Synthesis of h-BN nanosheets colloidal dispersion

To be encapsulated by the CaCO₃-SiO₂ doubled-shell obtained from the previous chapters (**Chapter 5** and **Chapter 6**), the h-BN nanosheets should be able to be dispersed in water and maintain a stable dispersion during the shell-forming processes. Since the pristine h-BN is

hydrophobic in nature,³⁵⁰ efforts should be made to increase the dispersion of h-BN nanosheets in an aqueous solution (e.g. water). From the literature, there are several approaches to achieve the goal that can be classified into two strategies including an application of dispersants and functionalization of the nanosheets.³⁵¹ However, using dispersants is considered not suitable for the encapsulation of h-BN nanosheets since the additional dispersants may interfere and destabilize the water-in-toluene inverse Pickering emulsion in this study. Since the dispersants are commonly amphiphilic, they can migrate to the water/oil interfaces to reduce the surface tension between two phases that detaches the stearic acid-modified CaCO₃ nanoparticles and *n*-hexylamine and resulting in the coalescence between the water droplets. Therefore, the functionalization of the nanosheets is an emerging option.

There are two strategies to functionalize the h-BN nanosheets involving non-covalent functionalization and covalent functionalization. The non-covalent functionalization depends on the use of some organic compounds that can enable connection with the basal plane of h-BN nanosheets via aromatic molecules, hydrophobic interactions, and π - π stacking.³⁵² Meanwhile, the covalent functionalization modifies the surface properties of the h-BN nanosheets based on the functional groups that chemically bonded at the edges.³⁵³ From these fundamental understandings, covalent functionalization is preferable since it will limit the unexpected interference of additional compounds to the stability of the inverse Pickering emulsion.

Therefore, in this chapter, h-BN nanosheets aqueous dispersion is fabricated by covalent functionalization method followed the approach of Lei et al.³⁵⁴ In a typical procedure, bulk h-BN and urea are mixed (1:60 weight ratio) in a steel milling container which is positioned in a planetary ball mill (Pulverisette 7, Fritsch). The mixture is ball milled at a rotation speed of 700 rpm for 20 h at room temperature under the nitrogen atmosphere. After intensive ball milling, the obtained powders are dissolved in deionized water under ultrasonication and the aqueous dispersion is dialyzed for a week (membrane cutoff: 3,500 kDa) in de-ionized water to remove the excessive urea. Stable h-BN nanosheets aqueous dispersions with a concentration of 2.8 mg/ml are then obtained. The concentration of the h-BN nanosheets can be further increased by heating the solution to evaporate water following by intense ultrasonication.

7.1.3. Synthesis of smart h-BN nanosheets-containing colloidal capsules

The smart functional colloidal capsules are synthesized based on the method proposed in **Chapter 5** with similar hybrid CaCO₃-SiO₂ double-shell materials. In general, stearic acid-coated calcium carbonate nanoparticles (0.5 g) are diluted in toluene (10 ml) by ultrasonication in 10 mins (Bandelin Ultraschall 1955, 6 mm tapered tip, 100 W output). Subsequently, 1 ml of h-BN nanosheets aqueous dispersions (5.6 mg/ml) is added to the mixture under high-shearing emulsification for 3 mins (Ultra Turrax T-25, 20000 rpm). 0.5 ml *n*-hexylamine is added thereafter to the emulsion under magnetic stirring which acts as the catalyzing agent for the shell formation.²¹⁶ A total of 1 ml TEOS is added dropwise to the emulsion multiple times (0.5 ml, 0.3 ml, and 0.2 ml). The time span for each addition is 8 hours and after the final addition, the mixture is left to react in 24 h, while the stirring is maintained. The resulting microcapsules are washed by

acetone, ethanol, and distilled water respectively. To identify the function of the h-BN nanosheets in lubrication performances, the colloidal capsules without h-BN nanosheets are synthesized, as a reference, by the optimized conditions in **Chapter 5**.

7.1.4. High-temperature oxidation and friction and wear testing

The high-temperature oxidation experiment and the hot-friction test are performed in a Bruker Universal Mechanical Tester (UMT) using the reciprocating module positioned in a furnace. Such a module has been acknowledged as suitable to simulate lubricated hot metal forming conditions such as in hot forging, hot stamping, and hot rolling.²⁸ A stainless steel plate (14x11x3 mm³, $R_a = 1 \mu\text{m}$) is chosen as the moving part, while a GCr15 ball (6.35 mm diameter, $R_a = 20 \text{ nm}$) is selected as a stationary part.

The setting temperature of the furnace for the friction test is 820°C, resulting in the actual temperature of the disc being 880°C. The discrepancy between the set and disc temperatures can be explained as following. The protective covers of the heating coils were made from high-temperature steel and they were in close contact with the heating coils. At high temperatures, these covers expanded and touched the heating coil which caused the short circuiting of the electrical coils and resulted in excessive current being supplied to the system, thus, resulting in a higher temperature than being set. The temperature measurement of the disc was frequently conducted before each test with an external thermocouple being positioned on the disc surface to confirm the disc temperature. The measurement showed a higher temperature, by approximately 60°C, compared to the set temperature and this difference was consistent during different repeated tests. The normal force is set at 10 N throughout the friction test (10 mins), which corresponds to an initial Hertzian contact pressure of 1.45 GPa between the two oxidized surfaces generated on the disc and ball. In addition, the sliding speed is kept at 1 Hz with a 10 mm stroke length. Before the friction test, a certain amount of the colloidal capsules is mixed into sodium borate aqueous solutions (0.5 wt.% sodium borate) that yield the capsule/borate weight ratio of 1:1. The tested lubricants are summarized and named in **Table 7-1**. They are drop-coated on the disc surface by water evaporation at 100°C that yields a lubricant concentration of 0.83 ml/cm² before conducting the high-temperature test. The hot lubrication test is performed at least three times to ensure reproducibility. A ContourGT-K 3D Optical Microscope is used to record the 2D/3D wear profile of the ball wear scar and the disc groove wear track. Vision64 software coupled with the microscope is used to calculate the wear loss volume in the middle areas of the wear track. In the case of the ball wear loss, the calculation for non-flat wear scars and compound curvatures is following the approach by Jun et al.³⁵⁵

Table 7-1 Composition and lubricant naming convention.

Composition	Lubricant name
Dry testing – no lubricant	D-L
1 wt.% colloidal capsule aqueous lubricant	C-L
1 wt.% sodium borate aqueous solution	B-L

1 wt.% (capsule (without h-BN) + sodium borate) (1:1) aqueous solution	C-B (1:1)
1 wt.% (capsule (with h-BN) + sodium borate) (x : y)* aqueous solution	BN@C-B (x:y)*
*x : y = 1:2, 1:1, 2:1, and 9:1	

7.2. Results and Discussion

7.2.1. Characterization of the amine-functionalized h-BN nanosheets

Shown in **Figure 7-2** is the characterization of the obtained h-BN nanosheets after an intense reactive ball milling process followed by dialysis in water. The obtained h-BN nanosheets after a one-step preparation have a lateral size of less than 200 nm with a lamellar morphology (**Figure 7-2a**). The TEM image suggests that the h-BN nanosheets are flat and quite thin. The high-resolution TEM (HRTEM) in **Figure 7-2b** shows the presence of the fringes from the h-BN nanosheets. It can be observed that there are less than ten parallel fringes from the observed regions which indicate the formation of few-layered h-BN nanosheets. The inverse fast fourier transition (IFFT) image at the selected area in **Figure 7-2b** shows the spacing distance between the layer of around 0.335 nm which is common for the layered 2D materials (**Figure 7-2c**). Additionally, the water contact angle droplet indicates increased hydrophilicity of the prepared few-layered h-BN nanosheets compared to the pristine h-BN (**Figure 7-2d**). It is due to the functionalization of the amine (NH₂) groups at the edges of the h-BN nanosheets which have a high affinity to water. As can be seen, the colloidal dispersion of the obtained h-BN nanosheets in water shows remarkable stability against phase separation and precipitation of solid particles even after 6 months. The structure, morphology, and characteristics of h-BN nanosheets obtained in this study show good agreement with the results from Lei et al.³⁵⁴ which indicates the reproducibility and efficiency of the approach.

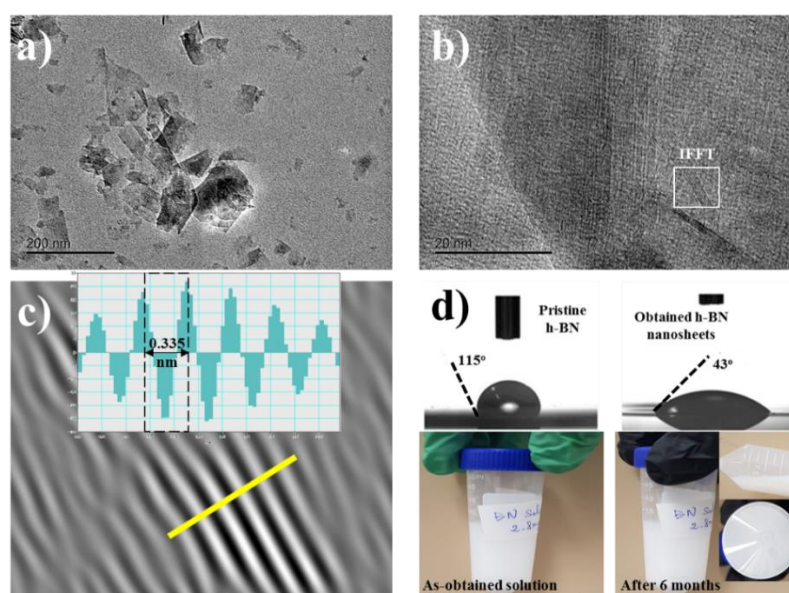


Figure 7-2. (a) Low-magnification TEM image of the h-BN nanosheets; (b) High-magnification TEM image of the h-BN nanosheets showing the layered structure; (c) Inverse Fast Fourier

Transform (IFFT) from the white marked area in (b). The inset picture in (c) indicating the d-spacing between each layer; (d) a photograph of the water droplet on pristine h-BN and amine-functionalized h-BN nanosheets from Lei et al.³⁵⁴. Digital images show the stable h-BN colloidal dispersion in water after 6 months.

7.2.2. Synthesis of a smart responsive h-BN-containing CaCO₃-SiO₂ hybrid colloidal capsules

The synthesis of smart-responsive colloidal capsules has been conducted by Pickering emulsion templated assembly with the use of dispersed phase of h-BN colloidal dispersion in water (**Figure 7-3**). The obtained colloidal capsule is applied as a multifunctional lubricant additive for hot metal forming lubricants to demonstrate the concept. The final BN-containing CaCO₃-decorated SiO₂ colloidal capsule comprises several functional solid lubricant additives for high-temperature lubrication such as: h-BN nanosheets, CaCO₃ nanoparticles, and SiO₂ glass. While h-BN nanosheets will contribute to friction reduction, silica glass and CaCO₃ nanoparticles will improve the wear resistance and oxidation-prevention of the tribofilm on the worn surfaces. Here a significant modification in the synthesis process compared to the previous chapters has been conducted to add the h-BN nanosheets to the water core. In principle, the h-BN nanosheets colloidal dispersion in water is used as the dispersed phase rather than pure water. The presence of amine-functionalized h-BN nanosheets may contribute to the stability of the inverse Pickering emulsion. Since the basal plane of h-BN is hydrophobic³⁵⁶ and the functionalization of amine groups at the edge can introduce hydrophilicity,³⁵⁴ it is expected that fraction of functionalized h-BN nanosheets with a large lateral size have an amphiphilic effect that can affect the stability of the emulsion. It is hypothesized that these amphiphilic nanosheets will migrate to the water/toluene interface and co-stabilize the water droplets simultaneously with *n*-hexylamine and CaCO₃ nanoparticles (**Figure 7-3**).

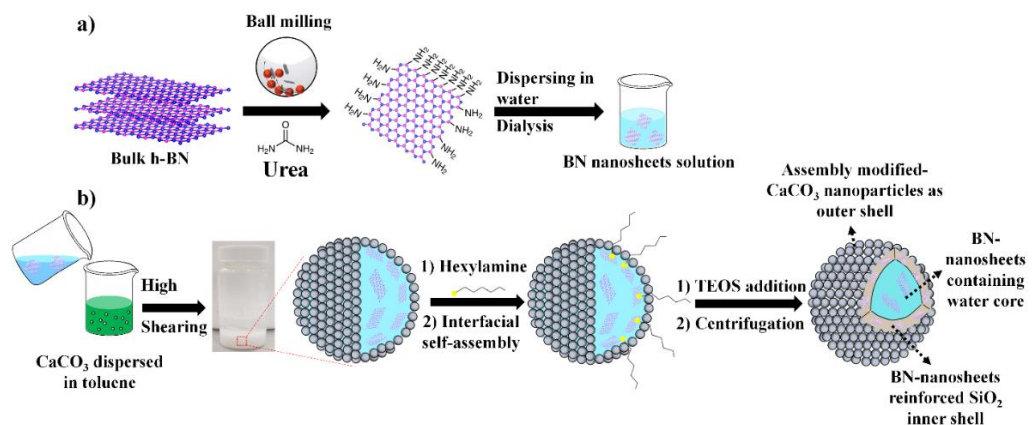


Figure 7-3. The synthesis process of the smart functional BN-containing colloidal capsules: a) h-BN nanosheets solution preparation; and b) Fabrication of BN-containing colloidal capsules.

It has been demonstrated in **Figure 7-4** that the concentration of the h-BN nanosheets in the water core plays a crucial role in the formation of the hybrid colloidal capsule. It can be seen that there

is a significant fracture of the hybrid colloidal capsule when no h-BN nanosheets are presented in the water core under the synthesis conditions applied in this study (**Figure 7-4a**). The size distribution in **Figure 7-4b** indicates that only small capsules survived after the synthesis processes. This significant fracture indicates that the inverse Pickering emulsion stabilized by 0.5 g stearic-acid modified CaCO_3 nanoparticles is not stable during the hydrolysis and condensation of TEOS. It is in good agreement with the results presented in **Chapter 5**. An addition of h-BN nanosheets can result in a more stable emulsion system since h-BN nanosheets in this study have an amphiphilic characteristic.³⁵⁴ It is hypothesized that a fraction of h-BN nanosheets will accumulate at the water/oil interfaces and contribute to the stabilization of the emulsion system besides the CaCO_3 nanoparticles. **Figure 7-4c** shows an increase in the amount of capsule formation. A size distribution (**Figure 7-4d**) reveals more capsules at larger diameters when 2.8 mg/ml h-BN nanosheets are applied in the water core. However, there are still a number of capsule fractures in this condition. Interestingly, almost no capsule fracture is observed when the concentration of h-BN nanosheets in water increases to 5.6 mg/ml (**Figure 7-4e**). Size distribution in this condition is identical to Gaussian distribution which indicates the mean average size of the colloidal capsules is $10.1 \pm 2.5 \mu\text{m}$. Thus, a successful formation of the colloidal capsule is observed in the case of 5.6 mg/ml h-BN nanosheets in water and this concentration is used to synthesize the hybrid colloidal capsule for high-temperature lubrication.

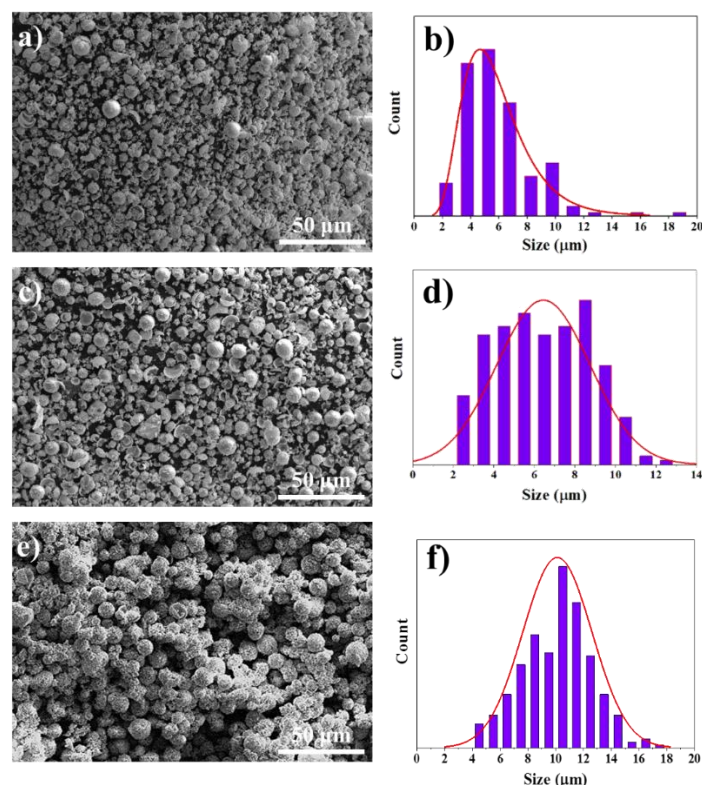


Figure 7-4. SEM image and size distribution of the formed colloidal capsule at different h-BN nanosheets concentration in water: (a)-(b) no h-BN nanosheets in water; (c)-(d) 2.8 ml/mg h-BN nanosheets in water; and (e)-(f) 5.6 mg/ml h-BN nanosheets in water.

7.2.3. Characterization of the as-prepared h-BN nanosheets-containing $\text{CaCO}_3\text{-SiO}_2$

hybrid colloidal capsule

XRD patterns indicate the calcite peaks (from CaCO_3 nanoparticles) and the broad hump of amorphous silica in both the capsule with and without h-BN nanosheets (**Figure 7-5a**). However, there is no obvious intensity signal of the h-BN nanosheets peaks in the XRD patterns of the capsule containing the h-BN (**Figure 7-5a**). It can be due to the low amount of the h-BN nanosheets added to the microcapsules compared to other existing materials (CaCO_3 nanoparticles and SiO_2). Therefore, Raman analysis is applied which detects a small peak at 1367.1 cm^{-1} (**Figure 7-5b**). It is related to the in-plane vibrating mode of h-BN (E_{2g})³⁵⁷ that further proves the presence of h-BN nanosheets in the microcapsules. Shown in **Figure 7-5c** is the intact spherical colloidal capsule which has rough external surfaces from the self-assembly of numerous CaCO_3 nanoparticles. The TEM image (**Figure 7-5d**) reveals the hollow interior structure of the obtained colloidal capsules with possible h-BN presenting but it is ambiguous.

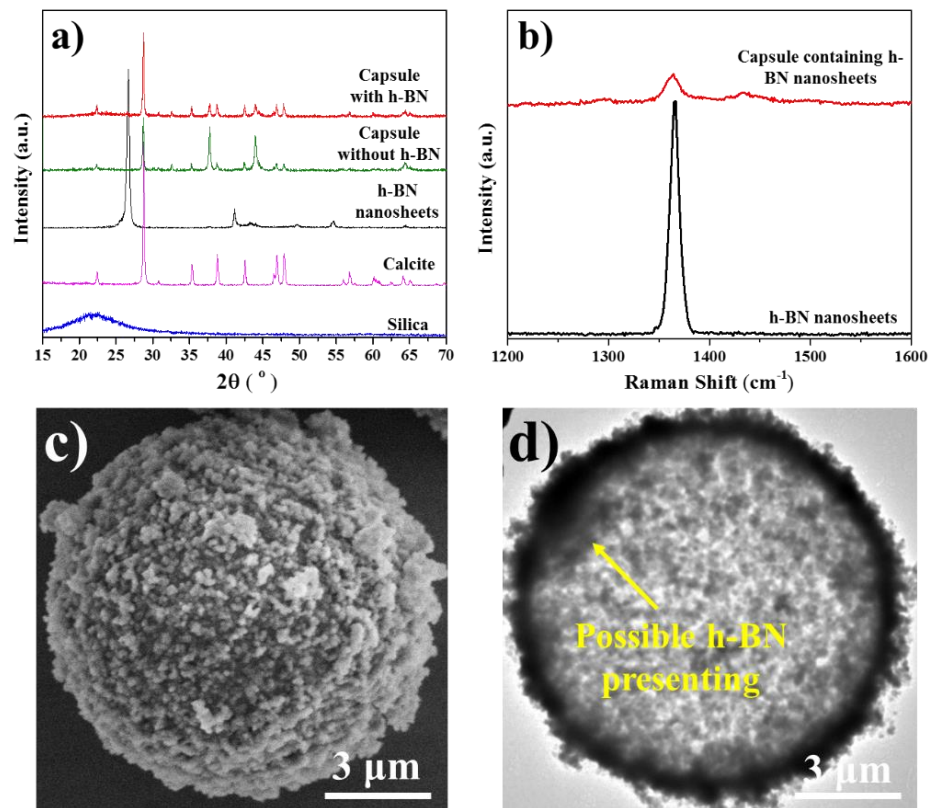


Figure 7-5. (a) X-ray diffraction analysis of the materials; (b) Raman analysis of the hybrid microcapsules and h-BN nanosheets; (c) SEM image of the external shell morphology of a single colloidal capsule; (d) Internal structure inspection by TEM.

From the previous Raman analysis (**Figure 7-5a**), it has been confirmed that there is the presence of h-BN nanosheets from the colloidal capsules. However, due to a significant aggregation of the CaCO_3 nanoparticles on the external shell, it is difficult to observe distinctively the encapsulated h-BN nanosheets. To determine the exact position of h-BN nanosheets, an individual colloidal capsule is cross-sectioned into a thin ring by FIB that is mounted on the M-copper grid for further STEM characterizations (**Figure 7-6a**). Shown in **Figure 7-6b** is the overview of the large ring

which is examined in detail by AC-STEM/EELS in the next section. There is damage at the top of the ring specimen which is due to the high applied current during the cross-sectioning process. However, the majority of the ring remains intact which can be further analyzed.

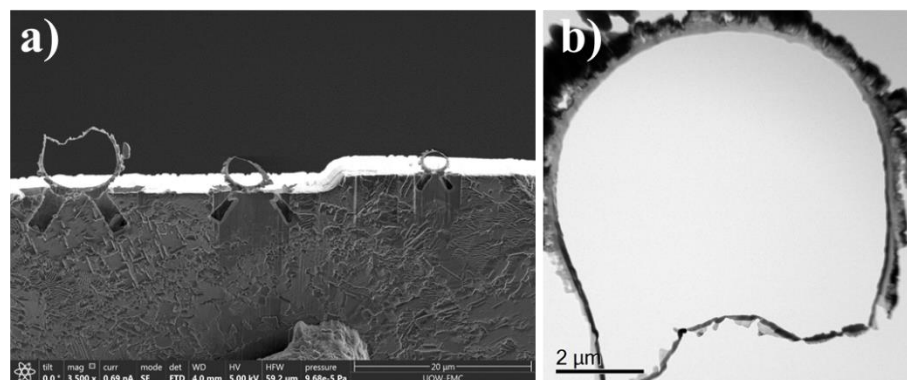


Figure 7-6. a) SEM image showing the cross-sectioned shells by FIB which were prepared for the STEM characterization; b) Bright-field (BF) STEM image of the biggest ring.

Scanning transmission electron microscope (STEM) bright-field (BF) image of the cross-sectioned ring at the region of interest (**Figure 7-7a**) shows small diffraction contrast areas at the CaCO_3 nanoparticles/ SiO_2 shell interface. These areas show the possibility of the nanosheets presenting. According to the high-angle annular dark-field image (HAADF), these areas have low atomic contrast (**Figure 7-7b**). EDS analysis across the ring specimen shows the presence of calcium (Ca) and carbon (C) at the external shell while silicon (Si) at the inner shell proving the formation of the hybrid doubled-shell (**Figure 7-7a**). The presence of silica skin covered the CaCO_3 nanoparticles is also observed with the existence of Si signal at the external shell where Ca presents (**Figure 7-7a**). Apart from these elements, boron (B) and nitrogen (N) signals are observable in EDS mapping analysis (**Figure 7-7c**). The signals of B and N are significant at the low diffraction and atomic contrast areas detected in **Figure 7-7a-Figure 7-7b** (**Figure 7-7c**).

Aberration corrected (AC)-STEM is conducted at the red square marked area in **Figure 7-7a** which reveals the presence of stacked nanosheet (lateral size of ~ 100 nm) (**Figure 7-7d**). The h-BN nanosheet contains several layers (total thickness of ~ 15 nm) with a d -spacing between each layer of 0.335 nm (**Figure 7-7d**). A further electron energy loss spectroscopy (EELS) analysis (Figure 1e) confirms the existence of electronic transitions involving σ^* (ii and iii) or π^* (i) states in B K edge and N K edge, which is characteristic of the h-BN nanosheets.^{358, 359} The finding of small h-BN nanosheets within the silica shell has proven the high water-affinity and amphiphilic characteristics of the synthesized h-BN nanosheets which act as the stabilizing agent in conjunction with CaCO_3 nanoparticles rather than diffuse to the toluene phase during the capsule formation. It is expected that a fraction of large h-BN nanosheets are contained in the water core and they will be released simultaneously with the h-BN nanosheets in the shell during the rupture of the capsules.

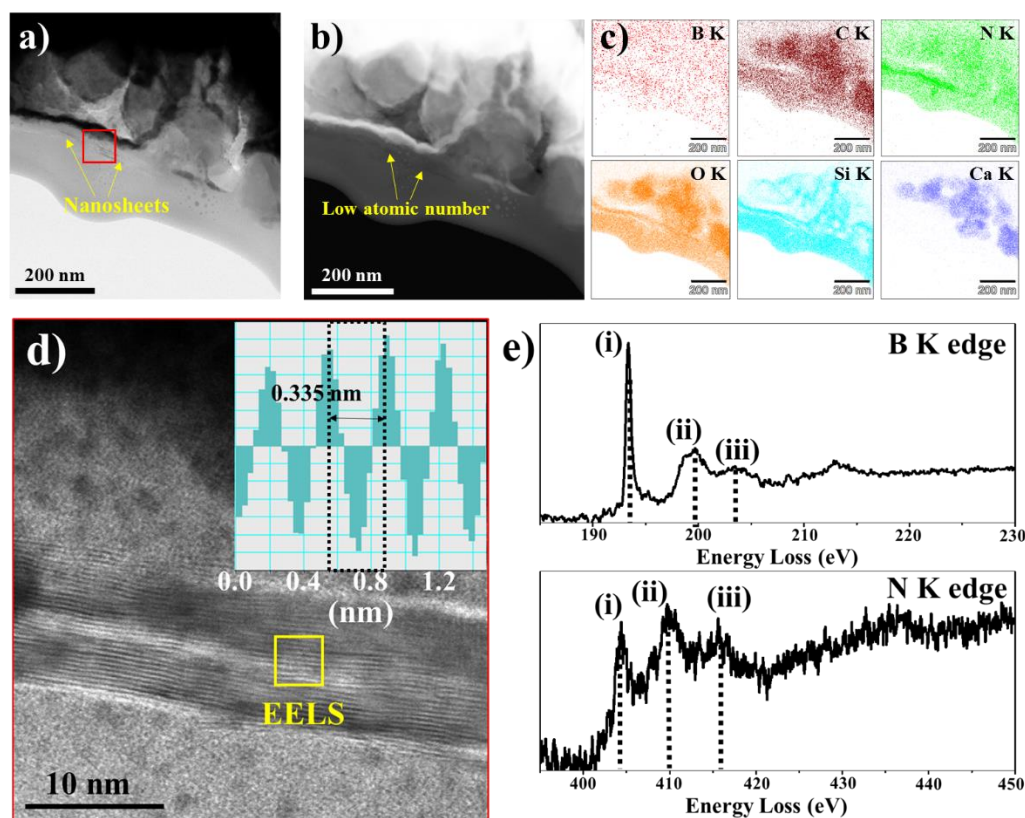


Figure 7-7. (a) STEM-BF image of the cross-sectioned shell; (b) High-angle annular dark-field (HAADF) image of the cross-sectioned shell; (c) EDS mapping showing the elemental distribution within the cross-sectioned shell; (d) AC-STEM image of the red square marked in (a); (e) EELS B-K edge and EELS N-K edge spectrums extracted from the yellow square marked in (d). An inset image in (d) is the d-spacing measurement between the fringes from the IFFT of the fringe area.

7.2.4. A smart-responsive colloidal capsule as a multifunctional additive for sodium borate melt lubricant at elevated temperatures

In this study, a certain amount of the colloidal capsules is mixed into sodium borate-containing aqueous solutions (0.5 wt.% sodium borate) that yield the capsule/borate weight ratio of 1:1. It can be seen that the colloidal capsules show an excellent dispersion in the aqueous medium after intense sonication and they can manually redisperse quite easily after long-time storage by simple handshaking (**Figure 7-8**). The mixture, named BN@C-B (1:1), is then coated on the ground stainless steel plate resulting in the 0.83 ml/cm² coated lubricant on the steel surfaces. To quantify the improvement in oxidation resistance and lubricity, other lubricants, including: dry (D-L), capsule-coating (C-L), borate-coating (B-L), and (capsule without h-BN + sodium borate)-coating (C-B (1:1)), are also tested.

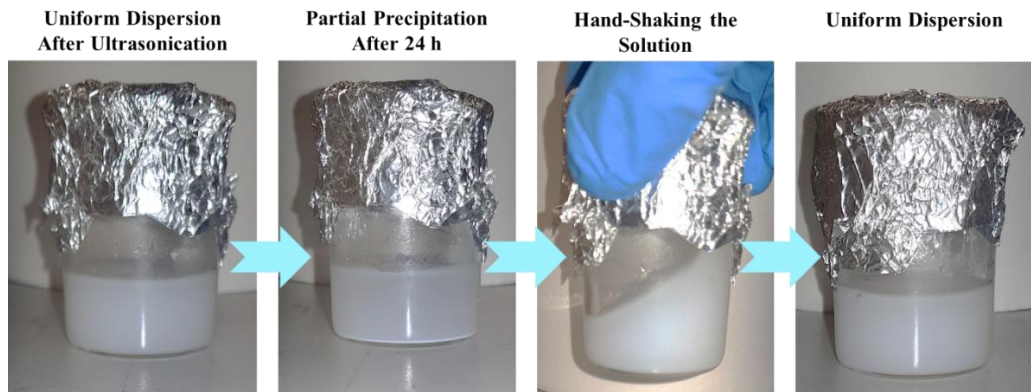


Figure 7-8. High dispersibility of the BN-containing colloidal capsules in the borate-based aqueous lubricant.

The following results show that the designed colloidal capsule can significantly enhance the anti-oxidation and the lubricity of existing melt lubricants. High-temperature oxidation tests are carried out under an air atmosphere at the disc temperature of 880°C for an hour. The coating of only colloidal capsules on the surface (**Figure 7-9b**) reveals a presence of serious thermal cracks and the peeling-off occurrence under isothermal oxidation test at 880°C which is similar to the non-coated steel surface (D-L) (**Figure 7-9a**). Although the coating of the only colloidal capsule can reduce the oxide thickness by a certain degree (from 66.9 to 41.9 μm) (**Figure 7-9a-Figure 7-9b**), it has been acknowledged that the peeling off and the thermal cracks are the results of the significant difference in hardness, ductility, and thermal expansion of steel and its oxide.³⁶⁰ They are the characteristic of poor anti-oxidation. In contrast, B-L, an excellent oxidation inhibitor, can reduce the oxide thickness by 81.7% (12.2 μm oxide thickness, **Figure 7-9c**) compared to the non-coating steel (D-L) (66.9 μm oxide thickness, **Figure 7-9a**). The C-B (1:1) (**Figure 7-9d**) and BN@C-B (1:1) (**Figure 7-9e**) deliver the best anti-oxidation among the tested coatings that produced a significantly thin oxide layer of 4.5-4.7 μm . It is a total of approximately 93.3% oxidation-reduction compared with the non-coated steel surface (D-L). Although an application of capsule-coating (C-L) and sodium borate-coating (B-L) reduces the oxidation of steel by a certain degree with a total oxide thickness reduction of 33.3% and 81.7% respectively (**Figure 7-9f**), they showed several limitations in their performances compared to C-B (1:1) and BN@C-B (1:1). Therefore, an addition of the colloidal capsule with or without h-BN nanosheets to the borate melt improves the anti-oxidation performances of sodium borate melt at elevated temperatures and results in smaller oxide scale development (**Figure 7-9f**). It can be concluded from the oxidation results that the CaCO_3 nanoparticles and SiO_2 shell play an important role in improving the oxidation resistance of sodium borate melt while h-BN shows a negligible effect.

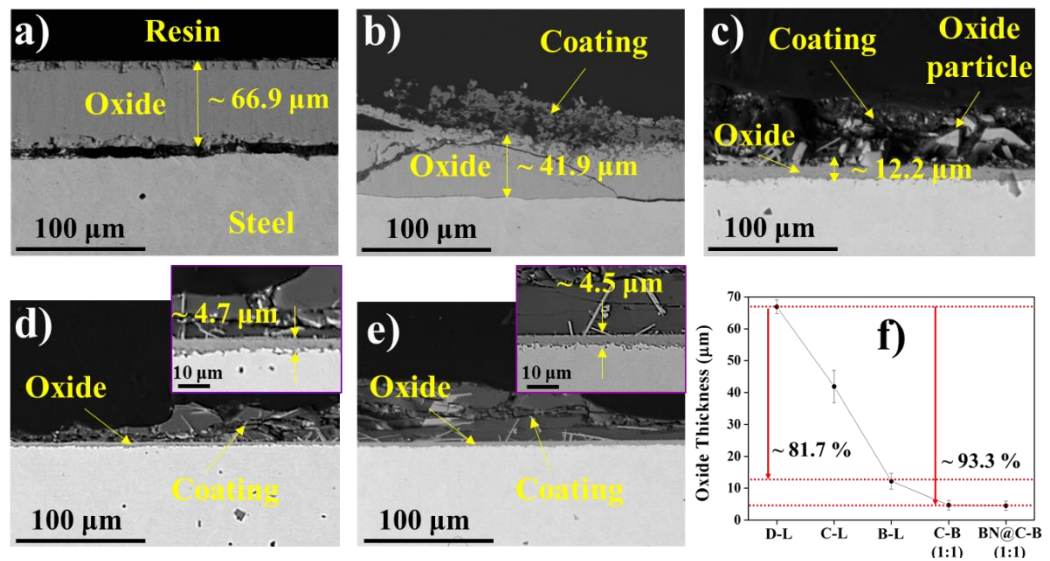


Figure 7-9. Oxide scale development after isothermal oxidation test at 880°C with different lubricant coatings: (a) no lubricant coating (D-L); (b) colloidal capsule-coating (C-L); (c) sodium borate melt coating (B-L); (d) colloidal capsule (without h-BN nanosheets) + sodium borate melt coating (C-B (1:1)); and (e) colloidal capsule (with h-BN nanosheets) + sodium borate melt coating (BN@C-B (1:1)). (f) Measured oxide thickness on steel under different coatings.

At elevated temperatures, the fully developed melt of sodium borate wet the hot steel surfaces and chemically entraps the ionic charge species (Fe^{2+} , Mn^{2+} , Cr^{2+} , etc.) generated from the steel base as confirmed by EDS in **Figure 7-10c**. It thus prevents the development of the oxide scale layer by inhibiting the further reaction of such charge species with the oxygen at the oxide/air interfaces.³⁶¹ The outward diffusion of alkali element (Na) from the melt lubricant plays a significant effect on the oxidation of the coated steel.³⁶¹ However, the significant diffusion of alkali to the oxide can cause a corrosion attack to the protective scale³⁶² and promote the formation of the cation vacancies.³⁶³ Particularly, sodium borate melt has a significantly strong alkali (Na) diffusion toward the oxide surfaces even under isothermal static heating conditions without the stressed-shearing applied.¹⁵⁵ Since the formation of iron boroferrite is thermodynamically favorable at high temperatures,³⁶⁴ the selective outward diffusion of iron occurs through the vacancies within the chromium oxide scale under sodium borate melt that results in the oxidation promotion (**Figure 7-10c**). Adding the colloidal capsules with and without h-BN nanosheets to the borate melt can hinder the development of the iron boroferrite and results in less oxide scale development (**Figure 7-10c-Figure 7-10e**). It is mainly due to the formation of the sodium-calcium borosilicate melt from the high-temperature reactions between the CaCO_3 nanoparticles, silica shell, and the sodium borate while h-BN nanosheets do not contribute much to the oxidation resistance. **Figure 7-10d** and **Figure 7-10e** show the existence of sodium (Na), calcium (Ca), and silicon (Si) within the melt which indicates the dissolution of the colloidal capsule's shell into sodium borate at elevated temperatures. Further details about the anti-oxidation mechanism of the resulted sodium-calcium borosilicate melt will be discussed in the next chapter.

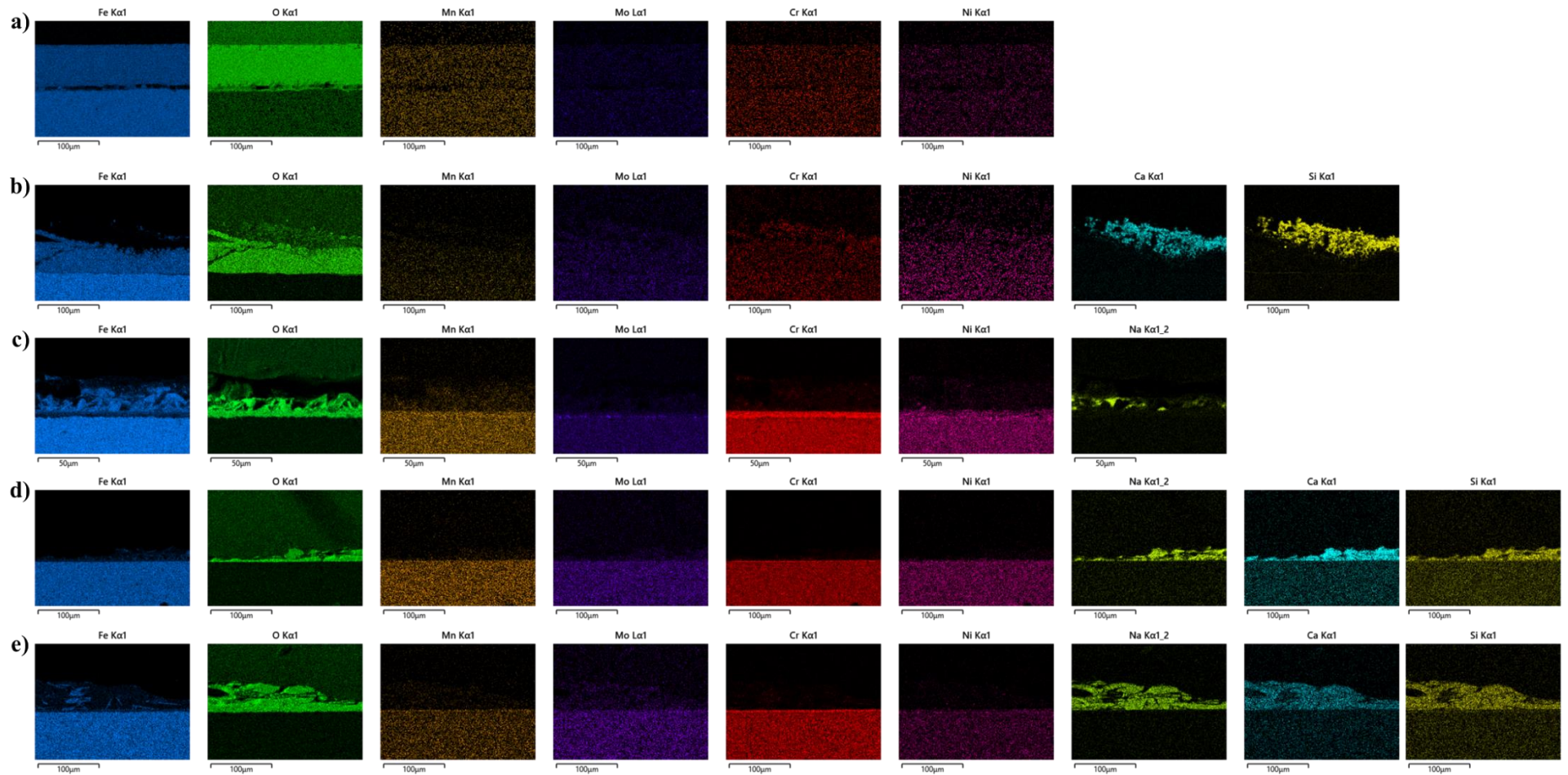


Figure 7-10. EDS mapping of the oxide and coating on the stainless steel after isothermally heat-treatment at 880°C from: a) Dry oxidation (D-L); b) Capsule-coating (C-L); c) Sodium borate-coating (B-L); d) capsule without h-BN + Sodium Borate (C-B (1:1)); and e) BN-containing capsule + Sodium Borate (BN@C-B (1:1)) test.

The friction and wear resistance of the steel/steel contact and the fundamental mechanisms of the *in-situ* formation of sodium-calcium borosilicate have been determined by a ball-on-plate tribometer at 820°C (disc temperature of 880°C) under an initially applied pressure of 1.45 GPa Hertzian pressure using the reciprocating module positioned in a furnace. In general, the presence of the only capsule particles at the sliding interfaces (C-L) increases significantly the steady-state friction coefficient (0.45) compared to the dry sliding (D-L) (0.36) (**Figure 7-11a-Figure 7-11b**). Such occurrence is expected since the colloidal capsules transform their doubled $\text{CaCO}_3\text{-SiO}_2$ hybrid shell structure into a single calcium silicate shell rather than melt at elevated temperatures.³²³ The resulted calcium silicate shell hollow sphere with high strength and excellent ductility³²³ may enter the sliding contacts and act as third-body abrasive particles.

Sodium borate melt (B-L) decreases the coefficient of friction by 32.1% compared with the D-L and establishes a steady-state value at 0.25 within 150 s (**Figure 7-11a-Figure 7-11b**). The addition of the colloidal capsules without h-BN nanosheets to sodium borate melt (C-B (1:1)) reduces the friction coefficient by 38.7% (**Figure 7-11a-Figure 7-11b**). Thus, it can be concluded that the sodium-calcium borosilicate melt can also provide excellent lubricity apart from the anti-oxidation performance. Interestingly, a total of 69.5% reduction in friction compared with the sodium borate melt (B-L) (**Figure 7-11b**) is achieved when the BN-containing colloidal capsules are applied with the sodium borate melt (**Figure 7-11a-Figure 7-11b**). Unprecedented ultralow friction of 0.07 (a total of 79.3% reduction compared with dry sliding) at elevated temperatures (880°C) is ultimately achieved after only less than 50 s of sliding (**Figure 7-11a-Figure 7-11b**). It can be due to the synergistic effect between the formation of sodium-calcium borosilicate melt and the release of h-BN nanosheets. Since h-BN nanosheets have a low-shearing effect and high-load carrying capability,¹⁰⁴ it can further reduce friction during sliding.

For the wear rate, the presence of the melt lubricants rendered a significant reduction in wear in the rubbing steel/steel contacts (**Figure 7-11c-Figure 7-11d**). Sodium borate melt (B-L) contributes to a reduction of wear rate by 27.5% and 37.8% for the plate and ball respectively compared with the dry sliding test (D-L). Unlike the melt lubricant, the wear losses of both counterparts increase dramatically when only the colloidal capsules are applied to the sliding surfaces (C-L), which increases the friction coefficient. The addition of the colloidal capsules with and without h-BN nanosheets to the borate melt (BN@C-B (1:1) and C-B (1:1)) reduces dramatically the wear rate of the counterparts by more than 70% compared to the case lubricated by sodium borate melt (B-L) (**Figure 7-11c-Figure 7-11d**). BN@C-B (1:1) delivers the best anti-wear performance with a total of 80% wear reduction compared to the dry sliding test (D-L).

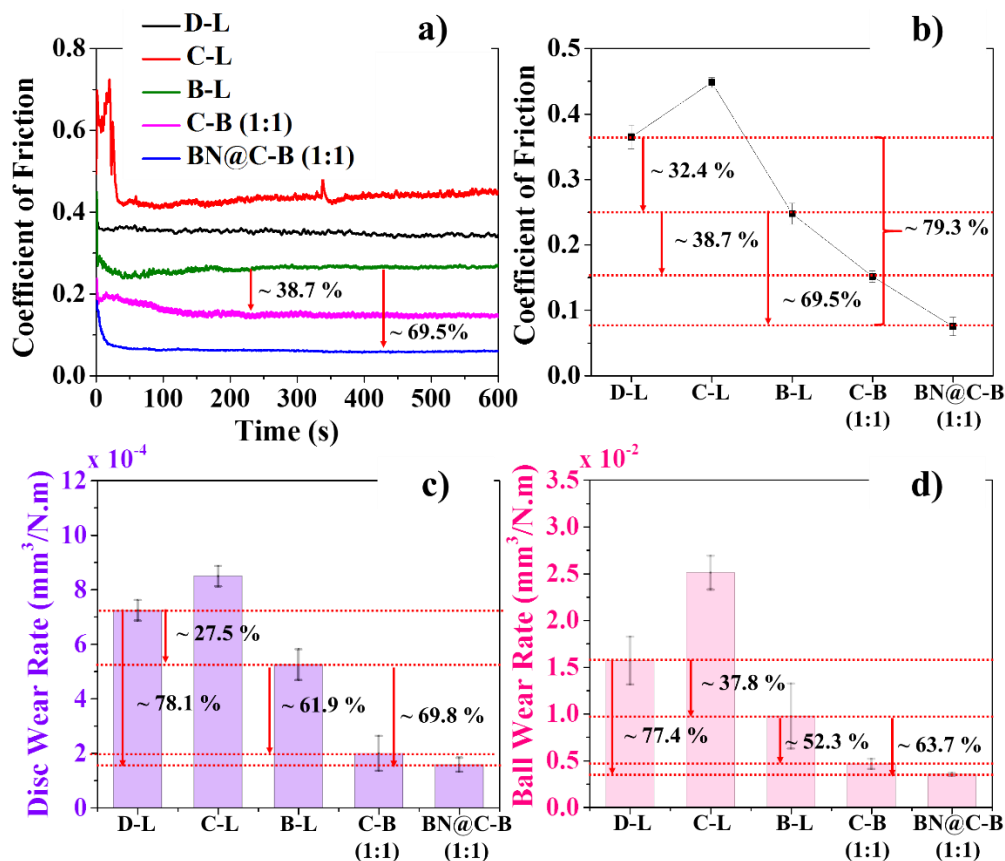


Figure 7-11. (a) Dynamic friction coefficient of the lubricants at 880°C, 10 N (1.04 GPa), and 1 Hz; (b) Average coefficient of friction at the steady-state; (c) Disc wear rate; and (d) Ball wear rate after hot friction tests with different lubricants.

Different testing conditions, including: temperature, loading, speed, and capsule/borate ratio, have been implemented. At first, the results demonstrate that BN-containing colloidal capsules probably improve the lubricity of sodium borate melt at 880°C even at low concentration (BN@C-B (1:2)) (Figure 7-12a-Figure 7-12d). However, the tribological performance of the borate-capsule mixture deteriorates at a higher colloidal capsule concentration (BN@C-B (2:1) and BN@C-B (9:1), at 880°C (Figure 7-12a-Figure 7-12d). It can be related to the presence of several unmelted capsules, due to an insufficient sodium borate melt, at the sliding interfaces that act as a third body abrasive. Thus, the borate-capsule mixture with the ratio of (1:1) (BN@C-B (1:1)) delivers the best lubrication in terms of friction reduction and wear alleviation among other ratios in the same testing conditions at 880°C.

It has been demonstrated that excellent lubricity emerges when: 1) the glass lubricants partially/fully melt on the hot surfaces; 2) the stable tribofilm is formed due to a sufficient reactivity of the glass lubricants toward the hot sliding surfaces.³⁶¹ In this study, the BN@C-B (1:1) performs its best lubrication at 880°C with ultralow friction and exceptional wear reduction in both counterparts (Figure 7-12e-Figure 7-12h). At 680°C, this lubricant retains its rigid and solid coating which leads to a massive friction coefficient of 0.88. A fluctuation in the friction curve at 680°C indicates the subsequent removal and delamination of the bulk materials during the sliding that results in a high wear rate in both plate and ball (Figure 7-12g-Figure 7-12h). When

the temperature reaches 780°C, the friction and wear rate of both counterparts decrease significantly. It is associated with the partial melting of the BN@C-B (1:1) lubricant and the sufficiently stable tribofilm formed on the wear tracks. However, at 980°C, the lubricity deteriorates significantly which results in a large increase in friction (**Figure 7-12e-Figure 7-12f**). A high ball wear rate and a negligible disc wear rate (**Figure 7-12g-Figure 7-12h**) indicate that the formation of hard abrasive iron boroferrite hardens the plate surfaces and causes the abrasion of the ball counterparts.³⁶⁵

Other hot friction tests at different operating conditions confirmed that the BN@C-B (1:1) provides an excellent lubricity under a mixed/boundary lubrication regime. An increase in applied pressure (up to 2.09 GPa) and a decrease in sliding velocity (to 0.5 Hz) cause an increase in friction and wear losses of both counterparts (**Figure 7-12i-Figure 7-12p**). In particular, the coefficient of friction increases slightly from 0.07 to 0.08 when the sliding velocity is doubled (**Figure 7-12m-Figure 7-12n**, from 1 Hz to 2 Hz). Meanwhile, a further increase or decrease in sliding velocity to 3 Hz or 0.5 Hz increases the friction coefficient to 0.16 and 0.2 respectively. It can be concluded that the testing conditions, where the ultralow friction and wear occur (1 Hz and 2 Hz), are in a mixed lubrication regime. An increase in friction coefficient at 0.5 Hz sliding speed is due to a shift toward boundary lubrication regime that causes more asperities contact between the sliding surfaces. On the other hand, the highest sliding velocity at 3 Hz shifts the lubrication toward the hydrodynamic regime where the viscosity of the melt lubricant plays a dominant role. According to the Stribeck curve,³⁶⁶ the lubrication at the mixed regime shows the best performance in friction coefficient compared to other regimes. It is believed that an increase in friction at the hydrodynamic regime in the presented case at elevated temperature is due to the high viscosity of the thin film melt lubricant between the sliding surfaces which will be demonstrated in the next chapter.

Meanwhile, at the higher applied pressures (increased loadings), it is expected that the boundary lubrication regime is dominant and it causes an increase in friction coefficient and wear losses of both counterparts which is consistent with the Stribeck curve.³⁶⁶ However, the friction coefficient under the lubrication of BN@C-B (1:1) remains below 0.2 even at the highest applied load of 30 N (maximum Hertzian pressure of 2.09 GPa) at 880°C (**Figure 7-12i-Figure 7-12l**). According to the results at different tested loading conditions, the disc and ball wear rate increases slightly when the load increases from 10 to 30 N. Moreover, the disc wear rate, and the ball wear rate only increases slightly (**Figure 7-12k-Figure 7-12l**) at the highest loading condition (30 N). Therefore, the results demonstrate the outstanding lubricity at the boundary lubrication regime of BN@C-B (1:1) at 880°C, thus, confirming the excellent load-carrying capability of the tribofilm formed on the counterparts.

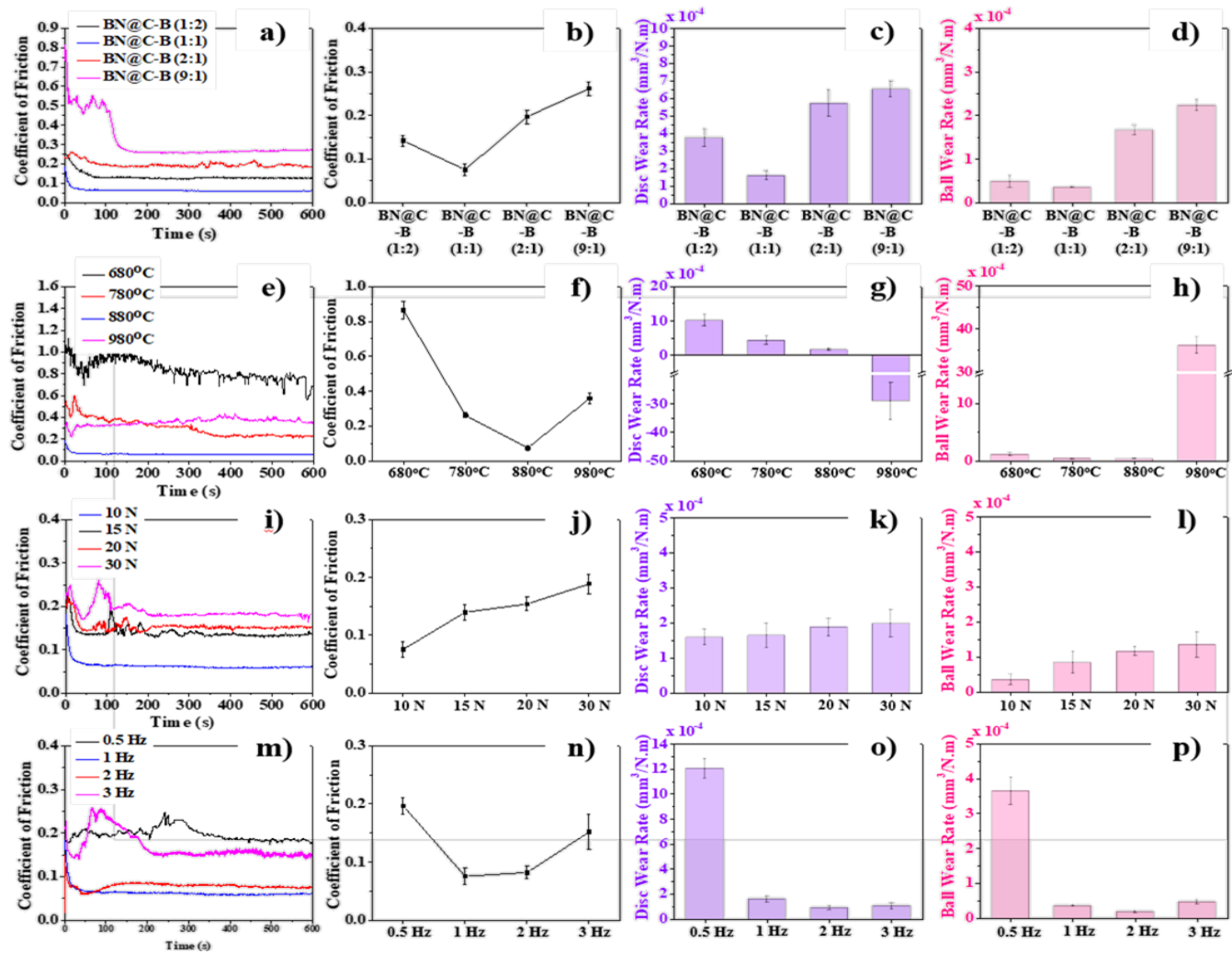


Figure 7-12. Friction and wear rate results of the hot friction tests at different conditions, including: a)-d) different capsule/borate ratios; e)-h) different temperatures; i)-l) different loadings; m)-p) different sliding velocity.

7.2.5. Wear surface analysis of the counterparts at the conditions with ultralow friction and wear

The essence of the friction reduction and anti-wear efficiency under mixed/boundary lubrication regimes from the melt lubricants can be attributed to the hierarchical tribofilm formed on the rubbing surfaces.¹¹⁹ During sliding, the melt lubricant BN@C-B (1:1) reacts tribochemically to the oxide and forms a compact tribofilm that results in a smoother wear surface and the lower width wear track on the disc (**Figure 7-13e**) compared to other tested lubricants (**Figure 7-13a-Figure 7-13d**). The disc wear track after friction tests of D-L and C-L show the presence of multiple ploughing and smearing streaks which is characteristic of abrasive wear. In the case of the C-L test, numerous debris particles agglomerate within the wear track which can probably be the oxides and the fractured microcapsules (EDS in **Figure 7-13b**). These debris particles can cause third-body abrasion to the wear surface during sliding which increases friction (**Figure 7-11a-Figure 7-11b**). According to EDS analysis, the disc wear surfaces of D-L and C-L show a prominent presence of iron oxide that indicates a high oxidation degree during sliding in these cases. For the B-L test, several micro-streaks are presented on the wear track surfaces with the presence of several laminated features (**Figure 7-13c**). EDS analysis confirms that these features are sodium borate which can be solidified during the cooling process (**Figure 7-13b**). Although the C-B (1:1) delivers the smooth worn surfaces analogous to BN@C-B (1:1), the wear width is moderately higher (**Figure 7-13d-Figure 7-13e**) implying that h-BN nanosheets improve the wear resistance of the melt lubricant. EDS spectrum on the disc wear surface (yellow square marked in **Figure 7-13d-Figure 7-13e**) in these cases confirms that these regions are rich in Fe, Cr, Ca, Na, O, and Si which demonstrates the formation of the composite tribolayer from the reactions between the sodium-calcium borosilicate melt and oxide layer. Noticeably, the intensity signal of Cr is higher than Fe in these cases which demonstrates limited oxidation of the worn surface due to the formation of the tribofilm (**Figure 7-13d-Figure 7-13e**).

For the ball-worn surface, the wear scar diameter in the case of BN@C-B (1:1) is the smallest among other lubricated systems (**Figure 7-14**). The wear scar surfaces of D-L and C-L reveal the presence of several streaks and the material deposition (**Figure 7-14a-Figure 7-14b**). From EDS analysis, the material deposition on the ball wear scar of C-L comprises microcapsule fragments and oxides (**Figure 7-14b**). These observations signify the occurrence of both abrasive and adhesive wear which is common in the high-temperature tribology of unlubricated systems.²⁸ An application of sodium borate melt (B-L) can reduce the wear scar diameter and material deposition to the ball, however, the worn surface shows multiple streaks of ploughing and smearing (**Figure 7-14c**). It indicates the limited function of sodium borate at the tested temperature which could be due to the presence of iron boroferrite and sodium-iron oxide reaction products as mentioned in the static oxidation test (**Figure 7-9-Figure 7-10**). Although the contact regions of BN@C-B (1:1) and C-B (1:1) are comparatively flat and uniform with the presence of similar elements from the composite tribofilm (**Figure 7-14d-Figure 7-14e**), the wear scar diameter of BN@C-B (1:1) is smaller than that of C-B (1:1) which is probably due to the presence of h-BN nanosheets. Elemental analysis confirms that the ball-worn surfaces in these cases contain dominantly Fe, Cr, Ca, Si, O,

and B (Figure 7-14d-Figure 7-14e) as the reaction products of the melt lubricant and oxide surface on the ball.

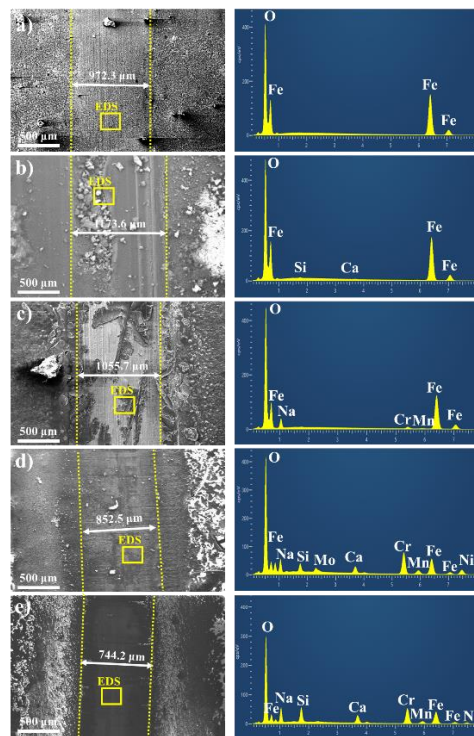


Figure 7-13. SEM/EDS inspection of the worn surfaces on the plate wear track after hot friction tests at 880°C from: (a) D-L; (b) C-L; (c) B-L; (d) C-B (1:1); and (e) BN@C-B (1:1).

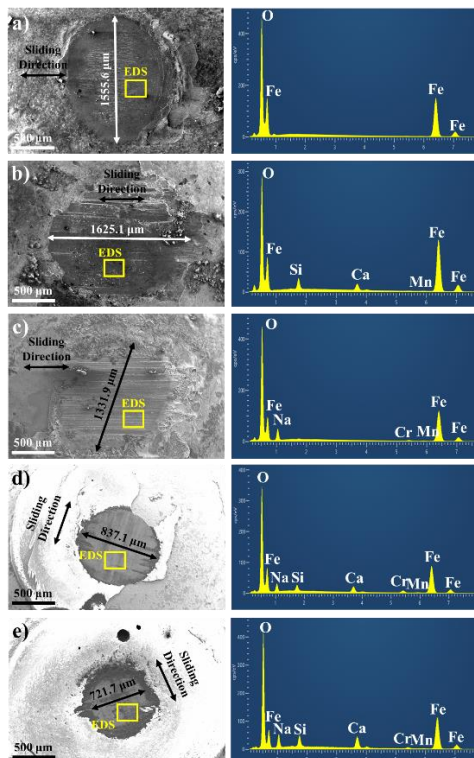


Figure 7-14. SEM/EDS inspection of the worn surfaces on the ball wear scar after hot friction tests at 880°C from: (a) D-L; (b) C-L; (c) B-L; (d) C-B (1:1); and (e) BN@C-B (1:1).

A high magnification observation on the wear track in the plate after lubrication by BN@C-B (1:1) reveals the smooth surface with the presence of several submicron-debris particles (**Figure 7-15a**). In addition, there is the existence of several areas covered by the excessive lubricant across the wear track (black contrast line areas) (**Figure 7-15a**). The grey-contrast areas are believed that present the surface with superficial tribofilm formation and these areas will be examined further by surface characterization techniques. Meanwhile, the formation of the nanometre spherical particles is evidenced (**Figure 7-15b**) and they are compacted neatly and tightly on the worn surfaces. The formation of the fine-grained particle with nano-/submicro-metre size at the contact interface suggests the ability to accommodate large plastic strain during the stressed-shearing conditions that contribute to the friction and wear reduction.^{367, 368}

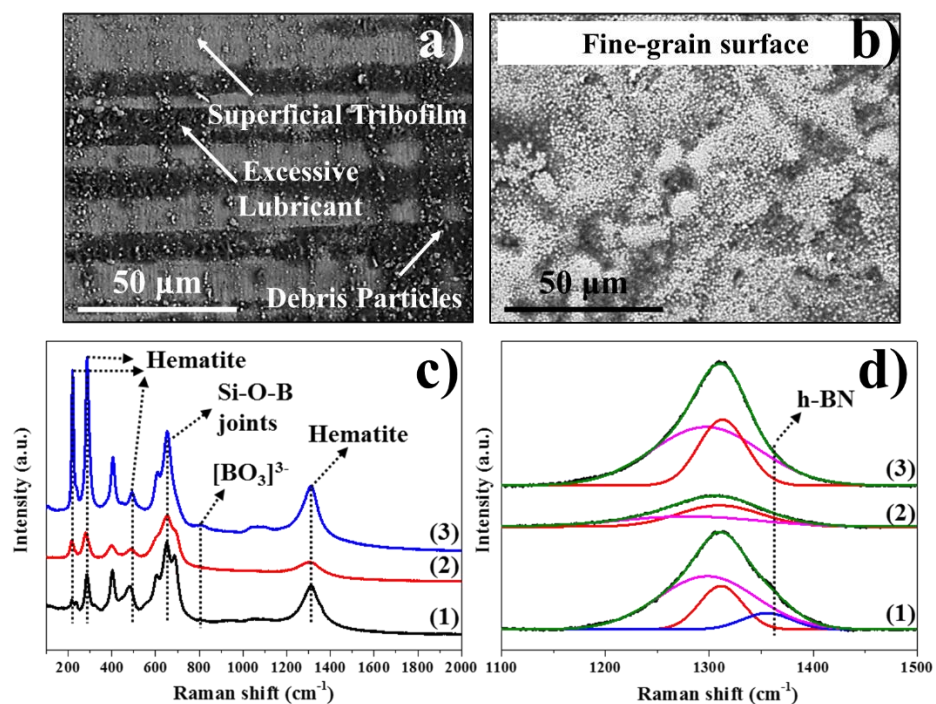


Figure 7-15. High magnification SEM images of the worn plate (a) and ball (b) surfaces. Wide-scan (c) and narrow-scan (d) Raman analysis conducted at (1) non-sliding area on the plate; (2) the disc wear track; and (3) the ball wear track.

Raman analysis is conducted on the wear track of the counterparts and the non-sliding area of the coated plate in the case of BN@C-B (1:1) to understand the chemistry of the superficial layer (**Figure 7-15c-Figure 7-15d**). The resulted spectrum indicates the formation of the borosilicate structure (Si-O-B joints) at around 655 cm^{-1} ³⁶⁹ in all examined areas (**Figure 7-15c**). There is a significant increase in the signal intensity of hematite (Fe_2O_3) on the disc and ball wear tracks, compared to that of the non-sliding area on the disc (**Figure 7-15c**). Intriguingly, the emergence of the $[\text{BO}_3]^{3-}$ unit at 868 cm^{-1} ³⁷⁰ is detected on the disc and ball wear track, but not for the non-sliding area on the disc (**Figure 7-15c**). In addition, Gaussian deconvolution of the peak from $1000\text{-}1500\text{ cm}^{-1}$ reveals the existence of the G band frequency in h-BN nanosheets (at 1366.7 cm^{-1})³⁷¹ at the non-sliding area whereas the sliding areas on the tribopairs show no presence of such

compound (**Figure 7-15d**). It does not mean that there are no h-BN nanosheets at the sliding areas as the strong excitation of iron oxide and other compounds may interfere with the G band frequency of a small amount of h-BN presence within the sliding contacts.

To verify the existence of h-BN nanosheets within the sliding contacts after lubrication by BN@C-B (1:1), XPS wide-scan spectrums of the sliding and non-sliding surfaces are shown in **Figure 7-16**. The presence of Si 2p, B 1s, N 1s, Ca 2p, O 1s, Fe 2p, and Na 1s are evidenced for these measured surfaces (**Figure 7-16a**). The deconvolution and a fitted peak of detailed analysis with B 1s show the small peak of B-N at 190.5 eV from these examined areas (**Figure 7-16b**) which indicates the possible presence of h-BN nanosheets.³⁷² Further deconvolution of the N 1s spectrum in the examined areas (**Figure 7-16c**) fortifies the existence of h-BN nanosheets at either non-sliding or sliding areas by the prominent emergence of the peak at 398 eV, which is characteristic of h-BN nanosheets.³⁷² Apart from the confirmation of the presence of h-BN at the sliding areas, the deconvolution and fitted peaks of B 1s additionally suggest the presence of the borosilicate structure (B-O-Si) at 103.5 and 193.1 eV on both the sliding and non-sliding areas (**Figure 7-16b**).³⁷³ These results confirm the reaction between the colloidal capsules and the borax at elevated temperatures that leads to the formation of the sodium-calcium borosilicate melt.

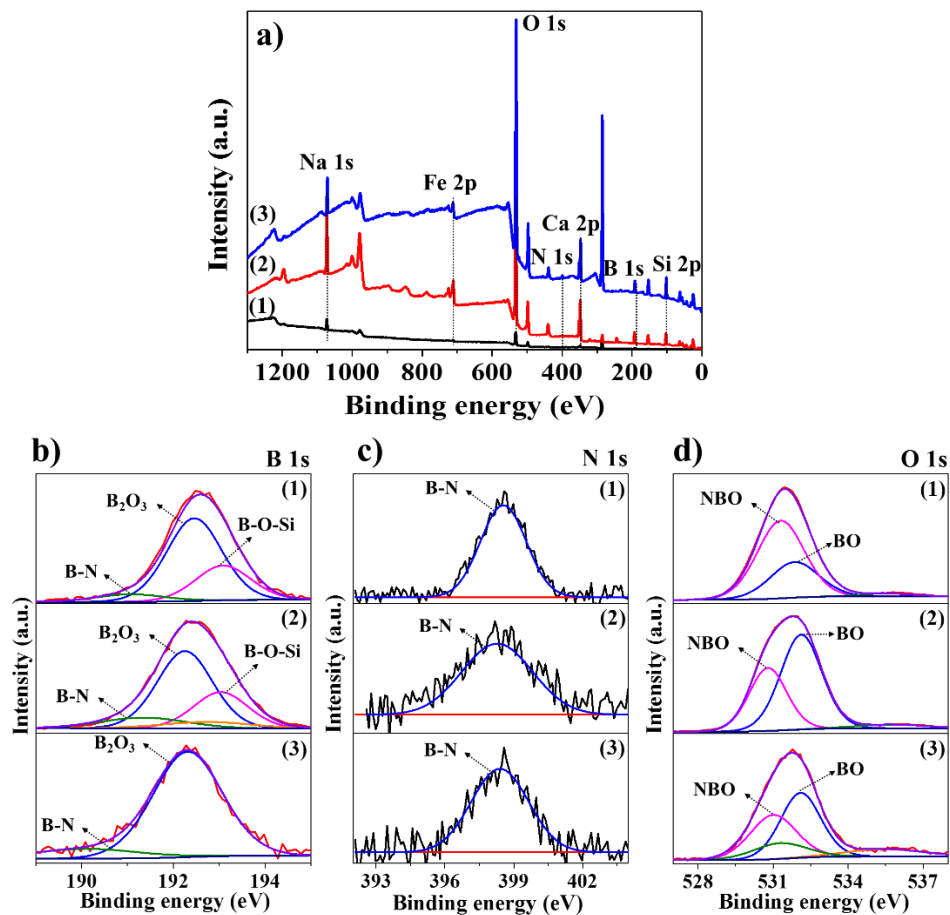


Figure 7-16. (a) XPS survey spectrum; (b) B 1s deconvolution; (c) N 1s deconvolution; and (d) O 1s deconvolution from the inspected regions of (1) non-sliding area on the plate; (2) the disc wear track; and (3) the ball wear track.

To understand how the borosilicate melt behaves under stressed-shearing stimulated conditions, the deconvolution of the O 1s spectrum is conducted (**Figure 7-16d**). The first peak at 529–530 eV is related to non-bridging oxygen (NBO) including Si–O–(Na, Ca) and B–O–(Na, Ca), while the second peak at 531–532 eV is associated with the presence of bridging oxygen (BO) such as Si–O–Si, Si–O–Bn, and Bn–O–Bn (where n is equal to 3 or 4, depending on the coordination of oxygen around boron atom).²⁸¹ It can be recognized that the BO/NBO ratio is around 0.47 for the non-sliding areas (1) on the disc, while the BO/NBO ratios in the wear track areas reveal a significant increase to 1.64 (from the disc) (2) and 1.27 (from the ball) (3) (**Figure 7-16d**). These results suggest a dramatic decrease in the concentration of the network modifiers within the borosilicate structure when stressed-shearing is applied.

According to the obtained results, it has been demonstrated that the mixed lubrication regime emerged. Thus, the friction performance depends strongly on both the viscosity of the lubricating melt and the tribofilm formed on the sliding surfaces. The thermal-chemical reactivity of the melt toward the oxide surface plays a crucial role in determining the friction under the boundary lubrication regime,³⁷⁴ but, rheological properties of the melt (e.g. viscosity) affect strongly the friction under the fluid film lubrication.¹¹⁹ The possible lubrication mechanism is displayed in **Figure 7-17**.

It is hypothesized that under the boundary lubrication regime, the shearing can produce a high frictional temperature that governed the diffusion of alkali and alkali earth elements out of the borosilicate melt (**Figure 7-16d**). The outward diffusion of these elements can cause the structural change of the borosilicate melt from the tetrahedral ^[4]B to the trigonal ^[3]B coordination (**Figure 7-15c**).³⁷⁵ Subsequently, the trigonal ^[3]B coordination undergoes a polymerization reaction to form B-O-B to maintain the charge neutrality across the melt network.¹³ Consequently, the highly polymerized amorphous borosilicate glass formed between the contact interfaces and may contribute to the ultra-low friction and excellent wear alleviation.¹⁴⁴ Meanwhile, the diffused charged species (Na⁺ and Ca²⁺) may react to the chromium oxide scale under boundary lubrication to form the reaction products. These products play a certain role in binding the amorphous borosilicate glass onto the asperity surfaces, thus, maintaining the stability and integrity of the hierarchical tribofilm.³⁷⁴ Simultaneously, the presence of h-BN nanosheets at the sliding interfaces (**Figure 7-16b-Figure 7-16c**) can provide the easy-shearing and load-carrying capabilities from the h-BN nanosheets, due to its weak layer interaction forces, under boundary lubrication³⁷⁶ that reduces the friction significantly even at high contact pressure. In addition, h-BN possesses superior mechanical strength and excellent thermal stability that can lower wear losses,¹⁰⁴ thus results in an excellent anti-wear performance from the BN@C-B (1:1) melt lubricant.

On the other hand, in the areas where the hydrodynamic lubrication was likely to occur, the diffusion of alkali and alkali earth cations is not significant. The sodium-calcium borosilicate melt is squeezed and compressed in these areas under high contact pressure and stressed-shearing effect, but the flash temperature may not be high enough due to a complete separation of two oxide surfaces by the fluid film. However, it is predicted that these occurrences may be sufficient to

accelerate the incorporation of Fe^{2+} into the melt which is thermodynamically favorable at elevated temperatures.³⁷⁷ It can shorten the chain length that results in the depolymerization of the melt and causes a decrease in the viscosity of the melt lubricant.³⁷⁷ Moreover, the presence of fine h-BN nanosheets, as 2D materials, within the melting fluid, can reduce the momentum transfer between the adjacent fluid layer that leads to a viscosity reduction.¹¹² As a decrease in viscosity reduces the friction at rubbing surfaces under hydrodynamic lubrication, these phenomena play an important role in achieving ultra-low friction.

In coupling with the shear-intermixing effects at the sliding contacts, the plastic deformation of the near-surface steel matrix results in both frictional energy dissipation⁷² and the formation of nano-grained materials (**Figure 7-15b**).³⁶⁷ For metals and alloys, surface microstructure refinement has been linked to improved friction and wear resistance³⁶⁸ due to the ability to accommodate large plastic strain from the stable gradient nanostructures. The ultralow friction and wear obtained in this study, at the boundary lubrication, are also intimately associated with the generation of the fine-grained oxide surfaces on the ball and plate. Therefore, unprecedented multi-functional properties of the hierarchical microstructure are obtained under capsule-added borate-based lubrication that includes exceptional wear resistance, ultralow friction, and excellent anti-oxidation. This is brought about by the addition of the smart functional BN-containing colloidal capsules under the tribo-stressed conditions. Hence, the developed colloidal capsules can be inferred to have smart functional behaviors that can tailor the hierarchical tribofilm structure on the sliding surfaces. Further studies will be conducted in the next chapter to track the formation of the tribofilm and investigate the high-temperature reactivity of the BN@C-B (1:1) lubricant to the oxide surfaces under simulated hot rolling conditions, and that in turn can clarify and confirm the lubrication mechanism proposed in this chapter.

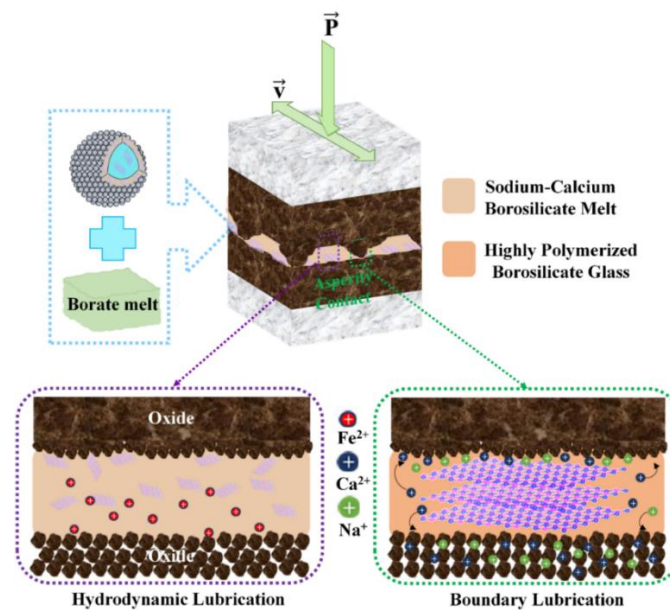


Figure 7-17. Schematic showing the potential lubrication mechanism of the BN@C-B (1:1) melt lubricant at 880°C.

7.3. Conclusions

In summary, this chapter has successfully demonstrated the accomplishment of ultralow friction, exceptional wear resistance, and superior anti-oxidation under high-temperature lubrication conditions by the developed h-BN-containing CaCO₃-decorated SiO₂ doubled-shell colloidal capsules as a smart-responsive functional additive in sodium borate-based melt lubricant. The results suggest significant and practical development of the microencapsulation technique based on the new proposed strategy for future research in formulating the next generation of smart lubricant additives. Technologically, several concluding remarks can be listed as follow:

- The hybrid colloidal capsules, manually developed following the proposed strategy, can significantly enhance the lubricity (by ~70%) and anti-oxidation (by ~93%) performances of the conventional sodium borate-melt lubricant at elevated temperatures (880°C).
- The lubrication mechanism is based on the synergy between the functional core additive (h-BN nanosheets), the shell materials (CaCO₃-decorated SiO₂ doubled-shell), and the melt-based lubricant (sodium borate).
- The proposed strategy also resolves the issues raised from the previous studies of using microcapsules as an effective cargo to control-release the functional core additive without considering the effect of the shell fractures in tribological behaviors of the sliding contacts when the capsules are broken under the stressed-shearing effect.
- A capability to tailor the hierarchical tribofilm structure on the sliding surfaces, which can be inferred to the smart functional behavior of the designed colloidal capsules, has also been emphasized.

Chapter 8

Anti-oxidation and lubrication mechanisms of the sodium borate formulated with the smart-responsive colloidal capsules under simulated hot rolling conditions at elevated temperatures

* This chapter content has been published in Applied Surface Science, 2021, 150556, <https://doi.org/10.1016/j.apsusc.2021.150556>

In the previous chapter (**Chapter 7**), hexagonal boron nitride (h-BN)-containing CaCO₃-SiO₂ hybrid shell microcapsule has been developed as a smart additive for high-temperature lubrication at 880°C.³⁷⁸ This capsule provides superior tribological improvements in terms of anti-friction, wear-alleviation, and oxidation inhibition to the conventional sodium borate melt. However, the interactions between the hybrid microcapsule and sodium borate melt, and the interfacial reactivity of the resulted lubricant toward the oxide/steel surfaces have not yet been elucidated.

In the present chapter, the thermo-responsiveness of the hybrid microcapsule under sodium borate melt and the interfacial chemistry between the resulted melt and the oxide/steel surfaces are further investigated comprehensively by multiple surface/interface characterizations. In particular, details in the microstructural evolutions and the chemistry of the hierarchical layers on the oxide surfaces are revealed under static and friction conditions at the steel/steel contacts at high temperatures. In this study, the testing temperature is chosen between 900-1000°C which is in the range of the hot rolling of steel processes.³⁴ This chapter will advance the understanding of how the formulated melt reacts to the oxide surfaces and how it performs the lubrication under steel/steel contacts at high temperatures with desirable corrosion characteristics. These results are important for a better design of the functional additives while contributing extensively to practical applications of the developed hybrid microcapsule in the hot metal forming industry.

8.1. Experimental details

8.1.1. *In-situ* high-temperature thermo-responsive testing of the hybrid microcapsules

The thermo-responsive behavior of the hybrid colloidal capsules under the presence of sodium borate melt at elevated temperatures has been investigated by the *in-situ* heating experiment. The experiment is conducted in the dual-beam FIB-SEM equipment (FEI Helios NanoLab G3 CX) with an aid of a Thermo Scientific™ μ Heater holder. The micro-electromechanical system (MEMS)-based chip, as a heater, is installed in the holder before the experiment which can rapidly heat a sample at a rate of 0.01 to 104°C/s with temperature settling to within 1°C. Typically, the cross-sectional specimen of sodium borate-coated stainless steel is lifted out from the bulk sample by FIB. Subsequently, the specimen is placed and welded onto the MEMS heating chip (**Figure 8-1a**). The *in-situ* heating is conducted up to 1000°C (heating rate of 5°C/sec) at which the sodium borate layer melt and wet the whole specimen (**Figure 8-1b**). Afterward, an individual microcapsule is manipulated and mounted to the tungsten tip by our previous approach (**Chapter**

6). The contacting experiment between the colloidal capsule and the borate-wetted steel specimen is then conducted from 200°C to 1000°C (heating rate of 1°C/sec). The thermo-responsive performances of the microcapsules are recorded in real-time during heating at elevated temperatures.

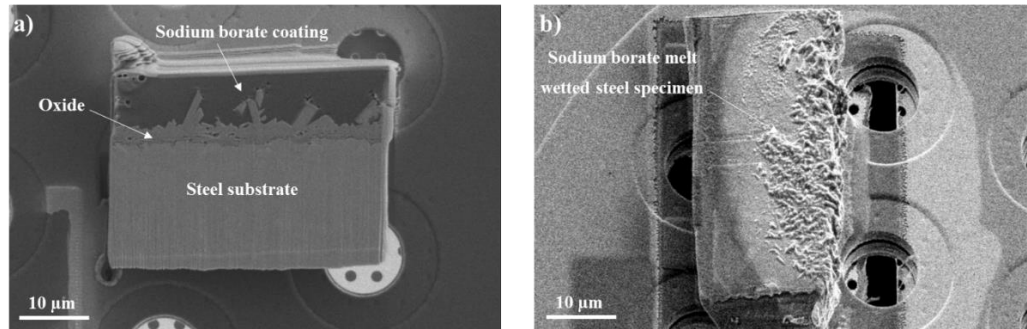


Figure 8-1. (a) Cross-section of sodium borate-coated steel specimen; (b) Sodium borate-wetted steel specimen from (a) after *in-situ* heating at elevated temperatures.

8.1.2. Static high-temperature corrosion and friction testing experiments

The high-temperature corrosion and lubrication experiments are performed in a Bruker Universal Mechanical Tester (UMT) platform. The test lubricant, denoted by MC@NBO, is formulated from the sodium borate aqueous solution (0.5 wt.%) (NBO) and the hybrid microcapsules (microcapsule/borate weight ratio of 1:1). Before the friction test, it is drop-coated on the disc surface by a hot plate. The lubrication performance is studied using a pin-on-disc rotation module positioned in a heating furnace. This testing module has been verified by Zhu et al.²²¹ as suitable to simulate the friction-wear behavior of hot metal rolling conditions. While the lubrication mechanism is studied from the disc and ball wear surfaces, the hot corrosion and static oxidation are investigated by characterizing the cross-sectional interface between the coated melt and the oxide surface. A 316 stainless steel disc (30 mm diameter) is chosen as a rotating part while a GCr15 steel ball (6.35 mm diameter) plays as a stationary part. The testing temperature is set at 940°C, yielding the actual temperature on the rotating disc of 930°C. During sliding, an applied load of 10 N (corresponding to the maximum Hertzian contact pressure of 1.45 GPa between the two oxidized surfaces) and a tangential sliding velocity of 0.1 m/s are set constant throughout the hot friction test (10 mins). The testing duration of hot friction tests is selected according to the previous studies^{13, 121, 361, 379} to ensure sufficient time to form the tribofilm on the sliding surfaces. Meanwhile, the soaking time for static oxidation and hot corrosion tests of the formulated lubricant on the disc steel surface is one hour by the same heating furnace under the air atmosphere.

8.2. Results and Discussion

8.2.1. Thermo-responsive behavior of the combined hybrid microcapsules and sodium borate melt at high temperatures

Figure 8-2a shows the TGA and DTG of the borate-capsule mixture during the heating from 50 to 1000°C. A sharp decrease of the mixture mass starts at the beginning from 50 to 200°C. There

are two distinct mass loss peaks at 100°C and 155°C from the DTG in **Figure 8-2a** which can be correlated to the water evaporation of the capsule's core and the hydrate from the sodium borate salt. This occurrence has been confirmed by the two endothermic peaks that appeared at the same temperatures from DSC analysis (**Figure 8-2b**). From 200 to 600°C, the mass of the mixture gradually decreases simultaneously with adsorbing heat (**Figure 8-2a-**Figure 8-2b****). It can be correlated to the phase change of sodium borate salt¹³ and the fusion of the microcapsule's doubled-shell.³²³ Above 600°C, there is a dramatic decrease in mass from 600 to 700°C with a corresponding DTG peak of 625°C (**Figure 8-2a**). A DSC analysis also reveals the emergence of two exothermic peaks at this temperature. Since sodium borate melts to a viscous liquid at 525°C,¹³ it is hypothesized that the dissolution of the hybrid microcapsules into the sodium borate melt occurs at 625°C. This phenomenon not only results in a generation of CO₂ from the decomposition of CaCO₃ but also generates heat since the dissolution process is exothermic.³⁸⁰ After 700°C, there is a slight increase in mass with a small exothermic peak at 900°C which can be correlated to the oxidation of the h-BN nanosheets to form the boron oxide melt.¹⁰¹

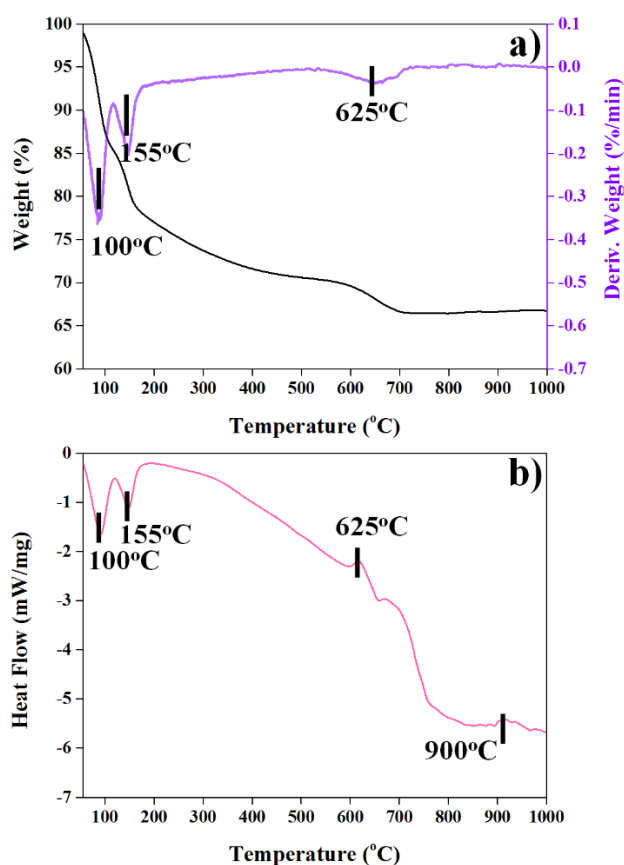


Figure 8-2. (a) Thermogravimetry (TGA) and Derivative thermogravimetry (DTA); (b) Differential scanning calorimetry (DSC) of the borate-capsule mixture (borate/capsule = 1:1 weight ratio).

To visualize the dissolution of the microcapsule into the borate melt, an *in-situ* contacting experiment is initially designed for an individual microcapsule and the borate melt at elevated temperatures. Shown in **Figure 8-3a** is a schematic representing an *in-situ* thermo-responsive

experiment of the single hybrid microcapsule under borate melt. Typically, the cross-sectional specimen of the borate-coated steel is prepared by FIB and is placed on the MEMS chip. Rapid heating from room temperature to 1000°C (5°C/sec) leads to the melting of the borate coating that wetted the surface of the steel specimen. The *in-situ* contact experiment is performed between the single microcapsule and the borate-wetted steel specimen from 200 to 850°C with a heating rate of 1°C/sec to visualize the dissolution of the microcapsule to the borate melt.

The microcapsule is subsequently manipulated to contact with the borate melt on the steel specimen at high temperatures. It can be seen that there is no dissolution of the microcapsule into the borate on the steel specimen at 500°C (**Figure 8-3b**). Since borate melts at 525°C,¹³ it is still in a rigid solid form at 500°C, hence it has a low reactivity toward the microcapsule particle. Increasing the temperature to 600°C-700°C (**Figure 8-3c-Figure 8-3d**) leads to a partial dissolution of the microcapsule into the borate melt which is in good agreement with the results from TGA, DTG, and DSC analysis (**Figure 8-2**). At 800°C, the dissolution of the microcapsule to the borate melt becomes significant. This occurrence creates a dragging force that detaches the microcapsule from the tungsten tip (**Figure 8-3e**). It can be seen that the microcapsule at 800°C is completely collapsed and dissolved into the liquid melt. Side-view in **Figure 8-3f-Figure 8-3g** reveals the steady dissolution of the microcapsule fragments to the liquid melt from 800 to 850°C simultaneously with the wetting of the liquid melt on the steel specimen.

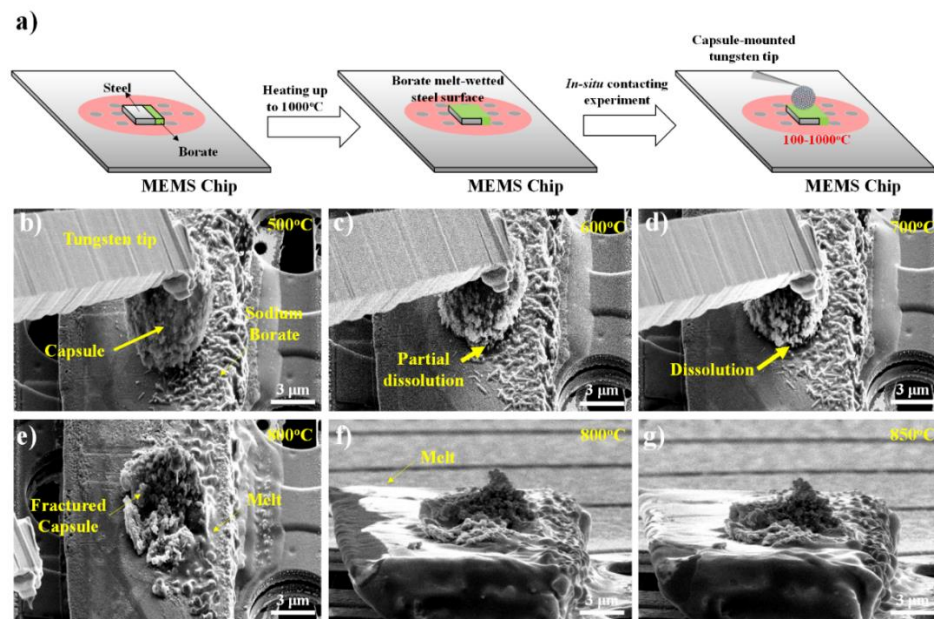


Figure 8-3. (a) Schematic representing the *in-situ* thermo-responsive experiment of the hybrid microcapsules under borate melt conditions. SEM image showing the visualization of how the single microcapsule responds to the borate melt at different temperatures: (b) 500°C; (c) 600°C; (d) 700°C; (e) 800°C; Side view at (f) 800°C and (g) 850°C.

From the *in-situ* contacting experiment, the responsiveness of the hybrid microcapsule under sodium borate melt is visualized in real-time. In particular, sodium borate melts the microcapsule shell at elevated temperature (started at 600°C) and results in a new melt that wets the steel surface.

Such observation shows a strong correlation to the results from other complementary analytical techniques such as TGA, DTG, and DSC which proves the efficiency of the developed *in-situ* contacting experiment in studying the behavior of the functional additives at high temperatures. It is believed that the successful visualization of the microcapsule's responsiveness will have a high impact on understanding how the formulated additive performs synergistically with the melt lubricant. This fundamental can potentially contribute to customize other functional additives that will be applied in different high-temperature lubrication processes involving the use of melt lubricants.

8.2.2. Static oxidation and hot corrosion of the MC@NBO lubricant toward the oxide layer

In this study, the testing temperature for oxidation is set at a higher temperature (930°C) than the previous study (880°C) to conform with the actual operating temperatures in the hot steel rolling processes (900-1100°C).³⁴ It can be seen from **Figure 8-4a** and **Figure 8-4c** that there is a formation of the thin chromium oxide scale layer (II) underneath the melted coating layer (I) in both cases of NBO-coated and MC@NBO-coated steels. EDS mapping in **Figure 8-4b** and **Figure 8-4d** show that sodium is concentrated mostly in the melt areas (I) with a negligible presence of sodium within the chromium oxide scales and oxide particles (II) in both cases. However, in the case of sodium borate melt coating, there is the presence of several large particles (> 20 μm) within coating (I). These particles are dominantly iron with a slight presence of chromium, manganese, and boron (**Figure 8-4b**). In some areas, particles comprising iron, manganese, and sodium are also observed. However, the significant formation of the reaction products in the sodium borate coating replaces totally the melt coating (**Figure 8-4a**). This phenomenon forms the secondary oxide layer above the primary chromium oxide layer, thus, demonstrates the loss of oxidation protection from sodium borate melt at the test temperature (930°C). The total oxide thickness after the oxidation test of sodium borate was 32.5 μm.

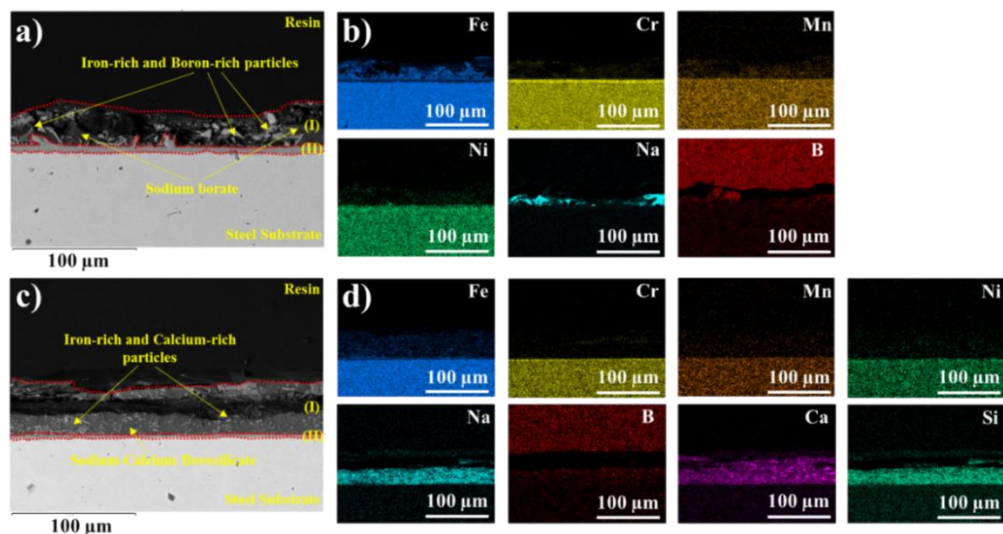


Figure 8-4. SEM and EDS analysis of the sodium borate (NBO) ((a)-(b)) and the capsule-added sodium borate (MC@NBO) ((c)-(d)) melt lubricants coated on the steel substrate after the static

heating conditions at 930°C.

Meanwhile, there is no formation of such large iron-rich particles within the MC@NBO coating, however, the nucleation of several small rod-like particles is observed (I) (**Figure 8-4c**). EDS in **Figure 8-4d** shows the presence of some local areas with high intensity of calcium, sodium, and slight intensity of iron in the coating region (I). It can be correlated to the nucleation of some single or spinel oxide particles within the melt due to the diffusion of iron cations from the steel into the melt. Intriguingly, there is no detection of the reaction layers containing sodium, iron, and manganese which indicates no formation of sodium iron/manganese oxides. The oxide thickness, in this case, is only the chromium oxide (~4.5 μm) beneath the melt coating layer. Thus, compared to sodium borate melt, the resulted sodium-calcium borosilicate melt on the steel shows a superior anti-oxidation performance (by 86.2%) with almost no secondary oxide scale developments.

To characterize the oxide compounds and phases in the oxide scale and coating, X-ray diffraction (XRD) is utilized. From the oxidation test of stainless steel at 930°C, the oxide is constructed dominantly by FeCr_2O_4 and Fe_2O_3 (**Figure 8-5a**) which is consistent with previous studies.³⁸¹ Generally, stainless steel has a certain degree of oxidation resistance at elevated temperatures owing to the formation of a slow-growing, continuous, and dense Fe-Cr spinel oxides layer on the steel surface.³⁸² However, an application of sodium borate as the melt coating layer on the steel surface can cause the breakdown of such protective oxide scale by the formation of several reaction products.^{383, 384} In particular, XRD reveals the complex mixture of several compounds on the surface of the sodium borate-coated steel after the isothermal oxidation test at 930°C (**Figure 8-5b**). Apart from the detection of Fe-Cr spinel oxide (FeCr_2O_4), there are several oxide compounds of Cr_2O_3 and Fe_2O_3 in the coating above the steel substrate. The formation of these oxides corresponds to the breakdown of the protective oxide scale on the stainless steel substrate.^{381, 385} The breakdown of the protective oxide scale can be due to the hot corrosion attack of sodium borate melt and the fluxing effect of molten liquid at elevated temperatures.³⁸⁶ Generally, a cycle of subsequent chemical reactions between the sodium in molten salt and the protective oxide scale takes place that gradually depletes the chromium from the steel substrate. As chromium is depleted, oxidation of the steel accelerates, and the porous scale forms with low mechanical integrity.³⁸⁷ It is evidenced by the detection of several sodium-metal oxides (Na_2MnO_4 , NaFeO_2 , and Na_2CrO_4) and the iron boroferrite (Fe_3BO_6 , $\text{Fe}_3(\text{BO}_3)\text{O}_2$, and $4\text{FeO}\cdot\text{Fe}_2\text{O}_3\cdot\text{B}_2\text{O}_3$) in the oxide scale after oxidation test at 930°C (**Figure 8-5b**).

However, when adding the developed colloidal capsules to sodium borate (MC@NBO-coated steel), the oxidation resistance improves significantly (**Figure 8-4c**). From the XRD analysis of the coating after the isothermal oxidation test (**Figure 8-5c**), the emergence of FeCr_2O_4 , Cr_2O_3 , and Fe-Cr spinel oxide ($\text{Fe}_{0.7}\text{Cr}_{1.3}\text{O}_3$) is observed. There is an additional presence of Cr_2NiO_4 , however, no presence of iron oxide phases is evidenced. Intriguingly, XRD analysis also shows no detection of sodium-metal oxides and iron boroferrite compounds in the MC@NBO coated steel compared to the NBO-coated steel (**Figure 8-5c**). Moreover, unlike the NBO-coated steel, the prominent appearance of the broad hump peak is evidenced for the MC@NBO coating which

indicates the retained amorphous melt structure on the steel substrate. From such observation, it can be concluded that the resulted sodium-calcium borosilicate melt has a lower reactivity toward the protective oxide scale compared to the sodium borate. Thus, a lower oxidation rate and reduced hot corrosion attack are eventually achieved by the addition of the microcapsules.

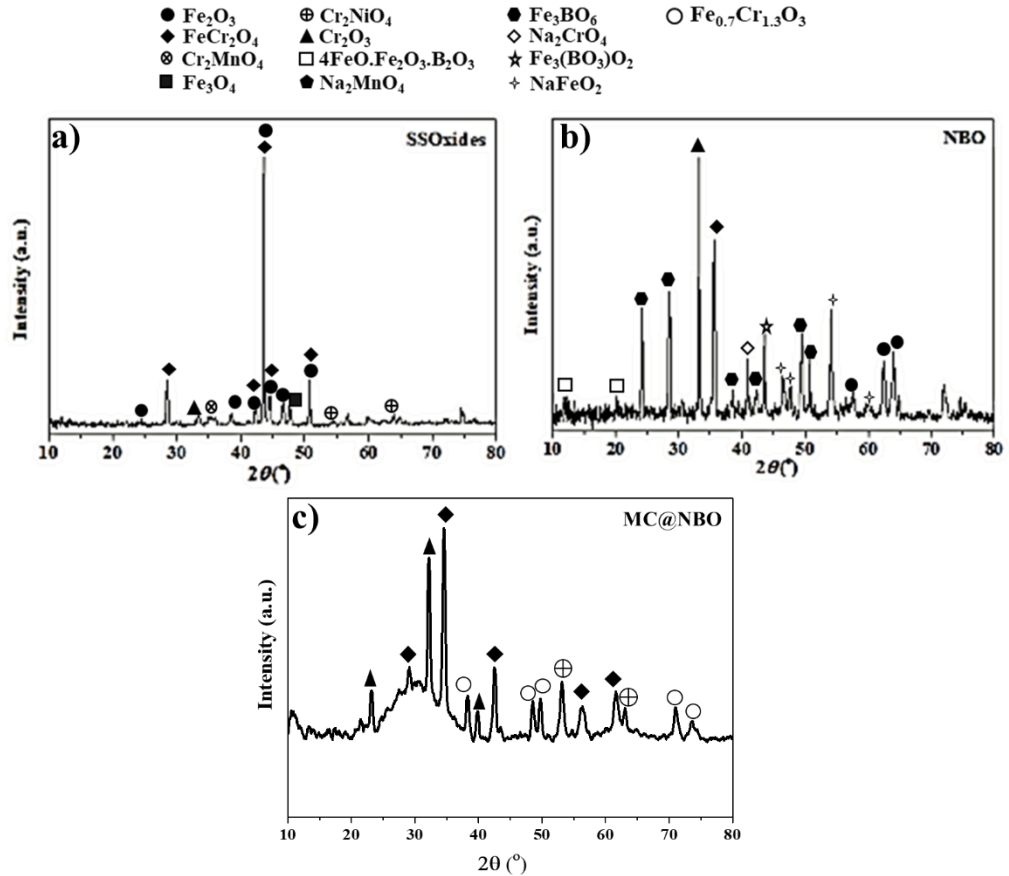


Figure 8-5. XRD surface analysis of the coated steel after oxidation test at 930°C: (a) no coating; (b) sodium borate (NBO) coating; and (c) capsule-added sodium borate (MC@NBO) coating.

To understand the high-temperature corrosion of the resulted melt toward the oxide, the interfacial chemistry of this melt is investigated by characterizing the oxide/melt interface on the coated steel. **Figure 8-6a** shows the cross-sectional microstructure of the glass melt and oxide layer on the steel substrate. The melt layer is amorphous and homogeneous (SADP1, **Figure 8-7**). EDS analysis in **Figure 8-6b** reveals that the melt mainly contains boron (B), sodium (Na), silicon (Si), and calcium (Ca) which indicates the formation of the sodium-calcium borosilicate melt. The oxide layer (~4 μm) beneath the amorphous melt is comprised of a mixture between the fine-grained particles and the large columnar particles (**Figure 8-6a**). It can be noticed that the columnar particles grow above the fine-grained particles. According to the EDS (**Figure 8-6b**) and SADP analysis (SADP2, **Figure 8-7**), the fine-grained oxide particles comprise dominantly of chromium oxide (Cr₂O₃) with a significant presence of manganese (Mn) and nickel (Ni) agglomerated at the top of the fine-grained layer. It is expected that the chromium oxide thin layer is formed at an initial stage of the oxidation process due to the high oxidation rate of chromium compared to other metallic elements.³⁸⁸ This layer acts as an oxidation protection layer for the steel substrate. Meanwhile, the

presence of Mn and Ni on the top of oxide can be due to the formation of several spinel oxides of (Ni, Fe, Mn-Cr)-O, which is common for the oxidation of stainless steel at 1000°C.³⁸⁸ Intriguingly, the large columnar particles on the fine-grained oxide are characterized as Fe-Cr spinel of FeCr_2O_4 by both EDS mapping (Figure 8-6b) and SAPD analysis (SADP2, Figure 8-7).

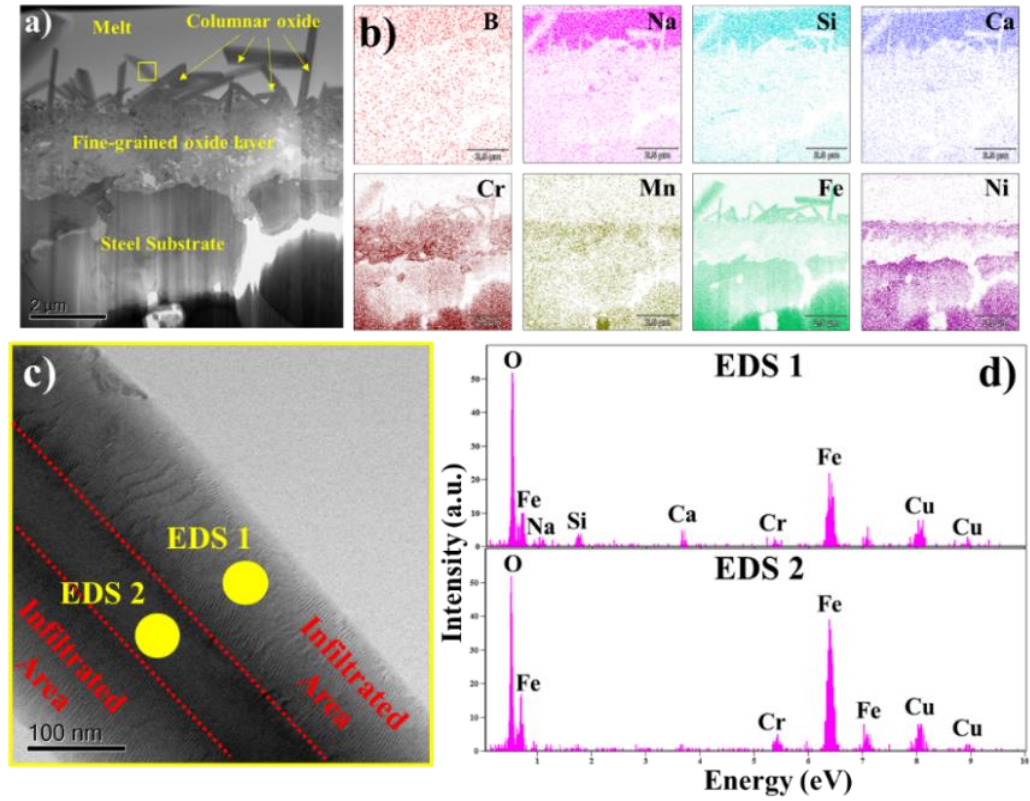


Figure 8-6. (a) Cross-section overview of the MC@NBO coated on the oxide-steel surfaces; (b) Aberration-corrected high-magnification bright field image of the single columnar oxide particle from the yellow square marked in (a); (c) EDS spectrum of the two distinct areas in the columnar oxide particle as spotted in (b).

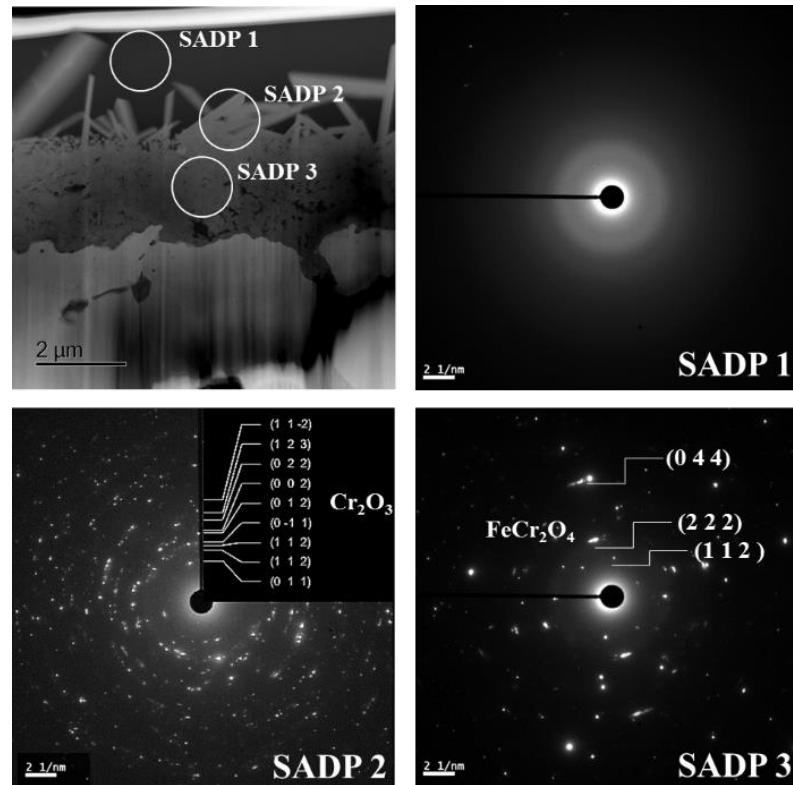


Figure 8-7. SADP analysis of the compound formation at different regions in the specimen from the capsule-added sodium borate-coated steel sample under static heating conditions at 940°C.

From the EDS mapping analysis (**Figure 8-6b**), there is no significant agglomeration of sodium (Na) or (Ca) on the oxide layer. These elements are rather distributed uniformly within the amorphous borosilicate glassy layer. However, an examination of the columnar particle at the yellow square marked in **Figure 8-6a** reveals the presence of two distinct areas: (1) infiltrated area at the outermost; and (2) the non-infiltrated area at the core of the particle (**Figure 8-6c**). The infiltrated area shows the presence of several large fringes with a brighter diffraction contrast compared to the non-infiltrated area. This observation indicates a formation of the porous structure at the infiltrated area that reduces the diffraction contrast at this area. EDS analysis at the infiltrated area (EDS 1, **Figure 8-6d**) indicates the presence of Na, Si, and Ca apart from the sharp signal intensity of Fe and Cr compared to the non-infiltrated area (EDS 2, **Figure 8-6d**). Therefore, it can be concluded that the melt still has a corrosive behavior that dissolved and infiltrated a fraction of the columnar spinel particles. However, such corrosive characteristic is negligible compared to the sodium borate that shows the significant generation of the reaction products (iron boroferrite and sodium iron/manganese oxide) on top of the chromium oxide scale (**Figure 8-4a** and **Figure 8-5b**).

8.2.3. Lubrication performances of MC@NBO under simulated hot rolling conditions at 930°C

Figure 8-8a shows the frictional behavior of the lubricants at 930°C with an applied maximum Hertzian contact pressure of 1.45 GPa. Typically, a hot friction test progresses in two consecutive stages starting with a running-in period (I) and followed by a steady stage (II) (**Figure 8-8a**). At

the running-in period (I) (in the first 100s), a significantly high and unstable coefficient of friction (COF) is recognized in the dry sliding test. It can be attributed to the continuous changes in the surface's primary topographies, microstructures, and chemical compositions of the steel counterparts with possible involvement of third-body formation. An application of melt lubricants can reduce such phenomena (**Figure 8-8a**). Sodium borate melt (NBO) directly enters a steady state and reduces the friction between the steel counterparts by 26.8% (**Figure 8-8a**). Meanwhile, the MC@NBO lubricant requires approximately 100 sec before entering a steady state. This implies that the resulted sodium-calcium borosilicate melt requires a certain time to form the stable tribofilm on the rubbing surfaces compared to sodium borate. At the steady state, a significant reduction of the COF by 71.2% is observed compared to sodium borate melt.

Figure 8-8b additionally reveals the excellent wear rate reduction of this melt under simulated hot rolling conditions compared to others. Under sodium borate lubrication, the wear loss reduces by 53.5% for the disc and 95.3% for the ball under the tested conditions. The inset SEM images show a significant decrease in the wear scar diameter on the ball and the wear track width on the disc in the case of sodium borate compared to the dry sliding test. An application of the functional colloidal capsule to sodium borate melt can dramatically reduce the disc wear loss by 40.2% and the ball wear loss by 78.4% compared to sodium borate lubrication. As shown in the inset SEM images, the resulted ball wear scar and the disc wear width after lubrication by MC@NBO are relatively smaller and narrower compared to those lubricated by sodium borate (NBO). It has been noticed that the resulted sodium-calcium borosilicate melt shows its best lubrication performance from 840 to 1000°C (COF below 0.20) (**Figure 8-8c**). The lowest coefficient of friction (< 0.07) is achieved at 930°C which is 3.7 times lower than sodium borate at the same testing temperature. Above this temperature, the friction gradually increases which indicates the loss in lubricity (**Figure 8-8c**). It is probably due to the significant diffusion of metallic ions to the melt network besides the effect of temperature that shortens the glass chain length and reduces the viscosity of the melt lubricant.¹² Due to a decrease in viscosity, the lubrication regime shifts toward the boundary condition which increases friction.

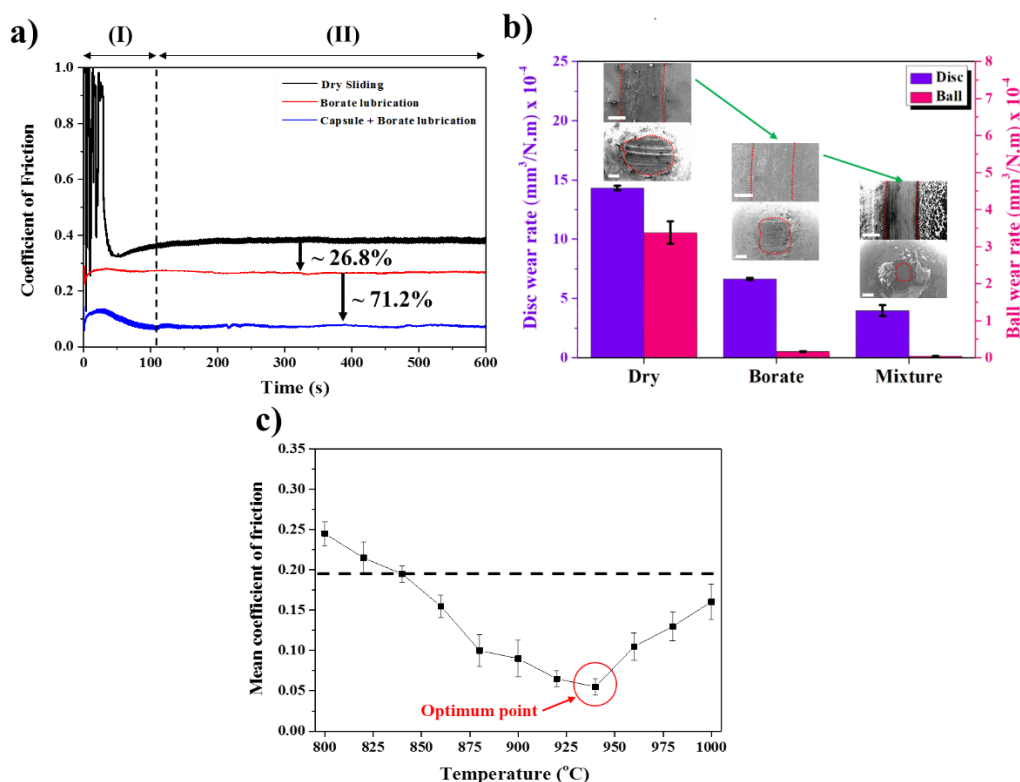


Figure 8-8. (a) Frictional behaviors of MC@NBO compared to NBO and dry sliding at 10 N, 930°C, 0.1 m/s; (b) Wear rate calculation of disc and ball for friction tests in (a); and (c) Mean friction coefficient of the MC@NBO melt lubricant at different temperatures.

Different loading conditions (at 940°C) are performed to evaluate the load-carrying capabilities of the capsule-added borate lubricant (**Figure 8-9a-c**). According to the friction results, the lubricant is capable to withstand the load up to 60 N (corresponding to the maximum Hertzian contact pressure of 2.61 GPa) while maintaining a low COF of around 0.1 (**Figure 8-9a-b**). However, the lubrication completely deteriorates at 80 N (corresponding to the maximum Hertzian contact pressure of 2.87 GPa) with a significant increase in friction to 0.28 (**Figure 8-9b**) and a dramatic variation in the friction curve (**Figure 8-9a**). Such a large variation can be translated to partial seizure which is a result of the unstable tribofilm formation. **Figure 8-9e** reveals the wear rate at different loads which shows a good agreement with the friction behavior. In particular, the wear rate of the ball and disc remains nearly constant when the load increases from 10 N to 40 N. At 60 N, the wear rate of the disc increases slightly by 14.8% while the ball wear rate increases by 60.7%. Such an increase can be correlated to the fluctuation of the friction curve as observed in **Figure 8-9a**. Although the mean friction still remains around 0.1, the fluctuation of the friction curve and an increase in the ball and disc wear loss indicates the destabilization of the tribofilm on the sliding surfaces. At 80 N, the wear rate of the disc and ball increases suddenly by 45.5% and 93.7% compared to the results from 10 N to 40 N, respectively. It is in agreement with the significant variation and dramatic increase of the friction curve (**Figure 8-9a**). Therefore, the tribofilm generated from the reactions between the sodium-calcium borosilicate melt and oxide demonstrates excellent load-carrying capability up to 60 N.

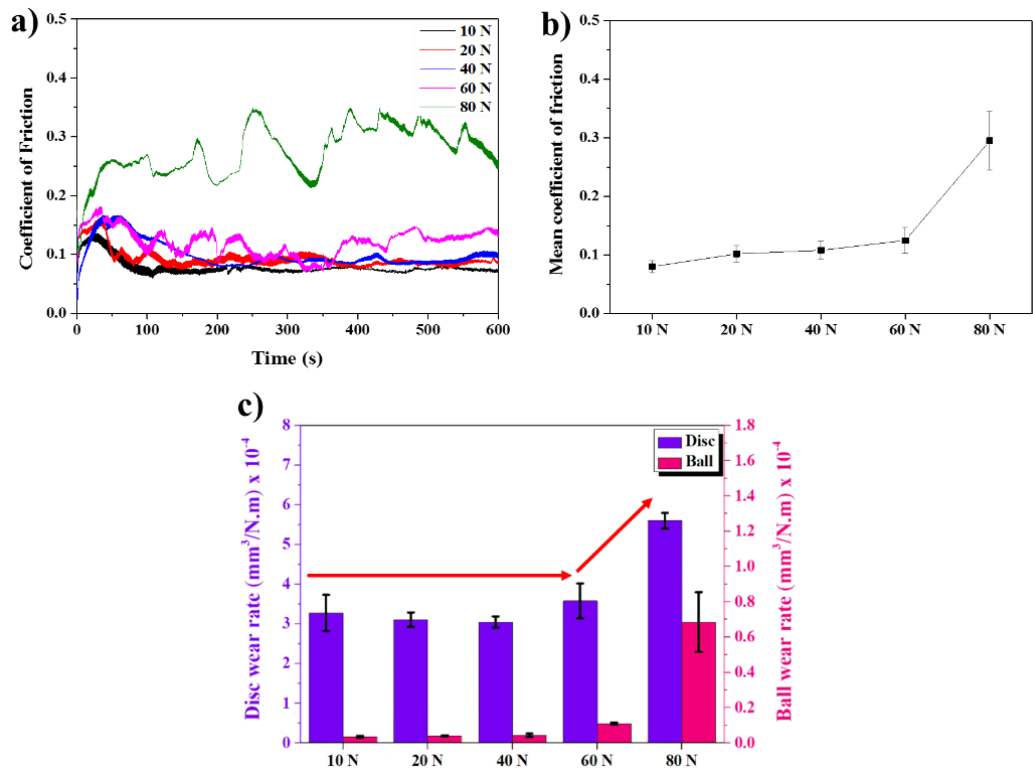


Figure 8-9 (a) Frictional behaviors of capsule-added borate melt lubricant at different loadings at 940°C, 0.1 m/s; (b) Mean friction coefficient at different loadings from (a); and (c) Wear rate calculation of disc and ball for capsule-added borate melt lubricant at different loads.

8.2.4. Friction-induced microstructural evolution of the oxide surface under MC@NBO lubrication at 930°C

The significant reduction at the optimum condition (10 N, 930°C, 0.1 m/s) can be associated with the microstructural evolution on the sliding surfaces. Disc wear track observation shows the smooth surfaces for the MC@NBO lubricant after the friction test (**Figure 8-10a**). There are several parallel streaks along the wear surface which may indicate the occurrence of the mixed lubrication regime. It is anticipated that the smooth and compact regions next to the streaks can experience the boundary lubrication regime while the streaks encounter the hydrodynamic regime. EDS mapping analysis (**Figure 8-10b**) indicates a uniform distribution of elements from the sodium-calcium borosilicate lubricant on the worn surfaces, however, the intensity signal of lubricant elements is stronger at the streak areas compared to the compacted areas. Further examination at a high-magnification of the streak areas (**Figure 8-10c**) reveals the agglomeration of the hexagonal oxide particles being immersed randomly in the glass melt with a fraction of them are aligned parallel to the sliding surfaces. The ball wear surface shows a similar pattern to the disc with the presence of several streaks along the sliding surfaces (**Figure 8-11a**). EDS mapping analysis confirms these streaks comprise the strong signal of lubricant elements (**Figure 8-11b**). High magnification examination at the compacted regions on the ball (**Figure 8-11c**) reveals the emergence of the submicron-spherical grains that assemble densely and neatly on the surfaces. These grains are covered by the glass melt as shown in **Figure 8-11c**.

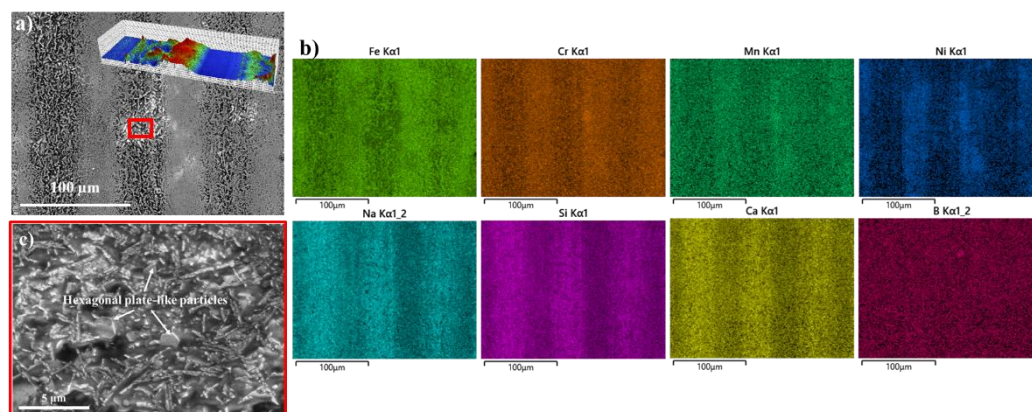


Figure 8-10. (a) SEM observation of disc worn surfaces; (b) corresponding EDS mapping; and (c) high-magnification SEM image of the disc worn surfaces after being lubricated by microcapsule-added sodium borate lubricant (MC@NBO). An inset image in (a) is the 3D profile of the disc wear track.

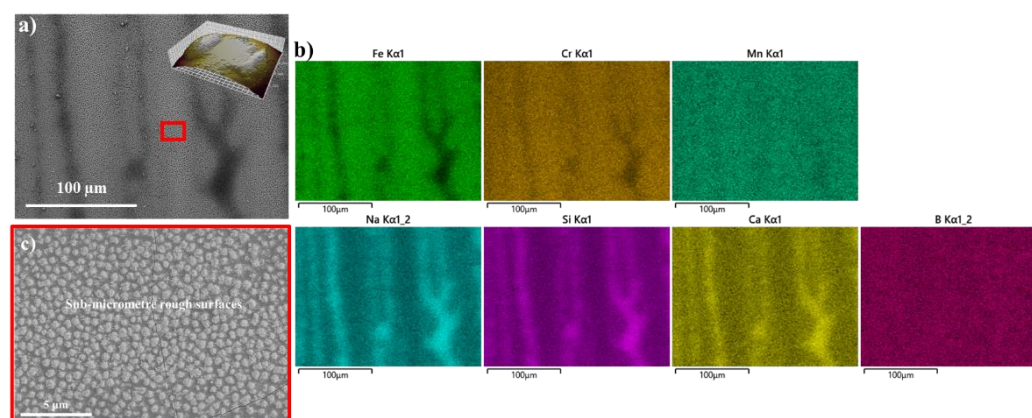


Figure 8-11. (a) SEM observation of ball worn surfaces; (b) corresponding EDS mapping; and (c) high-magnification SEM image of the ball worn surfaces after being lubricated by microcapsule-added sodium borate lubricant (MC@NBO). An inset image in (a) is the 3D profile of the ball wear track.

8.2.5. Hierarchical tribolayer formation and the reconstruction of the oxide after being lubricated by MC@NBO lubricant

Figure 8-12 details the cross-sectional analysis of the hierarchical tribofilm formed on the disc wear surface after friction test at 930°C. STEM-BF image shows the presence of a thin layer (~200 nm) located above the fine-grained oxide layer (~4 μm) (**Figure 8-12a**). This thin layer comprises boron (B), sodium (Na), calcium (Ca), and silicon (Si) (EDS mapping, **Figure 8-12b**) which is probably the glass tribofilm from the melt lubricant. The brighter diffraction contrast and SADP analysis of this layer indicate its amorphous nature (SADP 1, **Figure 8-13**). The signal intensity of the Fe, Ni, and Mn is concentrated at the top regions of the oxide layer while chromium shows its significant presence near the steel substrate (**Figure 8-12b**). The elemental distribution in the

oxide layer after the frictional event is consistent with that obtained under the static oxidation process (**Figure 8-6b**). However, a significant difference is observed at the oxide-melt interface that shows a refinement of the oxide particles with no presence of the large columnar particles (**Figure 8-12a**).

A high magnification BF image, at the yellow square marked in **Figure 8-12a**, reveals the agglomeration of the fine particles beneath the submicron particle at the oxide-melt interface (**Figure 8-12c**). Electron diffraction (SADP 2, **Figure 8-13**) shows a distinct pattern of the polycrystalline at the oxide area below the particle. However, based on the EDS mapping (**Figure 8-12b**), it is believed that this area is comprised of the mixture of the fine spinel oxides from (Ni, Fe, Mn-Cr)-O, which is characteristic of the stainless steel oxide scale.³⁸² The submicron particle on top of other fine particles (**Figure 8-12c**) can be the hexagonal particle observed in **Figure 8-10c**. From SADP analysis (**Figure 8-12d**), this particle has a hexagonal crystalline structure with indexing numbers that match the planes of (112), (114), and (107) from the M-type $M\text{Cr}_x\text{Fe}_{12-x}\text{O}_{19}$ hexaferrite^{389, 390} (with M = Mg, Ca, Ba). EDS line scanning (**Figure 8-12e**) shows the existence of a small amount of Ca with a significant amount of Fe and Cr at the center areas where no Na or Si is present. Thus, this particle is M-type $\text{CaCr}_x\text{Fe}_{12-x}\text{O}_{19}$ hexaferrite.

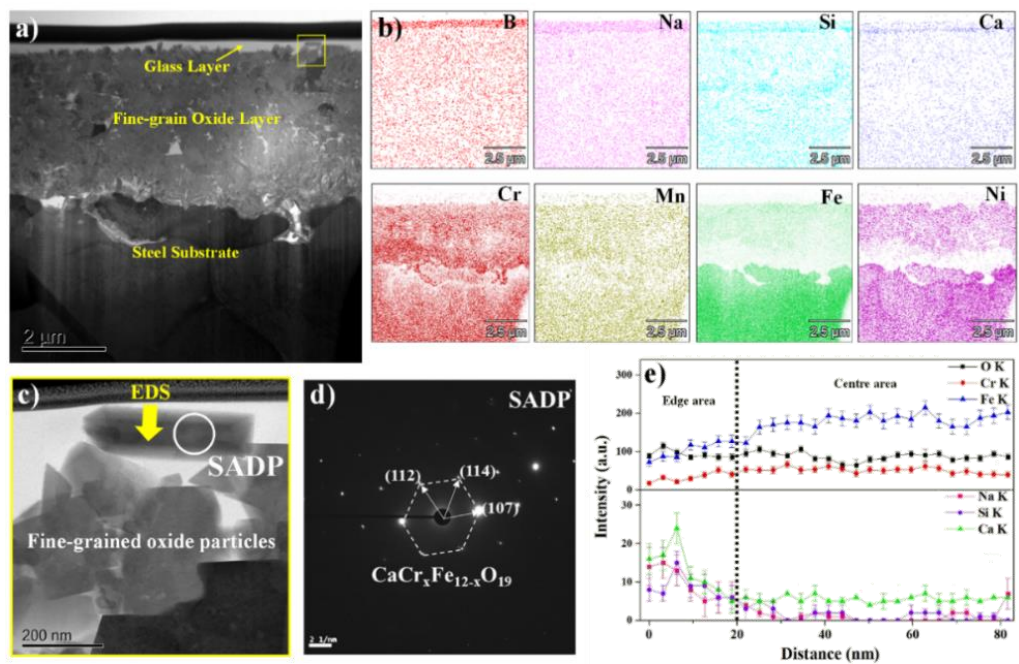


Figure 8-12. (a) Cross-section overview of the disc's hierarchical tribofilm after being lubricated by MC@NBO melt at 10 N, 930°C, 0.1 m/s; (b) Elemental distribution within the cross-sectional tribofilm by EDS mapping; (c) Aberration-corrected high-magnification bright field image of the yellow square marked in (a); (d) SAPD analysis of the marked particle; and (e) EDS line scanning analysis of the oxide particle as indicated in (c).

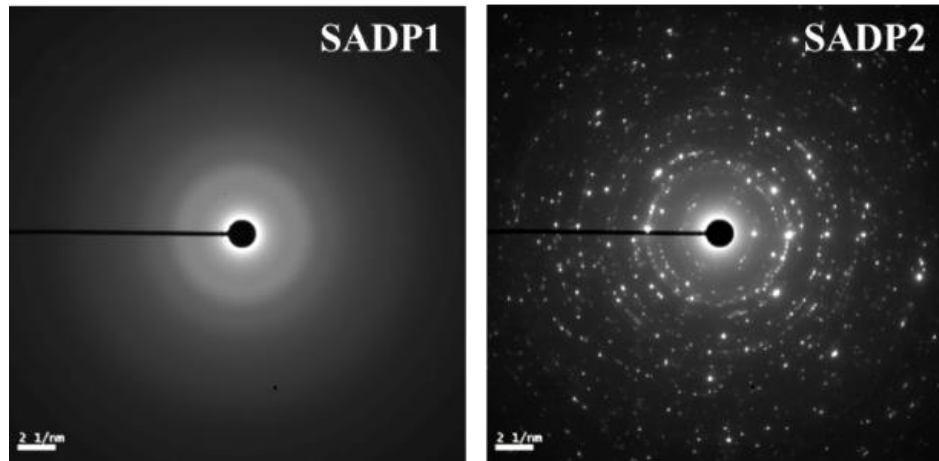


Figure 8-13. SADP analysis of the thin glass layer (SADP1) and the oxide scale layer (SADP2) on the disc after friction test at 930°C.

The cross-sectional tribofilm on the ball counterpart is characterized as shown in **Figure 8-14**. The tribofilm on the ball is comprised of a thin amorphous glass tribofilm positioned above the coarse-grain oxide layer (**Figure 8-14a**). The top layer on the ball is similar to the top layer on the disc (EDS in **Figure 8-14b** and **SADP1-Figure 8-15**). Meanwhile, the coarse grain oxide is constructed by dominant iron and chromium oxides with the presence of a small amount of manganese and nickel oxides (EDS mapping in **Figure 8-14b**). The formation of coarse-grained oxide with a significant amount of Fe indicates a high oxidation degree compared to a disc. It is reasonable since the ball is not protected when exposed to air at elevated temperatures before the friction test. In addition, the ball wear surfaces are constantly loaded and flash temperature during sliding, meanwhile, the disc wear surface is cyclically under loading and stressed-shearing every revolution.

High-magnification observation at the yellow square marked in **Figure 8-14a** shows the evolution of several fine-grained rod-like particles on top of the thick coarse-grained oxide layer (BF image in **Figure 8-14c**). These particles are characterized as the Fe-Cr spinel of FeCr_2O_4 by SADP and EDS (**Figure 8-14d** and **EDS 2-Figure 8-14e**). It can be seen that fraction of these particles floated within the amorphous layer. A significantly low diffraction contrast (**Figure 8-14c**) indicates the dissolution of these particles into the melt. EDS 1 (**Figure 8-14e**) indicates that these particles comprise the elements from both the melt (Na, Ca, Si) and Fe-Cr spinel. SADP analysis in **SADP 2-Figure 8-15** suggests that these low diffraction contrast particles match well with the FeCr_2O_4 spinel oxide but with a significant decrease in crystallinity. The observation of these floated particles within the amorphous areas reveals an occurrence of the (tribo)chemical reaction between the sodium-calcium borosilicate melt and the spinel oxide particles that gradually consume these particles.

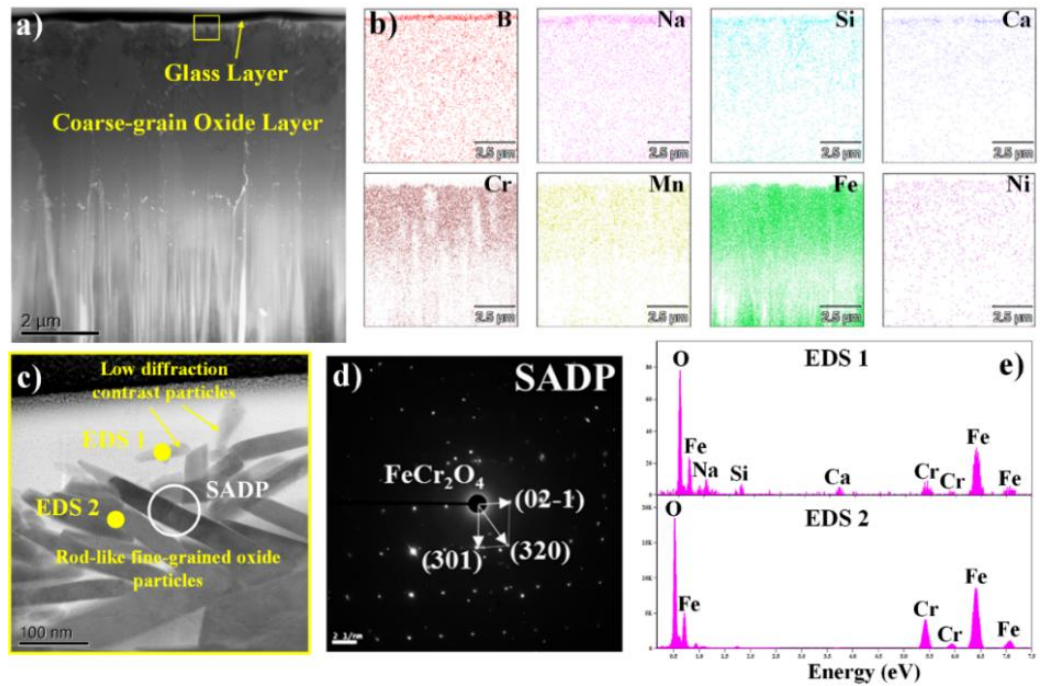


Figure 8-14. (a) Cross-section overview of the ball's hierarchical tribofilm after being lubricated by MC@NBO melt at 10 N, 930°C, 0.1 m/s; (b) Elemental distribution within the cross-sectional tribofilm by EDS mapping; (c) Aberration-corrected high-magnification bright field image of the yellow square marked in (a); (d) SADP of the marked particles; and (e) EDS spectrum of the spotted particles in (c).

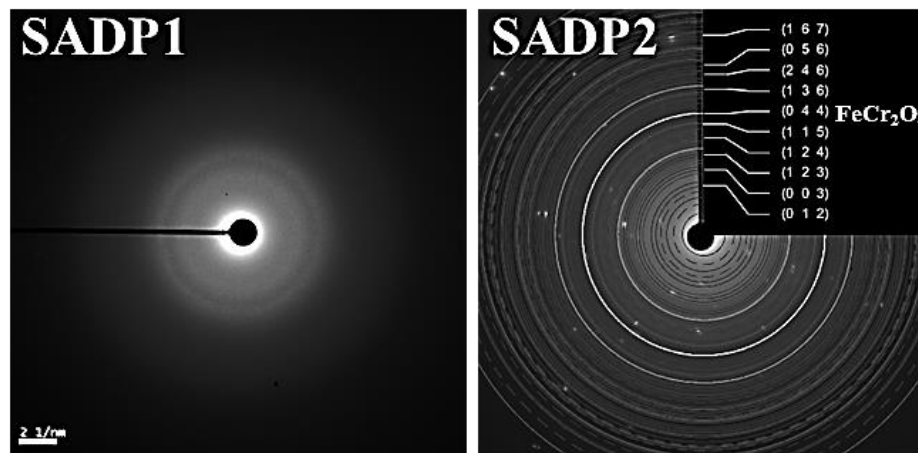


Figure 8-15. SADP analysis of the thin melt layer and the floated particles in the melt on the ball after friction test at 940°C.

8.2.6. Interfacial chemistry between the MC@NBO and oxide surfaces under static and friction conditions at 930°C governing the anti-oxidation and lubrication performances

Generally, the oxidation of steel is governed by both cationic outward diffusion (Cr^{2+} , Fe^{2+} , Mn^{2+} , etc.) and anionic inward diffusion (O^{2-}).³⁰ Sodium borate melt can provide excellent oxidation protection by hindering both these diffusions at high temperatures (up to 800°C).³⁶⁵ However, it

loses the anti-oxidation capability at significantly high temperatures (900-1000°C) (**Figure 8-4** and **Figure 8-5**). At this temperature range, sodium cations in the alkali-containing melt react significantly to the oxide surface or metallic cations (e.g. Fe^{2+} , Fe^{3+} , Mn^{2+} , Mn^{3+} ...) to form the reaction products.^{149, 155, 361, 365} This occurrence induces corrosion of the sodium to the oxide layer that promotes the formation and diffusion of the metallic cations from the steel. When the reactions between sodium and metallic oxides/cations reach equilibrium, these cations diffuse to the melt following the cationic exchange¹² which reduces the viscosity of the melt³⁹¹ and causes the formation of the cation vacancies within the oxide scale.³⁶³ The reduction in the melt viscosity manifests in the formation of O^{2-} within the melt by O_2 inward diffusion.³⁹² Meanwhile, the cation vacancies induce the infiltration of the melt to the oxide layer which facilitates the fluxing action of the grown scale.¹⁵⁵ Subsequently, the nucleation of the oxide particles in the melt expands due to the interactions between O^{2-} and metallic cations in the melt. These oxide particles grow substantially and gradually incorporate with the glass-former (SiO_2 , B_2O_3 , etc.) that forms the hard and rigid secondary scale^{361, 364} and finally replace the melts completely.³⁶⁵ For instance, the formation of iron boroferrite compounds along with the Fe-Cr spinel and the reaction products is observed in the sodium borate melt which is intermingled and compacted into the secondary oxide scale above the primary chromium oxide layer (**Figure 8-4a-Figure 8-4b** and **Figure 8-5**).

Here, negligible corrosion of the oxide scale by sodium is observed for the resulted sodium-calcium borosilicate melt (**Figure 8-6** and **Figure 8-7**). There are almost no reaction products of sodium and oxide compounds formed (EDS and SADP in **Figure 8-6** and **Figure 8-7**) and the oxide particles are only dissolved slightly (**Figure 8-6c**). This observation indicates the low reactivity of the sodium in the melt toward the oxide compounds compared to sodium borate. It can be explained based on the structural chemistry of the resulted sodium-calcium borosilicate melt. On the one hand, the silica phase in the borosilicate network slows down the ionic mobility of sodium due to an increase in the coordination number with more local constraints around it.²⁴⁹ On the other hand, alkali earth (Ca), supplies from the microcapsules, decreases the diffusion rate of the sodium since it increases the activation energy (E_a) for such diffusion.³⁹³ Based on Dietzel's structural field theory, the presence of alkali earth (Ca) can result in a more tightly bonded glass network with an alkali due to a large difference in the field strength (ΔF) values between alkali and alkaline earth ions.³⁹³ Consequently, these conditions result in low mobility of the sodium in the sodium-calcium borosilicate melt, thus, prevent the formation of the reaction products and reduce the oxidation rate of the steel substrate by 86.2%. Noticeably, the formation of iron boroferrite and the breakdown of the protective chromium oxide scale are inhibited (**Figure 8-4c-Figure 8-4d** and **Figure 8-6**).

Under stressed-shearing conditions, the excellent lubrication of the melt is observed. It can be partially associated with the presence of h-BN nanosheets at the sliding interfaces (**Figure 8-16**), as detected by Raman in **Chapter 7. Figure 8-16a** and **Figure 8-16b** reveal the clear detection of the layered h-BN nanosheets which are randomly oriented within the glass tribofilm layer. EELS B K edge at the white square marked area in **Figure 8-16a** shows a sharp peak at around 194 eV (**Figure 8-16c**). The shifting of this peak to the higher energy loss (EELS in (a) compared to the

EELS of h-BN nanosheets) is due to the presence of the $^{[3]}B$ coordination structure from the borosilicate glass. The disappearance of the σ^* (ii and iii) transition states (**Figure 8-16c**) indicates the decomposition of the h-BN nanosheets after sliding at elevated temperatures. From the analysis, it is believed that h-BN nanosheets with multilayers are released from the microcapsules and presented at the sliding interfaces when the capsule's shell is dissolved into the sodium borate.

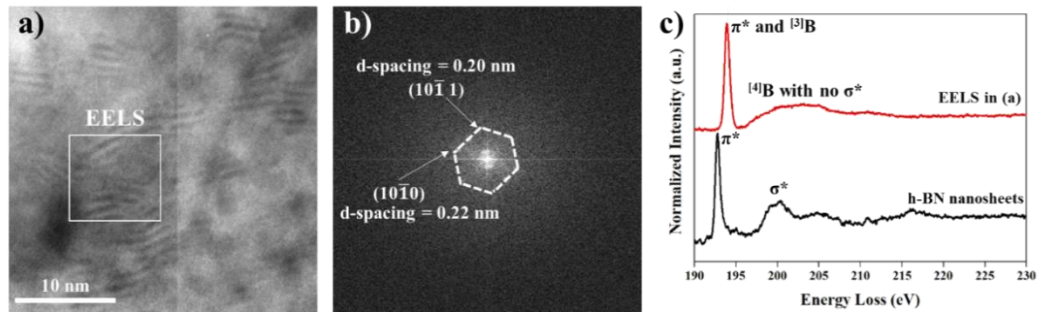


Figure 8-16. (a) HR-TEM image showing the presence of layered material within the melt; (b) Fast Fourier Transformation of (a) showing the hexagonal pattern of h-BN; and (c) EELS analysis of the white square marked in (a).

Apart from h-BN nanosheets, the microstructural transformation of the oxide surfaces also plays a significant role in producing excellent lubrication.²¹ When stressed-shearing is applied, the microstructure of the oxide scale on the disc and ball changes significantly (**Figure 8-12-Figure 8-14**). Compared to the static oxidation test, the oxide layer on the disc wear track is denser and more compacted with no appearance of rod-like microparticles at the oxide/melt interfaces. Meanwhile, the growth of several fine-grained rod-like particles on top of the coarse grain oxide scale is observed on the ball counterpart. The evolution of the disc and ball oxide surfaces in response to the friction behavior at different durations is shown in **Figure 8-17**.

In the 40 sec of the running-in stage, the oxide refinement on the disc and the nucleation of the fine particles on the ball takes place that increases steadily the friction (**Figure 8-17a1-Figure 8-17a3**). After 100 sec of sliding, the COF decreases dramatically and finally reaches the steady-state (**Figure 8-17b1**). The disc's oxide surface is constructed mainly with the very fine particles that are neatly and tightly compacted (**Figure 8-17b2**), whereas, the rod-like particles emerge significantly on the ball surfaces at this stage (**Figure 8-17b3**). **Figure 8-17c1** reveals a slight variation at the steady-state of COF during 600 sec. The oxide surface characterizations on the disc show the presence of plate-like particles (**Figure 8-17c2**) while the compact of the fine rod-like particles is evidenced on the ball (**Figure 8-17c3**). Chemical and phase analysis of the tribofilm areas at the oxide/melt interfaces shows no presence of the reaction products (**Figure 8-12-Figure 8-15**). Only spinel (Ni, Fe, Mn-Cr)-O oxides are found which are characteristics for the oxidation of the stainless steel. Besides, the plate-like particles on the disc are characterized as M-type $CaCr_xFe_{12-x}O_{19}$ hexaferrite (**Figure 8-12**) while the fine rod-like particles are $FeCr_2O_4$ spinel oxide (**Figure 8-14**). It can be concluded that the growth of the rod-like particles and the formation of M-type hexaferrite occur continuously at the steady-state process.

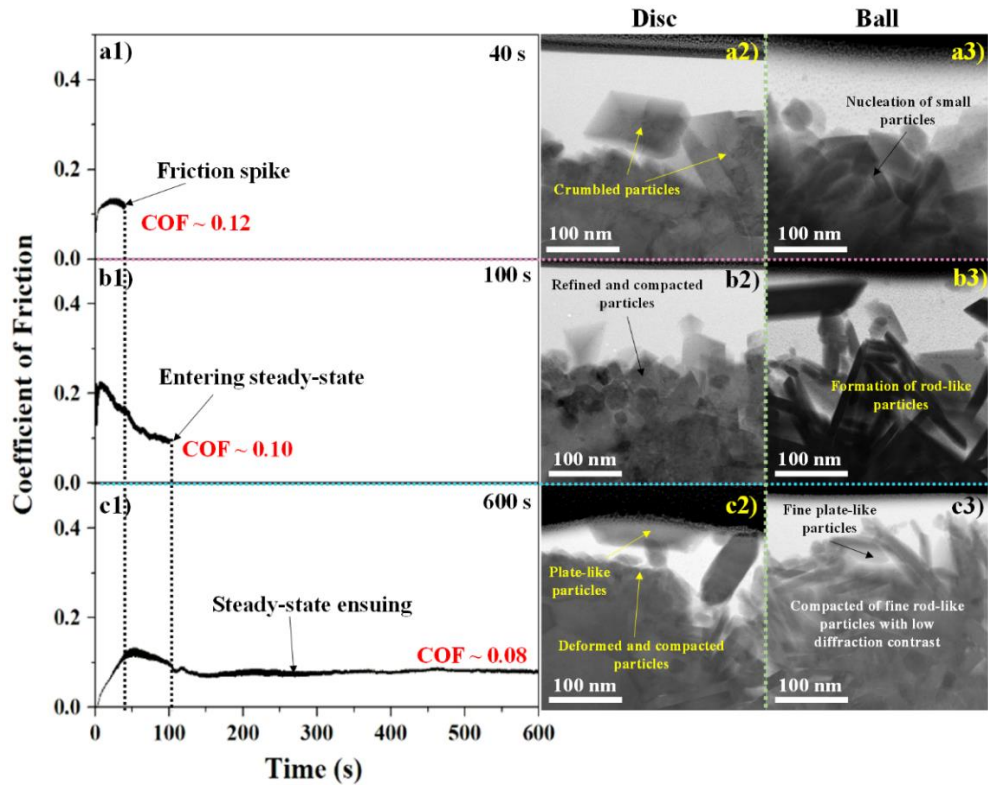


Figure 8-17. The structural transformation of the oxide surface on both counterparts at different frictional testing moments: Friction curve and microstructure of the oxide surfaces on (1) disc and (2) ball of the test stopped at 40 sec (a); 100 sec (b); and 600 sec (c).

An *in-situ* formation of the plate-like M-type $\text{CaCr}_x\text{Fe}_{12-x}\text{O}_{19}$ hexaferrite at the sliding interfaces can be explained by the principle of molten salt synthesis. Typically, molten salt acts as both a high-temperature solvent and reactant that accelerates the reaction rate (by ten orders of magnitude compared to solid-state reactions) and lowers the reaction temperature of the complex oxide particles (e.g. anisometric particles).³⁹⁴ In this formation route, the formation of the hexaferrite particles increases at higher temperatures following two stages: (1) a reaction stage including dissolution of the reactant particles in the molten salt and precipitation of the hexaferrite grains; (2) a growth stage including an increase in grain size.³⁹⁵

In this study, the generated sodium-calcium borosilicate melt acts as the molten salt solvent. However, the static heating condition cannot generate sufficient energy to trigger the dissolution of the spinel oxide particles to the melt (**Figure 8-6-[Figure 8-7](#)**) due to the low mobility of sodium and calcium in the melt. Conversely, friction-induced heat from the asperity contacts increases the temperature of the reaction medium,³⁹⁶ thereby, accelerating the dissolution of the Fe-Cr spinel oxide particles to the melt. On the other hand, the shearing under load also results in the refinement of the oxide particles (**Figure 8-17**) and induces an intermixing effect.⁵⁹ These occurrences increase the contacting area of the reactants (melt and Fe-Cr spinel oxide particles) that further promote the dissolution process. The very low diffraction contrast particles floated within the melt are strong evidence for the dissolution of the spinel oxide particles into the melt (**Figure 8-14c-[Figure 8-14e](#)**). Subsequently, the precipitation of the hexaferrite grains takes place within the melt

due to the reaction between the calcium in the melt and the spinel oxides. These grains grow in size by an Ostwald ripening which is supported by the continuous intermixing effect and flash temperature from sliding.³⁹⁷ During the frictional event, the Fe-Cr spinel oxide particles are dissolved into the melt simultaneously with the growth of the M-type hexaferrite. A decrease in the reactant (Fe-Cr spinel oxide particles) can trigger the growth of the Fe-Cr spinel rod-like oxide particles on the oxide surfaces, as shown on the ball since the ball is constantly under loading compared to the disc (**Figure 8-14c-Figure 8-14e** and **Figure 8-17**).

Overall, the precipitation of hexaferrite in the melt consumes a fraction of calcium in the melt which can change the structural network of the borosilicate melt. Here, the EELS analysis (**Figure 8-18**) shows an increase in $^{[3]}\text{B}$ trigonal intensity with the disappearance of $^{[4]}\text{B}$ tetrahedral peak from the analysis of the melt tribofilm on the wear surfaces of the counterparts compared to the non-sliding area. It is due to the loss of calcium that transformed the $^{[4]}\text{B}$ to $^{[3]}\text{B}$ coordination.³⁷⁵ Subsequently, the polymerization reaction of the trigonal $^{[3]}\text{B}$ coordination to form B-O-B in the borosilicate melt occurs to maintain the charge neutrality across the melt network.¹³ Such occurrence can result in a denser melt network and increase the viscosity of the melt that prevents the squeezing out and ensures good retention of the melt at the sliding interface even at high contact pressure (**Figure 8-9**).³⁹⁸ The summary of the M-type hexaferrite formation process is demonstrated in **Figure 8-19**.

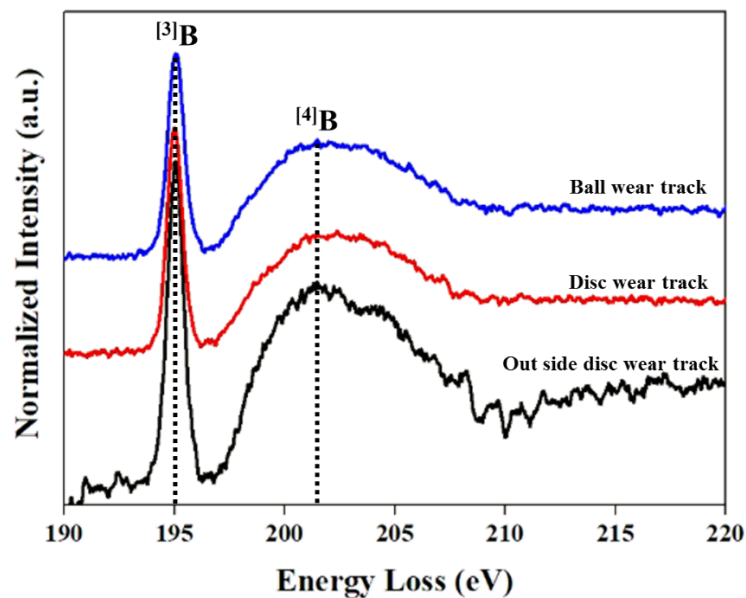


Figure 8-18. EELS B K edge analysis of the glass tribofilm on the ball wear track, disc wear track, and outside the disc wear track.

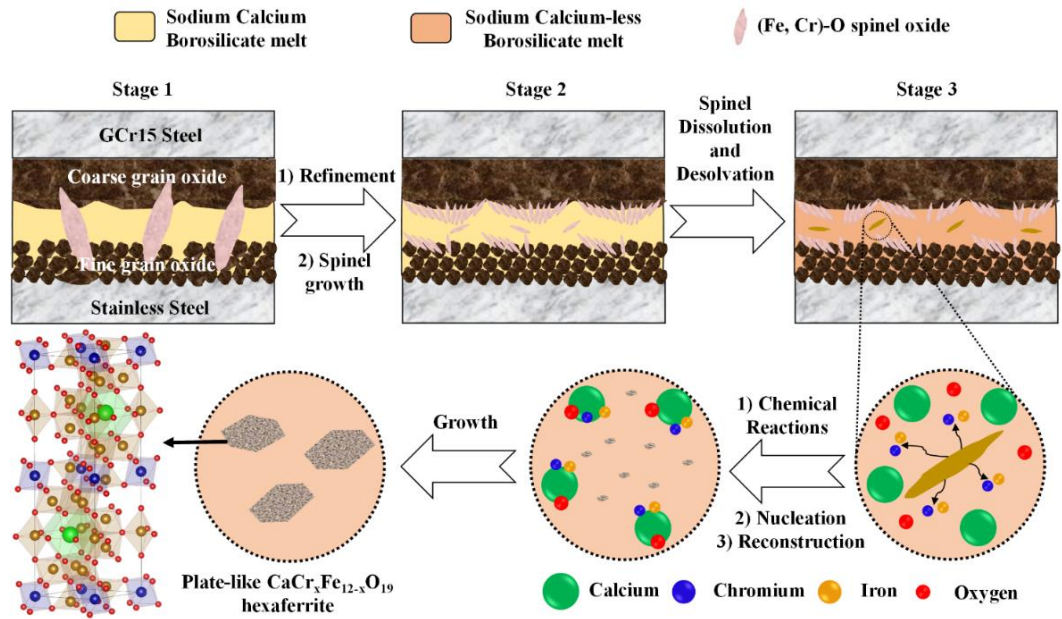


Figure 8-19. Schematic representing the effect of friction on the corrosion of the MC@NBO melt and the reconstruction of the oxide microstructure.

The reconstruction of the oxide microstructure under sodium-calcium borosilicate melt also plays a significant role in reducing the friction coefficient by 71.2% compared to sodium borate. In particular, the boundary friction can be significantly improved with the sliding between the fine-grained oxide layer on the disc and the fine-grained rod-like spinel oxide layer on the ball. According to the Hall-Petch behavior, the nanocrystalline layer has better yield strength due to the grain-boundary strengthening.³⁹⁹ During sliding, such fine-grained boundaries can stop the propagation of dislocation and dissipate the frictional energy from the plastic deformation of the near-surface steel matrix. Consequently, these fine-grain layers improve the tensile strength of the sliding surfaces and reduce the sticking between the sliding counterparts.⁴⁰⁰ Besides, the intercalation of M-type hexaferrite, as a non-layered two-dimensional material, between the sliding contacts, might contribute to separate the direct contact at the boundary regions. Due to its fine lateral size with a hexagonal shape, it is expected to accommodate large plastic strain during sliding which in turn reduces friction.³⁶⁸

8.3. Conclusions

In summary, the anti-oxidation and lubrication mechanisms of the BN@CaCO₃-SiO₂ hybrid microcapsule-added sodium borate melt on the sliding steel surfaces have been comprehensively investigated under the hot rolling conditions at 930°C. In particular, sodium borate melt dissolves the developed microcapsules that result in sodium-calcium borosilicate melt with excellent anti-oxidation and lubrication compared to sodium borate at elevated temperatures. The interfacial chemistry between the resulted melt and oxide surfaces has been investigated in detail which can reveal the chemistry underpinning the performance of the formulated lubricants. Several concluding remarks have been listed below:

- The developed colloidal capsule significantly improves the anti-oxidation of sodium borate by 82.6% at 930°C under simulated hot rolling conditions.
- The superior anti-oxidation mechanism with a less corrosive attack on the steel is due to the presence of calcium element and silica phase in the melt network that reduces the mobility and the reactivity of the sodium in the melt network.
- The complete dissolution of the Fe-Cr spinel oxides to the sodium-calcium borosilicate melt occurs apart from the refinement of the sliding surfaces. An intermixing effect and the flash temperature from the external stressed-shearing contribute significantly to the formation of the plate-like non-layered M-type hexaferrite particles at the sliding interfaces.
- There are no other reaction products containing sodium at the sliding interfaces which prove less corrosive attack of the melt toward the oxide even under external stimulations.
- A synergy between the h-BN nanosheets, the grain-refinement of the sliding surfaces, and the intercalation of the M-type hexaferrite at the sliding interfaces can deliver superior friction reduction (by 71.2%) compared to sodium borate under the mixed lubrication regime without the presence of sodium-containing reaction product layers.
- An insight into the interfacial chemistry between the newly formulated melt lubricant and oxide surfaces under harsh sliding conditions has been elucidated.

Chapter 9

Conclusions and recommendations for future work

This dissertation has successfully demonstrated a new strategy for developing the new generation of high-temperature lubricant additives for hot metal forming conditions. Particularly, microencapsulation based on the Pickering emulsion templated assembly has been applied to fabricate the novel lubricant additives for the first time which can greatly enhance the lubrication and anti-oxidation of the sodium borate melt at elevated temperatures. By conducting a large volume of experimental work ranging from the high-temperature tribological testing to the chemical synthesis and detailed analysis, potential solid lubricant additives that can function synergistically with sodium borate melt (**Chapter 4**) have been selected and the smart-responsive h-BN@CaCO₃-SiO₂ doubled-shell microcapsule has been successfully obtained (**Chapter 5** and **Chapter 7**). Furthermore, the high-temperature characteristics (**Chapter 6**), lubrication, and anti-oxidation mechanisms (**Chapter 8**) of the developed microcapsules under sodium borate melt have been elucidated. This final chapter (**Chapter 9**) aims to highlight the key findings in each chapter that contributes to the successful development of the innovative microcapsules, the detailed knowledge of the microcapsule mechanics via temperature, and the mechanisms by which the microcapsules perform in synergy with sodium borate melt under high-temperature lubrication. In addition, this final chapter also provides suggestions for future works which can be developed further from this dissertation.

9.1. Conclusions

Achieving high energy efficiency and reducing economic losses are particularly important in the steel manufacturing industries where significant yield losses of up to 40% of the production cost often emerge due to excessive friction, aggressive wear, and serious oxidation under severe high-temperature conditions. Glass-melt lubricants, comprising the derivatives of borate, silicate, phosphate, and the mixture thereof, offer an excellent solution for hot steel forming, however, they have reached the performance limits while posing the risk of sodium corrosion toward the oxide scale and steel substrate at high temperatures. Research on the formulation between the melt lubricants and other solid lubricant additives by physical blending is, thus, emerged recently to boost the lubricity of the melts and minimize the corrosion and oxidation rate of the steel substrate.

Nonetheless, the development of the lubricant package by such an approach has far-reaching implications in a simultaneous achievement in either cost-effectiveness or lubricity efficiency. A key challenge is the uncontrolled competitive and antagonistic effects between different lubricant additives within the base fluid which deteriorate their function. In this dissertation, rational designs and engineers of a compact hybrid colloidal capsule, which draws a series of “best in category” materials together into a single, monolithically integrated, micro-/nano-hierarchical structure with strong prospects for high-temperature lubrication, are presented.

Firstly, the tribological and anti-oxidation performances of sodium borate melt with added nano-

additives (SiO_2 , TiO_2 , Al_2O_3 , ZrO_2 , CaCO_3 , h-BN nanosheets, and graphite nanoplates) have been studied at 930°C . It has been found that the addition of SiO_2 nanoparticles improves (by over 50%) the anti-oxidation and lubrication performance of sodium borate due to the formation of sodium borosilicate melt at the sliding interfaces. Intriguingly, SiO_2 nanoparticle also inhibits the corrosion attack of sodium toward the oxide/steel surfaces and the boriding effect. It should also be noted that CaCO_3 nanoparticles can significantly reduce the corrosion attack of sodium and the boriding effect to the oxide scale due to the formation of the Ca-rich protective layer between the melt and the oxide surfaces. Meanwhile, other ceramic oxide nanoparticles can only either slightly improve the lubricity or anti-oxidation of sodium borate but fail to limit the corrosion of the oxide scale from sodium. Moreover, h-BN nanosheets and graphite nanoplates show no improvement in the anti-oxidation and lubrication performance of sodium borate at 930°C . Therefore, SiO_2 and CaCO_3 can be promising lubricant additives for the high-temperature lubrication of sodium borate.

In the next parts, the combination of SiO_2 and CaCO_3 into one body is first carried out by the utilization of Pickering emulsion templated assembly microencapsulation. Different synthesis conditions are conducted to examine the formation of an intact CaCO_3 -decorated SiO_2 double-shell colloidal capsule containing a water core. While the concentration of CaCO_3 and w/o ratio contribute significantly to the emulsion stability as the template for the capsule formation, the formation of the mechanically strong double-shell depends mainly on the TEOS addition and the reaction duration. The optimized conditions produce the intact spherical colloidal capsules with a size distribution of $7.5 \pm 1.8 \mu\text{m}$. Morphological and structural characterizations show the bi-layered hierarchical structure of the colloidal capsule with the densely packed CaCO_3 nanoparticles as an outer shell ($460 \pm 20 \text{ nm}$) and an inner homogeneous SiO_2 shell ($166 \pm 14 \text{ nm}$). The mechanical strength of this double shell is superior to the single SiO_2 shell due to the presence of a densely packed outer shell which chemically bonds to the inner shell. Intriguingly, the colloidal capsule can remain its intact spherical shape up to 1000°C while its mechanical behavior changes from brittleness to ductility with significant improvement in the compressive strength and strain at failure. This change is unusual and has not been observed before for the inorganic shell materials. It is due to the gradual dissolution of the outer shell into the inner shell during heating that results in the structural transformation at the nanoscale. By combining a newly developed multi-modal correlative *in-situ* TOF-SIMS heating technique and *in-situ* TEM heating, the mechanics of the double-shell at high temperatures has been elucidated.

Finally, it has been proven that the CaCO_3 -decorated SiO_2 double-shell has excellent thermo-mechanical stability that can provide full protection to the h-BN nanosheets at elevated temperatures. The innovative CaCO_3 -decorated SiO_2 double-shell colloidal capsule containing h-BN nanosheets has been applied as a lubricant additive in conjunction with sodium borate melt which improves the anti-oxidation of sodium borate melt by 93.3% while reducing friction and wear by over 70%. Advanced characterizations and analysis have also been performed to address the working mechanics of this additive under the sodium borate melt in terms of friction, wear, oxidation, and sodium corrosion at elevated temperatures. It has been found that the superior anti-oxidation mechanism with a less corrosive attack and boriding effect on the steel is due to the

presence of calcium and silica phase in the melt network that reduces the mobility and the reactivity of sodium toward the oxide scale. Meanwhile, the formation of plate-like non-layered M-type hexaferrite particles at the sliding interfaces in combination with the presence of h-BN nanosheets and the grain-refinement of the sliding surfaces is responsible for the superior friction reduction (by 71.2%) compared to sodium borate melt. The obtained results not only show the effectiveness of Pickering microencapsulation in tribology but also open a new avenue for the formulation and customization of the high-temperature lubricant packages. More importantly, an ability to control and manipulate the tribofilm formation by changing colloidal capsule components has also been suggested and emphasized.

9.2. Recommendations for future work

In the view of current research finding, the Pickering emulsion templated assembly microencapsulation have shown its huge potential for practical implementation in the development of not only the high-temperature lubricant additives but also the functional additives for the smart coatings. Besides, different new methodologies and analytical techniques for material characterizations and manipulations at submicron/nano-scale have also been demonstrated. In this part, the recommendations for future works are presented to fully utilize the potential of the developed colloidal capsules and their derivatives while advancing the application of the new analytical techniques in high-temperature tribology.

- i) The lubrication and anti-oxidation performances of the h-BN@CaCO₃-decorated SiO₂ doubled-shell colloidal capsules have been well validated by means of pin-on-disc testing under lab-scale conditions. Further experimental works and analysis in terms of static oxidation and tribology of the hot rolling processes should be carried out on the pilot-scale or real platform to justify the practical application of the microcapsules in conjunction with the sodium borate melt.
- ii) By conducting comprehensive tribological testing of sodium borate melt with different nanoparticles, it is feasible to proceed with the synthesis of different microcapsules by replacing CaCO₃ nanoparticles and h-BN nanosheets with different nanoparticles. For instance, ZrO₂ nanoparticles can be another option apart from CaCO₃ nanoparticles to construct the external shell since they can also limit the corrosion attack of the sodium toward the oxide scale. In addition, h-BN nanosheets can be replaced by graphene oxide or graphite oxide nanoplates. Mixtures of the core materials such as h-BN nanosheets and graphene/graphite oxide nanoplates should also be considered.
- iii) The methodology of utilizing AC-STEM/EELS and *in-situ* TEM mechanical compression has been successfully utilized to study the bonding information between the shells which can be linked with the mechanical behavior of the hybrid microcapsule. Further work on the *in-situ* observation of the external shell/inner shell interfacial transformation at the critical point under subsequent compression can be considered to understand how the external shell or inner shell supports the whole doubled-shell structure from breakage. In addition, the

proposed methodology can be applied to study *in-situ* the nano-tribology of the tribofilm on the wear track by means of correlating the obtained frictional forces with the deformation of the tribofilm during shearing under TEM observation.

- iv) The newly developed technique of combining MEMS-based microheater and TOF-SIMS analysis in the dual FIB-SEM chamber has shown its huge potential in real-time observation of chemical transportation at elevated temperatures. Further work can be considered by utilizing this technique to study how the sodium-containing melt corrodes the oxide scale at high temperatures under static heating. Moreover, an idea of incorporating AFM simultaneously with the MEMS + TOF-SIMS in the dual FIB-SEM chamber should be considered so that the *in operando* study of how shearing and pressure affect the sodium diffusion from the melt to the oxide can be conducted. Thus, detailed fundamentals about the high-temperature tribology of the sodium-containing melt at steel/steel contacts will be established.
- v) Other suggestions come from the further modification of the CaCO₃-decorated SiO₂ double-shell microcapsules for a better fit in different engineering applications. For instance, a replacement of the hollow sphere into the solid sphere should be better for an application in fabricating the mechanically durable superhydrophobic coatings since the colloidal capsule has an inherent micro-/nano-hierarchical structure. Besides, the double-shell of CaCO₃-decorated SiO₂ shows a promising thermal insulation effect with outstanding thermal stability which can be applied as fire-retardant additives for polymer-based coating. By adding some water-soluble flame-retardants into the core of the microcapsule, it is expected that the developed materials will deliver excellent flame retardancy and thermal protective effect to the polymer matrix.

Appendix A.

At elevated temperatures, the critical concern for elemental mapping using EDS is the significant interference of the infrared radiation.²⁹⁹ **Figure A-1** shows the MEMS chip appeared brightly when it was heated to 1000°C indicating significant infrared radiation. Since X-rays, visible light, and infrared are all part of the electromagnetic spectrum, they are all detected when using an EDS detector, and thus, the infrared radiation causes interferences to the X-ray input that impact peak resolution and position.

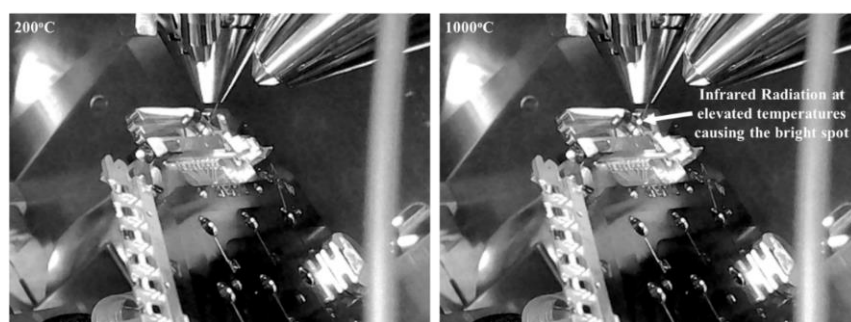


Figure A-1. Capturing images of the heater holder and the MEMS chip at 200°C and 1000°C indicating significant infrared radiation at high temperatures.

The contour plot of the XRD pattern with temperature (**Figure A-2a**) indicates phase changes during heating where the original peaks of calcite (CaCO_3) disappeared with an increase in temperature. There were several peaks of the new phases formed from 600°C to 1000°C which could be associated with the elemental diffusion of $^{40}\text{Ca}^{2+}$ from the external shell to the inner SiO_2 shell (**Figure 6-14c-Figure 6-14g**).

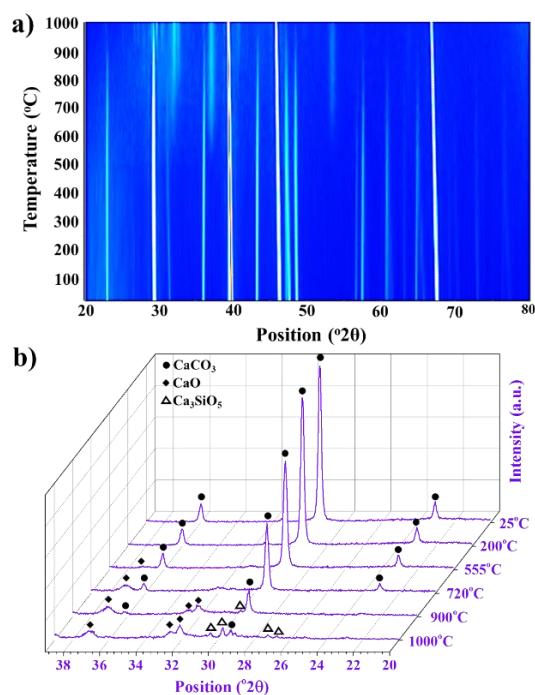


Figure A-2. (a) Contour plot and extracted 3D view of the X-ray diffraction pattern of the hybrid microcapsules via temperature changes, and; (b) The real-time phase changes from the doubled-shell colloidal microcapsules at selected temperatures measured by *in-situ* XRD heating.

To investigate the chemistry of the shell after annealing by *in-situ* TEM heating, EDS analysis is conducted after cooling down to room temperature on the specimen annealed at 555°C and 1000°C (**Figure A-3**). The results from the EDS post-mortem analysis of the samples after annealed at 555°C and 1000°C (**Figure A-3b** and **Figure A-3c**) are in good agreement with the elemental distribution obtained in *in-situ* TOF-SIMS analysis at the same temperatures (**Figure 6-14d** and **Figure 6-14g**). In particular, there is a clear observation of the inner shell and densely packed nanoparticles before the heating experiment (**Figure A-3a**). EDS mapping in **Figure A-3b** confirms the inner shell is SiO₂ and the packed external layer is CaCO₃. Signal-filtered merging analysis of Ca K and Si K in **Figure A-3c** reveals the agglomeration of the thin Ca layer in the SiO₂ shell proximity to the external shell/internal shell interfaces. It is consistent with the migration of the Ca at the external shell/internal shell interfaces to the SiO₂ shell observed by dynamically tracking the chemical diffusion at this temperature by *in-situ* TOF-SIMS analysis (**Figure 6-14d**). After the *in-situ* heating experiment at 1000°C, the migration of Ca from the external layer to the internal SiO₂ layer is observed followed by a decrease in the C intensity at the external shell (EDS mapping in **Figure A-3e**). Conducting the signal-filtered merging analysis of the chemical compositions affirms the complete incorporation of Ca within the SiO₂ shell layer while the external shell shows less intensity contrast. The EDS post-mortem analysis of the specimens after *in-situ* TEM heating shows consistent results with the results obtained from the *in-situ* TOF-SIMS heating experiment which eliminates the geometric concerns from the working nature of the SIMS technique.

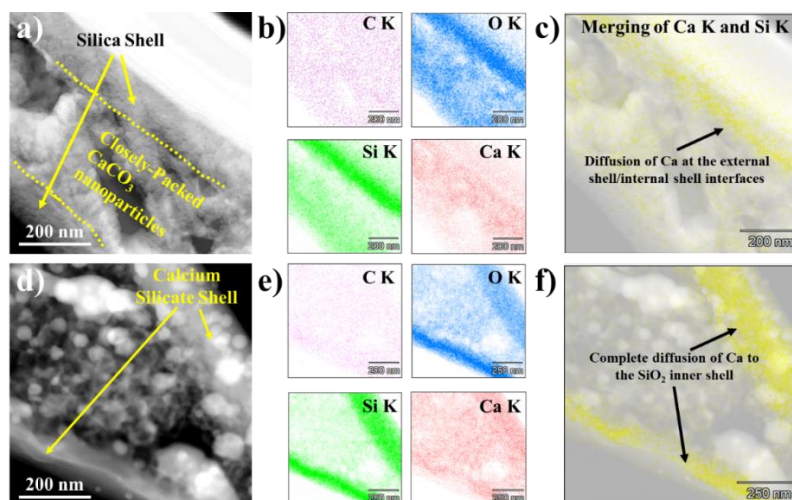


Figure A-3. EDS analysis of the interconnected rings after *in-situ* TEM heating at (a)-(c) 555°C and (d)-(f) 1000°C. The signal-filtered images of the merging between Ca K and Si K are presented in (c) and (f) showing the location of Ca in the SiO₂ shell layer.

The changes in the shell morphology from the *in-situ* TEM heating results in **Figure 6-15** are also supported by the N₂ adsorption and desorption experiment which shows an increase in the total BET surface area and average pore diameter of the capsule powders after annealed at different temperatures (**Figure A-4Error! Reference source not found.** and **Table A-1**). As shown in **Figure A-4Error! Reference source not found.**, the shape of the isotherms curves obtained from the non-annealed and majority of annealed samples resemble the reversible Type II isotherm which is the normal form for a non-porous or macroporous adsorbent⁴⁰¹. However, the characteristic feature of these isotherm curves is accordingly revealed through

the hysteresis loop which changes significantly via annealing temperature. The hysteresis loop becomes larger when the samples are annealed at 555°C and 650°C but they are still H3 type compared to the non-annealed one which is due to an increase in the number of macropores that are not completely filled with pore condensate⁴⁰². The formation of the macropores could be due to the release of CO₂ at the external shell/internal shell interfaces. This process accounted for the majority of the mass losses in the hybrid microcapsule according to TGA/DTG/DSC analysis. However, the sample annealed at 720°C shows the hysteresis of the H4 type loop and the adsorption branch is the composite of Types I and II indicating the presence of narrow slit-like pores and possible formation of microporosity⁴⁰³. The formation of microporosity increased the BET surface area (**Table A-1**) which could be due to the significant decomposition of the excessive CaCO₃ nanoparticles at the external shell. Further increasing annealing temperature to 900°C reduces the hysteresis loop of the N₂ isotherms from the annealed sample and the hysteresis loop completely disappears for the sample annealed at 1000°C. The BET surface areas decrease significantly in these two annealing temperatures indicative of the sintering effect that makes the shell denser.

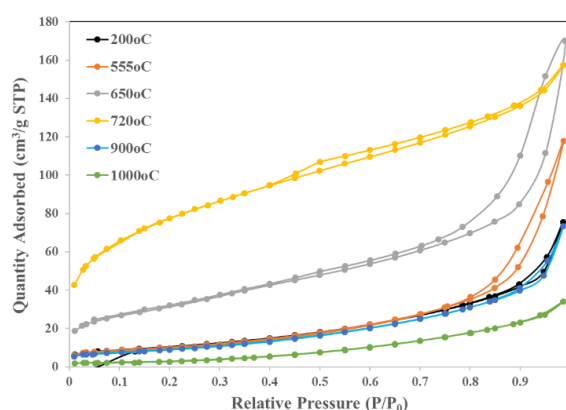


Figure A-4. N₂ adsorption-desorption isotherms of the microcapsule powders after annealed at different temperatures.

Table A-1. Total surface area, average pore size width, and pore volume of the non-annealed and annealed microcapsules.

Samples	BET* Surface Area (m ² /g)	Average Pore Width (nm)	Pore Volume (cm ³ /g)
200°C-annealed capsule	38.91 ± 0.42	6.91 ± 0.53	0.07 ± 0.00
555°C-annealed capsule	38.04 ± 0.43	5.41 ± 0.14	0.09 ± 0.00
650°C-annealed capsule	115.02 ± 0.63	4.63 ± 0.81	0.16 ± 0.02
720°C-annealed capsule	272.82 ± 3.71	3.48 ± 0.21	0.19 ± 0.02
900°C-annealed capsule	34.64 ± 0.60	5.74 ± 0.17	0.07 ± 0.01
1000°C-annealed capsule	12.63 ± 0.90	5.58 ± 0.31	0.04 ± 0.00

List of References

- (1). Holmberg, K.; Erdemir, A., Influence of Tribology on Global Energy Consumption, Costs and Emissions. *Friction*. **2017**, *5* (3), 263-284.
- (2). Krzyzanowski, M.; Beynon, J. H.; Farrugia, D. C., *Oxide scale behavior in high temperature metal processing*. John Wiley & Sons: 2010.
- (3). Spuzic, S.; Strafford, K.; Subramanian, C.; Savage, G., Wear of hot rolling mill rolls: an overview. *Wear*. **1994**, *176* (2), 261-271.
- (4). Wan, S.; Tieu, A. K.; Xia, Y.; Zhu, H.; Tran, B. H.; Cui, S., An Overview of Inorganic Polymer as Potential Lubricant Additive for High Temperature Tribology. *Tribol. Int.* **2016**, *102*, 620-635.
- (5). Ta, T. D.; Tran, B. H.; Tieu, K., Tribochemistry and Lubrication of Alkaline Glass Lubricants in Hot Steel Manufacturing. *Lubricants*. **2020**, *8* (7), 70.
- (6). Lavallée, Y.; Hirose, T.; Kendrick, J. E.; Hess, K.-U.; Dingwell, D. B., Fault rheology beyond frictional melting. *Proc. Natl. Acad. Sci. U.S.A.* **2015**, *112* (30), 9276-9280.
- (7). Frolenkova, L. Y.; Frolenkova, L. Y.; Shadrin, I., High-temperature oxidation of low-alloyed steel under glass coatings. *Protection of Metals and Physical Chemistry of Surfaces* **2010**, *46* (1), 103-109.
- (8). Feng, Z.-h.; Hu, X.-h.; Guo, H.-z.; Yao, Z.-k.; Lu, Z.; Gong, P., Study on protective lubricant technology for isothermal super plastic forging of Ti-1023 titanium alloy. *Forging & Stamping Technology* **2011**, (1), 32.
- (9). Li, L.; Peng, D.; Liu, J.; Liu, Z.; Jiang, Y., An experimental study of the lubrication behavior of A5 glass lubricant by means of the ring compression test. *Journal of Materials Processing Technology* **2000**, *102* (1-3), 138-142.
- (10). Furugen, M.; Matsuo, H.; Fukuyasu, T.; Nakanishi, T.; Yanagimoto, J., Characteristics of deformation in hot extrusion process of stainless steel tube. *Tetsu-to-Hagane* **1999**, *85* (11), 801-805.
- (11). Matsumoto, K.; Izawa, M.; Nakanishi, T.; Tsubouchi, K., Tribological properties of water glass lubricant for hot metalworking. *Tribol. T.* **2009**, *52* (4), 553-559.
- (12). Wan, S.; Tieu, A. K.; Zhu, Q.; Zhu, H.; Cui, S.; Mitchell, D. R. G.; Kong, C.; Cowie, B.; Denman, J. A.; Liu, R., Chemical Nature of Alkaline Polyphosphate Boundary Film at Heated Rubbing Surfaces. *Sci. Rep.* **2016**, *6* (1), 26008.
- (13). Tran, B. H.; Tieu, A. K.; Wan, S.; Zhu, H.; Mitchell, D. R.; Nancarrow, M. J., Multifunctional Bi-Layered Tribofilm Generated on Steel Contact Interfaces under High-Temperature Melt Lubrication. *J. Phys. Chem. C*. **2017**, *121* (45), 25092-25103.
- (14). Wang, L.; Tieu, A. K.; Cui, S.; Deng, G.; Wang, P.; Zhu, H.; Yang, J., Lubrication mechanism of sodium metasilicate at elevated temperatures through tribo-interface observation. *Tribol. Int.* **2019**, 105972.
- (15). Wang, L.; Tieu, A. K.; Zhu, H.; Deng, G.; Cui, S.; Zhu, Q., A study of water-based lubricant with a

- mixture of polyphosphate and nano-TiO₂ as additives for hot rolling process. *Wear*. **2021**, 203895.
- (16). ATC Lubricant Additives: Use and Benefits. <https://www.atc-europe.org/>.
- (17). Rudnick, L. R., *Lubricant Additives: Chemistry and Applications*. CRC press: 2009.
- (18). Chen, Y.; Renner, P.; Liang, H., Dispersion of Nanoparticles in Lubricating Oil: A Critical Review. *Lubricants*. **2019**, 7 (1), 7.
- (19). Scharf, T.; Prasad, S., Solid Lubricants: A Review. *J. Mater. Sci.* **2013**, 48 (2), 511-531.
- (20). Benita, S., *Microencapsulation: methods and industrial applications*. Crc Press: 2005.
- (21). Argibay, N.; Chandross, M.; Cheng, S.; Michael, J. R., Linking microstructural evolution and macro-scale friction behavior in metals. *J. Mater. Sci.* **2017**, 52 (5), 2780-2799.
- (22). Cvetkovski, K.; Ahlström, J.; Karlsson, B., Thermal softening of fine pearlitic steel and its effect on the fatigue behaviour. *Procedia. Eng.* **2010**, 2 (1), 541-545.
- (23). Wang, B. A simulation of roll wear in hot rolling processes. University of Wollongong, 1996.
- (24). Dünckelmeyer, M.; Kremaszky, C.; Werner, E.; Hein, G.; Schörkhuber, K., On the causes of banding failure. *Proc. of METEC InSteelCon 2011* **2011**, 1-9.
- (25). Hardell, J.; Hernandez, S.; Mozgovoy, S.; Pelcastre, L.; Courbon, C.; Prakash, B., Effect of oxide layers and near surface transformations on friction and wear during tool steel and boron steel interaction at high temperatures. *Wear*. **2015**, 330-331, 223-229.
- (26). Stott, F. H., The role of oxidation in the wear of alloys. *Tribol. Int.* **1998**, 31 (1-3), 61-71.
- (27). Padilla, H. A.; Boyce, B. L.; Battaile, C. C.; Prasad, S. V., Frictional performance and near-surface evolution of nanocrystalline Ni-Fe as governed by contact stress and sliding velocity. *Wear*. **2013**, 297 (1), 860-871.
- (28). Dohda, K.; Boher, C.; Rezai-Aria, F.; Mahayotsanun, N., Tribology in Metal Forming at Elevated Temperatures. *Friction*. **2015**, 3 (1), 1-27.
- (29). Chen, R. Y.; Yuen, W. Y. D., Review of the high-temperature oxidation of iron and carbon steels in air or oxygen. *Oxid. Met.* **2003**, 59 (5-6), 433-468.
- (30). Fromhold Jr, A., Theory of metal oxidation. Vol. 2. **1980**.
- (31). Cabrera, N.; Mott, N. F., Theory of the oxidation of metals. *Reports on Progress in Physics* **1949**, 12 (1), 163-184.
- (32). Cotell, C.; Yurek, G.; Hussey, R.; Mitchell, D.; Graham, M., The influence of grain-boundary segregation of Y in Cr₂O₃ on the oxidation of Cr metal. *Oxid. Met.* **1990**, 34 (3-4), 173-200.
- (33). Mrowec, S., On the mechanism of high temperature oxidation of metals and alloys. *Corros. Sci.* **1967**, 7 (9), 563-578.
- (34). DirectorateGeneralforResearchandInnovation, Oxidation management in hot rolling processes (Oxmapro). **2013**.
- (35). Chen, R. Y.; Yuen, W. Y. D., Oxide-Scale Structures Formed on Commercial Hot-Rolled Steel Strip

and Their Formation Mechanisms. *Oxid. Met.* **2001**, 56 (1), 89-118.

- (36). Chen, R. Y.; Yuen, W. Y. D., Examination of Oxide Scales of Hot Rolled Steel Products. *ISIJ. Int.* **2005**, 45 (1), 52-59.
- (37). Sun, W.; Tieu, A. K.; Jiang, Z.; Zhu, H.; Lu, C., Oxide scales growth of low-carbon steel at high temperatures. *Journal of Materials Processing Technology* **2004**, 155-156, 1300-1306.
- (38). Sun, W. A study on the characteristics of oxide scale in hot rolling of steel. University of Wollongong, 2005.
- (39). Suh, N. P., An overview of the delamination theory of wear. *Wear.* **1977**, 44 (1), 1-16.
- (40). Quinn, T. F. J., Oxidational wear modelling: Part II. The general theory of oxidational wear. *Wear.* **1994**, 175 (1), 199-208.
- (41). Stott, F.; Glascott, J.; Wood, G. C., Models for the generation of oxides during sliding wear. *Proceedings of the Royal Society of London. A. Mathematical and Physical Sciences* **1985**, 402 (1822), 167-186.
- (42). Pauschitz, A.; Roy, M.; Franek, F., Mechanisms of sliding wear of metals and alloys at elevated temperatures. *Tribol. Int.* **2008**, 41 (7), 584-602.
- (43). Rynio, C.; Hattendorf, H.; Klöwer, J.; Eggeler, G., The evolution of tribolayers during high temperature sliding wear. *Wear.* **2014**, 315 (1), 1-10.
- (44). Stott, F.; Lin, D.; Wood, G., The structure and mechanism of formation of the 'glaze' oxide layers produced on nickel-based alloys during wear at high temperatures. *Corros. Sci.* **1973**, 13 (6), 449IN3455-454IN6469.
- (45). Stott, F.; Wood, G., The influence of oxides on the friction and wear of alloys. *Tribol. Int.* **1978**, 11 (4), 211-218.
- (46). Inman, I.; Datta, S.; Du, H.; Burnell-Gray, J.; Luo, Q., Microscopy of glazed layers formed during high temperature sliding wear at 750° C. *Wear.* **2003**, 254 (5), 461-467.
- (47). Inman, I.; Datta, P.; Du, H.; Burnell-Gray, J.; Pierzgalinski, S.; Luo, Q., Studies of high temperature sliding wear of metallic dissimilar interfaces. *Tribology International* **2005**, 38 (9), 812-823.
- (48). Stott, F., The role of oxidation in the wear of alloys. *Tribol. Int.* **1998**, 31 (1), 61-71.
- (49). Stott, F., High-temperature sliding wear of metals. *Tribol. Int.* **2002**, 35 (8), 489-495.
- (50). Johnson, K.; Kendall, K.; Roberts, A. In *Surface energy and the contact of elastic solids*, Proceedings of the Royal Society of London A: Mathematical, Physical and Engineering Sciences, The Royal Society: 1971; pp 301-313.
- (51). Alison, P.; Wilman, H., The different behaviour of hexagonal and cubic metals in their friction, wear and work hardening during abrasion. *British Journal of Applied Physics* **1964**, 15 (3), 281.
- (52). Erdemir, A., A crystal-chemical approach to lubrication by solid oxides. *Tribology Letters* **2000**, 8 (2), 97-102.

- (53). Stott, F.; Jordan, M., The effects of load and substrate hardness on the development and maintenance of wear-protective layers during sliding at elevated temperatures. *Wear*. **2001**, *250* (1), 391-400.
- (54). Wang, S.; Wei, M.; Wang, F.; Cui, X.; Dong, C., Transition of mild wear to severe wear in oxidative wear of H21 steel. *Tribology Letters* **2008**, *32* (2), 67-72.
- (55). Lim, S., The relevance of wear-mechanism maps to mild-oxidational wear. *Tribol. Int.* **2002**, *35* (11), 717-723.
- (56). Meng, Y.; Xu, J.; Jin, Z.; Prakash, B.; Hu, Y., A Review of Recent Advances in Tribology. *Friction*. **2020**, *8* (2), 221-300.
- (57). Stribeck, R., Die wesentlichen eigenschaften der gleit-und rollenlager. *Zeitschrift des Vereines Deutscher Ingenieure* **1902**, *46*, 1341-1348, 1432-1438, 1463-1470.
- (58). Hersey, M. D., The laws of lubrication of horizontal journal bearings. *Journal of the Washington Academy of Sciences* **1914**, *4* (19), 542-552.
- (59). Furlong, O. J.; Miller, B. P.; Kotvis, P.; Tysoe, W. T., Low-Temperature, Shear-Induced Tribofilm Formation from Dimethyl Disulfide on Copper. *ACS Appl. Mater. Interfaces*. **2011**, *3* (3), 795-800.
- (60). Saito, K.; Iida, S. Lubricant for hot working and method for producing seamless steel pipe. 2011.
- (61). Plaza, S.; Margielewski, L.; Celichowski, G.; Wesolowski, R.; Stanecka, R., Tribological performance of some polyoxyethylene dithiophosphate derivatives water solutions. *Wear*. **2001**, *249* (12), 1077-1089.
- (62). Bay, N.; Azushima, A.; Groche, P.; Ishibashi, I.; Merklein, M.; Morishita, M.; Nakamura, T.; Schmid, S.; Yoshida, M., CIRP Annals-Manufac. *Technol* **2010**, *59*, 760-780.
- (63). Sliney, H. E., Solid lubricant materials for high temperatures—a review. *Tribology International* **1982**, *15* (5), 303-315.
- (64). Sliney, H. E., High temperature solid lubricants: When and where to use them. Design Engineering Conference: NASA Technical Memorandum, 1973.
- (65). Pownraj, C.; Valan Arasu, A., Effect of dispersing single and hybrid nanoparticles on tribological, thermo-physical, and stability characteristics of lubricants: a review. *J. Therm. Anal. Calorim.* **2021**, *143* (2), 1773-1809.
- (66). Lee, K.; Hwang, Y.; Cheong, S.; Choi, Y.; Kwon, L.; Lee, J.; Kim, S. H., Understanding the role of nanoparticles in nano-oil lubrication. *Tribology Letters* **2009**, *35* (2), 127-131.
- (67). Dai, W.; Kheireddin, B.; Gao, H.; Liang, H., Roles of Nanoparticles in Oil Lubrication. *Tribol. Int.* **2016**, *102*, 88-98.
- (68). Chou, C.-C.; Lee, S.-H., Tribological behavior of nanodiamond-dispersed lubricants on carbon steels and aluminum alloy. *Wear* **2010**, *269* (11), 757-762.
- (69). Zhao, F.; Bai, Z.; Fu, Y.; Zhao, D.; Yan, C., Tribological properties of serpentine, La (OH) 3 and their composite particles as lubricant additives. *Wear* **2012**, *288*, 72-77.
- (70). Tarasov, S.; Kolubaev, A.; Belyaev, S.; Lerner, M.; Tepper, F., Study of friction reduction by

nanocopper additives to motor oil. *Wear* **2002**, 252 (1), 63-69.

(71). Liu, G.; Li, X.; Qin, B.; Xing, D.; Guo, Y.; Fan, R., Investigation of the mending effect and mechanism of copper nano-particles on a tribologically stressed surface. *Tribology Letters* **2004**, 17 (4), 961-966.

(72). Bowden, F. P.; Bowden, F. P.; Tabor, D., *The Friction and Lubrication of Solids*. Oxford university press: 2001; Vol. 1.

(73). Ali, M. K. A.; Hou, X. J., Improving the tribological behavior of internal combustion engines via the addition of nanoparticles to engine oils. *Nanotechnol. Rev.* **2015**, 4 (4), 347-358.

(74). Tang, Z.; Li, S., A review of recent developments of friction modifiers for liquid lubricants (2007–present). *Current Opinion in Solid State and Materials Science* **2014**, 18 (3), 119-139.

(75). Asrul, M.; Zulkifli, N.; Masjuki, H.; Kalam, M., Tribological properties and lubricant mechanism of nanoparticle in engine oil. *Procedia Engineering* **2013**, 68, 320-325.

(76). Kao, M.-J.; Lin, C.-R., Evaluating the role of spherical titanium oxide nanoparticles in reducing friction between two pieces of cast iron. *Journal of Alloys and Compounds* **2009**, 483 (1-2), 456-459.

(77). Xia, X. T.; Zhang, Y. P.; Zhang, Y. Z.; Chen, S. C. In *Influence of ZrO₂ Nanoparticle as Additive on Tribological Property of Lithium Grease*, Applied Mechanics and Materials, Trans Tech Publ: 2010; pp 83-87.

(78). Bao, Y.; Sun, J.; Kong, L. In *Tribological properties and lubricating mechanism of SiO₂ nanoparticles in water-based fluid*, IOP Conference Series: Materials Science and Engineering, IOP Publishing: 2017; p 012025.

(79). Luo, T.; Wei, X.; Huang, X.; Huang, L.; Yang, F., Tribological properties of Al₂O₃ nanoparticles as lubricating oil additives. *Ceramics International* **2014**, 40 (5), 7143-7149.

(80). Zhao, C.; Chen, Y.; Ren, G., A study of tribological properties of water-based ceria nanofluids. *Tribology Transactions* **2013**, 56 (2), 275-283.

(81). Wu, L.; Zhang, Y.; Yang, G.; Zhang, S.; Yu, L.; Zhang, P., Tribological properties of oleic acid-modified zinc oxide nanoparticles as the lubricant additive in poly-alpha olefin and diisooctyl sebacate base oils. *RSC Advances* **2016**, 6 (74), 69836-69844.

(82). Zhang, X.; Xu, H.; Wang, J.; Ye, X.; Lei, W.; Xue, M.; Tang, H.; Li, C., Synthesis of ultrathin WS₂ nanosheets and their tribological properties as lubricant additives. *Nanoscale research letters* **2016**, 11 (1), 1-9.

(83). Xia, W.; Zhao, J.; Wu, H.; Zhao, X.; Zhang, X.; Xu, J.; Jiao, S.; Jiang, Z., Effects of oil-in-water based nanolubricant containing TiO₂ nanoparticles in hot rolling of 304 stainless steel. *Procedia Engineering* **2017**, 207, 1385-1390.

(84). Xia, W.; Zhao, J.; Wu, H.; Jiao, S.; Jiang, Z., Effects of oil-in-water based nanolubricant containing TiO₂ nanoparticles on the tribological behaviour of oxidised high-speed steel. *Tribology International* **2017**, 110, 77-85.

- (85). Zhu, Z. X.; Sun, J. L.; Wei, H. R.; Niu, T. L.; Zhu, Z. L. In *Research on Lubrication Behaviors of Nano-TiO₂ in Water-Based Hot rolling Liquid*, Advanced Materials Research, Trans Tech Publ: 2013; pp 139-143.
- (86). Wu, H.; Zhao, J.; Cheng, X.; Xia, W.; He, A.; Yun, J.-H.; Huang, S.; Wang, L.; Huang, H.; Jiao, S., Friction and wear characteristics of TiO₂ nano-additive water-based lubricant on ferritic stainless steel. *Tribology International* **2018**, *117*, 24-38.
- (87). Wu, H.; Zhao, J.; Xia, W.; Cheng, X.; He, A.; Yun, J. H.; Wang, L.; Huang, H.; Jiao, S.; Huang, L., A study of the tribological behaviour of TiO₂ nano-additive water-based lubricants. *Tribology International* **2017**, *109*, 398-408.
- (88). Wu, H.; Zhao, J.; Xia, W.; Cheng, X.; He, A.; Yun, J. H.; Wang, L.; Huang, H.; Jiao, S.; Huang, L., Analysis of TiO₂ nano-additive water-based lubricants in hot rolling of microalloyed steel. *Journal of Manufacturing Processes* **2017**, *27*, 26-36.
- (89). Gu, Y.; Zhao, X.; Liu, Y.; Lv, Y., Preparation and tribological properties of dual-coated TiO₂ nanoparticles as water-based lubricant additives. *Journal of Nanomaterials* **2014**, *2014*, 2.
- (90). Xi, W.; Zhao, J.; Wu, H.; Jiao, S.; Zhao, X.; Zhang, X.; Jiang, Z. In *A Novel Nano-TiO₂ Additive Oil-in-water Lubricant for Hot Steel Rolling*, Materials Science Forum, 2016.
- (91). Wu, H.; Zhao, J.; Xia, W.; Cheng, X.; He, A.; Yun, J. H.; Wang, L.; Huang, H.; Jiao, S.; Huang, L., Analysis of TiO₂ nano-additive water-based lubricants in hot rolling of microalloyed steel. *Journal of Manufacturing Processes* **2017**, *27*, 26-36.
- (92). Shimotomai, N.; Ihara, H.; Nanao, H., A Study of Hot Rolling Oil with Calcium Carbonate for Stainless Steel Process. *Tribol Online*. **2010**, *5* (3), 181-186.
- (93). Bao, Y.; Sun, J.; Kong, L., Effects of nano-SiO₂ as water-based lubricant additive on surface qualities of strips after hot rolling. *Tribol. Int.* **2017**, *114*, 257-263.
- (94). Allam, I. M., Solid lubricants for applications at elevated temperatures. *J. Mater. Sci.* **1991**, *26* (15), 3977-3984.
- (95). Xiaowei, L.; Jean-Charles, R.; Suyuan, Y., Effect of temperature on graphite oxidation behavior. *Nuclear Engineering and design* **2004**, *227* (3), 273-280.
- (96). Friedman, P.; Luckey, S., High-temperature lubricants for superplastic forming of metals. In *Superplastic Forming of Advanced Metallic Materials*, Elsevier: 2011; pp 72-82.
- (97). Kumar, U.; Mishra, A. K.; Ohdar, R., Hot forging lubricants. *International Journal of Mechanical Engineering and Robotics Research* **2014**, *3* (4), 155.
- (98). Cattell, H. G. Hot metal forging and stamping lubricant composition. 1981.
- (99). Jayaseelan, V.; Kalaichelvan, K., Lubrication effect on friction factor of AA6063 in forward extrusion process. *Procedia. Eng.* **2014**, *97*, 166-171.
- (100). Kimura, Y.; Wakabayashi, T.; Okada, K.; Wada, T.; Nishikawa, H., Boron nitride as a lubricant additive. *Wear.* **1999**, *232* (2), 199-206.

- (101). Kostoglou, N.; Polychronopoulou, K.; Rebholz, C., Thermal and chemical stability of hexagonal boron nitride (h-BN) nanoplatelets. *Vacuum*. **2015**, *112*, 42-45.
- (102). Pierson, H. O., *Handbook of chemical vapor deposition: principles, technology and applications*. William Andrew: 1999.
- (103). Spear, J. C.; Ewers, B. W.; Batteas, J. D., 2D-Nanomaterials for Controlling Friction and Wear at Interfaces. *Nano Today* **2015**, *10* (3), 301-314.
- (104). Çelik, O.; Ay, N.; Göncü, Y., Effect of Nano Hexagonal Boron Nitride Lubricant Additives on the Friction and Wear Properties of AISI 4140 Steel. *Particul. Sci. Technol.* **2013**, *31* (5), 501-506.
- (105). Wan, Q.; Jin, Y.; Sun, P.; Ding, Y., Tribological behaviour of a lubricant oil containing boron nitride nanoparticles. *Procedia. Eng.* **2015**, *102*, 1038-1045.
- (106). Cho, D.-H.; Kim, J.-S.; Kwon, S.-H.; Lee, C.; Lee, Y.-Z., Evaluation of hexagonal boron nitride nano-sheets as a lubricant additive in water. *Wear*. **2013**, *302* (1), 981-986.
- (107). Chen, B.; Bi, Q.; Yang, J.; Xia, Y.; Hao, J., Tribological properties of solid lubricants (graphite, h-BN) for Cu-based P/M friction composites. *Tribol. Int.* **2008**, *41* (12), 1145-1152.
- (108). Podgornik, B.; Kafexhiu, F.; Kosec, T.; Jerina, J.; Kalin, M., Friction and anti-galling properties of hexagonal boron nitride (h-BN) in aluminium forming. *Wear* **2017**, *388*, 2-8.
- (109). Hod, O., Graphite and Hexagonal Boron-Nitride Possess the Same Interlayer Distance. Why? *arXiv preprint arXiv:1109.3813* **2011**.
- (110). Zishan, C.; Hejun, L.; Qiangang, F.; Xinfu, Q., Tribological Behaviors of SiC/h-BN Composite Coating at Elevated Temperatures. *Tribol. Int.* **2012**, *56*, 58-65.
- (111). Erdemir, A.; Fenske, G.; Erck, R., A study of the formation and self-lubrication mechanisms of boric acid films on boric oxide coatings. *Surf. Coat. Technol.* **1990**, *43*, 588-596.
- (112). Xiao, H.; Liu, S., 2D Nanomaterials as Lubricant Additive: A Review. *Mater. Des.* **2017**, *135*, 319-332.
- (113). Barnes, A. M.; Bartle, K. D.; Thibon, V. R., A review of zinc dialkyldithiophosphates (ZDDPS): characterisation and role in the lubricating oil. *Tribology International* **2001**, *34* (6), 389-395.
- (114). Martin, J. M., Antiwear mechanisms of zinc dithiophosphate: a chemical hardness approach. *Tribol. Lett.* **1999**, *6* (1), 1-8.
- (115). Pearson, R. G., *Chemical hardness*. Wiley Online Library: 1997.
- (116). Kita, H.; Fukushima, M.; Jayaseelan, D. D.; Zeng, Y. P.; Ohsumi, K., Oxidation Resistance and High-Temperature Lubricating Properties of Magnesium-Phosphate-Treated Graphite. *Journal of the American Ceramic Society* **2005**, *88* (9), 2632-2634.
- (117). Kong, N.; Tieu, A. K.; Zhu, Q.; Zhu, H.; Wan, S.; Kong, C., Tribofilms generated from bulk polyphosphate glasses at elevated temperatures. *Wear* **2015**, *330*, 230-238.
- (118). Tieu, A. K.; Kong, N.; Wan, S.; Zhu, H.; Zhu, Q.; Mitchell, D. R.; Kong, C., The Influence of Alkali Metal Polyphosphate on the Tribological Properties of Heavily Loaded Steel on Steel Contacts at Elevated

- Temperatures. *Adv. Mater. Interf.* **2015**, 2 (6).
- (119). Tieu, A. K.; Wan, S.; Kong, N.; Zhu, Q.; Zhu, H., Excellent Melt Lubrication of Alkali Metal Polyphosphate Glass for High Temperature Applications. *RSC. Adv.* **2015**, 5 (3), 1796-1800.
- (120). Wan, S.; Tieu, A. K.; Zhu, Q.; Zhu, H.; Cui, S.; Mitchell, D. R.; Kong, C.; Cowie, B.; Denman, J. A.; Liu, R., Chemical nature of alkaline polyphosphate boundary film at heated rubbing surfaces. *Scientific reports* **2016**, 6.
- (121). Cui, S.; Wan, S.; Zhu, Q.; Tieu, A. K.; Zhu, H.; Wang, L.; Cowie, B., Tribochemical behavior of phosphate compounds at an elevated temperature. *J. Phys. Chem. C.* **2016**, 120 (45), 25742-25751.
- (122). Philippon, D.; De Barros-Bouchet, M.-I.; Lerasle, O.; Le Mogne, T.; Martin, J.-M., Experimental simulation of tribochemical reactions between borates esters and steel surface. *Tribology letters* **2011**, 41 (1), 73-82.
- (123). Shah, F. U.; Glavatskih, S.; Antzutkin, O. N., Boron in tribology: from borates to ionic liquids. *Tribology letters* **2013**, 51 (3), 281-301.
- (124). Boshui, C.; Jianhua, F.; Jiu, W.; Jia, L.; Fang, L., Friction and wear performances of borates and lanthanum chloride in water. *Journal of Rare Earths* **2008**, 26 (4), 590-593.
- (125). Hu, C. H.; Xue, J.; Deng, Z. C.; Wang, S. J.; Wang, H. T. In *Friction and Wear Performances of n-Na₂B₄O₇/Ion Nitrocarburized Duplex Layer at Different Frequencies*, Advanced Materials Research, Trans Tech Publ: 2014; pp 62-67.
- (126). Adams, J. H., Lubricant containing potassium borate. Google Patents: 1976.
- (127). Peeler, R. L., Alkali metal borate ep lubricants. Google Patents: 1967.
- (128). Liu, S.; Ott, W. K., Sodium silicate applications in oil, gas & geothermal well operations. *Journal of Petroleum Science and Engineering* **2020**, 107693.
- (129). Potužák, M. Physico-Chemical Properties of Silicate Melts. Imu, 2006.
- (130). Mackenzie, J., The physical chemistry of simple molten glasses. *Chem. Rev.* **1956**, 56 (3), 455-470.
- (131). Ehrt, D.; Keding, R., Electrical conductivity and viscosity of borosilicate glasses and melts. *Phys. Chem. Glasses.-B.* **2009**, 50 (3), 165-171.
- (132). Tran, B. H.; Tieu, K.; Wan, S.; Zhu, H.; Cui, S.; Wang, L., Understanding the Tribological Impacts of Alkali Element on Lubrication of Binary Borate Melt. *RSC. Adv.* **2018**, 8 (51), 28847-28860.
- (133). Tilley, R. J.; Tilley, R., *Understanding solids: the science of materials*. Wiley Online Library: 2004.
- (134). Takasu, H.; Hoshino, H.; Tamura, Y.; Kim, S. T.; Kato, Y., Sodium Ferrite/Carbon Dioxide Reactivity for High Temperature Thermochemical Energy Storage. *ISIJ. Int.* **2019**, 59 (4), 715-720.
- (135). Marugán, J.; Botas, J. A.; Molina, R.; Herradón, C., Study of the hydrogen production step of the Mn₂O₃/MnO thermochemical cycle. *Int. J. Hydrogen. Energ.* **2014**, 39 (10), 5274-5282.
- (136). Coudurier, L.; Hopkins, D. W.; Wilkomirsky, I., *Fundamentals of Metallurgical Processes: International Series on Materials Science and Technology*. Elsevier: 2013; Vol. 27.

- (137). Jacob, K.; Kumar, A.; Rajitha, G.; Waseda, Y., Thermodynamic data for Mn_3O_4 , Mn_2O_3 and MnO_2 . *High. Temp. Mat. Pr-Isr.* **2011**, *30* (4-5), 459-472.
- (138). Jabraoui, H.; Vaills, Y.; Hasnaoui, A.; Badawi, M.; Ouaskit, S., Effect of sodium oxide modifier on structural and elastic properties of silicate glass. *J. Phys. Chem. B.* **2016**, *120* (51), 13193-13205.
- (139). Young, D. J., *High temperature oxidation and corrosion of metals*. Elsevier: 2008; Vol. 1.
- (140). Barsoum, M.; Barsoum, M., *Fundamentals of ceramics*. CRC press: 2002.
- (141). Lei, X.; Jee, Y.; Huang, K., Amorphous $Na_2Si_2O_5$ as a fast Na^+ conductor: an ab initio molecular dynamics simulation. *J. Mater. Chem. A.* **2015**, *3* (39), 19920-19927.
- (142). Han, T.; Zhang, C.; Luo, J., Macroscale Superlubricity Enabled by Hydrated Alkali Metal Ions. *Langmuir.* **2018**, *34* (38), 11281-11291.
- (143). Gaisinskaya-Kipnis, A.; Ma, L.; Kampf, N.; Klein, J., Frictional Dissipation Pathways Mediated by Hydrated Alkali Metal Ions. *Langmuir.* **2016**, *32* (19), 4755-4764.
- (144). Donose, B. C.; Vakarelski, I. U.; Higashitani, K., Silica Surfaces Lubrication by Hydrated Cations Adsorption from Electrolyte Solutions. *Langmuir.* **2005**, *21* (5), 1834-1839.
- (145). Li, J.; Zhang, C.; Sun, L.; Lu, X.; Luo, J., Tribochemistry and Superlubricity Induced by Hydrogen Ions. *Langmuir.* **2012**, *28* (45), 15816-15823.
- (146). Dishon, M.; Zohar, O.; Sivan, U., From Repulsion to Attraction and Back to Repulsion: The Effect of NaCl, KCl, and CsCl on the Force between Silica Surfaces in Aqueous Solution. *Langmuir.* **2009**, *25* (5), 2831-2836.
- (147). Wright, A. C.; Dalba, G.; Rocca, F.; Vedishcheva, N. M., Borate versus silicate glasses: why are they so different? *Phys. Chem. Glasses.-B.* **2010**, *51* (5), 233-265.
- (148). Shivpuri, R.; Kini, S., *Lubricants and their applications in forging*. 2005; Vol. 14, p 84-92.
- (149). Cui, S. Lubrication mechanism investigation of alkali polyphosphate glass in hot rolling. University of Wollongong, School of Mechanical, Materials, Mechatronic and Biomedical Engineering, 2018.
- (150). Jennings, H.; Thomas, J. J.; Capito, R. M. Protective coatings for metals. 2012.
- (151). Suwattananont, N.; Petrova, R. S., Oxidation kinetics of boronized low carbon steel AISI 1018. *Oxid. Met.* **2008**, *70* (5-6), 307.
- (152). Davis, J. R., *Surface hardening of steels: understanding the basics*. ASM international: 2002.
- (153). Petrova, R. S.; Suwattananont, N., Surface modification of ferrous alloys with boron. *Journal of electronic materials* **2005**, *34* (5), 575-582.
- (154). Ptačinová, J.; Drienovský, M.; Palcut, M.; Čička, R.; Kusý, M.; Hudakova, M., Oxidation stability of boride coatings. *Kovove Mater* **2015**, *53*, 1-12.
- (155). Tran, B. H.; Tieu, A. K.; Wan, S.; Zhu, H.; Liu, R., Hot Corrosion of Borate Melt and Interface Chemistry of Borate-Coated Steel Under Tribological Stimulation. *Corros. Sci.* **2018**, *140*, 231-240.
- (156). Zhang, J. S.; Hu, Y.; Shelton, H.; Kung, J.; Dera, P., Single-crystal X-ray diffraction study of

Fe₂SiO₄ fayalite up to 31 GPa. *Phys. Chem. Miner.* **2017**, *44* (3), 171-179.

(157). Pourghahramani, P.; Altin, E.; Mallembakam, M. R.; Peukert, W.; Forssberg, E., Microstructural characterization of hematite during wet and dry millings using Rietveld and XRD line profile analyses. *Powder. Technol.* **2008**, *186* (1), 9-21.

(158). Leinonen, J., Superior properties of ultra-fine-grained steels. *Acta. Polytech.* **2004**, *44* (3).

(159). Shahraki, S.; Miyanaji, H.; Abdollahi, H., Microstructure and mechanical properties of ultrafine-grained IF steel sheets produced by constrained groove pressing. *Eng. Solid. Mech.* **2020**, *8* (1), 63-68.

(160). Shakhvorostov, D.; Gleising, B.; Büscher, R.; Dudzinski, W.; Fischer, A.; Scherge, M., Microstructure of tribologically induced nanolayers produced at ultra-low wear rates. *Wear.* **2007**, *263* (7-12), 1259-1265.

(161). Tekkaya, A. E.; Homberg, W.; Brosius, A., *60 Excellent Inventions in Metal Forming*. Springer: 2015.

(162). Wang, L.; Tieu, A. K.; Zhu, H.; Deng, G.; Hai, G.; Wang, J.; Yang, J., The Effect of Expanded Graphite with Sodium Metasilicate as Lubricant at High Temperature. *Carbon.* **2020**, *159*, 345-356.

(163). Bay, N.; Azushima, A.; Groche, P.; Ishibashi, I.; Merklein, M.; Morishita, M.; Nakamura, T.; Schmid, S.; Yoshida, M., Environmentally benign tribo-systems for metal forming. *CIRP annals* **2010**, *59* (2), 760-780.

(164). Hsu, S. M.; Zhao, F. Microencapsulation of chemical additives. 2017.

(165). Mitchell, K. C. Microencapsulation for Next Generation Lubricants. The University of Leeds, 2014.

(166). Pederson, T. C.; Sachdev, A. K.; Schneider, E. W. Microencapsulated engine lubricant additives. 2013.

(167). Calcavecchio, P.; Farg, L. O.; KRYLOWSKI, J. M.; Webster, M. N.; Minak-Bernero, V.; Drake, E. N. Microencapsulation of lubricant additives. 2014.

(168). Esser-Kahn, A. P.; Odom, S. A.; Sottos, N. R.; White, S. R.; Moore, J. S., Triggered release from polymer capsules. *Macromolecules* **2011**, *44* (14), 5539-5553.

(169). Dabbagh, A.; Mahmoodian, R.; Abdullah, B. J. J.; Abdullah, H.; Hamdi, M.; Abu Kasim, N. H., Low-melting-point polymeric nanoshells for thermal-triggered drug release under hyperthermia condition. *International Journal of Hyperthermia* **2015**, *31* (8), 920-929.

(170). Lin, C.-L.; Chiu, W.-Y.; Lee, C.-F., Thermal/pH-sensitive core-shell copolymer latex and its potential for targeting drug carrier application. *Polymer* **2005**, *46* (23), 10092-10101.

(171). Latnikova, A.; Yildirim, A., Thermally induced release from polymeric microparticles with liquid core: the mechanism. *Soft matter* **2015**, *11* (10), 2008-2017.

(172). Paramonov, S. E.; Bachelder, E. M.; Beaudette, T. T.; Standley, S. M.; Lee, C. C.; Dashe, J.; Fréchet, J. M., Fully acid-degradable biocompatible polyacetal microparticles for drug delivery. *Bioconjugate chemistry* **2008**, *19* (4), 911-919.

(173). Khaja, S. D.; Lee, S.; Murthy, N., Acid-degradable protein delivery vehicles based on metathesis

chemistry. *Biomacromolecules* **2007**, 8 (5), 1391-1395.

(174). Morinaga, H.; Morikawa, H.; Wang, Y.; Sudo, A.; Endo, T., Amphiphilic Copolymer Having Acid-Labile Acetal in the Side Chain as a Hydrophobe: Controlled Release of Aldehyde by Thermoresponsive Aggregation–Dissociation of Polymer Micelles. *Macromolecules* **2009**, 42 (6), 2229-2235.

(175). Chan, Y.; Wong, T.; Byrne, F.; Kavallaris, M.; Bulmus, V., Acid-labile core cross-linked micelles for pH-triggered release of antitumor drugs. *Biomacromolecules* **2008**, 9 (7), 1826-1836.

(176). Wang, Y.; Caruso, F., Template synthesis of stimuli-responsive nanoporous polymer-based spheres via sequential assembly. *Chemistry of materials* **2006**, 18 (17), 4089-4100.

(177). Kono, K.; Kawakami, K.; Morimoto, K.; Takagishi, T., Effect of hydrophobic units on the pH-responsive release property of polyelectrolyte complex capsules. *Journal of applied polymer science* **1999**, 72 (13), 1763-1773.

(178). Kokufuta, E.; Shimizu, N.; Nakamura, I., Preparation of polyelectrolyte-coated pH-sensitive poly(styrene) microcapsules and their application to initiation-cessation control of an enzyme reaction. *Biotechnology and bioengineering* **1988**, 32 (3), 289-294.

(179). Kozlovskaya, V.; Kharlampieva, E.; Drachuk, I.; Cheng, D.; Tsukruk, V. V., Responsive microcapsule reactors based on hydrogen-bonded tannic acid layer-by-layer assemblies. *Soft Matter* **2010**, 6 (15), 3596-3608.

(180). Borchert, U.; Lipprandt, U.; Bilanz, M.; Kimpfler, A.; Rank, A.; Peschka-Süss, R.; Schubert, R.; Lindner, P.; Förster, S., pH-induced release from P2VP–PEO block copolymer vesicles. *Langmuir* **2006**, 22 (13), 5843-5847.

(181). Williamson, T.; Buren, M. F. V.; Massucco, A. A.; Lindstrom, R. S. Cast material with encapsulated lubricant. US5250344 A, 1993.

(182). Guo, Q. B.; Lau, K. T.; Zheng, B. F.; Rong, M. Z.; Zhang, M. Q., Imparting Ultra-Low Friction and Wear Rate to Epoxy by the Incorporation of Microencapsulated Lubricant? *Macromolecular Materials and Engineering* **2009**, 294 (1), 20-24.

(183). Guo, Q. B.; Lau, K. T.; Rong, M. Z.; Zhang, M. Q., Optimization of tribological and mechanical properties of epoxy through hybrid filling. *Wear* **2010**, 269 (1), 13-20.

(184). Li, H.; Wang, Q.; Li, M.; Cui, Y.; Zhu, Y.; Wang, B.; Wang, H., Preparation of high thermal stability polysulfone microcapsules containing lubricant oil and its tribological properties of epoxy composites. *Journal of microencapsulation* **2016**, 33 (3), 286-291.

(185). Li, H.; Ma, Y.; Li, Z.; Ji, J.; Zhu, Y.; Wang, H., High temperature resistant polysulfone/silica double-wall microcapsules and their application in self-lubricating polypropylene. *RSC Advances* **2017**, 7 (79), 50328-50335.

(186). Mu, B.; Li, X.; Yang, B.; Cui, J.; Wang, X.; Guo, J.; Bao, X.; Chen, L., Tribological behaviors of polyurethane composites containing self-lubricating microcapsules and reinforced by short carbon fibers. *Journal of Applied Polymer Science* **2017**, 134 (43).

- (187). Li, H.; Wang, Q.; Wang, H.; Cui, Y.; Zhu, Y.; Wang, B., Fabrication of Thermally Stable Polysulfone Microcapsules Containing [EMIm][NTf₂] Ionic Liquid for Enhancement of In Situ Self-Lubrication Effect of Epoxy. *Macromolecular Materials and Engineering* **2016**, *301* (12), 1473-1481.
- (188). Mitchell, K.; Neville, A.; Walker, G. M.; Sutton, M. R.; Cayre, O. J., Synthesis and Tribological Testing of Poly(Methyl Methacrylate) Particles Containing Encapsulated Organic Friction Modifier. *Tribol. Int.* **2018**, *124*, 124-133.
- (189). Hsu, S.; Parab, S.; Zhao, F., Microencapsulation of additives. In *World Tribology Congress 2017*, Beijing-China, 2017.
- (190). Xu, S., Preparation and tribological behaviour of poly (methyl methacrylate)(PMMA) microcapsules containing friction modifiers. *J. Microencapsul.* **2020**, *37* (4), 314-323.
- (191). Yu, S.; Wang, X.; Wu, D., Microencapsulation of n-octadecane phase change material with calcium carbonate shell for enhancement of thermal conductivity and serving durability: synthesis, microstructure, and performance evaluation. *Appl. Energy.* **2014**, *114*, 632-643.
- (192). Wang, T.; Wang, S.; Luo, R.; Zhu, C.; Akiyama, T.; Zhang, Z., Microencapsulation of phase change materials with binary cores and calcium carbonate shell for thermal energy storage. *Applied Energy* **2016**, *171*, 113-119.
- (193). Zhao, Y.; Chen, Z.; Zhu, X.; Möller, M., A facile one-step approach toward polymer@ SiO₂ core-shell nanoparticles via a surfactant-free miniemulsion polymerization technique. *Macromolecules* **2016**, *49* (5), 1552-1562.
- (194). H.G, M. u.; Z, J.; W, Q., Synthesis of a Novel Nanoencapsulated n-Eicosane Phase Change Material with Inorganic Silica Shell Material for Enhanced Thermal Properties through Sol-Gel Route. *Journal of Textile Science & Engineering* **2017**, *7* (2).
- (195). Fang, G.; Chen, Z.; Li, H., Synthesis and properties of microencapsulated paraffin composites with SiO₂ shell as thermal energy storage materials. *Chemical engineering journal* **2010**, *163* (1), 154-159.
- (196). Tian, Y.; Zhou, W.; Yu, L.; Meng, F.; Yu, K.; Ding, X.; Li, M.; Wang, Z., Self-assembly of monodisperse SiO₂-zinc borate core-shell nanospheres for lubrication. *Materials Letters* **2007**, *61* (2), 506-510.
- (197). King, J. P. Recirculating powder lubricant delivery systems using thermally and oxidatively stable solid lubricants. 1992.
- (198). Zhang, G.; Li, J.; Chen, Y.; Xiang, H.; Ma, B.; Xu, Z.; Ma, X., Encapsulation of copper-based phase change materials for high temperature thermal energy storage. *Solar Energy Materials and Solar Cells* **2014**, *128*, 131-137.
- (199). Pendyala, S. Macroencapsulation of phase change materials for thermal energy storage. University of South Florida, University of South Florida, 2012.
- (200). Mathur, A. K. Thermal energy storage system comprising encapsulated phase change material. 2012.
- (201). MARUOKA, N.; SATO, K.; YAGI, J.-i.; AKIYAMA, T., Development of PCM for Recovering

High Temperature Waste Heat and Utilization for Producing Hydrogen by Reforming Reaction of Methane. *ISIJ. Int.* **2002**, *42* (2), 215-219.

(202). Hsu, S. M.; Zhao, F. Microencapsulation of Chemical Additives. 2015.

(203). Bollhorst, T.; Rezwan, K.; Maas, M., Colloidal capsules: nano-and microcapsules with colloidal particle shells. *Chem. Soc. Rev.* **2017**, *46* (8), 2091-2126.

(204). Salari, J. Pickering emulsions, colloidosomes & micro-encapsulation. Eindhoven: Technische Universiteit Eindhoven, 2011.

(205). Dinsmore, A.; Hsu, M. F.; Nikolaidis, M.; Marquez, M.; Bausch, A.; Weitz, D., Colloidosomes: selectively permeable capsules composed of colloidal particles. *Science.* **2002**, *298* (5595), 1006-1009.

(206). Pieranski, P., Two-dimensional interfacial colloidal crystals. *Phys. Rev. Lett.* **1980**, *45* (7), 569.

(207). de Folter, J. W.; Hutter, E. M.; Castillo, S. I.; Klop, K. E.; Philipse, A. P.; Kegel, W. K., Particle shape anisotropy in Pickering emulsions: cubes and peanuts. *Langmuir.* **2013**, *30* (4), 955-964.

(208). Gonzalez Ortiz, D.; Pochat-Bohatier, C.; Cambedouzou, J.; Bechelany, M.; Miele, P., Current Trends in Pickering Emulsions: Particle Morphology and Applications. *Engineering* **2020**, *6* (4), 468-482.

(209). Chevalier, Y.; Bolzinger, M.-A., Emulsions stabilized with solid nanoparticles: Pickering emulsions. *Colloids and Surfaces A: Physicochemical and Engineering Aspects* **2013**, *439*, 23-34.

(210). Kaptay, G., On the equation of the maximum capillary pressure induced by solid particles to stabilize emulsions and foams and on the emulsion stability diagrams. *Coll. Surf. A* **2006**, *282*, 387-401.

(211). Binks, B. P., Particles as surfactants—similarities and differences. *Curr. Opin. Colloid Interface Sci.* **2002**, *7* (1-2), 21-41.

(212). Tang, J.; Quinlan, P. J.; Tam, K. C., Stimuli-responsive Pickering emulsions: recent advances and potential applications. *Soft. Matter.* **2015**, *11* (18), 3512-3529.

(213). Jiang, J.; Zhu, Y.; Cui, Z.; Binks, B. P., Switchable Pickering emulsions stabilized by silica nanoparticles hydrophobized in situ with a switchable surfactant. *Angewandte Chemie International Edition* **2013**, *52* (47), 12373-12376.

(214). Thompson, K. L.; Williams, M.; Armes, S. P., Colloidosomes: synthesis, properties and applications. *Journal of colloid and interface science* **2015**, *447*, 217-228.

(215). van Wijk, J.; Salari, J. W.; Meuldijk, J.; Klumperman, B., Determination of the shell growth direction during the formation of silica microcapsules by confocal fluorescence microscopy. *J. Mater. Chem. B.* **2015**, *3* (39), 7745-7751.

(216). van Wijk, J.; Salari, J. W.; Zaquen, N.; Meuldijk, J.; Klumperman, B., Poly (methyl methacrylate)–silica microcapsules synthesized by templating Pickering emulsion droplets. *Journal of Materials Chemistry B* **2013**, *1* (18), 2394-2406.

(217). Schmitt, V.; Destribats, M.; Backov, R., Core-shell material, method for preparing same, and use thereof for the thermostimulated generation of substances of interest. Google Patents: 2015.

(218). Wang, Q. J.; Chung, Y.-W., *Encyclopedia of tribology*. Springer: 2013.

- (219). Schey, J. A., Tribology in metalworking: Friction. *Lubrication and wear* **1983**, 451.
- (220). Sheu, S., Tribology in Hot Rolling of Metal. In *Encyclopedia of Tribology*, Wang, Q. J.; Chung, Y.-W., Eds. Springer US: Boston, MA, 2013; pp 3830-3837.
- (221). Zhu, H.; Zhu, Q.; Tieu, A. K.; Kosasih, B.; Kong, C., A simulation of wear behaviour of high-speed steel hot rolls by means of high temperature pin-on-disc tests. *Wear*. **2013**, *302* (1-2), 1310-1318.
- (222). Morrell, R., *Handbook of properties of technical and engineering ceramics*. Hmsco: 1989.
- (223). Williams, J. A.; Dwyer-Joyce, R. S., Contact between solid surfaces. *Modern tribology handbook* **2001**, *1*, 121-162.
- (224). Duan, H.; Wang, D.; Sobal, N. S.; Giersig, M.; Kurth, D. G.; Möhwald, H., Magnetic colloidosomes derived from nanoparticle interfacial self-assembly. *Nano. Lett.* **2005**, *5* (5), 949-952.
- (225). Gabbott, P., *Principles and applications of thermal analysis*. John Wiley & Sons: 2008.
- (226). Bocklitz, T.; Dörfer, T.; Heinke, R.; Schmitt, M.; Popp, J., Spectrometer calibration protocol for Raman spectra recorded with different excitation wavelengths. *Spectrochim. Acta. A* **2015**, *149*, 544-549.
- (227). <https://www.uow.edu.au/research-and-innovation/our-research/research-institutes-and-facilities/australian-institute-for-innovative-materials/uow-electron-microscopy-centre/emc-facilities/>.
- (228). <https://www.globalsino.com/EM/page2489.html>.
- (229). Deepak, F. L.; Mayoral, A.; Arenal, R., *Advanced transmission electron microscopy: Applications to nanomaterials*. Springer: 2015.
- (230). Krivanek, O. L.; Lovejoy, T. C.; Dellby, N.; Aoki, T.; Carpenter, R.; Rez, P.; Soignard, E.; Zhu, J.; Batson, P. E.; Lagos, M. J., Vibrational spectroscopy in the electron microscope. *Nature* **2014**, *514* (7521), 209-212.
- (231). Deepak, F. L.; Casillas, G., Recent highlights in advanced transmission electron microscopy techniques: applications to nanomaterials. In *Nanoscience*, 2017; pp 29-56.
- (232). Tran, B. H.; Wan, S.; Tieu, A. K.; Zhu, H., Tribological Performance of Inorganic Borate at Elevated Temperatures. *Tribol. T.* **2020**, *63* (5), 796-805.
- (233). Tran, B. H. High-temperature lubrication mechanism of alkaline borates. University of Wollongong, 2019.
- (234). Pham, S. T.; Tieu, A. K.; Wan, S.; Hao, J.-C.; Zhu, H.; Nguyen, H. H.; Mitchell, D. R. G., Oxidative and Frictional Behaviour of Binary Sodium Borate-Silicate Composite as High Temperature Lubricant Applications. *Ind. Eng. Chem. Res.* **2019**.
- (235). Cheng, X.; Jiang, Z.; Wei, D.; Wu, H.; Jiang, L., Adhesion, friction and wear analysis of a chromium oxide scale on a ferritic stainless steel. *Wear*. **2019**, *426-427*, 1212-1221.
- (236). Zheng, Z.; Zu, X.; Jiang, X.; Xiang, X.; Huang, J.; Zhou, X.; Li, C.; Zheng, W.; Li, L., Effect of HF etching on the surface quality and laser-induced damage of fused silica. *Optics & Laser Technology* **2012**, *44* (4), 1039-1042.

- (237). Kaczmarek, D.; Domaradzki, J.; Wojcieszak, D.; Prociow, E.; Mazur, M.; Placido, F.; Lapp, S. In *Hardness of nanocrystalline TiO₂ thin films*, Journal of Nano Research, Trans Tech Publ: 2012; pp 195-200.
- (238). Rупpi, S.; Larsson, A.; Flink, A., Nanoindentation hardness, texture and microstructure of α -Al₂O₃ and κ -Al₂O₃ coatings. *Thin Solid Films*. **2008**, *516* (18), 5959-5966.
- (239). Dub, S. N.; Gogotsi, G. A.; Lomonova, E. E., Hardness and fracture toughness of tetragonal zirconia single crystals. *Journal of Materials Science Letters* **1995**, *14* (1), 46-49.
- (240). Lee, S.-W.; Kim, Y.-J.; Lee, Y.-H.; Guim, H.; Han, S. M., Behavior and characteristics of amorphous calcium carbonate and calcite using CaCO₃ film synthesis. *Mater. Des.* **2016**, *112*, 367-373.
- (241). Petrescu, M., Boron nitride theoretical hardness compared to carbon polymorphs. *Diamond and related materials* **2004**, *13* (10), 1848-1853.
- (242). Xia, W.; Zhao, J.; Wu, H.; Zhao, X.; Zhang, X.; Xu, J.; Jiao, S.; Wang, X.; Zhou, C.; Jiang, Z., Effects of oil-in-water based nanolubricant containing TiO₂ nanoparticles in hot rolling of 304 stainless steel. *Journal of Materials Processing Technology* **2018**, *262*, 149-156.
- (243). Meng, Y.; Sun, J.; Wu, P.; Dong, C.; Yan, X., The role of nano-TiO₂ lubricating fluid on the hot rolled surface and metallographic structure of SS41 steel. *Nanomaterials* **2018**, *8* (2), 111.
- (244). Li, L. H.; Cervenka, J.; Watanabe, K.; Taniguchi, T.; Chen, Y., Strong oxidation resistance of atomically thin boron nitride nanosheets. *arXiv preprint arXiv:1403.1002* **2014**.
- (245). Wang, L.; Tieu, A. K.; Zhu, H.; Deng, G.; Hai, G.; Wang, J.; Yang, J., The Effect of Expanded Graphite with Sodium Metasilicate as Lubricant at High Temperature. *Carbon*. **2019**.
- (246). Jimenez, P. S. V., Thermal decomposition of graphite oxidation products DSC studies of internal combustion of graphite oxide. *Mater. Res. Bull.* **1987**, *22* (5), 601-608.
- (247). Li, X.-G.; Lv, Y.; Ma, B.-G.; Wang, W.-Q.; Jian, S.-W., Decomposition kinetic characteristics of calcium carbonate containing organic acids by TGA. *Arabian Journal of Chemistry* **2017**, *10*, S2534-S2538.
- (248). Sangeetha, G.; Sekhar, K. C.; Hameed, A.; Ramadevudu, G.; Chary, M. N.; Shareefuddin, M., Influence of CaO on the structure of zinc sodium tetra borate glasses containing Cu²⁺ ions. *J. Non-Cryst. Solids*. **2021**, *563*, 120784.
- (249). Shih, Y. T.; Jean, J. H., Mixed Modifier Effect in Lithium-Calcium Borosilicate Glasses. *J. Am. Ceram. Soc.* **2017**, *100* (12), 5482-5489.
- (250). Pham, S. T.; Tieu, A. K.; Sencadas, V.; Lei, W.; Liu, D.; Wan, S.; Hao, J., Smart-Responsive Colloidal Capsules as an Emerging Tool to Design a Multifunctional Lubricant Additive. *ACS Appl. Mater. Interfaces*. **2021**, *13* (6), 7714-7724.
- (251). Du, L.-S.; Stebbins, J. F., Site connectivities in sodium aluminoborate glasses: multinuclear and multiple quantum NMR results. *Solid State Nuclear Magnetic Resonance* **2005**, *27* (1-2), 37-49.
- (252). Krishnamurthy, A.; Michaelis, V. K.; Kroeker, S., Network Formation in Borosilicate Glasses with

Aluminum or Gallium: Implications for Nepheline Crystallization. *J. Phys. Chem. C* **2021**, *125* (16), 8815-8824.

(253). Bertmer, M.; Züchner, L.; Chan, J. C.; Eckert, H., Short and medium range order in sodium aluminoborate glasses. 2. Site connectivities and cation distributions studied by rotational echo double resonance NMR spectroscopy. *J. Phys. Chem. B* **2000**, *104* (28), 6541-6553.

(254). Du, W.-F.; Kuraoka, K.; Akai, T.; Yazawa, T., Study of Al₂O₃ effect on structural change and phase separation in Na₂O-B₂O₃-SiO₂ glass by NMR. *J. Mater. Sci.* **2000**, *35* (19), 4865-4871.

(255). Connelly, A.; Hyatt, N.; Travis, K.; Hand, R.; Maddrell, E.; Short, R., The structural role of Zr within alkali borosilicate glasses for nuclear waste immobilisation. *J. Non-Cryst. Solids* **2011**, *357* (7), 1647-1656.

(256). Angeli, F.; Charpentier, T.; De Ligny, D.; Cailleteau, C., Boron speciation in soda-lime borosilicate glasses containing zirconium. *J. Am. Ceram. Soc.* **2010**, *93* (9), 2693-2704.

(257). Wahab, E. A.; Shaaban, K. S., Enhancement of optical and mechanical properties of sodium silicate glasses using zirconia. *Optical and Quantum Electronics* **2020**, *52* (10), 1-19.

(258). Amano, T.; Okazaki, M.; Takezawa, Y.; Shiino, A.; Takeda, M.; Onishi, T.; Seto, K.; Ohkubo, A.; Shishido, T. In *Hardness of oxide scales on Fe-Si alloys at room-and high-temperatures*, Materials science forum, Trans Tech Publ: 2006; pp 469-476.

(259). Gouma, P. I.; Mills, M. J., Anatase-to-rutile transformation in titania powders. *J. Am. Ceram. Soc.* **2001**, *84* (3), 619-622.

(260). Guo, W.; Hu, Y.; Wang, X.; Zhang, P.; Song, L.; Xing, W., Exceptional flame-retardant cellulosic foams modified with phosphorus-hybridized graphene nanosheets. *Cellulose* **2019**, *26* (2), 1247-1260.

(261). Siepmann, J.; Siegel, R. A.; Rathbone, M. J., *Fundamentals and applications of controlled release drug delivery*. Springer: 2012; Vol. 3.

(262). Avnir, D., Organic chemistry within ceramic matrixes: doped sol-gel materials. *Acc. Chem. Res.* **1995**, *28* (8), 328-334.

(263). Pagliaro, M., *Silica-based materials for advanced chemical applications*. Royal Society of Chemistry: 2009.

(264). Huang, L.; Yao, X.; Huang, Y.; Wang, Q., The Preparation of CaCO₃/Wood Composites Using a Chemical Precipitation Method and its Flame-Retardant and Mechanically Beneficial Properties. *Bioresources* **2018**, *13* (3), 6694-6706.

(265). Lin, S.; Kiga, T.; Wang, Y.; Nakayama, K., Energy analysis of CaCO₃ calcination with CO₂ capture. *Energy Procedia* **2011**, *4*, 356-361.

(266). Odler, I., *Special inorganic cements*. CRC Press: London, 2003.

(267). Shi, X.; Rosa, R.; Lazzeri, A., On the coating of precipitated calcium carbonate with stearic acid in aqueous medium. *Langmuir* **2010**, *26* (11), 8474-8482.

(268). Dusza, L., Combined solution of the simultaneous heat loss and finite pulse corrections with the

- laser flash method. *High Temperatures. High Pressures (Print)* **1995**, 27 (5), 467-473.
- (269). Cai, G.-B.; Chen, S.-F.; Liu, L.; Jiang, J.; Yao, H.-B.; Xu, A.-W.; Yu, S.-H., 1, 3-Diamino-2-hydroxypropane-N, N, N', N'-tetraacetic acid stabilized amorphous calcium carbonate: nucleation, transformation and crystal growth. *Cryst. Eng. Comm.* **2010**, 12 (1), 234-241.
- (270). Horozov, T. S.; Binks, B. P., Particle-stabilized emulsions: a bilayer or a bridging monolayer? *Angewandte Chemie International Edition* **2006**, 45 (5), 773-776.
- (271). Yi, H.; Yang, Y.; Gu, X.; Huang, J.; Wang, C., Multilayer composite microcapsules synthesized by Pickering emulsion templates and their application in self-healing coating. *Journal of materials chemistry A* **2015**, 3 (26), 13749-13757.
- (272). Arditty, S.; Schmitt, V.; Giermanska-Kahn, J.; Leal-Calderon, F., Materials based on solid-stabilized emulsions. *J. Colloid. Interface. Sci.* **2004**, 275 (2), 659-664.
- (273). Binks, B. P.; Lumsdon, S. O., Catastrophic Phase Inversion of Water-in-Oil Emulsions Stabilized by Hydrophobic Silica. *Langmuir*. **2000**, 16 (6), 2539-2547.
- (274). Ikeda, Y.; Poompradub, S.; Morita, Y.; Kohjiya, S., Preparation of high performance nanocomposite elastomer: effect of reaction conditions on in situ silica generation of high content in natural rubber. *J. Solgel. Sci. Technol.* **2008**, 45 (3), 299-306.
- (275). Venditti, F.; Angelico, R.; Palazzo, G.; Colafemmina, G.; Ceglie, A.; Lopez, F., Preparation of nanosize silica in reverse micelles: Ethanol produced during TEOS hydrolysis affects the microemulsion structure. *Langmuir*. **2007**, 23 (20), 10063-10068.
- (276). Abend, S.; Lagaly, G., Bentonite and double hydroxides as emulsifying agents. *Clay minerals* **2001**, 36 (4), 557-570.
- (277). Stöber, W.; Fink, A.; Bohn, E., Controlled growth of monodisperse silica spheres in the micron size range. *J. Colloid. Interface. Sci.* **1968**, 26 (1), 62-69.
- (278). Fisichella, M.; Dabboue, H.; Bhattacharyya, S.; Lelong, G.; Saboungi, M.-L.; Warmont, F.; Midoux, P.; Pichon, C.; Guérin, M.; Hevor, T., Uptake of functionalized mesoporous silica nanoparticles by human cancer cells. *J. Nanosci. Nanotechnol.* **2010**, 10 (4), 2314-2324.
- (279). Jiao, Y.; Stillinger, F.; Torquato, S., Optimal packings of superdisks and the role of symmetry. *Phys. Rev. Lett.* **2008**, 100 (24), 245504.
- (280). Wang, H.; Zhu, X.; Tsarkova, L.; Pich, A.; Möller, M., All-Silica Colloidosomes with a Particle-Bilayer Shell. *ACS Nano*. **2011**, 5 (5), 3937-3942.
- (281). Miura, Y.; Kusano, H.; Nanba, T.; Matsumoto, S., X-ray Photoelectron Spectroscopy of Sodium Borosilicate Glasses. *J. Non-Cryst. Solids*. **2001**, 290 (1), 1-14.
- (282). Chu, D. H.; Vinoba, M.; Bhagiyalakshmi, M.; Baek, I. H.; Nam, S. C.; Yoon, Y.; Kim, S. H.; Jeong, S. K., CO₂ mineralization into different polymorphs of CaCO₃ using an aqueous-CO₂ system. *RSC. Adv.* **2013**, 3 (44), 21722-21729.
- (283). Szcześ, A., Effect of the enzymatically modified supported dipalmitoylphosphatidylcholine (DPPC)

- bilayers on calcium carbonate formation. *Colloid. Polym. Sci.* **2016**, *294* (2), 409-419.
- (284). Estrada-Flores, S.; Martínez-Luévanos, A.; Bartolo-Pérez, P.; García-Cerda, L. A.; Flores-Guia, T. E.; Aguilera-González, E. N., Facile synthesis of novel calcium silicate hydrated-nylon 6/66 nanocomposites by solution mixing method. *RSC. Adv.* **2018**, *8* (73), 41818-41827.
- (285). Jaw, K.-S.; Hsu, C.-K.; Lee, J.-S., The thermal decomposition behaviors of stearic acid, paraffin wax and polyvinyl butyral. *Thermochim. Acta.* **2001**, *367*, 165-168.
- (286). Gabal, M.; Hoff, D.; Kasper, G., Influence of the atmosphere on the thermal decomposition kinetics of the CaCO₃ content of PFBC coal flying ash. *J. Therm. Anal. Calorim.* **2006**, *89* (1), 109-116.
- (287). Dollimore, D.; Tong, P.; Alexander, K. S., The kinetic interpretation of the decomposition of calcium carbonate by use of relationships other than the Arrhenius equation. *Thermochim. Acta.* **1996**, *282*, 13-27.
- (288). Sinkó, K.; Pöpl, L.; Gábor, M.; Migály, B., Study of the binary CaCO₃-SiO₂ system by quantitative DTA. *J. Therm. Anal. Calorim.* **1988**, *33* (3), 1003-1011.
- (289). Koryttseva, A.; Navrotsky, A., High-temperature calorimetric study of oxide component dissolution in a CaO-MgO-Al₂O₃-SiO₂ slag at 1450°C. *J. Am. Ceram. Soc.* **2017**, *100* (3), 1172-1177.
- (290). Mustafa, M.; Arif, A.; Masood, K. In *Approximate analytic solutions of transient nonlinear heat conduction with temperature-dependent thermal diffusivity*, Abstract and Applied Analysis, Hindawi: 2014.
- (291). Muller, D. A., Structure and bonding at the atomic scale by scanning transmission electron microscopy. *Nat. Mater.* **2009**, *8* (4), 263-270.
- (292). Chakraborty, J.; Welzel, U.; Mittemeijer, E., Interdiffusion, phase formation, and stress development in Cu-Pd thin-film diffusion couples: Interface thermodynamics and mechanisms. *J. Appl. Phys.* **2008**, *103* (11), 113512.
- (293). Bayon, A.; Liu, M.; Sergeev, D.; Grigore, M.; Bruno, F.; Müller, M., Novel solid-solid phase-change cascade systems for high-temperature thermal energy storage. *Solar Energy* **2019**, *177*, 274-283.
- (294). Yao, L.; Shao, Q.; Xu, X.; Dong, Y.; Liang, C.; He, J.; Jiang, J., Broadband emission of single-phase Ca₃Sc₂Si₃O₁₂: Cr³⁺/Ln³⁺ (Ln= Nd, Yb, Ce) phosphors for novel solid-state light sources with visible to near-infrared light output. *Ceramics International* **2019**, *45* (11), 14249-14255.
- (295). Smentkowski, V. S.; Keenan, M. R.; Arlinghaus, H., Using ToF-SIMS to study industrial surface phenomena. *Surf. Sci.* **2016**, *652*, 39-45.
- (296). Weibel, D.; Wong, S.; Lockyer, N.; Blenkinsopp, P.; Hill, R.; Vickerman, J. C., A C60 primary ion beam system for time of flight secondary ion mass spectrometry: its development and secondary ion yield characteristics. *Anal. Chem.* **2003**, *75* (7), 1754-1764.
- (297). Hoshi, T.; Kudo, M., High resolution static SIMS imaging by time of flight SIMS. *Appl. Surf. Sci.* **2003**, *203*, 818-824.
- (298). Egerton, R. F., *Electron energy-loss spectroscopy in the electron microscope*. Springer Science & Business Media: Boston, 2011.
- (299). Heard, R.; Huber, J. E.; Siviour, C.; Edwards, G.; Williamson-Brown, E.; Dragnevski, K., An

investigation into experimental in situ scanning electron microscope (SEM) imaging at high temperature. *Rev. Sci. Instrum.* **2020**, *91* (6), 063702.

(300). Liang, S.; Li, Q.; Zhu, Y.; Chen, K.; Tian, C.; Wang, J.; Bai, R., Nanoencapsulation of n-octadecane phase change material with silica shell through interfacial hydrolysis and polycondensation in miniemulsion. *Energy* **2015**, *93*, 1684-1692.

(301). Yang, W.; Mao, S.; Yang, J.; Shang, T.; Song, H.; Mabon, J.; Swiech, W.; Vance, J. R.; Yue, Z.; Dillon, S. J., Large-deformation and high-strength amorphous porous carbon nanospheres. *Sci. Rep.* **2016**, *6*, 24187.

(302). Sun, D.; Zhang, H.; Zhang, X.; Yang, J., Robust Metallic Microcapsules: A Direct Path to New Multifunctional Materials. *ACS Appl. Mater. Interfaces.* **2019**, *11* (9), 9621-9628.

(303). Lewis, E. A.; Slater, T.; Prestat, E.; Macedo, A.; O'brien, P.; Camargo, P.; Haigh, S., Real-time imaging and elemental mapping of AgAu nanoparticle transformations. *Nanoscale* **2014**, *6* (22), 13598-13605.

(304). Wang, Z.; Gu, L.; Jeurgens, L. P.; Phillipp, F.; Mittemeijer, E. J., Real-time visualization of convective transportation of solid materials at nanoscale. *Nano. Lett.* **2012**, *12* (12), 6126-6132.

(305). Gorsd, M. N.; Pizzio, L. R.; Blanco, M. N., Synthesis and characterization of hollow silica spheres. *Procedia. Mater. Sci.* **2015**, *8*, 567-576.

(306). Pan, W.; Ye, J.; Ning, G.; Lin, Y.; Wang, J., A novel synthesis of micrometer silica hollow sphere. *Mater. Res. Bull.* **2009**, *44* (2), 280-283.

(307). Du, X.; He, J., Spherical silica micro/nanomaterials with hierarchical structures: Synthesis and applications. *Nanoscale* **2011**, *3* (10), 3984-4002.

(308). Zhang, L.; D'Acunzi, M.; Kappl, M.; Imhof, A.; van Blaaderen, A.; Butt, H.-J.; Graf, R.; Vollmer, D., Tuning the mechanical properties of silica microcapsules. *Phys. Chem. Chem. Phys.* **2010**, *12* (47), 15392-15398.

(309). Song, L.; Ge, X.; Wang, M.; Zhang, Z., Direct preparation of silica hollow spheres in a water in oil emulsion system: The effect of pH and viscosity. *J. Non-Cryst. Solids.* **2006**, *352* (21), 2230-2235.

(310). Teng, Z.; Han, Y.; Li, J.; Yan, F.; Yang, W., Preparation of hollow mesoporous silica spheres by a sol-gel/emulsion approach. *Microporous and Mesoporous Materials* **2010**, *127* (1), 67-72.

(311). Bao, Y.; Shi, C.; Wang, T.; Li, X.; Ma, J., Recent progress in hollow silica: Template synthesis, morphologies and applications. *Microporous and Mesoporous Materials* **2016**, *227*, 121-136.

(312). Da Silva, L. F.; Rodrigues, T.; Figueiredo, M.; De Moura, M.; Chousal, J., Effect of adhesive type and thickness on the lap shear strength. *J. Adhesion.* **2006**, *82* (11), 1091-1115.

(313). Dowling, N. E., *Mechanical behavior of materials: engineering methods for deformation, fracture, and fatigue.* Pearson: 2012.

(314). Chen, Y.-C.; Lu, Z.; Nomura, K.-i.; Wang, W.; Kalia, R. K.; Nakano, A.; Vashishta, P., Interaction of voids and nanoductility in silica glass. *Phys. Rev. Lett.* **2007**, *99* (15), 155506.

- (315). Ševčík, R.; Šašek, P.; Viani, A., Physical and nanomechanical properties of the synthetic anhydrous crystalline CaCO₃ polymorphs: vaterite, aragonite and calcite. *J. Mater. Sci.* **2018**, *53* (6), 4022-4033.
- (316). Zheng, K.; Wang, C.; Cheng, Y.-Q.; Yue, Y.; Han, X.; Zhang, Z.; Shan, Z.; Mao, S. X.; Ye, M.; Yin, Y., Electron-beam-assisted superplastic shaping of nanoscale amorphous silica. *Nat. Commun.* **2010**, *1* (1), 1-8.
- (317). Golla-Schindler, U.; Benner, G.; Orchowski, A.; Kaiser, U., In situ observation of electron beam-induced phase transformation of CaCO₃ to CaO via ELNES at low electron beam energies. *Microsc. Microanal.* **2014**, *20* (3), 715-722.
- (318). Jiang, N.; Silcox, J., Electron irradiation induced phase decomposition in alkaline earth multi-component oxide glass. *J. Appl. Phys.* **2002**, *92* (5), 2310-2316.
- (319). Lichtenberger, O.; Neumann, D., A study of Si-L and O-K ELNES in plant material: SiO₂, Ca-and Zn-silicate in *Minuartia*. *J. Microsc.* **1996**, *183* (1), 45-52.
- (320). Lee, S. W. The Plasticity of Metals at the Sub-micrometer Scale and Dislocation Dynamics in a Thin Film. Stanford University, 2011.
- (321). Mordehai, D.; Lee, S.-W.; Backes, B.; Srolovitz, D. J.; Nix, W. D.; Rabkin, E., Size effect in compression of single-crystal gold microparticles. *Acta. Mater.* **2011**, *59* (13), 5202-5215.
- (322). Liu, M. Understanding the mechanical strength of microcapsules and their adhesion on fabric surfaces. University of Birmingham, 2010.
- (323). Pham, S. T.; Tieu, K. A.; Wan, S.; Hao, J.; Nguyen, H. H.; Mitchell, D. R. G.; Sencadas, V., Intrinsic Effect of Nanoparticles on the Mechanical Rupture of Doubled-Shell Colloidal Capsule via In Situ TEM Mechanical Testing and STEM Interfacial Analysis. *Small.* **2020**, 2001978.
- (324). Parakhonskiy, B. V.; Parak, W. J.; Volodkin, D.; Skirtach, A. G., Hybrids of Polymeric Capsules, Lipids, and Nanoparticles: Thermodynamics and Temperature Rise at the Nanoscale and Emerging Applications. *Langmuir.* **2019**, *35* (26), 8574-8583.
- (325). McNamara, A. K.; Van Keken, P. E.; Karato, S.-I., Development of anisotropic structure in the Earth's lower mantle by solid-state convection. *Nature* **2002**, *416* (6878), 310-314.
- (326). Yin, Y.; Rioux, R. M.; Erdonmez, C. K.; Hughes, S.; Somorjai, G. A.; Alivisatos, A. P., Formation of hollow nanocrystals through the nanoscale Kirkendall effect. *Science.* **2004**, *304* (5671), 711-714.
- (327). De Angeli, M.; Laguardia, L.; Maddaluno, G.; Cippo, E. P.; Ripamonti, D.; Apicella, M.; Bressan, C.; Caniello, R.; Conti, C.; Ghezzi, F., Investigation on FTU dust and on the origin of ferromagnetic and lithiated grains. *Nucl. Fusion.* **2015**, *55* (12), 123005.
- (328). Kanyal, S. S.; Jensen, D. S.; Zhu, Z.; Linford, M. R., Silicon (100)/SiO₂ by ToF-SIMS. *Surf. Sci. Spectra* **2015**, *22* (2), 1-6.
- (329). Pillatsch, L.; Östlund, F.; Michler, J., FIBSIMS: A review of secondary ion mass spectrometry for analytical dual beam focussed ion beam instruments. *Prog. Cryst. Growth Charact. Mater.* **2019**, *65* (1), 1-19.

- (330). Vogel, W., *Glass chemistry*. Springer Science & Business Media: Berlin, 2012.
- (331). Parisini, A.; Angelucci, R.; Dori, L.; Poggi, A.; Maccagnani, P.; Cardinali, G.; Amato, G.; Lerondel, G.; Midellino, D., TEM characterisation of porous silicon. *Micron* **2000**, *31* (3), 223-230.
- (332). Hoog Antink, M. M.; Beutel, S.; Rezwan, K.; Maas, M., Tailoring electrostatic surface potential and adsorption capacity of porous ceramics by silica-assisted sintering. *Materialia* **2020**, *12*, 100735.
- (333). Matsuda, A.; Matsuno, Y.; Tatsumisago, M.; Minami, T., Changes in Porosity and Amounts of Adsorbed Water in Sol-Gel Derived Porous Silica Films with Heat Treatment. *J. Solgel. Sci. Technol.* **2001**, *20* (2), 129-134.
- (334). Zhabrev, V.; Sviridov, S., Ion diffusion in oxide glasses and melts: I. Bibliography. *Glass. Phys. Chem.* **2003**, *29* (2), 140-159.
- (335). Fu, K.; Zhao, Z.; Jin, L., Programmable Granular Metamaterials for Reusable Energy Absorption. *Adv. Funct. Mater.* **2019**, *29* (32), 1901258.
- (336). Chen, X.; Wu, S.; Zhou, J., Influence of porosity on compressive and tensile strength of cement mortar. *Constr. Build. Mater.* **2013**, *40*, 869-874.
- (337). Shan, Z.; Adesso, G.; Cabot, A.; Sherburne, M.; Asif, S. S.; Warren, O.; Chrzan, D.; Minor, A.; Alivisatos, A., Ultrahigh stress and strain in hierarchically structured hollow nanoparticles. *Nat. Mater.* **2008**, *7* (12), 947-952.
- (338). Venkateswara Rao, G.; Shashikala, H. D., Optical and mechanical properties of calcium phosphate glasses. *Glass. Phys. Chem.* **2014**, *40* (3), 303-309.
- (339). Qu, R. T.; Zhang, Z. F., Compressive fracture morphology and mechanism of metallic glass. *J. Appl. Phys.* **2013**, *114* (19), 193504.
- (340). Vaills, Y.; Qu, T.; Micoulaut, M.; Chaimbault, F.; Boolchand, P., Direct evidence of rigidity loss and self-organization in silicate glasses. *J. Phys. Condens. Matter* **2005**, *17* (32), 4889.
- (341). Kilinc, E.; Hand, R. J., Mechanical properties of soda–lime–silica glasses with varying alkaline earth contents. *J. Non-Cryst. Solids.* **2015**, *429*, 190-197.
- (342). Xing, L. Q.; Eckert, J.; Schultz, L., Deformation mechanism of amorphous and partially crystallized alloys. *NsM* **1999**, *12* (1), 503-506.
- (343). Gensamer, M., Strength and ductility. *Metallography, Microstructure, and Analysis* **2017**, *6* (2), 171-185.
- (344). Kim, Y.-H.; Inoue, A.; Masumoto, T., Ultrahigh Tensile Strengths of Al₈₈Y₂Ni₉M₁ (M=Mn or Fe) Amorphous Alloys Containing Finely Dispersed fcc-Al Particles. *Mater. Trans. JIM.* **1990**, *31* (8), 747-749.
- (345). Yang, J.; Keller, M. W.; Moore, J. S.; White, S. R.; Sottos, N. R., Microencapsulation of isocyanates for self-healing polymers. *Macromolecules* **2008**, *41* (24), 9650-9655.
- (346). Patchan, M. W.; Fuller, B. W.; Baird, L. M.; Gong, P. K.; Walter, E. C.; Vidmar, B. J.; Kyei, I.; Xia, Z.; Benkoski, J. J., Robust composite-shell microcapsules via pickering emulsification. *ACS Appl. Mater.*

Interfaces. **2015**, 7 (13), 7315-7323.

(347). Zhang, G. S., Z, Mechanical properties of melamine-formaldehyde microcapsules. *J. Microencapsul.* **2001**, 18 (5), 593-602.

(348). Jacob, R.; Bruno, F., Review on shell materials used in the encapsulation of phase change materials for high temperature thermal energy storage. *Renew. Sust. Energ. Rev.* **2015**, 48, 79-87.

(349). Wang, B.; Sheng, H.; Shi, Y.; Hu, W.; Hong, N.; Zeng, W.; Ge, H.; Yu, X.; Song, L.; Hu, Y., Recent advances for microencapsulation of flame retardant. *Polym. Degrad. Stab.* **2015**, 113, 96-109.

(350). Wagemann, E.; Wang, Y.; Das, S.; Mitra, S. K., Wettability of nanostructured hexagonal boron nitride surfaces: molecular dynamics insights on the effect of wetting anisotropy. *Phys. Chem. Chem. Phys.* **2020**, 22 (4), 2488-2497.

(351). Weng, Q.; Wang, X.; Wang, X.; Bando, Y.; Golberg, D., Functionalized hexagonal boron nitride nanomaterials: emerging properties and applications. *Chem. Soc. Rev.* **2016**, 45 (14), 3989-4012.

(352). Georgakilas, V.; Otyepka, M.; Bourlinos, A. B.; Chandra, V.; Kim, N.; Kemp, K. C.; Hobza, P.; Zboril, R.; Kim, K. S., Functionalization of Graphene: Covalent and Non-Covalent Approaches, Derivatives and Applications. *Chem. Rev.* **2012**, 112 (11), 6156-6214.

(353). Yadav, V.; Kulshrestha, V., Boron nitride: a promising material for proton exchange membranes for energy applications. *Nanoscale* **2019**, 11 (27), 12755-12773.

(354). Lei, W.; Mochalin, V. N.; Liu, D.; Qin, S.; Gogotsi, Y.; Chen, Y., Boron Nitride Colloidal Solutions, Ultralight Aerogels and Freestanding Membranes Through One-step Exfoliation and Functionalization. *Nat. Commun.* **2015**, 6 (1), 1-8.

(355). Qu, J.; Truhan, J. J., An Efficient Method for Accurately Determining Wear Volumes of Sliders With Non-Flat Wear Scars and Compound Curvatures. *Wear.* **2006**, 261 (7-8), 848-855.

(356). Gonzalez Ortiz, D.; Pochat-Bohatier, C.; Cambedouzou, J.; Balme, S.; Bechelany, M.; Miele, P., Inverse Pickering Emulsion Stabilized by Exfoliated Hexagonal-Boron Nitride (h-BN). *Langmuir.* **2017**, 33 (46), 13394-13400.

(357). Gorbachev, R. V.; Riaz, I.; Nair, R. R.; Jalil, R.; Britnell, L.; Belle, B. D.; Hill, E. W.; Novoselov, K. S.; Watanabe, K.; Taniguchi, T., Hunting for monolayer boron nitride: optical and Raman signatures. *Small.* **2011**, 7 (4), 465-468.

(358). Peter, R.; Bozanic, A.; Petravic, M.; Chen, Y.; Fan, L. J.; Yang, Y. W., Formation of Defects in Boron Nitride by Low Energy Ion Bombardment. *J. Appl. Phys.* **2009**, 106 (8), 083523.

(359). McDougall, N. L.; Partridge, J. G.; Nicholls, R. J.; Russo, S. P.; McCulloch, D. G., Influence of Point Defects on the Near Edge Structure of Hexagonal Boron Nitride. *Phys. Rev. B.* **2017**, 96 (14), 144106.

(360). Barrau, O.; Boher, C.; Gras, R.; Rezai-Aria, F., Analysis of the Friction and Wear Behaviour of Hot Work Tool Steel for Forging. *Wear.* **2003**, 255 (7-12), 1444-1454.

(361). Pham, S. T.; Tieu, A. K.; Wan, S.; Hao, J.; Zhu, H.; Tran, N. V.; Do, P. T., Intrinsic Effect of Alkali Concentration on Oxidation Reactivity and High-Temperature Lubricity of Silicate Melts between Rubbed

Steel/Steel Contacts. *Langmuir*. **2020**.

(362). Tsaur, C.-C.; Rock, J. C.; Chang, Y.-Y., The Effect of NaCl Deposit and Thermal Cycle on an Aluminide Layer Coated on 310 Stainless Steel. *Mater. Chem. Phys.* **2005**, *91* (2), 330-337.

(363). Bourhis, Y.; John, C. S., Na₂SO₄-and NaCl-Induced Hot Corrosion of Six Nickel-Base Superalloys. *Oxid. Met.* **1975**, *9* (6), 507-528.

(364). Rolls, R.; Shaw, R., The Influence of Borate Coatings on the High-Temperature Oxidation of Iron. *Corros. Sci.* **1974**, *14* (7), 431-441.

(365). Pham, S. T.; Tieu, A. K.; Wan, S.; Hao, J.; Zhu, H.; Nguyen, H. H.; Mitchell, D. R. G., Oxidative and Frictional Behavior of a Binary Sodium Borate–Silicate Composite in High-Temperature Lubricant Applications. *Ind. Eng. Chem. Res.* **2020**, *59* (7), 2921-2933.

(366). Lu, X.; Khonsari, M.; Gelinck, E., The Stribeck Curve: Experimental Results and Theoretical Prediction. *J. Tribol.* **2006**, *128* (4), 789-794.

(367). Greiner, C.; Liu, Z.; Strassberger, L.; Gumbsch, P., Sequence of Stages in the Microstructure Evolution in Copper under Mild Reciprocating Tribological Loading. *ACS Appl. Mater. Interfaces.* **2016**, *8* (24), 15809-15819.

(368). Curry, J. F.; Babuska, T. F.; Furnish, T. A.; Lu, P.; Adams, D. P.; Kustas, A. B.; Nation, B. L.; Dugger, M. T.; Chandross, M.; Clark, B. G., Achieving Ultralow Wear with Stable Nanocrystalline Metals. *Adv. Mater.* **2018**, *30* (32), 1802026.

(369). Fuhrmann, S.; Deschamps, T.; Champagnon, B.; Wondraczek, L., A Reconstructive Polyamorphous Transition in Borosilicate Glass Induced by Irreversible Compaction. *J. Chem. Phys.* **2014**, *140* (5), 054501.

(370). Winterstein-Beckmann, A.; Möncke, D.; Palles, D.; Kamitsos, E. I.; Wondraczek, L., Structure and properties of orthoborate glasses in the Eu₂O₃–(Sr, Eu) O–B₂O₃ quaternary. *J. Phys. Chem. B.* **2015**, *119* (7), 3259-3272.

(371). Cai, Q.; Scullion, D.; Falin, A.; Watanabe, K.; Taniguchi, T.; Chen, Y.; Santos, E. J. G.; Li, L. H., Raman Signature and Phonon Dispersion of Atomically Thin Boron Nitride. *Nanoscale* **2017**, *9* (9), 3059-3067.

(372). Rastogi, P. K.; Sahoo, K. R.; Thakur, P.; Sharma, R.; Bawari, S.; Podila, R.; Narayanan, T. N., Graphene–hBN non-van der Waals vertical heterostructures for four- electron oxygen reduction reaction. *Phys. Chem. Chem. Phys.* **2019**, *21* (7), 3942-3953.

(373). Bois, L.; L'Haridon, P.; Laurent, Y.; Gouin, X.; Grange, P.; Létard, J.-F.; Birot, M.; Pillot, J.-P.; Dunoguès, J., Characterization of a boro-silicon oxynitride prepared by thermal nitridation of a polyborosiloxane. *Journal of alloys and compounds* **1996**, *232* (1-2), 244-253.

(374). Pham, S. T.; Tieu, A. K.; Wan, S.; Hao, J.; Zhu, H.; Tran, N. V.; Do, P. T., Intrinsic Effect of Alkali Concentration on Oxidation Reactivity and High-Temperature Lubricity of Silicate Melts between Rubbed Steel/Steel Contacts. *Langmuir*. **2020**, *36* (27), 7850-7860.

(375). Michel, F.; Cormier, L.; Lombard, P.; Beuneu, B.; Galois, L.; Calas, G., Mechanisms of Boron

- Coordination Change between Borosilicate Glasses and Melts. *J. Non-Cryst. Solids*. **2013**, 379, 169-176.
- (376). Ouyang, J.-H.; Liang, X.-S., High-Temperature Solid Lubricating Materials. In *Encyclopedia of Tribology*, Wang, Q. J.; Chung, Y.-W., Eds. Springer US: Boston, MA, 2013; pp 1671-1681.
- (377). Wan, S.; Tieu, A. K.; Zhu, Q.; Zhu, H.; Cui, S.; Mitchell, D. R.; Kong, C.; Cowie, B.; Denman, J. A.; Liu, R., Chemical Nature of Alkaline Polyphosphate Boundary Film at Heated Rubbing Surfaces. *Sci. Rep.* **2016**, 6 (1), 26008.
- (378). Pham, S. T.; Tieu, A. K.; Sencadas, V.; Lei, W.; Liu, D.; Wan, S.; Hao, J., Smart-Responsive Colloidal Capsules as an Emerging Tool to Design a Multifunctional Lubricant Additive. *ACS Appl. Mater. Interfaces*. **2021**.
- (379). Wang, L.; Tieu, A. K.; Wang, J.; Sang, P. T.; Xia, C.; Zhu, H.; Deng, G., High load capability, sticking scale inhabitation and promising lubrication of sodium carbonate coating for steel/steel contact at high temperature. *Tribol. Int.* **2021**, 153, 106594.
- (380). Doan, L. C.; Ohmori, Y.; Nakai, K., Precipitation and dissolution reactions in a 6061 aluminum alloy. *Mater. Trans. JIM*. **2000**, 41 (2), 300-305.
- (381). Habib, K. A.; Damra, M. S.; Saura, J. J.; Cervera, I.; Bellés, J., Breakdown and Evolution of the Protective Oxide Scales of AISI 304 and AISI 316 Stainless Steels under High-Temperature Oxidation. *International Journal of Corrosion* **2011**, 2011, 824676.
- (382). Vesel, A.; Mozetic, M.; Drenik, A.; Hauptman, N.; Balat-Pichelin, M., High temperature oxidation of stainless steel AISI316L in air plasma. *Appl. Surf. Sci.* **2008**, 255 (5, Part 1), 1759-1765.
- (383). Yan, Y.; Xu, X.; Zhou, D.; Wang, H.; Wu, Y.; Liu, X.; Lu, Z., Hot corrosion behaviour and its mechanism of a new alumina-forming austenitic stainless steel in molten sodium sulphate. *Corros. Sci.* **2013**, 77, 202-209.
- (384). Eliaz, N.; Shemesh, G.; Latanision, R. M., Hot corrosion in gas turbine components. *Engineering Failure Analysis* **2002**, 9 (1), 31-43.
- (385). Jonsson, T.; Karlsson, S.; Hooshyar, H.; Sattari, M.; Liske, J.; Svensson, J.-E.; Johansson, L.-G., Oxidation after breakdown of the chromium-rich scale on stainless steels at high temperature: internal oxidation. *Oxid. Met.* **2016**, 85 (5), 509-536.
- (386). Stringer, J., High-temperature corrosion of superalloys. *Mater. Sci. Technol.* **1987**, 3 (7), 482-493.
- (387). Lai, G. Y., High temperature corrosion of engineering alloys. **1990**.
- (388). Stott, F.; Wei, F., High temperature oxidation of commercial austenitic stainless steels. *Mater. Sci. Technol.* **1989**, 5 (11), 1140-1147.
- (389). Kumar, S.; Supriya, S.; Pandey, R.; Pradhan, L. K.; Kar, M. In *Crystal structure and magnetic properties of Cr doped barium hexaferrite*, AIP Conference Proceedings, AIP Publishing LLC: 2018; p 130040.
- (390). Shinde, V.; Dahotre, S.; Singh, L., Synthesis and characterization of aluminium substituted calcium hexaferrite. *Heliyon* **2020**, 6 (1), e03186.

- (391). Borisov, A.; Behrens, H.; Holtz, F., Effects of strong network modifiers on Fe³⁺/Fe²⁺ in silicate melts: an experimental study. *Contrib. Mineral. Petr.* **2017**, *172* (5), 34.
- (392). Abdullah, T. K. Study of the redox and acid-base properties of soda-lime silicate glass: application to the high temperature corrosion of Ni-based alloys and ceramic materials. Université de Lorraine, 2013.
- (393). Mishra, R. K.; Kumar, S.; Tomar, B. S.; Tyagi, A. K.; Kaushik, C. P.; Raj, K.; Manchanda, V. K., Effect of Barium on Diffusion of Sodium in Borosilicate Glass. *J. Hazard. Mater.* **2008**, *156* (1), 129-134.
- (394). Kimura, T., Molten salt synthesis of ceramic powders. *Advances in ceramics-synthesis and characterization, processing and specific applications* **2011**, 75-100.
- (395). Rahaman, M. N., *Ceramic processing and sintering*. CRC press: 2017; Vol. 1.
- (396). Sutter, G.; Ranc, N., Flash temperature measurement during dry friction process at high sliding speed. *Wear.* **2010**, *268* (11-12), 1237-1242.
- (397). Baldan, A., Review progress in Ostwald ripening theories and their applications to nickel-base superalloys Part I: Ostwald ripening theories. *J. Mater. Sci.* **2002**, *37* (11), 2171-2202.
- (398). Selway, N.; Chan, V.; Stokes, J. R., Influence of fluid viscosity and wetting on multiscale viscoelastic lubrication in soft tribological contacts. *Soft. Matter.* **2017**, *13* (8), 1702-1715.
- (399). Farhat, Z. N.; Ding, Y.; Northwood, D. O.; Alpas, A. T., Effect of grain size on friction and wear of nanocrystalline aluminum. *Mater. Sci. Eng. A* **1996**, *206* (2), 302-313.
- (400). Jin, W.; Choi, J.-Y.; Lee, Y.-Y., Effect of roll and rolling temperatures on sticking behavior of ferritic stainless steels. *ISIJ. Int.* **1998**, *38* (7), 739-743.
- (401). Cychosz, K. A.; Guillet-Nicolas, R.; García-Martínez, J.; Thommes, M., Recent advances in the textural characterization of hierarchically structured nanoporous materials. *Chem. Soc. Rev.* **2017**, *46* (2), 389-414.
- (402). Thommes, M.; Kaneko, K.; Neimark, A. V.; Olivier, J. P.; Rodriguez-Reinoso, F.; Rouquerol, J.; Sing, K. S., Physisorption of gases, with special reference to the evaluation of surface area and pore size distribution (IUPAC Technical Report). *Pure. Appl. Chem.* **2015**, *87* (9-10), 1051-1069.
- (403). Rasmussen, C. J.; Vishnyakov, A.; Thommes, M.; Smarsly, B. M.; Kleitz, F.; Neimark, A. V., Cavitation in metastable liquid nitrogen confined to nanoscale pores. *Langmuir.* **2010**, *26* (12), 10147-10157.